ICE-MARGINAL SUBGLACIAL CHANNELS AND THEIR RELATIONSHIP TO THE RAPID RETREAT OF TEMPERATE ALPINE GLACIERS

Egli Pascal Emanuel

UNIL | Université de Lausanne

Faculté des Géosciences et de l'Environnement

Ice-marginal subglacial channels and their relationship to the rapid retreat of temperate Alpine glaciers

PHD THESIS

presented at the

Faculté des Géosciences et de l'Environnement de l'Université de Lausanne,

Institute of Earth Surface Dynamics

To obtain the degree of

Doctor in Geography

by

Pascal Emanuel Egli

B.Sc École Polytechnique Fédérale de Lausanne, Switzerland

M.Sc Eidgenössische Technische Hochschule Zürich, Switzerland

Thesis director

Prof. Dr. Stuart N. Lane (IDYST/UNIL)

Thesis co-director

Dr. James Irving (ISTE/UNIL)

Jury

Jury president:	Prof. Dr. Marie-Elodie Perga (IDYST/UNIL)
Internal expert:	Dr. Christophe Lambiel (IDYST/UNIL)
External expert:	Prof. Dr. Daniel Farinotti (ETH Zurich)
External expert:	Dr. Tristram Irvine-Fynn (Aberystwyth University)

Lausanne, August 2022

UNIL | Universite de Lausanne
Faculte des geosciences et de l'environnement
batiment Geopolis bureau 4631

IMPRIMATUR

Vu le rapport présenté par le jury d'examen, composé de

Présidente de la séance publique :	Mme la Professeure Marie-Elodie Perga
Présidente du colloque :	Mme la Professeure Marie-Elodie Perga
Directeur de thèse :	M. le Professeur Stuart Lane
Co-directeur de thèse :	M. le Professeur James Irving
Expert interne :	M. le Docteur Christophe Lambiel
Expert externe :	M. le Docteur Tristram lrvine-Fynn
Expert externe :	M. le Docteur Daniel Farinotti

Le Doyen de la Faculté des géosciences et de l'environnement autorise l'impression de la thèse de

Monsieur Pascal Emanuel EGLI

Titulaire d'un
Master of Environmental Engineering
de Swiss Federal Institute of Technology in Zurich

intitulée

ICE-MARGINAL SUBGLACIAL CHANNELS AND THEIR RELATIONSHIP TO THE RAPID RETREAT OF TEMPERATE ALPINE GLACIERS

Lausanne, le 19 août 2022

Pour le Doyen de la Faculté des géosciences et de l'environnement

Professeure Marie-Elodie Perga

To my mother, Marianne Vera Staub (9.1.1964 – 14.10.2017). Thank you for everything.

To Rahel Egli & Thomas Egli – thank you for your continuing support and love.

Summary

Temperate Alpine glaciers have been retreating rapidly since the late 1980s, changing the hydrology and sediment regimes of Alpine streams and modifying entire glacial landscapes in the process. How glaciers and their outlet streams react to rapid atmospheric warming depends not only on melt processes at their surface, but also on the structure and functioning of their sub- and englacial hydrological systems. Whilst there has been substantial attention given to changes in surface-melt-driven ablation, much less attention has been given to internal melt and the role of snout margin collapse, especially relating to the combined effects of surface and subglacial channel melt. This thesis aims: (1) to quantify the planform morphology of subglacial channels at the snout margin of two Alpine glaciers; (2) to establish the relationship between this morphology, ice deformation and snout collapse; and (3) to assess which properties determine surface ablation patterns near the glacier terminus.

The first section of the thesis focuses on the detection of subglacial channels in the snout marginal areas of the Haut Glacier d'Arolla and the Glacier d'Otemma using high density ground-penetrating radar (GPR) surveys. Three-dimensional data processing and amplitude analysis of the GPR reflection along the glacier bed was used to map the channels. At the Haut Glacier d'Arolla, two relatively straight channels were identified, the positions of which corresponded well to the locations of channel outlets at the glacier terminus. At the Glacier d'Otemma, a major subglacial conduit was detected having similar dimensions to those identified at the Haut Glacier d'Arolla, but with greater sinuosity. The position of this channel was confirmed by UAV-based imagery acquired after glacier margin collapse. The results of this section confirm that high-density 3D GPR surveys can be used to map subglacial channels near temperate Alpine glacier margins.

Section two of the thesis investigates the ice-marginal collapse that occurred at the Glacier d'Otemma. In addition, we examine 21 other Swiss glaciers for the presence of similar features, to generalize the conditions driving collapse events. High resolution UAV data from the Glacier d'Otemma were compared with ablation stake data and with GPR-derived channel outlines to determine whether enhanced surface lowering was due to the presence of a subglacial channel or to other factors. A pattern of surface lowering was detected which matches the position of the main subglacial outlet channel. This suggests that ice creep towards major subglacial channels can be detected at the glacier surface, and that channel features may develop into a collapse feature if the melt is strong enough, the ice is shallow enough, and longitudinal ice flow is negligible. The analysis of other Swiss glaciers suggests that collapse features tend to occur when mean air temperatures increase strongly, making valley glaciers retreat rapidly.

The third section of the thesis systematically analyzes melt patterns at the margin of the Glacier d'Otemma for 10 distinct areas having varying topography and surface texture by subtracting multi-day high-resolution DEMs, obtained from UAV data via a standard SfM-MVS photogrammetric procedure, to obtain DEMs of difference. The analysis shows that the spatial variability of ablation in the snout marginal area of a temperate Alpine glacier is controlled not only by the effect of shortwave radiation on microtopography, but also by surface roughness and albedo, as well as by debris cover. Supraglacial channels can have a significant impact on ablation patterns due to their surface topography, more so than previous studies assumed.

This PhD thesis provides new insights into processes in the snout marginal zone of temperate Alpine glaciers. It provides new knowledge about the geometry of large subglacial channels, and methods to investigate such channels, which tend to be wide, shallow and meandering, it sheds light on the origin and evolution of channel collapse features, and it contributes to a better understanding of the properties influencing the spatial distribution of surface melt.

Résumé

Les glaciers alpins tempérés ont reculé rapidement depuis la fin des années 1980, entraînant un changement de l'hydrologie et du transport des sédiments dans les rivières alpines, et modifiant des paysages glaciaires entiers. La réponse des glaciers et de ses torrents à un réchauffement rapide de l'atmosphère ne dépend pas seulement des processus d'ablation à la surface, mais aussi du fonctionnement de leur système hydrologique à l'intérieur du glacier. Alors que les processus de fonte à la surface ont été largement étudiés, on sait beaucoup moins sur la fonte interne et sur les processus d'effondrement des chenaux sous-glaciaires. Les objectifs de cette thèse de doctorat sont : (1) De quantifier la morphologie en plan des chenaux sous-glaciaires dans la zone terminale de deux glaciers alpins ; (2) d'établir la relation entre cette morphologie, la déformation à la surface du glacier et l'effondrement d'une zone au terminus du glacier ; et (3) de déterminer quels processus contrôlent la distribution spatiale de l'ablation à la surface du glacier.

La première partie de la thèse se focalise sur la détection des chenaux sous-glaciaires dans la zone frontale du Haut Glacier d'Arolla et du Glacier d'Otemma en utilisant des relevés au géoradar (GPR) à haute résolution. Le traitement des données en 3D et l'analyse de l'amplitude du signal radar au niveau du lit du glacier a été utilisé pour cartographier les chenaux sous-glaciaires. Pour le Haut Glacier d'Arolla deux chenaux plutôt droits ont été identifiés, et leurs positions correspondaient bien avec l'emplacement des exutoires des chenaux. Pour le Glacier d'Otemma un chenal sous-glaciaire majeur a été détecté, avec une largeur de 10 à 20 mètres, et une sinuosité supérieure à celle des chenaux détectés au Haut Glacier d'Arolla. La position de ce chenal a été confirmée par l'imagerie du drone après l'effondrement du chenal. Ces résultats confirment que les relevés 3D à haute résolution au radar peuvent être utilisés pour cartographier les chenaux sous-glaciaires en proximité des marges d'un glacier alpin tempéré.

La deuxième partie de la thèse étudie en détail l'effondrement du glacier proche de la marge qui s'est produit au Glacier d'Otemma. En plus, 21 glaciers suisses ont été examinés, dont 11 avec des événements d'effondrement similaires, afin de généraliser les conditions qui conduisent à l'effondrement. Des MNTs, créés par l'imagerie du drone, ont été comparés aux données d'ablation mesurés manuellement afin de déterminer l'affaissement de la glace au-dessus du chenal principal dont la position avait été déterminée avec le géoradar. L'affaissement observé indique que des effondrements peuvent se produire à l'emplacement des chenaux principaux si l'ablation est suffisamment forte, la dynamique de glace est réduite et la glace est peu épaisse. L'analyse des autres glaciers suisses montre que la fréquence de ces effondrements a augmenté avec une augmentation moyenne marquée de la température de l'air en été.

La troisième partie de cette thèse analyse systématiquement la variabilité spatiale de l'ablation proche de la marge du Glacier d'Otemma en examinant 10 zones avec des topographies et textures de surface différentes. Des modèles numériques de terrain créés à partir de la photogrammétrie du drone sont soustraits l'un de l'autre afin de calculer l'ablation. Les résultats montrent que l'ablation est d'abord contrôlée par l'effet de la radiation solaire sur la microtopographie, mais aussi par l'effet de la rugosité et de l'albedo, ainsi que par le débris supraglaciaire. Aussi les cours d'eau supraglaciaires ont un impact significatif sur l'ablation – probablement plus important qu'estimé par des études précédentes.

Cette thèse produit du nouveau savoir sur les processus dans la marge des glaciers alpins tempérés. Le travail a produit des nouveaux résultats sur la géométrie des grands chenaux sous-glaciaires et les méthodes pour les investiguer. De plus, il fait comprendre l'origine et l'évolution des effondrements de chenaux sous-glaciaires, et il améliore la compréhension des facteurs qui influencent l'ablation à la surface du glacier.

Acknowledgements

Several people have contributed to the writing and publication of this thesis, both in technical ways and in personal aspects. Without them, this work would not have been possible.

First and foremost, I would like to thank my thesis supervisor, Dr. Stuart Lane, for his invaluable support during my time at UNIL. His optimistic and positive attitude made many seemingly 'impossible' things possible. He was very patient despite timewise slow progress, he supported my athlete activities which sometimes took up a great amount of time, and he kept pushing me to think differently. His technical support and help with paper editing was very appreciated and significantly contributed to the success of this thesis.

I would like to thank my thesis co-supervisor, Dr. James Irving, for his very valuable and dedicated support in technical aspects of geophysics, for help with paper editing, for interesting discussions and practical help with fieldwork, as well as personal and moral support when things got tough. His patience and kindness have been of great help. Thanks to him I have acquired new knowledge and skills about geophysics and GPR and been able to publish an impactful paper about high-resolution mapping of subglacial marginal channels.

Further, I would like to thank Dr. Christophe Lambiel and Dr. Frédéric Hermann, who were part of my internal thesis committee with the aim of assessing annual progress. I would like to thank them for their support, critical assessment of my work, and technical inputs, as well as for their availability during my time at UNIL.

I would like to thank Dr. Aurélien Ballu and Micaela Faria for their technical and logistical support with fieldwork and lab use.

Big thanks also go to Dr. Ludovic Baron for his support with setting up the GPR antenna in conjunction with the dGPS system and for teaching me many important perks about electronics, geophysics and field applications.

In our research group I would like to thank my former and present collaborators for their friendship, help with fieldwork, exchanges about research, moral support as well as technical support: Gilles Antoniazza, Maarten Bakker, Christelle Gabbud, Gelare Moradi, Romain Cardot, Annegret Larsen, Matteo Roncoroni, Davide Mancini, Romain Cardot, Jamal Shokory, Wen Dai, Jufang Ni, Matt Jenkin, Flo Miesen, Nazimul Islam, Tom Müller, Mathilde Bayens, Valentin Pipoz, Bruno Belotti and Boris Ouvry.

I would like to thank former and present members of the Institute of Earth Surface Dynamics at UNIL for their friendship, collaboration and both technical and personal help during my thesis: Sebastián Vivero, Ignes Castro, Elisa Giaccone, Vjeran Visnievic, Benjamin Lehmann, Mike Rowley, Fien De Doncker, Pascal Perolo and many more.

I would like to thank my family for their continuous support and friendship. Specifically, I would like to thank my mother, Marianne Vera Egli-Staub, who passed away during my thesis, for everything that she did for me as a mother and friend and for being the wonderful human that she was. I would like to thank my father, Thomas Egli, for his continuous support both in life questions, his friendship and for his collaboration within Egli Engineering AG. I would like to thank my beloved sister, Rahel Egli, for always being there – both in difficult and in bright times – with her patient and strong mood and physical and mental support, as a sister, medical doctor, and best friend. Further, I am thanking my grand-parents Dora & Lucas, and Betty & Fritz (†), my uncle Martin & family, Regi & fam and Elisabeth & fam for support and interesting conversations whenever we spent time together.

I would like to thank my partner, Sofiya Cox, for being there for me and for being my best friend. I also thank her for her mental support and for her love.

I would like to thank all my friends, close and far, for their continuous support, exchange, and friendship: Roberto & Camille-Charlotte, Giulia, Fränzi, Mélina, Gerard, Seb, Pere, Benjamin, Jonas, Francesco, Hillary, Mathilde, Tom, Emmanuel, Bastien, Carolina, Karl, Nico, Sam, Stian, Katrine, and several more who will certainly recognize themselves. Thank you!

Finally, I would like to thank my sponsors and collaborators in the world of trail running who made it possible to combine an ambitious athletic career in trail running and ski mountaineering with a PhD thesis and assistantship: Dynafit, Perennial SA, Fonds du Sport du Canton de Vaud, ATALC, MotionLab, Mulebar Suisse, Sponsor Sports Food, KAEX, Polar, Fairphone, Farmy, Skyrunning, Golden Trail Series, World Mountain Running Association, Swiss Athletics Federation, Vert.Run, MotionLab, Lyneline, Hefti Sports, Sports Universitaires UNIL/EPFL, Protect Our Winters Switzerland, Organi Coach.

Special thanks go to the external experts who assessed this thesis and helped improve it with valuable comments both in the document and during the private thesis defense: Dr. Tristram Irvine-Fynn from Aberystwyth University and Prof. Dr. Daniel Farinotti from ETH Zurich.

Crans-Montana, August 2022 Pascal E. Egli

Financial support

This thesis and the fieldwork conducted at Glacier d'Otemma in conjunction with other projects of the AlpWISE research group was supported by the Canton de Vaud and by the Swiss National Science Foundation. The financial contribution by the University of Lausanne was essential for the acquisition of technical equipment, for financing field campaigns, and for the completion of this work in general.

We thank the foundation "La Murithienne" (Société valaisanne des Sciences Naturelles) for contributing with a grant for fieldwork at Glacier d'Otemma in summer 2018.

Thanks go to the "Société Académique Vaudoise" for a grant obtained by Pascal Egli that covered the living expenses for the last 4 months of thesis writing.

Table of contents

Basic acronyms

ABL	**Atmospheric Boundary Layer**
a.s.l	**Above sea level**
DEM	**Digital Elevation Model**
DoD	**DEM of Difference**
GdO	**Glacier d'Otemma**
dGPS	**Differential Global Positioning System**
GCP	**Ground Control Point**
GLAMOS	**Glacier Monitoring Switzerland**
GLIMS	**Global Land Ice Measurements from Space**
GLOF	**Glacier Lake Outburst Flood**
GPR	**Ground Penetrating Radar**
HGdA	**Haut Glacier d'Arolla**
IPCC	**Intergovernmental Panel on Climate Change**
IDYST	**Institute of Earth Surface Dynamics (University of Lausanne)**
MVS	**multi-view stereo (from photogrammetry)**
LiDAR	**Light Detection and Ranging (laser scanner)**
RTK	**Real-Time Kinematic (dGPS measurement mode)**
SfM	**Structure from Motion (from photogrammetry)**
SNF	**Swiss National Science Foundation**
UAV	**Uncrewed Aerial Vehicle (drone)**
UNIL	**Université de Lausanne**
VAW	**Laboratory of Hydraulics, Hydrology and Glaciology (ETH Zurich)**

Prologue

Glaciers are intriguing and complex systems that are in constant evolution. Studying their nature and processes requires reuniting a vast bandwidth of disciplines: from meteorology and climatology to snow hydrology and micrometeorology, to the dynamics of a viscous fluid, over karst-like systems, hydraulics of pressurized and open channel flow, to sediment transport and sediment mechanics. Besides the value of glaciers as a resource and a landscape feature, it is this diversity of processes that attracts me most when it comes to studying them. And yet, even during this 5.5 year-long PhD thesis and assistantship, I have not been able to fully understand even just a fraction of all those processes happening at the surface and in the inside of Alpine glaciers. Conducting fieldwork has significantly contributed to a better understanding of processes, but reading past studies and assessing modelling results were just as important.

My dream for this PhD thesis was to combine my favorite disciplines in science to gain new knowledge: fluid dynamics and glacier hydrology. I must say that my expectations were maybe too high in this regard and that studying subglacial channels via detailed fluid dynamics modelling, in conjunction with ground-penetrating radar surveys and LiDAR surveys, remains an objective. But this thesis has given me lots of knowledge, skills and experience that I would not have anticipated, including fieldwork and logistics experience using different methods, the capacity to refocus when something unexpected happens, the capacity to acquire new skills (GPR) and the belief in reaching my objectives even when things don't go as planned.

I can say that I know glaciers. I have crossed dozens of different glaciers in North America, South America, the Alps, the Caucasus, and the Himalayas. Nevertheless, 'getting to know' glaciers can happen in different ways. During 3-4 field seasons at the Glacier d'Otemma I spent countless hours walking and standing in the same 300 × 500 m area just to record GPR data, fly the drone, inject tracer into moulins or to measure ground targets. Then, in April 2021, I traversed several glaciers in 17.7 h, when we skied the Haute Route from Chamonix to Zermatt non-stop over 108 km, including Glacier d'Otemma, which we crossed in about 1.5h. That bigger perspective helps to understand the greater connections, local climate zones, and the morphology of the Alps, but it is nothing compared to a global perspective that we obtain thanks to satellite imagery, climate models and glacier inventories. I believe that all three perspectives are necessary to truly understand how glacial systems work: The detailed and local, intensely studied one, the regional perspective and the global perspective that spans mountain ranges. The main positive out-take from this work is that it has only stimulated my appetite for studying glacial processes more thoroughly, and to discover more remote glacial systems. P.E.

I INTRODUCTION

I.1 Aims and objectives

This thesis has a core focus on the margins of temperate Alpine glaciers. These are retreating rapidly, whether by melt at the surface or at the glacier bed. Thus, the aim of this thesis is to improve our knowledge of ice melt at such margins from both below and above. In turn this requires consideration of the geometry of subglacial channels that form at the beds of temperate Alpine glaciers; their relationship with rapid glacier retreat due to channel melt-out and collapse; and surface patterns of melt on what is often a morphologically heterogenous surface.

Existing literature has investigated the geometry, functioning and pathways of subglacial channels with tracer experiments, boreholes, numerical modelling and subglacial exploration as well as using Ground Penetrating Radar (GPR) surveys (Nienow et al., 1998; Fountain et al., 2005; Gulley et al., 2009; Werder et al., 2013; Gulley et al., 2014; Beaud et al., 2018; DeFleurian et al., 2018). Such research has yielded substantial knowledge of the likely nature of the subglacial drainage system, of discharge hydrographs (Nienow et al., 1998) and of the large-scale geometry of channels in the ablation zone of glaciers (Gulley et al., 2012). Theoretical considerations have hypothesized that subglacial channels underneath shallow ice would be non-pressurized and deviate from the traditional semi-circular model (Hooke, 1990). But there has been little field evidence confirming this theory. The precise geometry of subglacial channels in the snout marginal area of Alpine glaciers is still largely unknown due to their inaccessibility during the ablation season, when channels carry a substantial discharge of water, of several cubic meters per second for a medium-sized Alpine glacier (Hubbard & Nienow, 1997).

Besides evacuating meltwater, subglacial channels transport sediment and they provide an environment for sub- and englacial melt processes to act (Hooke, 1989; Hock, 2005). A subglacial melt process that has seen little attention so far is internal channel melt-out, leading to glacier surface collapse. This process has been described since the 1950s, but only few studies have tried to understand the underlying mechanisms and the frequency of occurrence (Paige, 1954; Stocker-Waldhuber et al., 2017; Kellerer-Pirklbauer & Kulmer, 2019). The discovery and monitoring of such a collapse feature at the Glacier d'Otemma, during the ablation season of 2018, has made it one of the primary objectives of this thesis to study and to improve understanding of the processes leading to such a collapse event.

Glacier surface melt is the predominant mechanism driving glacier retreat in the Alps (Oerlemans et al., 1998; Arnold, 2005; Zekollari et al., 2019), but it is also important for enabling ice surface collapse, since substantial ice thinning due to both surface melt and melt-out from below is a prerequisite for a collapse feature to form (Stocker-Waldhuber et al., 2017). Therefore, the study of surface melt in the ice marginal zone of Glacier d'Otemma was another important topic of this PhD thesis, with the objective to better understand what processes control the spatial distribution of surface ablation.

In summary, this thesis has three aims;

1. to assess the potential of high-resolution three-dimensional (3D) GPR surveys of the snout marginal zone of temperate Alpine glaciers for deriving the detailed geometry of major subglacial channels;

2. to determine under what conditions such subglacial channels are prone to form collapse features in the vicinity of the termini of Alpine glaciers and thereby contribute to rapid glacier retreat by accelerating internal glacier melt due to air incursion and block caving; and

3. to quantify the spatial variability of ablation over a short time scale of a few days in the snout marginal area of a temperate Alpine glacier to improve understanding of the controls of spatial variability of ablation, such as the effect of solar radiation on microtopography and the presence of supraglacial streams.

Fulfilling these aims will provide a more complete picture of the processes occurring in the snout marginal area of a temperate Alpine glacier during rapid retreat which in turn regulate the connections between glaciers and their proglacial margins.

I.2 Justification of thesis focus

The focus of this thesis is subglacial channels, channel collapse, rapid glacier retreat and ablation processes. In the context of global warming, the glaciers of the European Alps have been retreating at very high rates since the end of the 1980s (Paul et al., 2004; Haeberli et al., 2007; Diolaiuti et al., 2011; Fischer et al., 2015; Sommer et al., 2020; IPCC, 2021) and will most likely continue to do so until most of them completely vanish before the end of the 21st century (Huss et al., 2010; Salzmann et al., 2010; Huss & Hock, 2015; Huss et al., 2017; IPCC, 2019; Zekollari et al., 2019). Glacier retreat affects many sectors of human life in the Alps: hydropower production (Schaefli et al., 2019), drinking water supply (Haeberli & Weingartner,

2020), agriculture, tourism, and industry, to name just a few (Beniston et al., 2018). Therefore, it has become even more important to improve understanding of the processes that influence both the pace and mechanisms of glacier recession, as well as the resulting sediment supply and changes in the hydrographs of Alpine streams (Lane and Nienow, 2019; Perolo et al., 2019). The remaining years until 2050 are deciding for the Alpine countries (IPCC, 2019): Glacier retreat and associated processes need to be predicted as accurately as possible, and adaptation measures in response to changing climate and its effects on the hydrology and landscape need to be put in place to avoid catastrophic impacts on life in the Alpine regions. For example, if adaptation and planning is done soon enough, it is possible to compensate for the shrinking ice masses and thus reduced water supply from melt by making use of deglaciated terrain for water storage (natural and artificial lakes) as well as for hydropower production (Farinotti et al., 2019). Another issue is natural hazards related to rapidly retreating glaciers and to a changing hydrological regime. Glacier lake outburst floods (GLOFs), the collapse of hanging glaciers (Kääb et al., 2018), rock falls, sliding processes in thawing moraines, debris flows and floods are some of the hazards that may be increasing in many places in the near future (Marchi et al., 2002; Chiarle et al., 2007; Vincent et al., 2012; Vincent et al., 2015; Margreth et al., 2017). Some of these, like GLOFs, may also decrease in some instances due to the disappearance of entire glaciers (Zemp et al., 2006; Huss, 2010).

This thesis aims at investigating the link between supraglacial and subglacial melt processes by conducting detailed measurements at a new research site, the Glacier d'Otemma in the Val de Bagnes / Valais / south-western Swiss Alps, a temperate glacier that is representative of many glaciers at medium elevations in the Swiss Alps (Figure I-1). A particularity of Glacier d'Otemma is that the mean elevation of its accumulation area is relatively low compared to other glaciers of this size in the Alps. That's why Glacier d'Otemma has lost approximately 63% of its ice volume between the end of the LIA and 2010 (Lambiel et al., in preparation).

This thesis combines the introduction and exploration of a new field site with intensive research both in the ablation zone, in the proglacial area, and in the downstream Alpine stream. Included in this work are the testing of new measurement methods and technologies, including high-density GPR surveys, and the investigation of processes that had been mostly studied individually, but not in connection to each other, until now. Thereby, this thesis contributes new knowledge about a previously little studied glacier and its surroundings, it creates new knowledge about ablation processes in the snout marginal zone of an Alpine valley glacier, and it tests and improves existing fieldwork methods.

(a) (b)

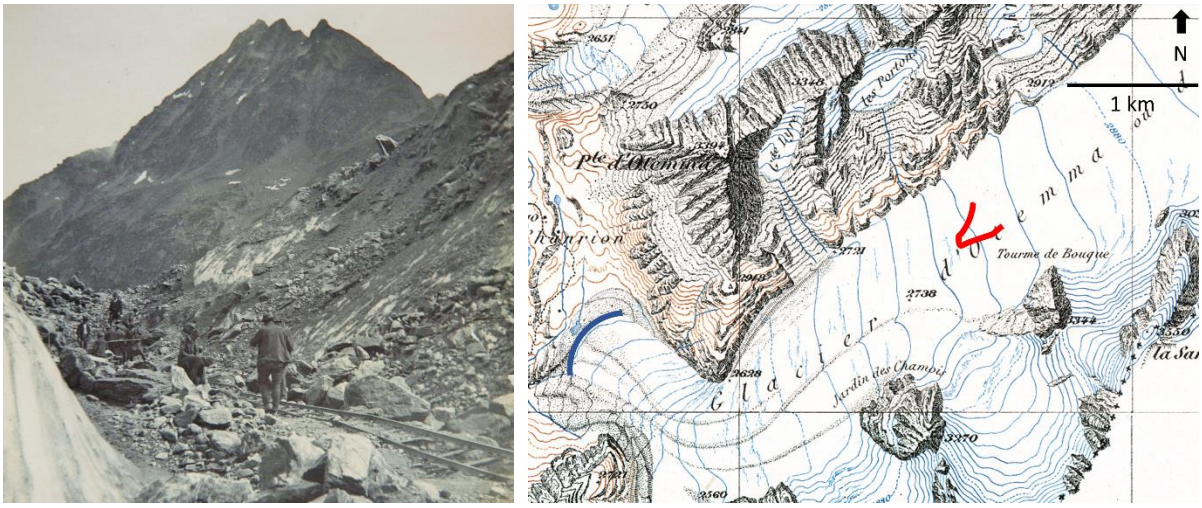

Figure I-1: (a) Works near the partly debris covered terminus of the Glacier d'Otemma in August 1890 (looking towards the north-east from the glacier terminus, photo by the Archives Mariétan, Archives de l'État du Valais, Sion. (b) Topographic map of 1890, when the glacier terminus (blue line) of Glacier d'Otemma was located 3.7 km downstream of the 2020 glacier terminus (red line).

I.3 State of the art

Since this thesis encompasses a number of research elements that are quite diverse, the state of the art in each research field is explained separately below.

I.3.1 Ground Penetrating Radar (GPR) surveys to investigate the geometry of englacial and subglacial channels

The most efficient way to investigate the position and shape of a subglacial channel, if it is not accessible via glacial speleological methods, is with GPR (Schroeder et al., 2020). In the following, the history and different applications of GPR in glaciology along with relevant literature are explained. Specifics about the application of GPR to temperate Alpine glaciers for the detection and characterization of englacial and subglacial channels are outlined.

I.3.1.1 Beginnings of GPR

The potential of Radio Echo Sounding as a powerful tool for measuring the thickness of ice caps and glaciers was first discovered in the 1930s when NASA pilots noticed that the radio altimeter systems of their airplanes did not function properly above ice surfaces such as the Greenland Ice Sheet (Gogineni et al., 1998). It turned out that the radar signal could penetrate the cold ice that was several hundred meters thick, and the signal recorded by the flight altimeter corresponded to the bedrock reflection.

Subsequently, airplane-mounted radar was used by glaciologists to map bedrock topography of ice sheets (Evans, 1967; Robin et al., 1969; Gogineni et al., 2001). The ice thickness of the Western Antarctic Ice Sheet and its ice streams have been derived from airplane-based radar surveys (Shabtaie & Bentley, 1987, 1988). Airborne radar has been used in combination with a digital elevation model to derive the bed topography and ice thickness of the Greenland ice sheet (Gogineni et al., 1998; Bamber et al., 2001; Gogineni et al., 2001; Layberry & Bamber, 2001; Morlighem et al., 2017; Figure I-2). All of these surveys consisted of single (usually straight) lines for which the derived ice thickness was interpolated between lines to yield the bedrock topography for the surveyed area.

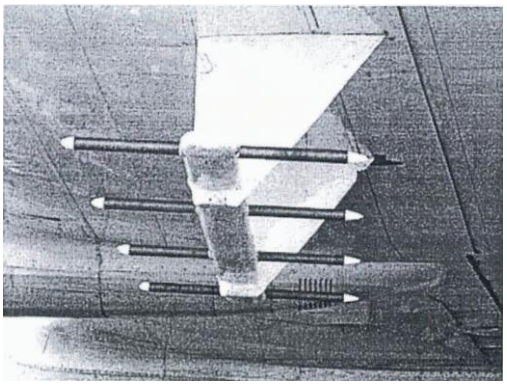

(a)

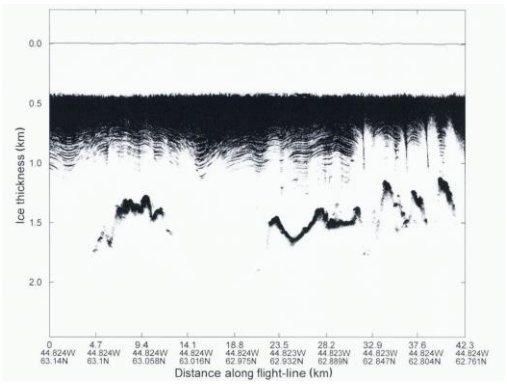

(b)

Figure I-2: Figure 8 and Figure 12 from Gogineni et al. (1998). (a) "Transmit antenna mounted under the wing of the N426NA (NASA P3-B) aircraft", (b) "Radio echogram data collected over the southern Greenland ice sheet during 1997 field season."

I.3.1.2 Different applications of GPR

GPR has been applied to learn about different properties of glaciers, such as (i) to determine the water content of the ice (Murray et al., 2000a; Bradford et al., 2005; Murray et al., 2007; Bradford et al., 2009), (ii) to study the nature of and conditions at the glacier bed (Arcone et al., 1995; Murray et al., 2000b; Kulessa et al., 2008; King et al., 2008), (iii) to identify crevasses and shear zones (e.g., Glover and Rees, 1992; Goodsell et al., 2002; Harper et al., 2010), (iv) to assess the nature of the glacier bed (e.g., Arcone et al., 1995; Gades et al., 2000; Murray et al., 2000b; Kulessa et al., 2008; Gades et al., 2012; Wilson et al., 2014), (v) to map internal water bodies (e.g., Jacobel and Anderson, 1987; Vincent et al., 2012; Garambois et al., 2016), and (vi) to detect the presence of and characterize the nature of en- and subglacial channels

(e.g., Jacobel and Raymond, 1984; Fountain and Jacobel, 1997; Moorman and Michel, 2000; Stuart et al., 2003; Irvine-Fynn et al., 2006; Bælum and Benn, 2011; Hart et al., 2015).

I.3.1.3 GPR on temperate Alpine glaciers

An overview about the use of GPR on temperate glaciers, both Alpine and others, is given by Navarro et al. (2005). Beginning in the 1990s, GPR technology was frequently applied to temperate Alpine glaciers, starting with manual point measurements on smaller glaciers such as the Haut Glacier d'Arolla (Sharp et al., 1993). Over a period of 15 years, Unteraargletscher was mapped with a radar device in order to determine the ice thickness distribution and bed topography (Bauder et al., 2003). Detecting the glacier bed, or internal structures of a glacier, is more difficult for a temperate glacier because the higher water content attenuates and scatters the incoming radar signal. In the Swiss Alps, GPR has been applied extensively and increasingly systematically since the 2000s to map the ice thickness distribution of all Swiss glaciers with helicopter-based GPR (Gabbi et al., 2012; Linsbauer et al.,2012; Rutishauser et al., 2016; Grab et al., 2021). Areas with extensively mapped glacier ice thickness in Switzerland are described by Rutishauser et al. (2016) and include large parts of the Bernese Alps (Aletsch, Gauli, Lötschental, Aare) and large parts of the Valais (Trient, Mauvoisin, Mattmark, Gorner). These geographical areas are all relevant for hydropower exploitation. Examples in other parts of the Alps involve sparse and locally dense ice thickness measurements on several Austrian glaciers between 1995 and 2008 (Fischer, 2009) as well as in the French Alps on glaciers such as the Glacier d'Argentière and the Glacier de Tête Rousse (Vincent et al., 2012; Garambois et al., 2016; Gimbert et al., 2021).

I.3.1.4 Mapping and characterization of englacial and subglacial features

Researchers have attempted to map englacial and subglacial features and processes with GPR at shallow ice depths, for example on a small Alpine glacier (Kulessa et al., 2008) and for disconnected ice bodies and permafrost features in the Eastern Canadian Arctic (Moorman & Michel, 1998; Moorman & Michel, 2000). Wilson et al. (2014) mapped bed reflection power with GPR at a polythermal glacier in order to obtain information about subglacial conditions and processes. Bælum & Benn (2011) surveyed the subglacial structure of a small valley glacier with GPR and detected locations of en- and subglacial conduits and channels. The spacing of the GPR survey lines for these studies was relatively large, which gives rise to concerns regarding the continuity and possible tortuosity of channels. Intersections of individual channels cannot be detected with certainty if the GPR line spacing is too wide. Many of these applications have involved antenna frequencies of 50 MHz or higher, i.e., greater than those

typically employed for ice thickness determination, as the ability to resolve subsurface details increases with the antenna frequency, albeit at the cost of a lesser depth of investigation due to increased attenuation and scattering (Davis and Annan, 1989).

Previously to this PhD thesis, all the attempts to determine the locations and geometry of en- and subglacial channels using GPR were based either on 2D surveys, or at most coarsely spaced 3D surveys (Church et al, 2019). They are limited in that the data cannot be visualized in three dimensions and it is not ideal to apply a 3D migration algorithm to them, given the wide GPR line spacing. Such data can indicate possible channel locations, but it cannot confirm any continuous pathways because we do not know what happens in-between two GPR lines if they are spaced several meters apart. Densely spaced 3D GPR surveys can help to map the locations of subglacial channels with greater confidence by reducing data gaps, thus providing information about the tortuosity of channels. Further, it is possible to apply 3D processing to such a dataset, including 3D migration and attribute analysis (e.g., Allroggen et al., 2014; Schneider, 1978). In parallel to this PhD thesis, 3D GPR surveys were performed, analyzed and published for Rhone Glacier in Switzerland by Church et al. (2021). The results of this work are important in that they obtain new knowledge about sub- and englacial channels, prove the feasibility of the concept of 3D GPR at a temperate Alpine glacier and confirm the validity of the results obtained in this PhD thesis.

I.3.1.5 Survey geometry and orientation

An assessment of different helicopter-based radar set-ups for 1200 km of measurements in the Swiss Alps showed that the detectability of bedrock below the ice depends not only on the system used, but also on the geometry of the glacier bed relative to the antenna orientation (Rutishauser et al., 2016). A study of the influence of the orientation of the GPR antenna on the detectability of the glacier bed, based on both measurements and numerical simulation of the GPR signal, was conducted for the Otemma glacier (Langhammer et al., 2017). The results demonstrate that the radar survey lines must be chosen perpendicularly to the flow lines of the ice and the radar antenna aligned parallel to the flow lines in order to deal with the concave shape of the glacier bed and to obtain the best possible signal.

I.3.1.6 Radar propagation velocity

Radar propagation velocities in glacier ice depend on ice density, water and air content and impurities. Literature values for velocity in pure ice vary between 0.1677 m/ns (Glen & Paren, 1975) and 0.1690 m/ns (Kovacs et al., 1995). The most widely used value for radar velocity in

ice is 0.1677 m/ns, with an uncertainty of 0.0003 m/ns (Robin, 1975). Without boreholes and knowledge of the precise ice thickness, if no Common-Midpoint-Surveys are available, it is difficult to know the exact radar propagation velocity for a given location because rock inclusions, water content and voids including en- and subglacial channels can lead to large differences in local velocities and also provoke significant errors in the assumed depth-averaged radar propagation velocity. In case the ice pores are partially or completely filled with water, the radar wave propagation velocity can decrease significantly, because radar waves propagate approximately five times more slowly in water (wave velocity in water is 0.0330 m/ns) than in ice (Murray et al., 2007). For low water contents of 0.09 – 0.34 % Murray et al. (2000) report similar velocity values as cited above (i.e., 0.1660 – 0.1670 m/ ns), but for higher water contents of 2.4 – 4.1 % the wave velocity drops as low as 0.1490 – 0.1520 m/ns. In this thesis a standard literature value of 0.167 m/ns was used as a realistic radar wave velocity in ice since it enabled the collapse of diffraction hyperbolae during migration and it made for a realistic representation of ice thickness when converting time to depth.

I.3.1.7 Antenna frequency

Depending on the application, different antenna center frequencies are used for the investigation of ice bodies. These depend mainly on the ice thickness and on the spatial resolution needed at the bed of the glacier or ice sheet. For relatively thick ice bodies, lower frequencies tend to be more appropriate as the signal undergoes less scattering losses. However, spatial resolution is lost as the antenna frequency decreases. For shallow ice thicknesses and higher resolution applications, on the other hand, higher frequencies are desired. Center frequencies found in the literature range from a few MHz, e.g., 3.8 MHz for the lightweight portable system by Narod & Clarke (1994), to values of 620 MHz (Goodman, 1975) and 840 MHz (Narod & Clarke, 1980). In the case of temperate Alpine glaciers, low frequencies are preferable to reduce losses due to internal reflections and scattering. But in order to detect subglacial channels a minimum resolution (and therefore a high enough frequency) is needed. The aim is to find the highest frequency that still shows a good enough signal at the depth that we are interested in. At Rhone glacier a 25 MHz center frequency system with two antennas was used to detect an englacial channel, and this frequency has proven low enough to penetrate 200 m of temperate ice, but high enough to detect an englacial channel of several meters width and 0.5 – 4 m height at a depth of ~120 m (Church et al., 2019). The system used in GPR measurements for this PhD thesis consists of a single Radarteam® transmitter-receiver antenna with a nominal center

frequency in air of 70 MHz, mounted on a backpack to be able to conduct surveys in zones with heavy and irregular debris cover (Figure I-3). No other center frequencies were tested.

Figure I-3: GPR survey at Glacier d'Otemma in summer 2018, using a single Radarteam® transmitter-receiver antenna mounted on a backpack, and a dGPS rover antenna for positioning and navigation. Photo: Pascal Egli.

I.3.2 Surface collapse features and local surface lowering on temperate Alpine glaciers

The earliest documented surface collapse feature on a mountain glacier was at Black Rapids Glacier in Alaska by Paige (1956) and Dr. John G. McCall (Figure I-4). The feature, which was observed in April and September 1954 on aerial imagery and during field visits (Paige, 1956), strongly resembles the collapse feature observed during fieldwork at Glacier d'Otemma in the summers of 2017 and 2018 (Egli et al., 2021a). Paige (1956) describes the collapse process at Black Rapids Glacier as likely driven by lateral erosion in a meander bend of a wide subglacial stream (reported to be at least 13.7 m wide), leading to internal melt-out of the channel and the detachment of large blocks of ice from the channel roof ('block caving'). Concentric crevasses are observed upstream of the collapse feature, indicating the position of the underlying subglacial channel where the ceiling of the channel is thinning. The heavily crevassed zones described and shown (Figure I-4) for such collapse features, with shear and thrust faults, are reminiscent of features observed in areas with 'glacier karst' (Clayton, 1964) – an environment observed on low-gradient stagnant glacier tongues especially on paleo-glaciers and ice sheets, but also on contemporary glaciers (Clayton, 1964; Mavlyudov, 2005).

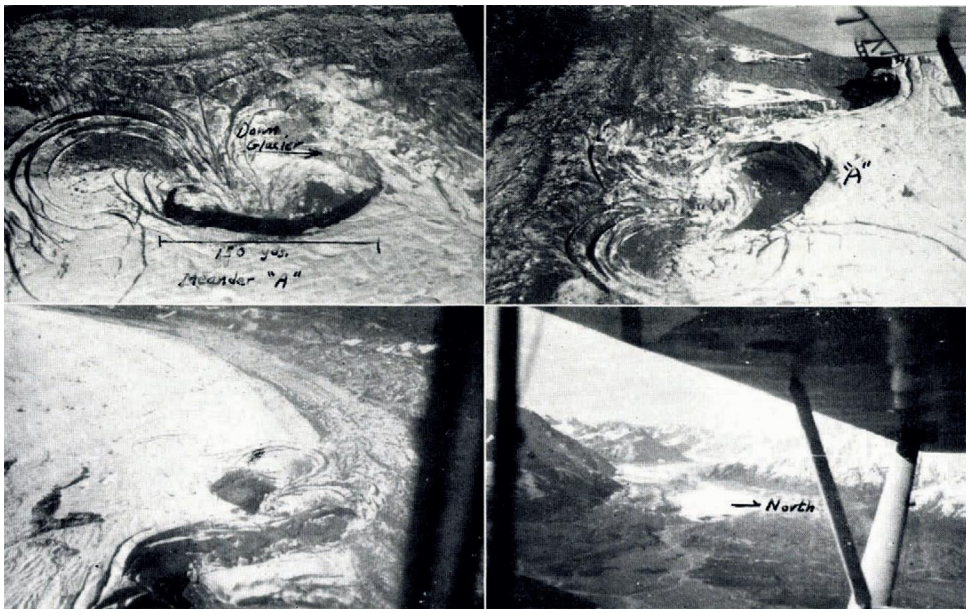

Figure I-4: Collapse feature with concentric crevasses and a meander bend at Black Rapids Glacier, Alaska, 1954. Figure 1 in Paige (1956). The photographs were taken from an airplane.

Several decades after the documentation by Paige (1956), collapse features were described and measured at debris covered glaciers in the Sierra Nevada of California (Konrad, 1998) as well as at glaciers in the Austrian Alps by Kellerer-Pirklbauer and Kulmer (2019) and by Stocker-Waldhuber et al. (2017) (Figure I-5). These structures have a similar appearance and were located in a similar situation as those observed for the structures at Black Rapids Glacier, although the glaciers in the Austrian Alps are much smaller Alpine glaciers. All features so far documented occur close to a low-gradient glacier snout, are in areas of relatively thin ice, are surrounded by concentric crevasses, and a subglacial channel is located in close vicinity, or immediately underneath the feature. There is documentation about 'Esker enlargements' in palaeo ice sheets that seems to look at very similar (albeit past) features (Dewald et al., 2021). Despite these observations, there is no literature available that systematically assesses a larger number of such present-day collapse features to find common attributes and compare the occurrences of features to situations where they do not occur. Chapter III in this thesis aims at filling this gap, and also contribute to a better process understanding.

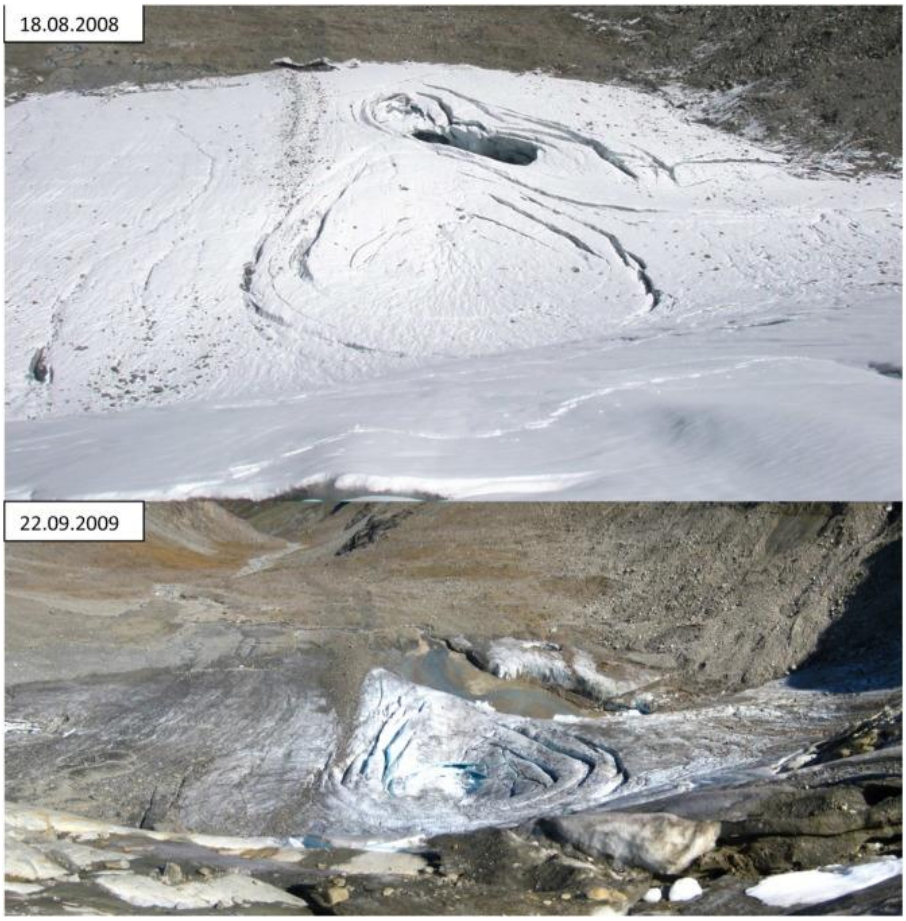

Figure I-5: Figure A3 in Stocker-Waldhuber et al., 2017: "Depressions on the flat tongue on Sulztalferner (Photographs: M. Olefs)"

I.3.3 The spatial distribution of surface ablation patterns on temperate Alpine glaciers

Warmer summer air temperatures lead to an increase in ablation (Braithwaite, 1995). They may also reduce solid precipitation, reducing the duration of snow cover, and thereby lead to more rapid exposure of lower albedo ice as well as a reduction in accumulation. If total ablation exceeds total accumulation over the time span of several years this leads to glacier retreat (e.g., Zekollari et al., 2020).

Surface ablation on glaciers has been studied repeatedly (e.g., Braithwaite, 1995; Hock, 1999; Vincent et al., 2004; Hock, 2005; Pellicciotti et al., 2005), and the first distributed models of glacier melt were developed in the 1990s (Arnold et al., 1996; Arnold et al.; 1998). But the detailed spatial distribution of ablation has been studied only recently with the advent of Uncrewed Aerial Vehicle (UAV) based structure-from-motion (SfM) multi-view stereo (MVS) photogrammetry methods (Westoby et al., 2015; Bash et al., 2018; Rossini et al., 2018). Ablation can vary spatially over very small distances due to heterogeneity in surface reflectance

related to the presence of debris cover, dust, surface roughness, aspect, slope, and the presence of supraglacial streams (Parker, 1975; Strasser et al., 2004; Gabbud et al., 2015; Rossini et al., 2018). Several studies have analyzed melting patterns for both Alpine and Arctic glaciers and their dependence on glacier surface properties (Figure I-6; Cathles et al., 2011; Rippin et al., 2015; Bash et al., 2018; Rossini et al., 2018; Bash & Moorman, 2020; Wojcik and Sobota, 2020). Others have focused on the effect of albedo and supraglacial dust on ablation (Brock et al., 2000; Adhikary et al., 2002; Brock, 2004; Azzoni et al., 2016; Naegeli et al., 2019). Also, researchers have become increasingly interested in the impact of supraglacial debris cover on glacier melt, especially in the Hindu-Kush-Himalaya-Karakoram region (Nicholson & Benn, 2005), but also in other regions of the world such as Alaska (Herreid & Pelliciotti, 2020; Herreid, 2021). While the influence of supraglacial debris cover on ablation has been studied intensely, the interplay between solar radiation and microtopography that affects ablation rates, the influence of supraglacial streams on ablation as well as the importance of surface roughness for ablation have received less interest (Isenko & Mavlyudov, 2002; Brock et al., 2006; Rippin et al., 2015). There are few studies of Alpine glacier ablation at a high temporal resolution of a few days that also have a high horizontal resolution (decimeter-scale). Yet, such studies are important if we are to improve the parameterization of surface melt models.

A spatially highly resolved approach considering several key variables is important to better understand distinctive melt patterns. An assessment at the decimeter scale and over a short time span of a few days is important especially to better understand the formation of features such as deeply incised or shallow supraglacial streams (e.g., Pitcher et al., 2019), debris cones, or highly irregular glacier surfaces, as well as the influence of ablation patterns on the formation of surface collapse features (e.g., Stocker-Waldhuber et al., 2017). Besides ablation patterns, structural weaknesses such as differences in foliation, or former large-scale flow-units may also have an impact on the formation of such features, and they may influence melt patterns (Gulley, 2009).

The principal methods used to study the spatial distribution and the temporal variability of ablation at a local scale on temperate Alpine glaciers are; (a) manual measurements of ablation stakes (Ahlmann & Thorarinsson, 1938; Brock et al., 2000), (b) Light Detection and Ranging (LiDAR) measurements (e.g., Gabbud et al., 2015), and (c) UAV-based SfM-MVS photogrammetry (Westoby et al., 2012; Bash et al., 2018; Figure I-7). While ablation stakes in combination with other methods are rather accurate and useful to distinguish between elevation change due to ice dynamics and elevation change due to ablation, they cannot be employed to

quantify such changes for a high spatial resolution or for larger spatial extents. LiDAR is a method with high accuracy and precision, as well as fast acquisition. But the properties of glacier ice are not always ideal for the reflection of LiDAR rays due to the high water-content of melting ice (Gabbud et al., 2015). The incidence angle of the laser beam, if not performed from a helicopter, is often sub-optimal for low-gradient glacier tongues, and LiDAR devices suitable for glacier ice and operating at long range are rather expensive and heavy to transport. UAV-based SfM-MVS photogrammetry, if carried out correctly, can cover large surfaces and produce dense point clouds which can be interpolated to generate Digital Elevation Models (DEMs) of high resolution (Gindraux et al., 2017; Vivero & Lambiel, 2019). Compared to LiDAR, UAVs are relatively cheap, but a large number of Ground Control Points (GCPs) needs to be measured with a differential Global Positioning System (dGPS) to reduce systematic error in the point cloud and to georeferenced the point cloud (James et al., 2017). The latter can be omitted if an UAV carrying an RTK-receiver is used. But GCPs remain useful for reducing systematic error and to be used as validation points (James et al., 2019; James et al., 2020). In this thesis, the focus is on the use of ablation stakes and UAV-based SfM-MVS photogrammetry to quantify ablation as well as elevation change and surface displacement due to ice dynamics and subglacial processes.

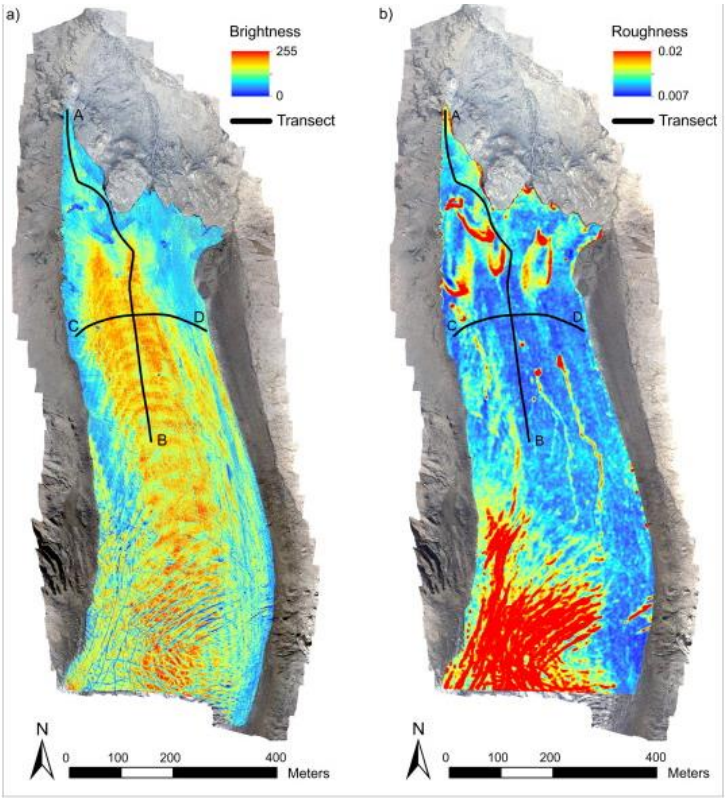

Figure I-6: Figure 9 in Rossini et al. (2018), showing surface brightness and surface roughness in the ablation area of Morteratsch Gletscher.

Figure I-7: Landing of a UAV 'Phantom 4 Pro' by DJI® in the ablation zone next to the lateral moraine of Glacier d'Otemma. Photo by Katrine Villumsen.

I.4 Thesis structure

This thesis is subdivided into three research chapters, where each chapter contains a scientific article preceded by chapter aims and objectives as well as details about my personal contribution to the work. Each article also comes with a supplementary materials section, which contains valuable information about data processing and validation. Finally, each article is followed by a conclusion that assesses the wider implications of the research findings. As two of the articles are now published, they are included in this thesis without modification.

The first article focuses on high-density GPR measurements at Glacier d'Otemma and determination of subglacial channel outlines based on the analysis of that radar data.

- Egli, P. E., Irving, J., & Lane, S. N. (2021). Characterization of subglacial marginal channels using 3-D analysis of high-density ground-penetrating radar data. *Journal of Glaciology*, *67*(264), 759-772.

The second article consists of a statistical analysis of 22 Swiss glaciers investigating the factors associated with the presence of collapse features, as well as a detailed analysis of a collapse feature at Glacier d'Otemma with means of UAV-based DEMs, ablation stakes and GPR.

- Egli, P. E., Belotti, B., Ouvry, B., Irving, J., & Lane, S. N. (2021). Subglacial channels, climate warming, and increasing frequency of Alpine glacier snout collapse. *Geophysical Research Letters*, *48*(21), e2021GL096031.

The third article investigates surface melt patterns derived from UAV-based DEMs in the snout marginal zone of Glacier d'Otemma at a scale of 8 – 16 days and the impact of solar radiation and microtopography, surface roughness, supraglacial streams, and albedo on ablation:

- Egli, P. E., Belotti, B., Lane, S. N. (to be submitted to The Cryosphere). Quantitative analysis of high-resolution ablation patterns for a temperate Alpine glacier derived using repeated UAV SfM-MVS photogrammetry

The thesis ends with a conclusion that comprises a synthesis of the major research findings of each article as well as an assessment of the future research needs in each area.

II CHARACTERIZATION OF SUBGLACIAL MARGINAL CHANNELS USING 3D ANALYSIS OF HIGH-DENSITY GROUND-PENETRATING RADAR DATA

Pascal E. Egli, James Irving, Stuart N. Lane

Journal of Glaciology, 67(264), 759-772, published on 18th March 2021

II.1 Chapter aims and objectives

The aim of this chapter is the study of subglacial channels with the help of 3D ground-penetrating radar (GPR) data. The main objective is to derive the detailed planform geometry of major ice-marginal subglacial channels at two glaciers: Haut Glacier d'Arolla (HGdA) and Glacier d'Otemma (GdO). Both glaciers are medium-sized temperate Alpine glaciers in the South-Western Swiss Alps and they can serve as a proxy for similar glaciers in the European Alps. The aims are two-fold: (1) to acquire more knowledge about the geometry of largely inaccessible subglacial channels during the peak melt season; and (2) to investigate the methodological development of gridded high-density GPR measurements and 3D analysis of such data in the ablation zone of a temperate glacier. High-density GPR measurements are well established in environments other than temperate glaciers (Booth et al., 2008). But its application to temperate glaciers is challenging both from the point of view of fieldwork adversities and logistical obstacles, and from the point of view of processing, due to the high water-content of temperate glacier ice.

II.2 Personal contribution to the article

The idea to acquire a set of densely spaced GPR datasets to map subglacial channels at the bed of a temperate alpine glacier was developed by James Irving, in collaboration with Stuart Lane and myself. My personal contribution to this article spans from planning of the field work campaign at Glacier d'Otemma to the processing of GPR data and writing up of the article that has been published in the Journal of Glaciology.

The data acquisition was done with the help of Bachelor and Master students, especially Martino Sala who was doing his Master's thesis with James Irving, and Boris Ouvry, who was employed to help with fieldwork in the summers of 2017 through 2020. Acquisition of UAV data and ablation stake data in August 2018 was completed with the help of Bruno Belotti as part of his Bachelor's thesis. Processing of the GPR data was done with our own customized

MATLAB ® codes, written largely by myself and by James Irving. The processing and validation of the UAV data was done with the Metashape Pro® software in collaboration with Bruno Belotti. The field measurements at Haut Glacier d'Arolla (HGdA) were collected by James Irving and Ludovic Baron in the summer of 2015, before I was employed at UNIL. The processing of these data from the HGdA was done by James Irving. In summary, the tasks that I completed to write this article involved:

1. Communication and negotiations with the municipality of Bagnes together with Stuart Lane to obtain the rights to undertake fieldwork in a protected area and to obtain a road permit.

2. Planning of the 2017 and 2018 field work campaigns at Glacier d'Otemma, planning and execution of three exploratory field campaigns at Glacier d'Otemma in April and June 2017 and July 2018.

3. Planning and execution of logistics for two 2-3-weeks-long fieldwork campaigns in August of 2017 and 2018 at Glacier d'Otemma.

4. Presentation of preliminary results at three conferences (Alpine Glaciology Meeting Chamonix 2017, Polar Davos 2018, IGS Glacial Erosion and Sedimentation Symposium Madison, 2019) in order to obtain valuable feedback on the method and data.

5. Processing of GPR data, dGPS data, ablation stakes data and UAV data.

6. Writing of the article in original and revised form with inputs from James Irving and Stuart Lane.

II.3 Article 1

II.3.1 Introduction

Understanding the hydrology of alpine glaciers, and in particular the geometry and dynamics of the channels that form within and beneath glacier ice, has been an important research interest since at least the 1950s (Fountain and Walder, 1998). It is well-established that channelized subglacial drainage may occur via semicircular Röthlisberger channels carved into glacier ice (Röthlisberger, 1972), Nye channels eroded into bedrock (Nye, 1959), channels carved into both subglacial sediments and ice (Walder and Fowler, 1994) or some combination thereof. Although we know that subglacial channels may be either pressurized or open to the atmosphere, their geometry and behavior under given flow conditions are not well understood. Learning more about the pathways of channels close to the terminus of glaciers may provide important knowledge about their origin and dynamics. For instance, if a channel meanders strongly, its shape is likely a result of interactions with the glacier bed such as erosion, deposition, sediment transport and deviation by bedrock outcrops (Alley et al., 1997). Such knowledge is critically important for understanding how glaciers transfer eroded sediment through their marginal zones and for parameterizing models of subglacial sediment export (Beaud et al., 2018; Perolo et al., 2019).

Despite the importance of quantifying subglacial channels, the last 25 years have not changed the fundamental observation of Walder and Fowler (1994) that little data are available to provide details on their geometry. This is not surprising as accessing such channels is difficult. Glacial speleological methods have yielded valuable information (Benn et al., 2009a, 2009b; Gulley et al., 2009, 2012a, 2012b, 2014; Mankoff et al., 2017; Temminghoff et al., 2019), but entry during the melt season may not be possible and channels must be large and stable enough for physical access.

One alternative is ground-penetrating radar (GPR). GPR has a long history of use in the field of glaciology, which began over a half century ago in the form of radio-echo sounding (~1–40 MHz) to map the thickness of glaciers and ice sheets (e.g. Steenson, 1951; Cook, 1960). Since that time, GPR has grown to become a standard glaciological tool and its applications have greatly expanded (e.g. Plewes and Hubbard, 2001; Bingham and Siegert, 2007; Schroeder et al., 2020). In the context of alpine glaciers, the GPR method has been successfully used (i) to map internal layering; (ii) to identify crevasses and shear zones; (iii) to assess and to monitor the nature of the glacier bed; (iv) to map internal water bodies; (v) to estimate ice water content; (vi) to distinguish between regions of cold and temperate ice and (vii) to identify, characterize

and monitor englacial and subglacial channels. Many of these applications require GPR antenna frequencies of 50 MHz or higher (i.e. greater than those typically employed for ice thickness determination) as our ability to resolve subsurface detail increases with the antenna frequency, albeit at the cost of a reduced depth of investigation (Davis and Annan, 1989).

With respect to identifying the location and geometry of en- and subglacial channels using GPR, virtually all previous attempts have been based upon two-dimensional (2-D) profiles, or at the very most quasi-three-dimensional (3-D) surveys involving multiple parallel 2-D acquisitions with a large spacing between the survey lines (e.g. Moorman & Michel, 2000; Zirizzotti et al., 2010; Bælum and Benn, 2011; Church et al., 2019, 2020; Temminghoff et al., 2019). Although these types of surveys can provide highly useful information, they are limited in the sense that the corresponding data cannot be properly imaged and visualized in 3-D because of the strong sampling bias in the along-line direction and the high degree of spatial aliasing in the cross-line direction. As a result, previous research has successfully detected en- and subglacial channels, but has only rarely been able to confirm continuous pathways or provide detailed information on channel planform geometries (Church et al., 2020). Densely-spaced parallel GPR survey lines, processed within a fully 3-D framework, have the potential to overcome this limitation. Such surveys, which have become common and are highly valued in environmental and archeological applications of GPR (e.g. Grasmueck et al., 2005; Booth et al., 2008) are now feasible for glaciological applications thanks to the increased acquisition speed and portability of modern real-time-sampling GPR instruments, combined with improvements to real-time differential GPS navigation.

The objective of this study is the detection and the characterization of ice-marginal subglacial channels using high-resolution, densely spaced, GPR measurements. To this end, we acquire and present ~70 MHz data from two temperate glaciers in the southwestern Swiss Alps having similar geological and climatic settings, but different bed sediment thicknesses and topographies: the Haut Glacier d'Arolla (HGdA) and the Glacier d'Otemma (GdO). Detailed 3-D processing and analysis of the amplitude characteristics of the GPR reflections from the glacier beds allow us to map the position of subglacial channels. Aerial imagery of the HGdA and drone-acquired imagery of the GdO, acquired over two successive summers, along with the partial collapse of a snout marginal channel at the GdO site, provide validation of the GPR results. Maps of the Shreve hydraulic potential (Shreve, 1972) are also used for comparative purposes.

II.3.2 Methodology

II.3.2.1 Field sites

The HGdA and GdO are temperate valley glaciers located in the southwestern Swiss Alps (Figure II-1). The glaciers are separated by a distance of ~3 km. Due to their proximity, both glaciers have a similar climate forcing.

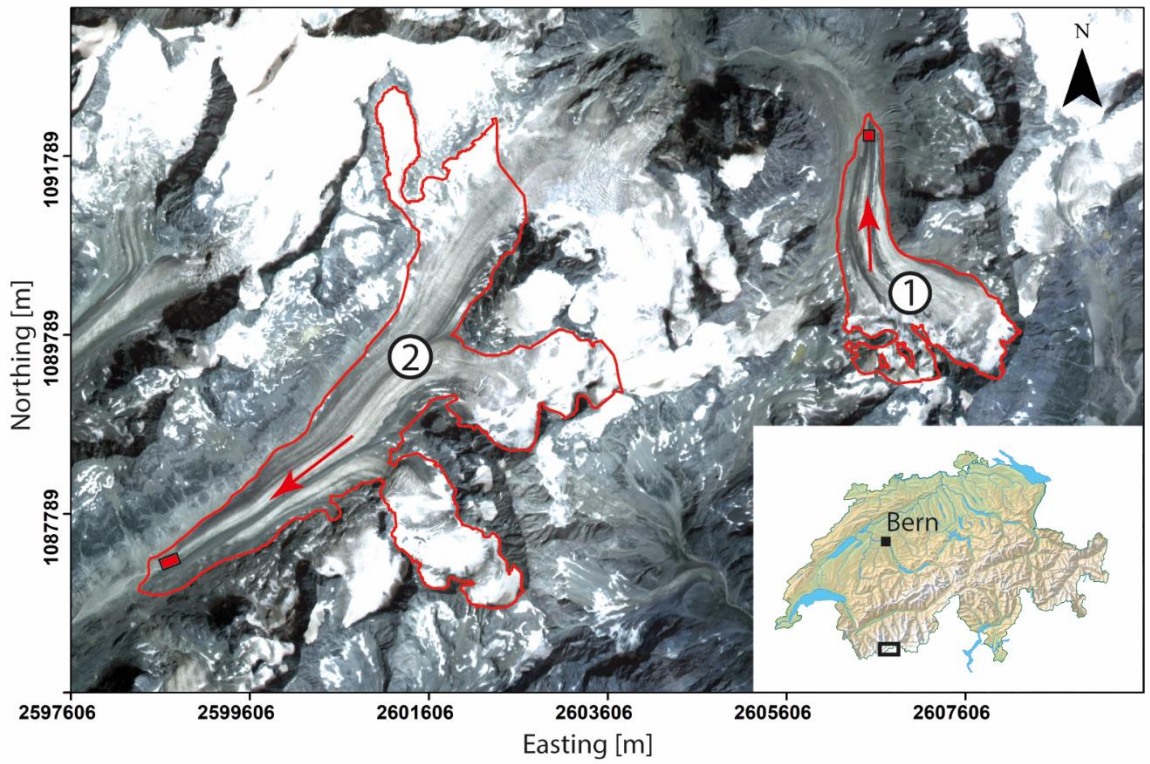

Figure II-1: Location of the field sites in southwestern Switzerland. The black square on the insert map indicates the region covered by the satellite photo showing (1) the Haut Glacier d'Arolla and (2) the Glacier d'Otemma. The glacier outlines correspond to the most recent GLIMS data (Paul et al., 2019), and are based on satellite imagery from 2015. The red squares near the end of each glacier tongue indicate the location of the GPR datasets analyzed in this study. The background satellite image was obtained from 2019 imagery (Planet Team, https://api.planet.com). The insert map was obtained from the Swiss Federal Office of Topography (http://map.geo.admin.ch). Please note that all coordinates in the figures of this paper are given in meters in the local Swiss coordinate system 'CH1903+'.

The HGdA is 3.3 km long and extends from 3500 to 2600 m a.s.l., with its terminus located at 45°58′58.366″ N / 7°31′24.979″ E in the summer of 2020. The glacier initially flows from southeast to northwest from the Mont Brûlé, turning to flow from south to north toward the terminus. The subglacial hydrology of the HGdA has been investigated extensively in the scientific literature (e.g. Hubbard et al., 1995; Nienow et al., 1996; Nienow et al., 1998; Mair et al., 2002a, 2002b). For several years, the glacier has had two main subglacial outlet channels, located along the eastern side of the glacier terminus (Figure II-2). More recently, the sediment

dynamics have also been studied (Swift et al., 2005; Perolo et al., 2019). The bedrock underlying the glacier is composed of schistose granites, gneiss and metagranitoides (Tranter et al., 2002; Geological Atlas of Switzerland, 2020). This is covered by a layer of sediment, which in most places is several decimeters thick (Mair et al., 2003). The ice volume of the HGdA in the year 1999 was estimated to be 0.25 ± 0.07 km^3 based on topographic data (Farinotti et al., 2009a, 2009b). By far the biggest part of the glacier volume is located below the equilibrium-line altitude (ELA), meaning that the HGdA is highly sensitive to increases in average air temperature. Indeed, the tongue of the HGdA has retreated by more than 400 m in length over the past 20 years (Gabbud et al., 2016) and serves as a proxy for alpine glaciers at medium to low elevations having a proportionately small accumulation area. Such glaciers are expected to continue to retreat rapidly over the next few decades (Salzmann et al., 2012; Huss et al., 2010).

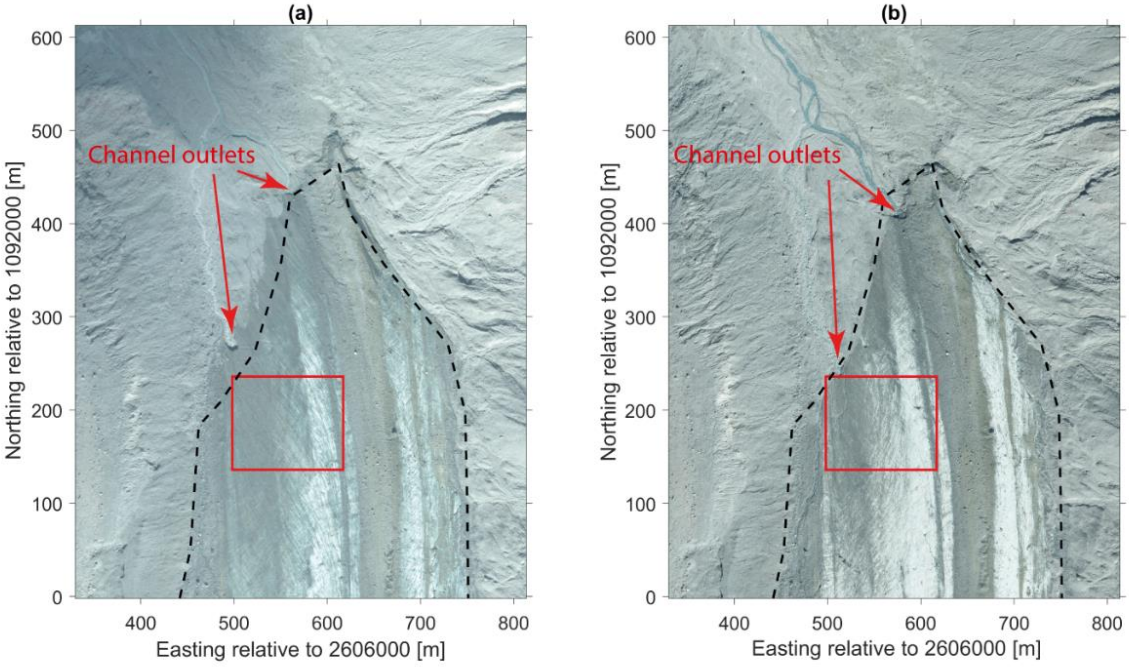

Figure II-2:. Aerial orthoimagery of the tongue of the Haut Glacier d'Arolla taken in (a) September 2014 and (b) September 2015. The red square indicates the area over which high-density GPR measurements were acquired in August 2015. The GPR survey lines were oriented east–west. The dashed black line represents the most recent GLIMS glacier outline based on satellite imagery from 2015 (Paul et al., 2019).

The much-less-studied GdO is 7 km long and extends from 3790 to 2500 m a.s.l., flowing from northeast to southwest from the summit of the Pigne d'Arolla, with its terminus located at 45°56′18.908″ N / 7°25′20.212″ E in the summer of 2020. There are two active tributary

glaciers: de Blanchen and du Petit Mont Collon. The bedrock underlying the glacier is composed of a mixture of metagranitoides and metagabbros (Geological Atlas of Switzerland, 2020). Field observations where the glacier has recently receded show that this is typically covered by a thin layer of sediment, having a thickness of between a few centimeters and a few decimeters. The ice volume of the GdO was determined in 2009 to be 1.05 ± 0.08 km^3 based on airborne GPR and topographic data (Farinotti et al., 2009b; Gabbi et al., 2012). Since, similar to the HGdA, most of the glacier volume is currently located below the ELA, the GdO is sensitive to increases in average air temperature and has been retreating rapidly at an average rate of 40 m in length per year over the past 60 years (GLAMOS, 1881–2019).

II.3.2.2 GPR measurements

Zero-offset, high-density GPR data were acquired on both the HGdA and GdO using a lightweight, real-time-sampling GPR instrument manufactured by Radarteam, Sweden. The single transmitter–receiver antenna employed for the surveys has a nominal center frequency in air of ~70 MHz with a bandwidth between 20 and 140 MHz. To maximize portability, the GPR system was suspended from a backpack with the antenna located 0.4 m above the ground, which was found to provide good antenna coupling and a measurement quality that was virtually the same as that obtained with the antennas located directly on the ice surface. Data were collected on foot following parallel lines that were spaced either 1- or 2-m apart. GPR traces were recorded continuously at a frequency of ~3.5 Hz using a time-sampling interval of 3.125 ns, the latter of which was sufficient to avoid temporal aliasing. The system has a fixed scan time of 1600 ns, which corresponds to a depth of investigation of ~134 m assuming a radar wave speed in glacier ice of 0.167 m ns^{-1} (Murray et al., 2000). In the current study we focus on areas where the ice thickness was <60 m.

GPR lines spaced 1-m apart were surveyed over a 120 m × 100 m region of the snout marginal zone of the HGdA in August 2015 (Figure II-2). On the GdO, an ~200 m × 100 m region was surveyed using a 2-m line spacing in August 2017 (Figure II-3). Over the latter period, a 200-m-long GPR line was also repeatedly measured over 24 h (hourly from 7 a.m. to 9 p.m. and every 3 h from 9 p.m. to 6 a.m.) in order to investigate the repeatability of the measurements over the course of a summer day (Figure II-3). Although previous work has suggested that radar velocity, attenuation and reflectivity in porous near-surface ice may vary strongly because of changing water content (Kulessa et al., 2008), no significant changes in the positions of the glacier bed or other major reflectors were detected, and relative reflection amplitudes remained stable (Figure II-10 and Figure II-11 in Supplementary material). The influence of the

orientation of the GPR antenna on the detectability of the glacier bed was also studied for the GdO (Langhammer et al., 2017), with results suggesting that GPR survey lines are best run perpendicular to ice flow with the radar antenna oriented perpendicular to the line direction. We adopted the latter strategy when acquiring the GPR data in this study, meaning that the parallel survey lines were oriented east–west at the HGdA, and northwest–southeast at the GdO.

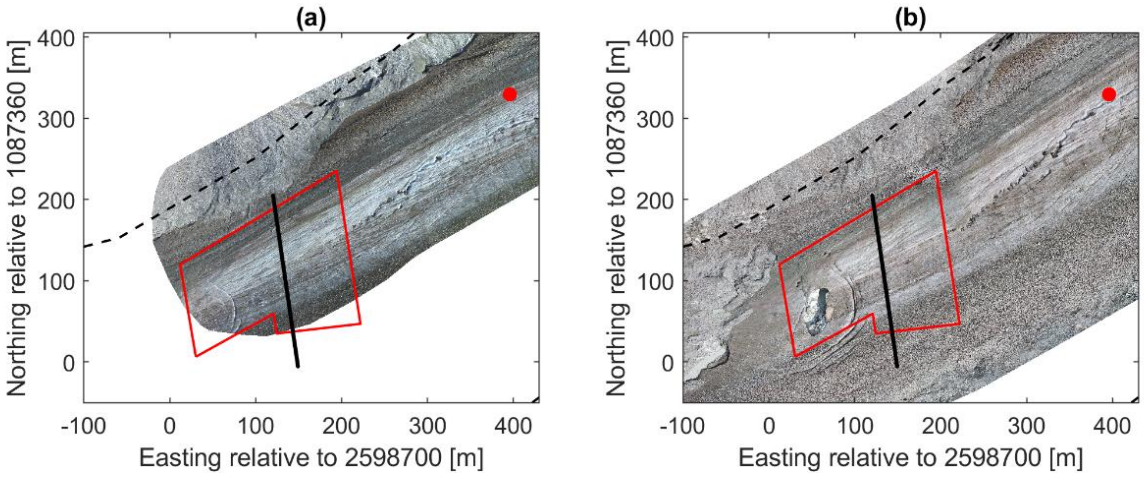

Figure II-3: Drone-based orthoimagery of the tongue of the Otemma glacier taken in (a) August 2017 and (b) August 2018. The red polygon indicates the area over which high-density 3-D GPR measurements were acquired in August 2017. The GPR survey lines were oriented northwest–southeast. The black line indicates the location of the GPR repeat profile analyzed in the Supplementary material (Figs S1 and S2). The red dot displays the location of a moulin. The region not covered by the drone survey is indicated in white. The dashed black line represents the most recent GLIMS glacier outline based on satellite imagery from 2015 (Paul et al., 2019).

For the GPR surveys on both the HGdA and the GdO, accurate positioning was achieved along each profile line using real-time dGPS navigation. A dGPS base station was installed at both sites close to the glacier terminus. Two operators were used to collect the GPR data, each of whom carried a dGPS rover antenna. One operator walked ahead and navigated along a pre-programmed path, whereas the other followed with the GPR system. The position of the GPR antenna was logged at a frequency of 10 Hz in order to provide GPS coordinates for each recorded trace with ~±10 cm precision. GPR survey lines were found to deviate from the pre-programmed paths by no more than 25 cm.

II.3.2.3 Data processing

Processing of the data from the HGdA and the GdO consisted of an initial series of steps to obtain a migrated 3-D GPR data volume, which was followed by picking and attribute analysis of the reflection from the glacier bed in order to identify subglacial channels. Note that, in general, such channels are not easily seen on the individual GPR profile lines because of the limited vertical resolution of the data. That is, for our 70-MHz antenna with a dominant radar

wavelength in ice of over 2 m, it is generally not possible to image separately the channel roofs and floors and thus unambiguously identify these features (Figure II-12 in Supplementary material), in particular if the channels are at least partially air-filled. However, as the channels represent a strong contrast in radar reflection coefficient compared to their surroundings, they can be imaged via amplitude analysis along the bed. All processing was done in the MATLAB computing environment using customized codes. Table 1 summarizes the initial steps carried out on the data. During the GPR data acquisition, the dGPS rover antenna logging the GPR instrument position experienced occasional drops in precision leading to local shifts in recorded elevation which had to be manually removed and replaced using linear interpolation. An acquisition pattern adjustment of 0.4 m was also necessary between GPR lines run in opposite directions (i.e., a position shift of 0.2 m in each direction) in order to correct for positioning errors related to system timing delays and the angle of the GPS rover antenna.

Table II-1: Initial processing steps applied to the 3-D GPR data

Step Number	**Activity**	**Description**
1	GPS data cleaning	Remove clearly erroneous GPS coordinates and replace them with interpolated coordinates such that each GPR trace has an accurate horizontal and vertical position.
2	GPR data binning	Bin the GPR data to create a regular (0.2-m) trace spacing along the lines by assigning the closest GPR trace to each cell of a predefined grid. Each GPR survey line was binned separately, which was possible because of the limited deviation of the true line coordinates from their theoretical positions thanks to real-time dGPS navigation.
3	Acquisition pattern correction	Correct for a systematic spatial offset between survey lines run in opposite directions, related to small errors in timing and the angle of the dGPS rover antenna. This was done by finding the constant position shift between lines run in opposite directions that maximized the line-to-line correlation (0.4 m).
4	Time zero correction	Adjust the zero time of the GPR recordings such that the time on each trace accurately represents the two-way travel time. Calibration tests involving suspending the GPR antenna from a known height have indicated that a correction of -25 ns is necessary.
5	Trace normalization	Normalize each trace in the dataset by its maximum amplitude in order to correct for varying coupling between the GPR instrument and the glacier surface.
6	Mean trace removal	Subtract the mean trace determined over a sliding 30-trace window, only in the upper part of the GPR section from 0 to 175 ns, in order to remove the emitted GPR pulse from the dataset.
7	De-wow filter	Remove low-frequency “wow” superimposed upon the reflection data using a 13-point residual median filter.
8	Gain	Boost signal amplitudes using a single, smooth, time-varying gain function that is derived from the inverse average absolute amplitude decay curve in the dataset. This is used to compensate for losses due to geometrical spreading, attenuation,

		and scattering without imposing any spatial amplitude trends upon the data that could be misinterpreted in our analysis.
9	Trace interpolation	Reduce the time sampling interval along each trace to 0.7812 ns using Fourier interpolation in order to quadruple the number of points per trace for improved display, migration, and analysis.
10	Time migration	Perform 3D topographic time migration using the algorithm of Allroggen et al., (2014), which is based on the general Kirchhoff scheme presented in Schneider, (1978). A constant migration velocity of 0.16 m/ns and migration aperture of 10 m were utilized, which were found to effectively collapse diffraction hyperboloids in the data.
11	Time-to-depth conversion	Convert time-migrated GPR section to depth using the same constant velocity of 0.16 m/ns.
12	Topographic correction	Move traces vertically according to the measured topography by applying a linear Fourier phase shift, which allows for trace adjustment by a fractional number of time samples.

Figure II-4 shows the results of applying the processing steps described in Table 1 to a single east–west GPR survey line from the HGdA dataset collected along 1'092'150-m northing. In Figure II-4a, we see that the GPS-corrected and binned raw data do not allow for easy identification of subglacial structure due to the presence of: (i) the emitted GPR pulse; (ii) unwanted low frequencies ('wow') upon which the GPR reflections are superimposed and (iii) amplitude variations due to signal attenuation and differences in antenna coupling. After amplitude normalization, removal of the emitted pulse, dewow, gain and time interpolation (Figure II-4b), the data become easier to interpret but are still contaminated by numerous hyperbolic diffraction events related to the presence of small scatterers (water pockets, air voids and boulders) within the ice. Figure II-4c shows the result of 3-D topographic time migration using the algorithm of Allroggen et al., (2015) with a migration aperture of 10 m and assuming a constant radar wave velocity of 0.16 m ns^{-1}. The latter value was found to provide the best collapse of diffraction hyperboloids in the 3-D volume and is appropriate for temperate ice (Plewes and Hubbard, 2001; Murray et al., 2007). Finally, Figure II-4d shows the final GPR image after time-to-depth conversion and topographic correction, where we see in blue and red the glacier surface topography and position of the bed, respectively.

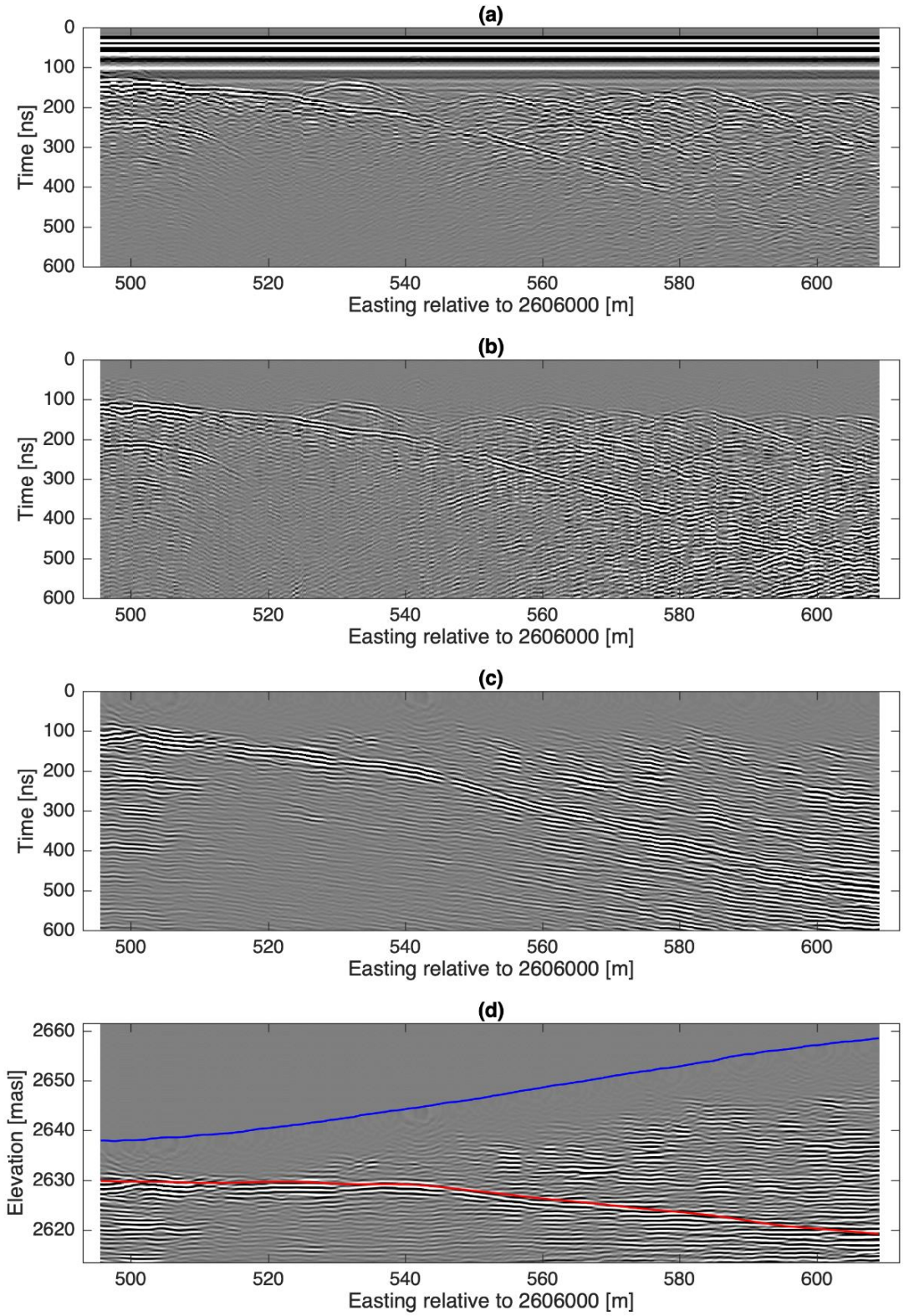

Figure II-4. Demonstration of the GPR processing described in Table 1 for one east–west survey line from the HGdA acquired along 1092150 m northing: (a) binned and time-zero-corrected raw data (steps 1–4); (b) after trace normalization, direct arrival removal, dewow, gain and trace interpolation (steps 5–9); (c) after subsequent 3-D topographic Kirchhoff time migration (step 10) and (d) after time-to-depth conversion and correcting for topography (steps 11 and 12). The blue line shows the ice surface whereas the red line indicates the picked glacier bed reflection.

After the initial processing described above, the migrated 3-D GPR image was analyzed to quantify the amplitude characteristics of the reflection along the glacier bed. Subglacial channel locations are expected to correspond with anomalously high bed reflection amplitudes because they represent a strong contrast in dielectric permittivity (e.g. ice/air or ice/water) compared to their surroundings (e.g. ice/bedrock) (Wilson et al., 2014; Church et al., 2019). To this end, we first performed a manual line-by-line picking of the glacier bed reflection (Figure II-4d), the results of which were used to fit a thin plate smoothing spline to the glacier bed surface. For the HGdA, the mean deviation between this modeled surface and the glacier-bed picks was 0.27 m. For the GdO, it was 0.39 m. Next, the 3-D GPR image was 'flattened' along the modeled bed surface by applying a linear Fourier phase shift to each trace, the latter of which allowed us to conform the data smoothly to the picked bed topography. Although not essential for the amplitude analysis described below, flattening the data in this manner greatly facilitated the extraction of bed reflection profiles, in the sense that they could be obtained by slicing horizontally through the 3-D data matrix. Next, we calculated the magnitude of the Hilbert transform of each trace (i.e. the so-called 'instantaneous amplitude'), which provides the trace amplitude envelope and is commonly used in seismic data processing to quantify reflection strength (e.g. Taner et al., 1979). Finally, the maximum of this result was computed over a small (2-m) window containing the bed reflection in order to compensate for any errors in our determination of the precise location of the bed. The resulting 2-D map of maximum reflection strength along the glacier bed can be examined for spatial patterns indicative of subglacial channels.

In Figure II-5, we show the application of our amplitude processing to the single GPR profile from the HGdA dataset presented in Figure II-4. Figure II-5a shows the GPR image from Figure II-4d after flattening the data to the picked glacier bed surface. In Figure II-5b, we plot the absolute value of the Hilbert transform, where a strong increase in reflection strength around the location of the bed can be seen. Note, however, that the distribution of amplitudes along the bed is highly non-uniform due to the variability in reflectivity at this interface. An image plot of the maximum instantaneous amplitude over a small window containing the bed reflection, for all of the survey lines in the 3-D dataset, is used to identify coherent trends related to the presence of subglacial channels. These latter results are presented and described in Sections II.3.3.1 and II.3.3.2 for the HGdA and GdO datasets, respectively.

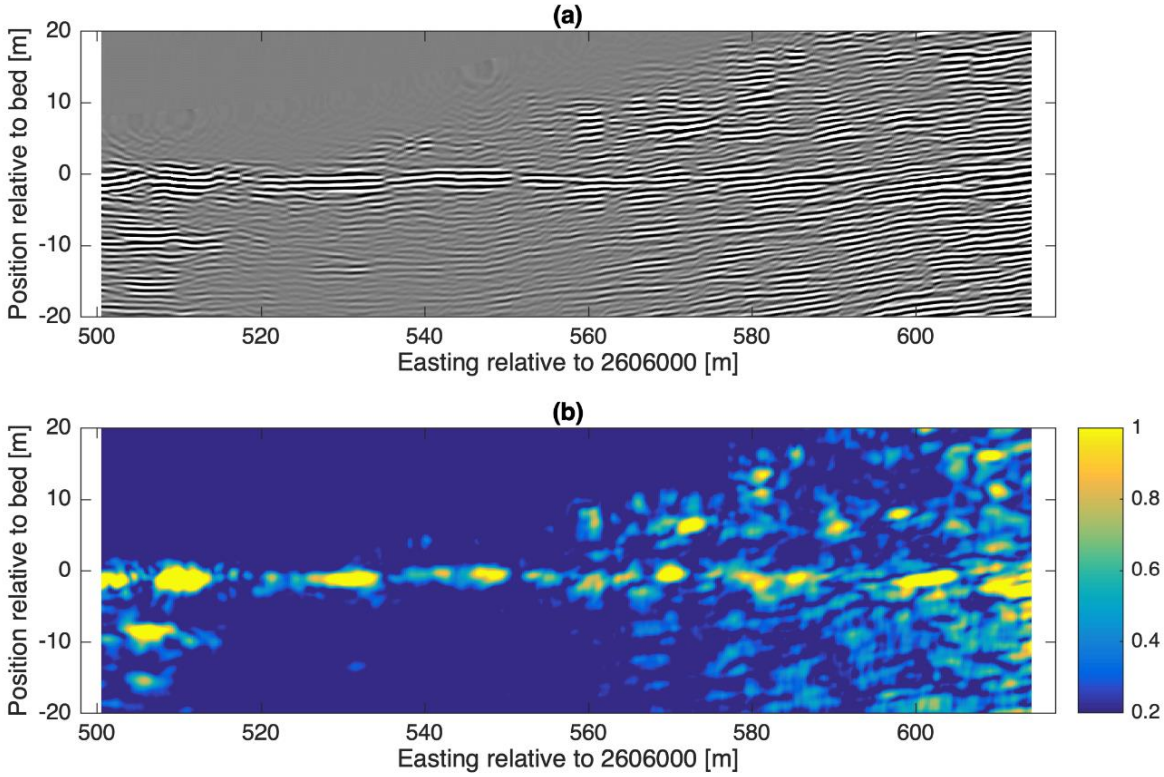

Figure II-5: Illustration of our amplitude analysis of the glacier bed reflection: (a) processed GPR survey line from Figure II-4d 'flattened' to the bed reflection event and (b) corresponding normalized absolute value of the Hilbert transform along each trace, which quantifies reflection strength.

II.3.2.4 Validation of results

The results of our analysis were assessed using two different strategies. The first one involved comparison with aerial orthoimagery acquired at some time after the GPR surveys, where it was possible to either see directly the investigated subglacial channels, or evidence thereof, due to glacier retreat and ice-marginal breakup. At the HGdA, although glacier retreat between 2014 and 2015 was rapid (30 m in length), it was not enough to reveal directly the channels identified with GPR. However, we could compare our results with the location of subglacial channels exiting the glacier snout in 2014 and 2015. Ortho-rectified aerial imagery acquired by Flotron SA in two consecutive years (September 2014 and September 2015) also indicated the development of two large fractures on the HGdA surface within 1 month of our GPR survey. These were later verified in the field to be places where the ice ruptured, which we believe occurred due to instabilities related to surface melting and the enlargement of marginal subglacial channels below. At the GdO, drone imagery was acquired in August 2017 and

August 2018 using DJI Phantom 3 and Phantom 4 drones, respectively. The corresponding orthoimages documented the collapse of a large portion of the main outlet channel in the summer of 2018 along with rapid glacier retreat, which provided direct validation of the GPR findings ~1 year after the measurements.

As a second validation method, we estimated the hydraulic potential at the glacier bed (Shreve, 1972) in order to predict the theoretically most likely trajectories of subglacial channels. This was done by summing contributions to the potential related to elevation and ice overburden pressure as follows:

II-1

$$\varphi = \rho_w g z + c(\rho_i g (H - z))$$

where φ is the hydraulic potential, ρ_w = 1000 kg m^{-3} is the density of water, g = 9.81 m s^{-2} is the acceleration of gravity, z is the glacier bed elevation, ρ_i = 910 kg m^{-3} is the density of ice, H is the ice surface elevation and c is a constant that accounts for the degree of pressurization of the channels. A value of c = 0 represents unpressurized flow, whereas a value of c = 1 represents fully pressurized flow where the ice overburden pressure significantly influences the hydraulic gradient and thereby the flow paths. Ice surface topography data for the HGdA and GdO were obtained from the SwissAlti3D Digital Elevation Model for the summers of 2012 and 2009, respectively (SwissTopo, 2020). These data have horizontal and vertical resolutions of 2 m and were derived from aerial imagery. Glacier bed elevations for the HGdA at 20-m horizontal resolution, derived from irregularly spaced GPR surveys, were supplied by Dr Ian Willis at the University of Cambridge (Sharp et al., 1993). For the GdO, bed elevations at 50-m horizontal resolution were obtained from Dr Mauro Werder at ETH Zurich and derived from helicopter-borne GPR surveys conducted in 2009 (Gabbi et al., 2012). Considerations by Hooke (1984) show that, given high enough discharge and bed slope, especially when ice thicknesses are small (i.e. <50 m), the flow in subglacial channels may not be pressurized. It is also unlikely that such channels close during winter due to insufficient ice overburden weight. Channel positions, however, may be inherited from when they formed under deeper ice in pressurized conditions. As these aspects remain uncertain, we apply Eqn (II-1) using values of c = 0, c = 0.5 and c = 1 in our analysis.

The gradient of the Shreve potential yields the local flow direction, which is used to compute flow accumulation and estimate the most likely subglacial flow pathways. The latter was done

using the Topotoolbox package in MATLAB (Schwanghart et al., 2013; Schwanghart and Scherler, 2014). To form a channel feature, flow accumulation thresholds of 180 upstream cells for the HGdA (cell size 20 m × 20 m) and 60 upstream cells for the GdO (cell size 50 m × 50 m) were considered. These values are different for each glacier because of the different sizes of the bed topography grid cells in each case; a lower number of larger cells is needed to achieve the same amount of flow as when using smaller cells. Note that the computed channel features reflect the hydraulic conditions according to the Shreve potential at the times when the SwissAlti3D DEMs for each glacier were acquired, which are not the same as the acquisition dates of the GPR datasets. However, given the fact that neither the overall surface topography nor the contributing areas of each glacier changed substantially between the DEM and GPR acquisitions, we do not expect a significant change in the predicted subglacial channel locations. Therefore, the considered DEM and bed topography datasets and resulting Shreve calculations provide the best available theoretical insight into the hydraulic potential underneath the two glacier tongues for comparison with our GPR data.

II.3.3 Results

II.3.3.1 Haut glacier d'Arolla

In Figure II-6, we present the results of our analysis of the HGdA GPR dataset. Figure II-6a shows the measured ice surface topography over the GPR survey region. The local slope of the glacier surface can be seen to be approximately constant and is oriented toward the northwest. In Figure II-6b, we plot the GPR-derived glacier bed topography. Unlike the ice surface topography, the glacier bed is seen to slope toward the north in the western half of the profile and toward the northeast in the eastern half of the profile, with a faint rise separating these two regions. Figure II-6c shows the calculated ice thickness over the survey region, which was obtained by subtracting the elevations in Figure II-6b from those in Figure II-6a.

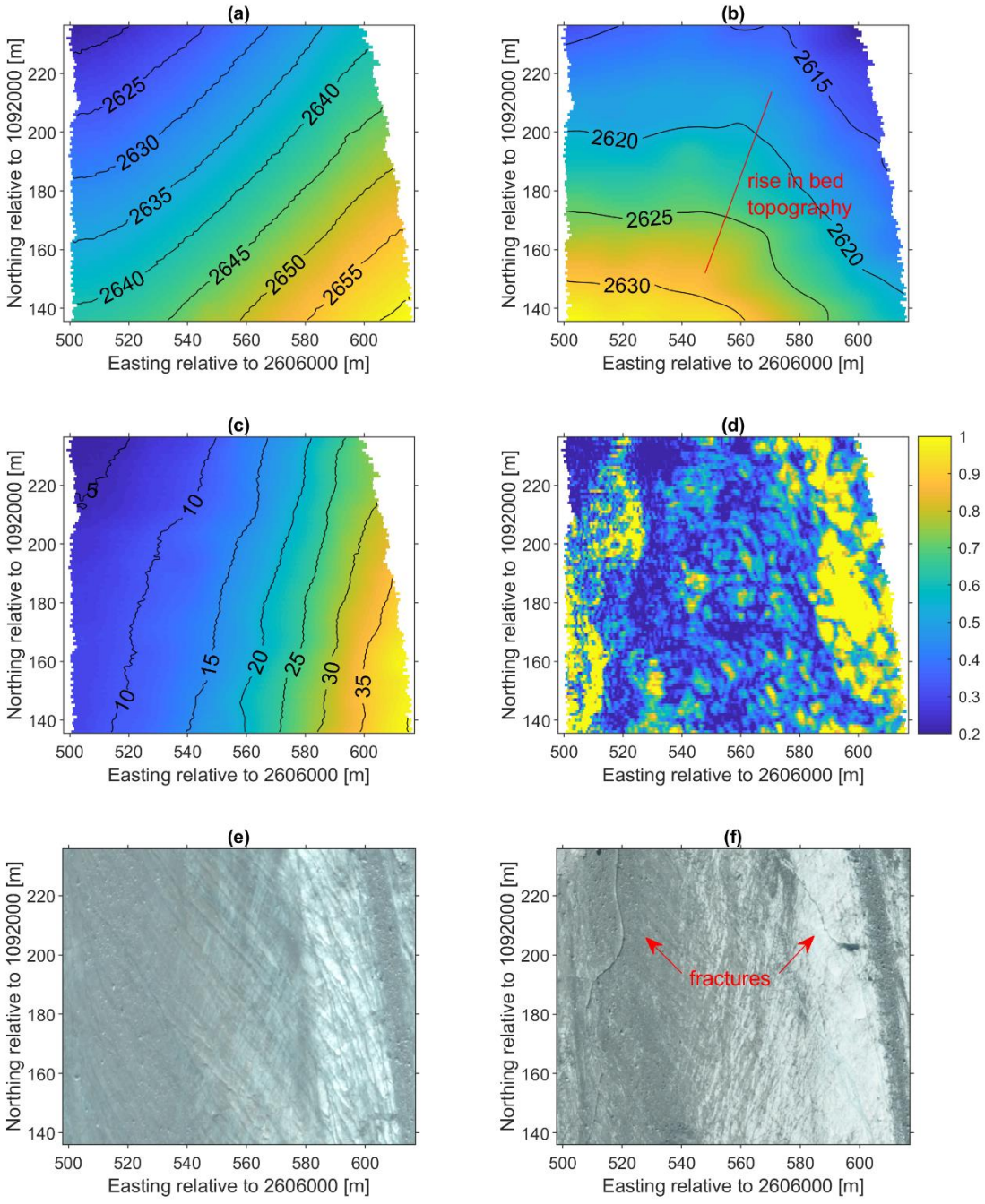

Figure II-6: GPR data analysis results for the HGdA site: (a) glacier surface elevation (m a.s.l.); (b) glacier bed elevation (m a.s.l.); (c) ice thickness (m); (d) maximum normalized reflection strength along the glacier bed; (e) zoom of September 2014 orthophoto from Figure II-2a and (f) zoom of September 2015 orthophoto from Figure II-2b.

Here, we observe that the ice thickness decreases both in the direction of the glacier terminus toward the north, as well as strongly toward the western edge of the glacier where thinning is more significant. The eastern part of the zone of interest has more bare ice whose higher albedo leads to less melting in this region. Further east outside of the GPR survey region, a morainic debris cover of up to several decimeters thick reduces melting due to insulation (Figure II-2b).

Figure II-6d shows the maximum absolute value of the Hilbert transform of the GPR data in the location of the glacier bed for the HGdA dataset, which again quantifies the reflection strength. In this image, higher values are expected to correspond with the location of subglacial channels due to a stronger contrast in dielectric permittivity. We see in the figure that there are two main zones where the amplitude increases significantly; one with small bends on the western side of the survey grid and another primarily linear zone on the eastern side. Both of these zones are oriented approximately north–south and measure several meters in width. The fact that they show continuity perpendicular to the direction of the GPR survey lines (which were run east–west) suggests that they are not artifacts of the data acquisition or processing, but rather represent real differences in GPR bed reflectivity. The western-most zone ends at the glacier terminus at a channel outlet (Figure II-2) and is aligned with the topographic gradient of the bedrock topography (Figure II-6b). It is situated in a region of shallow ice having a thickness of <15 m. The zone on the eastern side, on the other hand, is located in region having ice thickness between 20 and 35 m. It is wider and appears to be associated with a higher bed reflectivity, and may represent a subglacial channel that continues toward the northeast, ending at the second, eastern channel outlet (Figure II-2). Both zones are separated by the rise in bed topography near the center of the glacier tongue (Figure II-6b).

Figure II-6e and Figure II-6f show zooms of the orthoimages from Figure II-2a and II-2b over the GPR survey region, respectively. The image in Figure II-6e was acquired in September 2014, and reflects quite well the conditions of the glacier surface when the GPR data were acquired in August 2015, aside from some recession near the glacier terminus. The image in Figure II-6f, on the other hand, was acquired in September 2015 ~1 month after the GPR acquisition. Here, we see that two notable fractures have developed on the glacier surface in the western and eastern parts of the survey region, which were not present during the GPR survey. A subsequent visit to the HGdA in October 2015 confirmed that the ice ruptured in these locations and that the fractures continued all the way to the glacier bed, where the sound of rushing water could be heard. With regard to the western-most fracture, we observe that its overall trend is remarkably similar to that of the western zone of increased reflection amplitude in Figure II-6d. This suggests that the fracture represents the beginning of the collapse of unstable ice over a shallow subglacial channel, and that the GPR survey allowed for detection of this channel before the fracturing occurred. With regard to the eastern-most fracture, we see that it loosely corresponds to a region of high reflectivity in roughly the same location (Figure

II-6d), which suggests that it may represent a small branch of the larger eastern-most subglacial channel that has ruptured to the surface.

Figure II-7 shows the results of our Shreve hydraulic potential analysis for the HGdA site, which was performed over a broad region encompassing the entire glacier tongue (Figure II-7a). In Figure II-7b we plot the Shreve potential computed for $c = 0$ in Eqn (II-1), which corresponds to the case of unpressurized (open-channel) flow. The main drainage pathways obtained via flow accumulation, as well as the suspected channel locations digitized from the GPR results in Figure II-6d, are shown as red and yellow lines, respectively. Similarly, Figure II-7c and II-7d plot the results obtained for values of $c = 0.5$ (partially pressurized flow) and $c = 1$ (fully pressurized flow). We observe that the GPR-derived channel locations correspond well with the Shreve hydraulic potential scenarios for unpressurized and partly pressurized flow, although the best correspondence would result from a combination of these two scenarios. The location of the western channel also corresponds to the Shreve hydraulic potential for fully pressurized flow. In the location of the GPR survey, the glacier ice was relatively shallow with a maximum thickness of 45 m, which suggests that pressurized flow there is unlikely. Further upstream, however, the flow may be (or have been) pressurized several years ago due to greater ice thicknesses, which may have established the channels in their present positions (Sharp et al., 1993), explaining the current location of channels further downstream. Also note that the Shreve potential was computed based on glacier surface elevation data from 2012, whereas the GPR data were recorded in 2015, which may account for some of the differences between the two results.

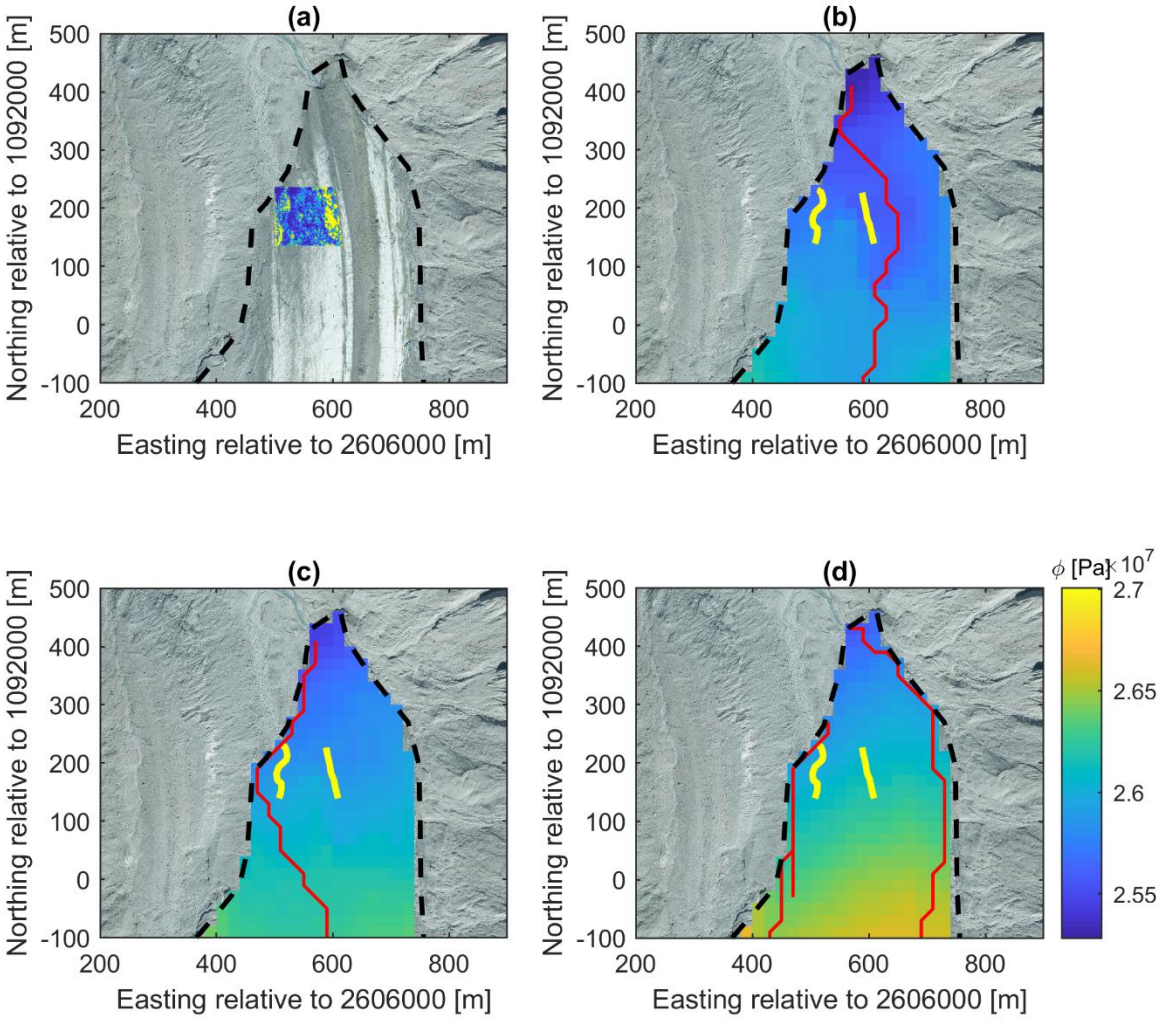

Figure II-7: Zoom of September 2015 orthophoto from Figure II-2b in the region of the tongue of the HGdA, upon which the GPR amplitude analysis results from Figure II-6d are superposed; (b–d) calculated Shreve hydraulic potential along with the theoretically most likely flow paths (red lines) and the manually digitized GPR-derived subglacial channel positions (yellow lines). The Shreve hydraulic potential is presented for (b) open-channel flow (c = 0); (c) partly pressurized flow (c = 0.5) and (d) fully pressurized flow (c = 1). The dashed black line represents the GLIMS glacier outline for the summer of 2015 (Paul et al., 2019).

II.3.3.2 Glacier d'Otemma

In Figure II-8, we present the results of our analysis of the GdO GPR dataset. Figure II-8a, II-8b and II-8c show the measured ice surface topography, GPR-derived glacier bed elevations and calculated ice thickness over the survey region, respectively. All of these are superposed on a drone orthophoto from August 2018. We see in the figure that the local surface topography slopes uniformly toward the glacier terminus, but on the lower part of this slope there is a slight surface depression which was developing into a channel collapse at the time of the GPR survey.

Compared to the HGdA, the bed topography at the GdO is relatively flat over most of the survey region, with the exception of a ~3-m-deep depression toward the northeast. Toward the southern edge of the survey area, there are strong increases in the elevation of both the glacier bed and the ice surface, which are related to the valley's U-shape and reduced melting in this location due to the large amount of debris cover. The ice thickness is seen to follow the commonly observed pattern of decreasing toward the glacier terminus, and is roughly constant across the glacier width with the exception of the zone near the terminus associated with the developing channel collapse.

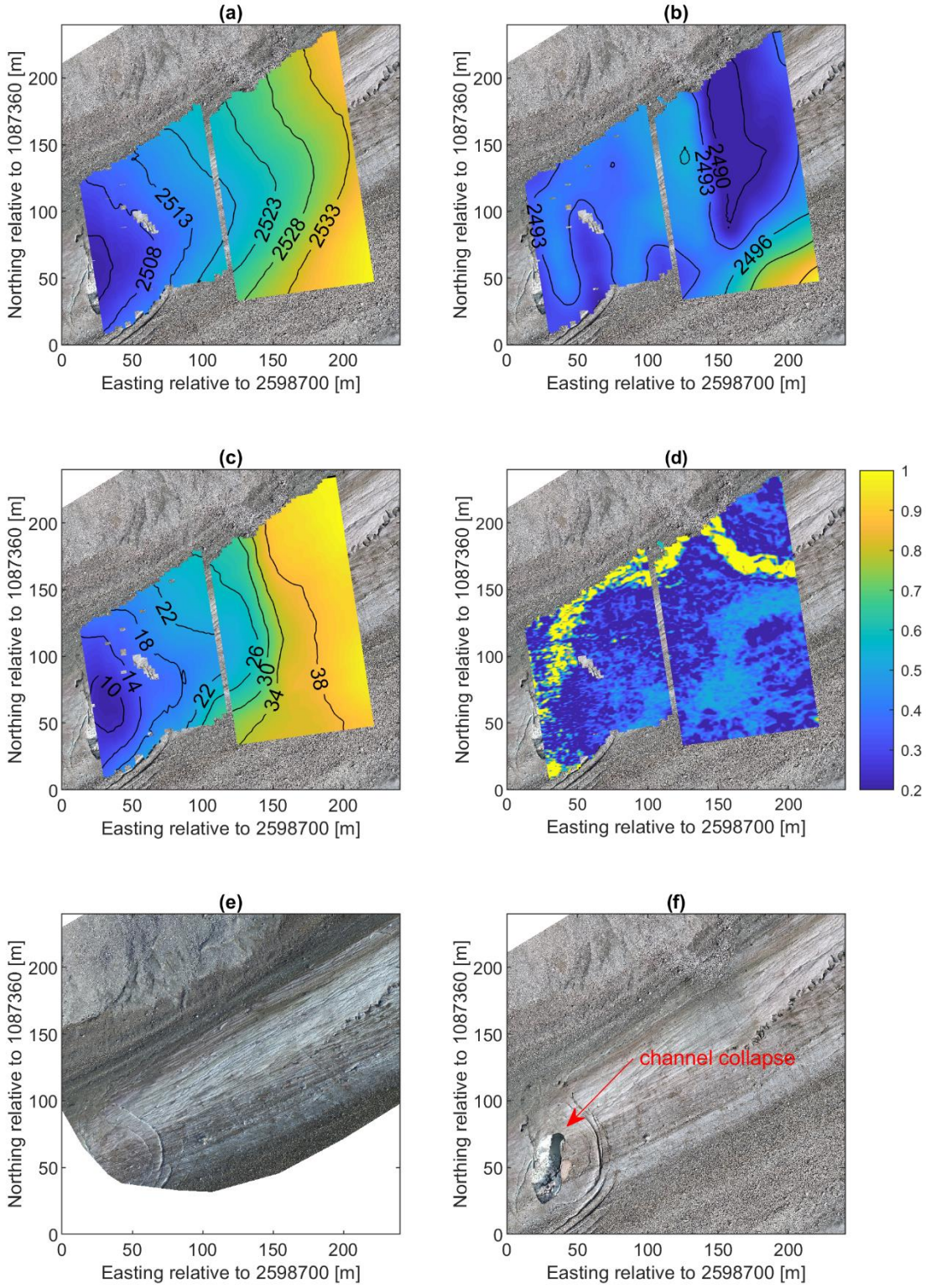

Figure II-8: GPR data analysis results for the GdO site: (a) glacier surface elevation (m a.s.l.); (b) glacier bed elevation (m a.s.l.); (c) ice thickness (m); (d) maximum normalized reflection strength along the glacier bed; (e) zoom of August 2017 orthophoto from Figure II-3a and (f) zoom of August 2018 orthophoto from Figure II-3b.

Figure II-8d shows the maximum absolute value of the Hilbert transform of the GPR data in the location of the glacier bed for the GdO dataset. In contrast to the HGdA, we see that there is a single clear zone showing a strong increase in reflection strength that extends across the entire GPR survey region. This zone, which we believe represents a large subglacial channel, appears to be up to 10 m in width. It originates in the east near the center of the glacier, makes a turn toward the northern boundary of the survey region, and then continues along the northern glacier margin before making a relatively sharp turn back toward the center of the glacier. The latter trajectory appears logical in the sense that it tends to avoid the higher areas of the bedrock topography (Figure II-8b). Similar to the HGdA, the fact that the high-amplitude region shows continuity perpendicular to the direction of the GPR survey lines (which were run roughly south–north) indicates that it is not an artifact of the data acquisition or processing, but rather reflects real differences in bed reflectivity.

Figure II-8e and II-8f show zooms of the orthophotos presented in Figure II-3a and II-3b, respectively. The image in Figure II-8e was acquired in August 2017 during the acquisition of the GPR data, whereas the image in Figure II-8f was acquired ~1 year later. Between these acquisition dates, the GdO retreated by ~40 m on its northern side. A large portion of the region surveyed in 2017 also collapsed sometime between mid-July 2018 and early August 2018, revealing a cavity ~60-m long, 20-m wide and 10-m deep. The position of this cavity coincides well with the suspected subglacial channel location from Figure II-8d, and we believe that surface downwasting combined with channel melting from the inside led to the ice becoming unstable. We also see in Figure II-8f that the channel enters from the northeast into the collapsed area and continues toward the south before turning westward out of the collapsed area, which is consistent with the GPR results in Figure II-8d. Note that collapse of the channel roof during the autumn of 2018 was observed in the field and confirms the channel outflow and inflow positions downstream and upstream of the collapsed section in Figure II-8f, respectively. Finally, a moulin was detected further upstream of the main channel (Figure II-3), whose location may provide further validation for the location of the subglacial channel.

Figure II-9 shows the results of our Shreve hydraulic potential analysis for the GdO site, which, like the HGdA, was performed over a broad region encompassing the entire glacier tongue (Figure II-9a). Figure II-9b, II-9c and II-9d show the hydraulic potential calculated for *c* values of 0, 0.5 and 1, respectively. The main drainage pathways obtained via flow accumulation, as well as the suspected channel location digitized from the GPR results in Figure II-8d, are again shown as red and yellow lines, respectively. We see that the three flow scenarios lead to

reasonably similar drainage patterns that correspond quite well with the GPR results, except for the fact that they do not predict the meandering shape of the identified channel. This may be a result of the significantly lower (50-m) resolution bed topography measurements used for the generation of the Shreve hydraulic potential maps in this case. Indeed, we believe that the meandering shape of the subglacial channel identified in the GPR results reflects strong bedrock control on flow at the GdO via local changes in bed topography and roughness (Alley, 1992; Gulley et al., 2014).

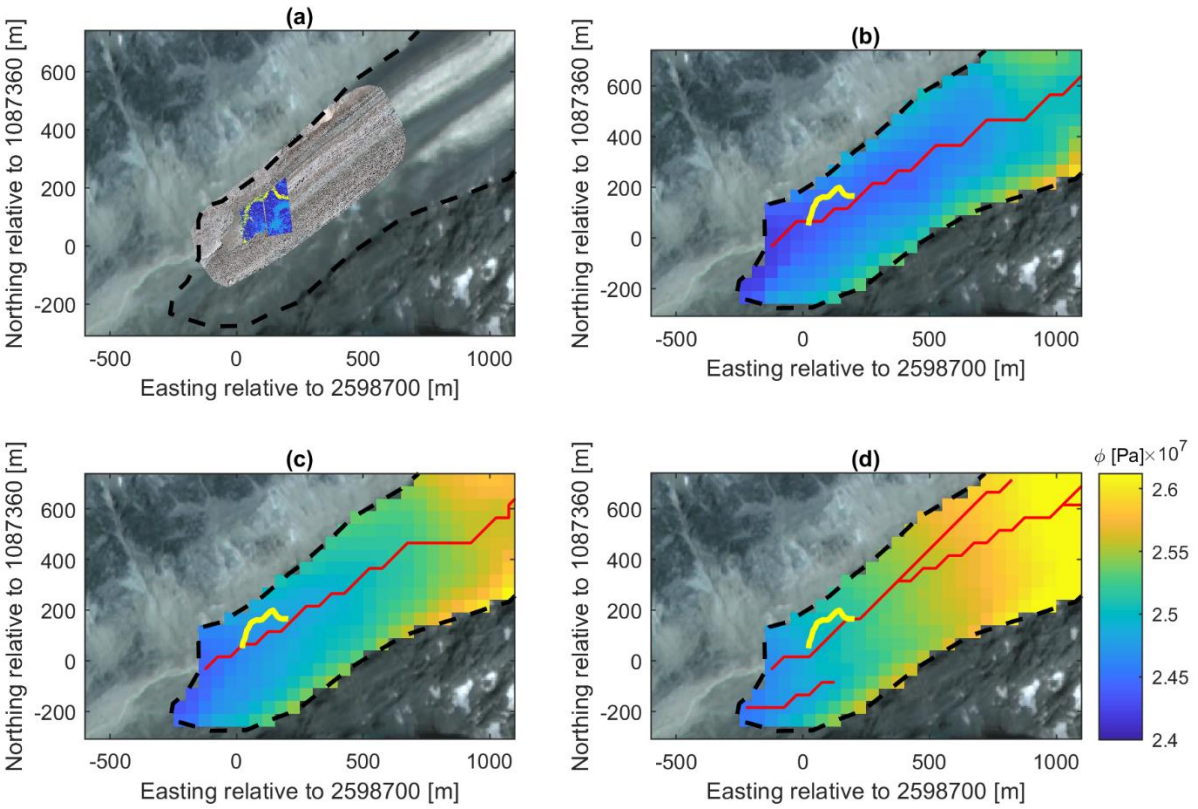

Figure II-9: (a) August 2018 orthophoto from Figure II-3b overlain on a 2019 satellite image in the region of the tongue of the GdO, upon which the GPR amplitude analysis results from Figure II-8d are superposed; (b–d) calculated Shreve hydraulic potential along with the theoretically most likely flow paths (red lines) and the manually digitized GPR-derived subglacial channel position (yellow lines). The Shreve hydraulic potential is presented for (b) open-channel flow (c = 0); (c) partly pressurized flow (c = 0.5) and (d) fully pressurized flow (c = 1). The dashed black line represents the GLIMS glacier outline for the summer of 2015 (Paul et al., 2019).

II.3.4 Discussion

II.3.4.1 Substantive findings

Marginal subglacial channels at the HGdA and GdO were mapped via amplitude analysis of the glacier bed reflection identified in high-resolution 3-D GPR data. The corresponding results were validated using aerial orthoimagery acquired after the GPR surveys, as well as calculation and analysis of the Shreve hydraulic potential. In the case of the HGdA, two subglacial channels were identified; a slightly tortuous one on the western side of the glacier tongue, and a second larger and more linear channel on the eastern side (Figure II-6d). At the GdO, one main, tortuous channel was detected (Figure II-8d), which follows the northern edge of the glacier tongue before turning toward the center of the glacier.

The locations of en- and subglacial channels within temperate Alpine glaciers have been previously identified with GPR measurements. However, existing data were generally not acquired at high enough density for processing and analysis in 3-D, which here allows for the mapping of subglacial channels continuously with meter-scale resolution. Indeed, past research has largely involved channel detection along 2-D GPR survey lines and subsequent interpolation of flow pathways when multiple line data were available (e.g. Bælum and Benn, 2011; Temminghoff et al., 2019). Our study, in contrast, focuses on analysis of the amplitude characteristics of the glacier bed reflection in order to create a detailed map of the suspected channel pathways. This also has the advantage of being able to detect channels that may not be easily seen as distinct reflections on individual GPR profiles. Although the acquisition of such high-density GPR data for 3-D analysis is highly laborious, in particular with regard to surveying areas much larger than those considered here on foot, recent technological developments in lightweight, real-time-sampling GPR instruments and drone-based sensing provide promise for carrying out such surveys over larger regions in an automated manner.

The western marginal subglacial channel detected beneath the HGdA (Figure II-6d) corresponds well with the position of a western channel outlet visible on the aerial orthoimages from both 2014 and 2015 (Figure II-2), whereas the wider eastern channel appears to lead toward an eastern channel outlet. Previous subglacial hydrological studies noted two main flow pathways in this area of the HGdA glacier tongue (Sharp et al., 1993). Perhaps most importantly, fractures appearing on the glacier surface ~1 month after the GPR data acquisition (Figure II-6f) follow closely the western subglacial channel trajectory identified in the GPR data. These fractures were later verified in the field and are likely to be the result of ice weakening in the marginal zone due to surface downwasting combined with channel melting.

In contrast to the eastern channel location, the western channel location at the HGdA was found to agree with the Shreve hydraulic potential results for fully pressurized and partially pressurized flow (c = 1, Figure II-7d; c = 0.5, Figure II-7c). Based on this result, it may be possible that the marginal channel positions are inherited from when the ice was thicker and flow conditions were predominantly pressurized. Once established and eroded into the sediment and bedrock, they could only migrate a small amount during the relatively short summer season. In winter, creep closure due to ice overburden pressure would not be strong enough to close the pre-existing channels entirely as the ice is too thin in this zone. Calculation using Glen's flow law (Glen, 1958; Hooke, 1984) for an ice thickness of 45 m and a subglacial channel diameter of 4 m yields a channel closure rate of 1.2 m per year meaning that, assuming an 8-month-long winter season, channels would close only by up to one-fifth of their total estimated height.

The detected approximate channel planform geometry at the GdO is different from that at the HGdA in that the channel is more tortuous and resembles a meandering river (Figure II-8d). It eventually reaches a principal outlet at the glacier terminus, which is not directly visible in the orthoimage in Figure II-3b but was verified in the field in the autumn of 2018. The channel position was also confirmed by aerial imagery acquired in 2017 and 2018 (Figure II-8e and 8f), which document the progressive collapse of the glacier at the precise location where the channel was identified using GPR. The fact that the detected channel roughly coincides with the drainage pathway determined from the Shreve potential calculations, but deviates from the main pathway in a large meandering turn, suggests that local bedrock topography and sediment dynamics may be important factors controlling its course, rather than ice overburden pressure as suggested by Shreve (1972) and the simplest form of the theory of Röthlisberger (1972).

Both the HGdA and GdO were found to have similar ice thicknesses at their glacier tongues (Figure II-6c and Figure II-8c), and are underlain by similar types of bedrocks. However, their glacier bed compositions differ. At the GdO, field observations indicate that the glacier bed consists of uneven bedrock partly covered by a thin sediment layer (i.e. hummocky terrain) whereas at the HGdA it consists of bedrock covered by a thicker and more even sediment layer (Fischer and Hubbard, 1999). This leads to a more uniform glacier bed topography at the HGdA and to less tortuous subglacial channel planforms.

Both the cracks in the ice above the identified subglacial channels at the HGdA, visible on the aerial photo of September 2015 (Figure II-6f), and the channel breakdown at the GdO, shown on the orthophoto of August 2018 (Figure II-8f) point to a potentially important mechanism

that has been rarely documented. It appears that temperate Alpine glaciers in a rapidly warming climate are not only losing mass due to melting at the surface and via basal melting, but also due to the removal of large volumes of ice via the collapse and disintegration of subglacial channels. Subglacial channel collapse has indeed been observed in a small number of other studies (Konrad, 1998; Bartholomaus et al., 2011; Stocker-Waldhuber et al., 2017), and the research presented here leads us to the hypothesis that the collapse is related to a situation where surface melt reduces ice thickness at the snout margin and thereby also the extent of winter closure of the subglacial channel. Continued surface melt eventually leads to structural weaknesses in the ice and collapse. If this hypothesis can be confirmed with a detailed analysis of surface displacement and melt, it would corroborate the findings of the above studies, as well as suggest that the effects of subglacial channel collapse may be more important for rapid glacier retreat on a global scale than previously assumed.

Our results for the HGdA and GdO show that 3-D analysis of high-resolution, densely acquired GPR data is useful for detecting channel planforms underneath temperate Alpine glaciers. Such channel planforms are important for understanding the role that snout marginal channels play in the export of sediment. Depending on the channel geometry and glacier bed topography, the shear stress distribution at the glacier bed varies and this in turn will influence the sediment transport capacity of the channel (Chen et al., 2018; Perolo et al., 2019). With future glacier retreat and thinning, the subglacial drainage networks underneath the HGdA and the GdO are likely to extend further up-glacier due to an upward shift of the ELA, leading to more meltwater input at higher elevations (Nienow et al., 1998; Beaud et al., 2018). The drainage networks will thereby access new sediment sources underneath the glaciers (Nienow et al., 1998; Swift et al., 2005; Gulley et al., 2012a), leading to changes in sediment fluxes further downstream.

II.3.4.2 Methodological challenges

Reliable identification of the glacier bed reflection is critical for the successful detection of subglacial channels using the methodology described in this paper. In this regard, a number of factors can affect the quality and interpretability of this reflection. First, englacial scattering due to inclusions of water or voids in temperate ice may strongly attenuate the GPR signal, thereby reducing the radar energy reaching the bed as well as adding significant complexity to the corresponding data (Plewes and Hubbard, 2001; Figure II-4b). Second, the combination of GPR antenna radiation pattern, survey line orientation, and underlying bedrock topography may lead to poor visibility and detection of the glacier bed in some cases (Moran et al., 2003; Rutishauser et al., 2016; Langhammer et al., 2017). Finally, internal layering of the glacier ice,

including sediment layers, may complicate the interpretation of the GPR data because layering close to the glacier bed may be difficult to distinguish from the bed reflection (Lapazaran et al., 2016). Despite these challenges, we found that we were able to easily identify the glacier bed in both the HGdA and GdO datasets along most of our survey lines. Indeed, GPR measurements made using the same real-time-sampling instrument much higher up on the HGdA (data not shown) indicated that identification of the bed reflection was even possible where the ice thickness was on the order of 100 m. Note that, in instances where identification of the bed reflection was difficult, analysis of the 3-D GPR datasets in both the survey in-line and cross-line directions proved to be helpful.

Another important consideration for the success of the methodology presented in this paper is the reliability of the amplitude information extracted at the glacier bed. A number of factors can influence the spatial pattern of such amplitudes, which include the quality of the data migration as well as spatial variations in englacial attenuation and scattering that are not taken into account when using a standard, spatially invariant gain function. Furthermore, even in a best-case scenario where the data have been perfectly migrated and attenuation and scattering in the ice have been perfectly compensated, the horizontal resolution of the GPR image at the glacier bed will still be on the order of the dominant wavelength of the GPR pulse (e.g. Stolt and Benson, 1986), which for our 70-MHz system is ~2 m. This means that, at the very least, the images of bed reflection amplitude obtained from the GPR data will represent laterally smeared versions of reality, and that the results presented in Figure II-6d and Figure II-8d must therefore be considered as noisy, low-pass-filtered versions of the true bed reflectivity distribution. Nevertheless, the research presented in this paper demonstrates that such GPR-derived amplitude maps can still offer clear and insightful information regarding the location of subglacial channels. Indeed, the uncertainties that we observed through our repeat-line analysis at the GdO (Figure II-10 andFigure II-11 in Supplementary material) showed that variations in the recovered amplitudes along the line with time were significantly less than those associated with the presence of subglacial channels.

A further factor influencing the accuracy of our processed GPR images is spatial variability in the subsurface radar wave velocity, the latter of which we assumed to be equal to a constant value of 0.16 m ns^{-1} in our analysis. Because of the common-offset nature of the acquired data, more detailed velocity information was not available and the selected value, which is consistent with other velocities published for temperate ice (Plewes and Hubbard, 2001; Murray et al., 2007), tended to provide the best collapse of diffraction hyperboloids. As a result, errors may

exist in the identified location of the glacier bed due to localized velocity variations caused by zones of increased ice water content and the presence of water- and air-filled channels. Nevertheless, these types of errors do not impact the determined planform geometry of the subglacial channels because reflection amplitudes are analyzed along the manually picked glacier-bed reflection.

Finally, despite the fact that we have considered 3-D GPR datasets consisting of densely spaced parallel survey lines in this study, a strong spatial sampling bias exists in these data in the sense that the line spacing (1 m for the HGdA and 2 m for the GdO) is significantly greater than the spacing of measurements along the lines (~0.2 m for both datasets). Consequently, migration will not perfectly collapse hyperboloids into points and artifacts may exist in the processed data (Grasmueck et al., 2005). Close examination of GPR profiles before and after migration (Figure II-4) was performed in order to check for major artifacts that may have significantly altered our results. In future studies, the line spacing for such 3-D analyses should be kept as small as possible (ideally 0.5–1.0 m), although the corresponding surveys would become extremely laborious for regions larger than those considered here. One potential solution is to perform the GPR work via drone, following a precise grid with dGPS navigation and maintaining a minimum distance from the glacier surface.

II.3.5 Conclusions

The use of densely spaced survey lines in conjunction with dGPS navigation enabled us to record high-resolution 3-D GPR datasets in the snout marginal zones of two Alpine glaciers. Amplitude analysis of the GPR reflection along the glacier bed made it possible to reveal areas with a significant change in bed reflectivity, which allows for the identification of subglacial channels that may otherwise be difficult to detect on individual GPR profiles.

The subglacial channels detected at the HGdA and GdO sites measure several meters in width but exhibit different planform geometries. The two channels observed at the HGdA are only slightly meandering, whereas the channel detected at the GdO meanders strongly. We suspect that this difference is a result of differences in glacier bed topography, with the GdO bed being composed of bedrock outcrops and a thin sediment layer, and the HGdA bed being overlain by a thicker sediment layer and presenting a more uniform topography.

Assessment of aerial imagery acquired before and after the GPR surveys, as well as computation and analysis of the Shreve hydraulic potential, allowed us to validate the channel positions identified in the GPR results. The occurrence of cracks at the glacier surface at the

HGdA and the collapse of a subglacial channel at the GdO coincide perfectly with the GPR-derived channel positions. The principal flowpaths computed from the Shreve potential closely match these channel positions, despite the relatively coarse grid size available for the Shreve analysis.

The results presented in this paper show the potential for 3-D analysis of high-density GPR data acquired on temperate Alpine glaciers to provide detailed information about subglacial hydrology. Future drone-supported GPR surveys with a larger spatial extent may yield valuable knowledge about en- and subglacial channel pathways, possibly in 3-D, underneath rapidly retreating Alpine glaciers. This information is critical for better understanding of the drainage pathways, hydraulic properties and sediment export potential of such channels as glaciers retreat and new sediment sources at the glacier bed become accessible due to upstream extension of the subglacial drainage network. With further atmospheric warming, the disintegration and collapse of subglacial channels may become an even more important mechanism contributing to the rapid retreat of temperate Alpine glaciers in the near future.

II.3.6 Acknowledgements

We thank Ludovic Baron for help with development of the GPR acquisition system and fieldwork at the HGdA, as well as Boris Ouvry and Martino Sala for help with fieldwork at the GdO. GPR-derived bed topography data for the HGdA were provided by Ian Willis at the University of Cambridge. GPR-derived bed topography data for the GdO were provided by Mauro Werder at ETH Zurich. This research was supported by the University of Lausanne and the Canton de Vaud, Switzerland. Two anonymous reviewers and Editor Dustin Schroeder provided very valuable comments on a previous version of this manuscript.

II.3.7 Supplementary Material

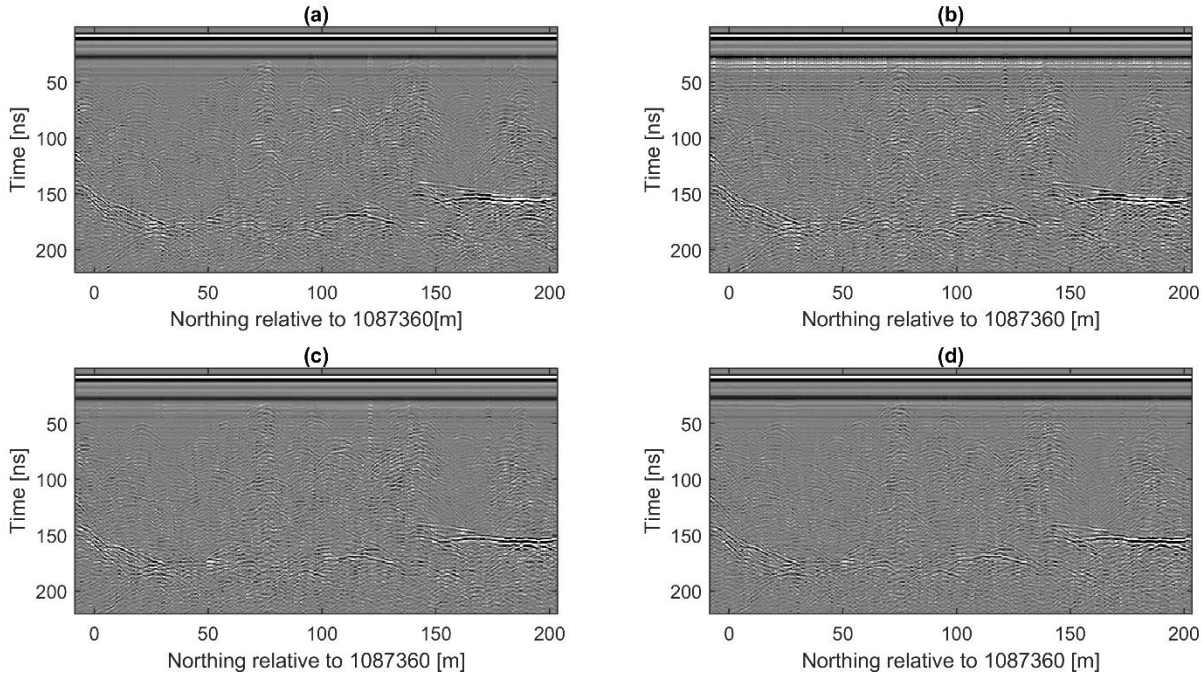

Figure II-10 (Figure S1 in the article): Reflection profiles corresponding to the repeated survey line from the GdO, whose position is shown in Figure II-3. The presented data were acquired at (a) 06:00h; (b) 12:00h; (c) 18:00h; and (d) 00:00h. The amplitude scale on each image is the same. The suspected subglacial channel at the GdO (Figure II-8d) is visible as a high-amplitude reflection around 200 m.

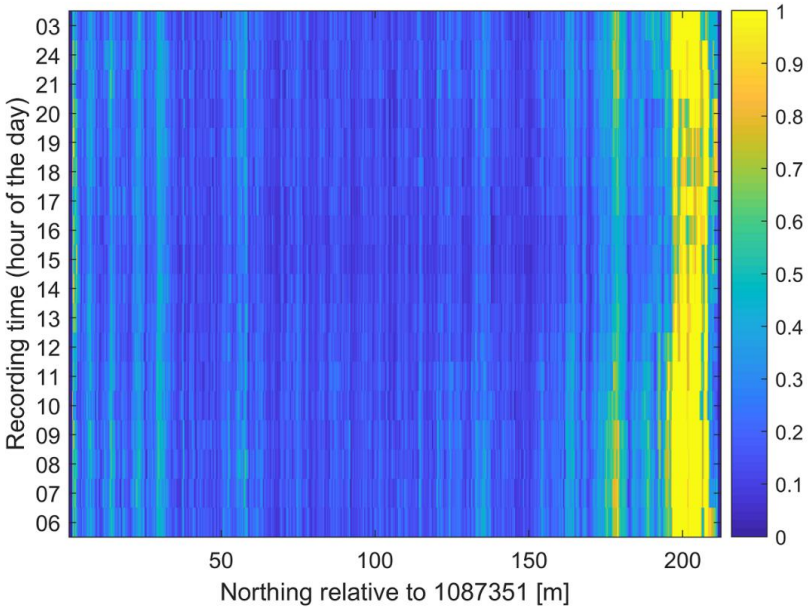

Figure II-11 (Figure S2 in the article): Maximum normalized reflection amplitude at the glacier bed for the repeated survey line from the GdO presented in Figure II-10. The plotted data show the evolution of the amplitude over the course of 22 hours, from 06:00h to 03:00h the following day. The suspected subglacial channel at the GdO (Figure II-8d in the main text) is located at around 200 m. Note that, although the reflection amplitude at the bed does exhibit some temporal variation, this variation is minimal compared to the amplitude variation associated with the presence of the subglacial channel.

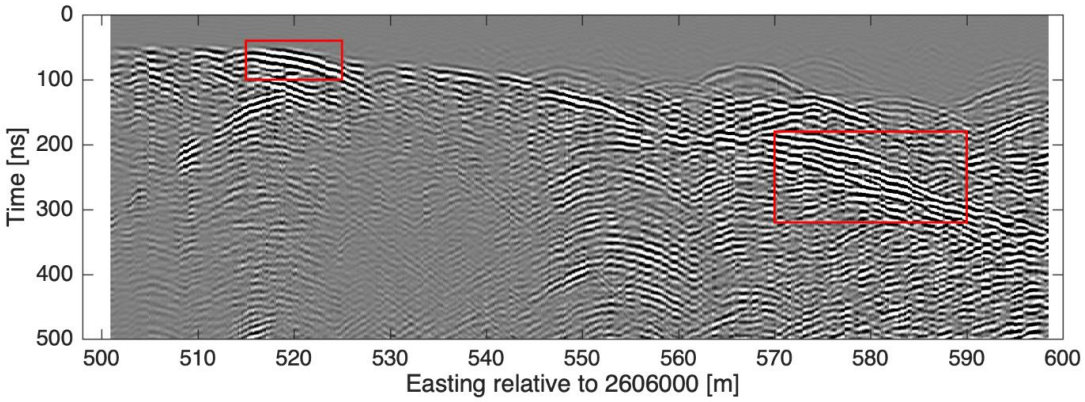

Figure II-12 (Figure S3 in the article): GPR profile from the HGdA collected along 1092236-m northing. The red squares indicate regions along the glacier bed that were identified as subglacial channels in Figure II-6d. These regions correspond with an increase in bed reflection amplitude, but they are not easy to identify as channels on the GPR cross-section because of insufficient vertical resolution.

II.4 Wider implications

The results of this article suggest that high-resolution GPR surveys have the potential to reveal precious information about subglacial channels. We mapped the outline of two major subglacial channels at the Haut Glacier d'Arolla and at the Glacier d'Otemma in the south-western Swiss Alps. These surveys were limited to a maximum ice thickness of 60 m, both due to strong signal attenuation (due to a high water-content) and due to limitations of the GPR antenna used. With a better GPR antenna (possibly a system with two transmitters and two receivers), a slightly lower center frequency and a longer listening time to probe for depths greater than 134 m (in temperate ice) it should be possible to explore sub- and englacial channels at greater ice thicknesses. A further objective would be to determine also the channel heights and therewith also obtain true 3D results.

If such surveys can be executed at a larger spatial scale and at a higher resolution in the future (e.g. for survey areas covering large parts of a glacier tongue with a line spacing of 1-2 m), they have the potential to reveal large parts of the network of subglacial channels underneath temperate Alpine glaciers – at least for the lower half of the glacier tongue where the ice is shallower. UAV-supported GPR surveys have now been undertaken at the Glacier d'Otemma, showing that a larger area of e.g. 400 x 150 m can be surveyed with 2-m line spacing in only one day of fieldwork. Such larger scale surveys could provide important information for the

calibration of glacio-hydrological models and to obtain a better understanding of the behavior of subglacial streams.

In conclusion, this study really served as a launchpad for further, more systematic studies of subglacial stream geometry with GPR, hopefully also involving 4-dimensional surveys to track changes of channel positions, geometry and extent over time.

III SUBGLACIAL CHANNELS, CLIMATE WARMING, AND INCREASING FREQUENCY OF ALPINE GLACIER SNOUT COLLAPSE

Pascal E. Egli, Bruno Belotti, Boris Ouvry, James Irving, Stuart N. Lane

Geophysical Research Letters

Volume 48, Issue 21, 16th November 2021, e2021GL096031

III.1 Chapter aims and objectives

The aim of this chapter is to examine the mechanisms and conditions leading to Alpine glacier snout collapse and potentially to an accelerated retreat of temperate Alpine glaciers. This article addresses subglacial channel collapse at the margin of temperate glaciers in the Swiss Alps from two different angles: (1) statistical analyses to examine the conditions leading to glacier snout collapse features at 12 Swiss glaciers and the factors that distinguish these glaciers from 10 similar glaciers that have not shown collapse features over the last 60 years or so; (2) detailed study of a collapse event at one glacier, the Glacier d'Otemma in the south-western Swiss Alps, in order to confirm the findings from the statistical analysis. Although previous studies have assessed collapse features based on field measurements and process description (Stocker-Waldhuber et al., 2017; Kellerer-Pirklbauer & Kulmer, 2019), the statistical approach presented here and based on the examination of a larger number of glaciers is new for this phenomenon.

The objective is to show which processes and which environmental conditions favor the collapse of the glacier surface, and how the frequency of occurrence of such collapse features has evolved over time.

III.2 Personal contribution to the article

I acquired the field data for the detailed study of Glacier d'Otemma with the help of Martino Sala, Bruno Belotti, Boris Ouvry, Valentin Pipoz and Stuart Lane who assisted with UAV

operation, dGPS measurements of Ground Control Points (GCPs) and ablation stakes, as well as with GPR measurements. Further, I conducted data analysis of the UAV field data with the help of Bruno Belotti (mainly for the processing of UAV data and generation of DEMs), processed GPR data with the help of James Irving and analyzed the DEMs, DoDs and ablation stakes data with the help of Bruno Belotti and Stuart Lane.

For the statistical analysis of 22 Swiss glaciers I assembled data by Grab et al. (2021), by Meteo Suisse (1960 – 2020), by Swiss Topo (2020) and by Glacier Monitoring Switzerland (1881-2020). I converted the data into a suitable format to visualize and extract the important pieces of information using the software packages ArcGIS®, Excel® and MATLAB ®. I viewed aerial imagery for 22 Swiss glaciers from 1938 through 2020 using the LUBIS visualization system (Swiss Topo, 2020) in order to identify occurrences of ice surface collapse events and I noted the presence or absence of events for each glacier over this time period whenever aerial imagery was available. Further, I identified 24 variables relevant for the outline, topography and dynamics of these 22 glaciers and I performed statistical tests on these variables in order to identify their significance for the occurrence of glacier collapse features. Data analysis, including statistical tests, were performed upon advice from Stuart Lane.

I processed the data of annual glacier length change and the temperature data for each glacier. With Stuart Lane's help I performed a statistical analysis on the sensitivity and correlation between the length change and the mean annual summer temperature at each glacier terminus. I used MATLAB® to produce all the figures shown in the Supporting Information and in the main text of this article, except for three figures about the photogrammetric processing (shown in Supporting Information), which were adopted from Bruno Belotti.

I led on writing the article and on its revision with the help of Stuart Lane and James Irving.

III.3 Article 2

III.3.1 Introduction

Alpine glaciers have been retreating rapidly since the 1980s because of rapid climate warming (Paul et al., 2004; Haeberli et al., 2007; Diolaiuti et al., 2011; Fischer et al., 2015; Sommer et al., 2020). Retreat is forecast to accelerate in the coming decades (Zekollari et al., 2019). The primary mechanism of mass loss for Alpine glaciers is surface melt (Oerlemans et al., 1998;

Vincent et al., 2004; Arnold, 2005). Negative glacier mass balance can also be driven by reduced snow accumulation. Less considered is basal or internal ablation. This can involve the collapse of subglacial channels in the snout marginal zone, driven by thinning ice combined with slow creep closure. After collapse, ice is removed via the channel to the glacier outlet. This mechanism of glacier retreat was first described some time ago as 'subglacial stoping' or 'block caving' (Paige, 1956; Loewe, 1957).

There are very few documented or quantified examples of this process (Lindström, 1993; Konrad, 1998; Bartholomaus et al., 2011; Stocker-Waldhuber et al., 2017; Kellerer-Pirklbauer & Kulmer, 2019; Dewald et al., 2021). As a result, little is known about where and when collapse features form and whether or not their formation frequency is changing due to climate warming. We hypothesise that their formation is driven by three interconnected mechanisms: (1) long-term negative mass balance leads to shallow ice in glacier snout margins; (2) shallow ice means reduced longitudinal ice flow velocities and reduced creep closure of subglacial channels; and (3) presence of a subglacial channel underneath shallow ice can initiate collapse due to upwards melting and detachment of ice blocks.

Here, we perform statistical analysis on a sample of 22 Swiss glaciers based on 24 glacier properties, climate data, and historical aerial imagery in order to investigate how pervasive these collapse events are becoming and to test the abovementioned hypotheses. We support our conclusions with the intensive study of a retreating glacier, Glacier d'Otemma, which experienced a recent (2017-2018) collapse event and where we measured ablation, surface elevation change, flow speed and the position of a principal subglacial channel in the snout zone.

III.3.2 Materials and Methods

III.3.2.1 Overview

Conditions driving snout margin collapse were examined by analysis of topography, ice thickness, historical aerial imagery, air temperature, and glacier length change data for 22 glaciers in the western and central Swiss Alps (Figure III-1). We focus on Swiss glaciers because of the widespread availability of measurements, notably glacier bed topography, ice thickness, and aerial imagery, from which we could build an extensive database of the conditions at glacier snout margins. We focus on a single region under the assumption that all

glaciers should have experienced relatively similar climate warming. Based on historical and contemporary aerial imagery, 12 glaciers were selected that showed at least one subglacial channel collapse feature near their terminus since 2015. In addition, 10 glaciers not exhibiting collapse features since 1938 (the first imagery date) were chosen in order to do a balanced statistical comparison (Figure III-1). Their choice reflected (1) relatively close proximity to the glaciers where collapse was observed; (2) having comparable topography and size to nearby glaciers with collapse features; and (3) being in the databases we used to calculate glacier retreat, topography and ice thickness.

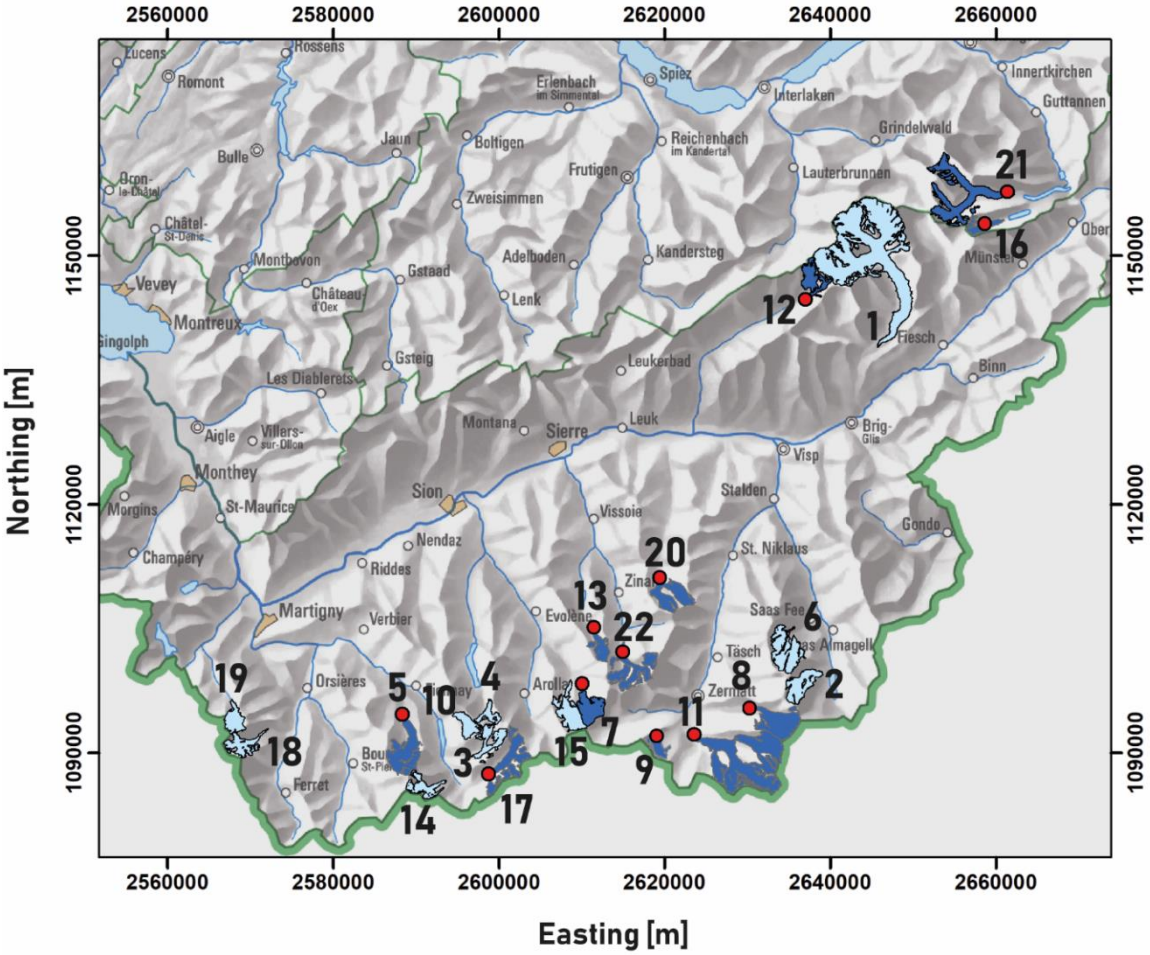

Figure III-1: Map showing the 22 glaciers examined in this study. Glaciers in dark blue exhibited a subglacial channel collapse feature in aerial imagery (red points) whereas glaciers in light blue have not had any collapse features since 1938. Coordinates are in the local Swiss Grid CH1903+ system, in meters. Legend: 1) Aletschgletscher, 2) Allalingletscher, 3) Glacier du Brenay, 4) Glacier de Cheilon, 5) Glacier de Corbassière, 6) Feegletscher, 7) Glacier de Ferpècle, 8) Findelgletscher, 9) Furggletscher, 10) Glacier de Giétro, 11) Gornergletscher, 12) Langgletscher, 13) Glacier de Moiry, 14) Glacier du Mont Durand, 15) Glacier du Mont Miné, 16) Oberaargletscher, 17) Glacier d'Otemma, 18) Glacier de Saleina, 19) Glacier du Trient, 20) Turtmanngletscher, 21) Unteraargletscher, 22) Glacier de Zinal.

Second, we examined in detail the ice surface lowering, subglacial channel position, and ice ablation measured using uncrewed aerial vehicle (UAV) imagery, ground-penetrating radar (GPR) measurements, and ablation stakes, respectively, before and during a collapse event at the Glacier d'Otemma (2017-2018). This allowed investigation of the mechanisms leading to collapse and the exent to which unpressurised subglacial marginal channels can extend up-glacier.

III.3.2.2 Frequency of collapse events

To test whether the frequency of snout marginal channel collapse events is increasing with time, we used the SwissTopo LUBIS visualization system. LUBIS contains all of the digitized aerial imagery held by SwissTopo back to 1938. We inspected the imagery available for each glacier in order to determine whether or not a collapse feature was present. In all cases, collapse features were only observed in snout marginal zones. Each instance showing the snout of one of the glaciers was considered an observation. On some aerial images several of the chosen glacier snouts were visible, meaning that the same image could be counted more than once. There were 179 observations in total. Of these, 29 showed a collapse feature and 150 did not. To avoid the same collapse feature being counted twice, a collapse observation was only retained if it had the same snout showing no collapse in the last previous observation. On this basis, we removed two counts. We considered the cumulative number of identified collapses through time as compared with the cumulative number of observations made in order to account for an increase in the frequency of image acquisition after 1980.

III.3.2.3 Characterization of collapse conditions

For each of the 22 glaciers considered, we assembled a database consisting of (i) surface elevation information from the SwissAlti3D Digital Elevation Model (SwissTopo, 2020); (ii) bed topography and ice thickness distribution based on GPR data and modelling (Grab et al., 2021); and (iii) length change history information from Glacier Monitoring Switzerland (GLAMOS, 1881-2020). Supporting Information (section 3.1) explains how this database was compiled. Table S2 lists the 24 properties considered in our analysis and how they were derived directly (e.g., ice thickness in the snout marginal zone) or inferred from basic process laws. Notably, mean snout marginal glacier velocity was computed as a function of shear stress and ice thickness, using Glen's flow law (Haeberli and Hölzle, 1995; Cuffey and Paterson, 2010;

Gantayat et al., 2014; Supporting Information section III.4.1), with values comparable to those obtained from large-scale observations (Millan et al., 2019).

To investigate the extent to which glaciers showing collapse features are likely to have lower longitudinal ice flux and subglacial channel closure, we considered mean ice thickness, bed slope and surface slope for the entire glacier and for the first 2 km of each glacier tongue. These properties were also determined for a 100 m radius around each of the most recent collapse zone locations. As all glaciers showing collapse features had a collapse event between 2015 and 2020, the values of these properties derived for ice thickness distributions dating from 2016 are comparable (Table S6). The mean distance between the center of the most recent collapse feature and the glacier terminus for the 12 glaciers showing collapse features was found to be ~250 m. Thus, for glaciers not showing collapse features, a hypothetical collapse zone of 100 m radius, positioned at the centerline at a horizontal distance of 250 m from the terminus, was used (details in Supporting Information section 3.5.1).
We also characterized glacier length change using Glacier Monitoring Switzerland (GLAMOS, 1881-2020) data to determine length change and variability in length change since 1987, which is the date considered for the onset of rapid recession related to climate warming in the study region (Costa et al., 2018).

Finally, Jarque and Bera (1980) tests of the 22 samples of each property in Table S2 suggested that 13 out of 24 properties were non-Gaussian. Ho, the null hypothesis, was that the distribution was normal; the test required a probability, p, of 0.05 or less, for 95% or more confidence that it can be rejected. Consequently, we used Mann and Whitney (1947) U tests to evaluate whether the 24 properties differed between those glaciers showing channel collapse and those not showing collapse.

III.3.2.4 Relationship between summer air temperatures and retreat

If collapse formation is driven by incursion of warm air underneath snout margins via unpressurised subglacial channels, we might expect variation in annual snout recession to be more sensitive to mean annual summer air temperature variations than for glaciers where snout recession is driven by temperature effects on surface melt and long-term mass balance. To investigate this hypothesis, we identified for each glacier the year of onset of continuous retreat of the tongue, using the GLAMOS (1881-2020) database (Supporting Information section 3.7). We calculated a time-series of annual retreat rate ($R_{A,}$ variables are listed in Table S1) and its

mean (R_M) for each glacier for the period of continuous retreat. For the same period, we determined annual mean summer air temperature in the snout region (T_{SA}) and its mean (T_{SM}). This used spatially interpolated and gridded MeteoSwiss data (temperature 2 m above the ground between the 1st of June and the 31st of August) from the center of the 1x1 km grid cell located closest to the glacier terminus. We determined the coefficient of variation of retreat (R_{CV}) by dividing the standard deviation of retreat by the mean annual retreat rate. We computed the Pearson correlation coefficient between T_{SA} *and* R_A (P_{RT}) and we calculated the sensitivity of R_A to T_{SA} (S_{RT}) using simple linear regression. Testing for normality using the Jarque and Bera (1980) test allowed us to compare glaciers with and without collapse features using Student's t, for all parameters except S_{RT}. The latter was not normally distributed and so we used the Mann and Whitney (1947) U test.

III.3.2.5 Surface dynamics and subglacial channel collapse at the Glacier d'Otemma

In August 2017, densely-spaced GPR lines were acquired in the snout zone of the Glacier d'Otemma. This region collapsed during the summer of 2018. These lines allowed mapping of the planform of a major subglacial channel (Egli et al., 2021). During the summer 2018 collapse, high-resolution UAV surveys were acquired on the 7th of August and on the 23rd of August. The positions of 54 Ground Control Points (GCPs) were measured on the same days using a differential global positioning system (dGPS) for the purpose of structure from motion multi-view stereo (SfM-MVS) photogrammetry (Supporting Information section 3.3, Figures S3, S4, S5). Ablation measurements were carried out at 49 regularly distributed ablation stakes (Figure III-6).

Digital elevation models (DEMs) were produced applying a standard processing workflow (James et al., 2020; Rossini et al., 2018, Gindraux et al., 2017; Westoby et al., 2012; Supporting Information section III.4.3; Figure III-6) using Agisoft Metashape© software. A DEM of difference (DoD; dz_{net}) showing the difference in surface elevation between the two surveys (16 days apart) was then computed. Independent validation of the DEM data suggested that the DEM elevations were precise to +/- 0.011 m such that for 95% confidence of significant change (see Lane et al., 2003), the limit of detection is +/-0.031 m. We did not correct the surface elevation change for lateral ice flux as the longitudinal velocity in the snout margin was measured by dGPS at the ablation stakes, as well as from the UAV imagery using the ImGraft template matching algorithm (Messerli and Grinsted, 2015), to be less than 10 centimeters over 16 days.

To distinguish between ablation and ice dynamics, we consider the measured net surface height change (dz_{net}) to be equal to the sum of components due to vertical deformation ($dz_{dynamics}$) and ablation ($dz_{ablation}$):

III-1

$$dz_{net} = dz_{dynamics} + dz_{ablation}$$

$dz_{ablation}$ was estimated by spatially interpolating ablation stake measurements using kriging. The $dz_{ablation}$ was subtracted from d_{znet} to estimate the surface change due to $dz_{dynamics}$ (Supporting Information section 3.4). To test for the influence of variables such as aspect, reflectance or slope on ice surface elevation changes and melt, we computed their correlations with dz_{net} and $dz_{ablation}$ (Figure III-10, Figure III-11, Table III-4). As a proxy for the albedo we consider surface reflectance (Rippin et al., 2015).

Finally, we tested for a relationship between the presence of a subglacial channel and increased ice surface elevation changes. Based on GPR-derived channel outlines and supported by calculations of the Shreve hydraulic potential (Shreve, 1972; Figure III-17; section 3.2 in Supporting Information), ablation stakes were classified according to the likelihood that they were located over a subglacial channel (Supporting Information section 4.3.8).

III.3.3 Results

III.3.3.1 Collapse events and their changing frequency

The most recent channel collapse features identified for the "collapse" glaciers are illustrated in Supplementary Figure S1 (Figure III-4). They differ in the detail of their form, but most have concentric crevasse-like features present in the early stages of development (e.g. Figure III-4c, III-4i), during collapse (e.g. Figure III-4a) and afterwards (e.g. Figure III-4e, III-4j). The images confirm that they can develop in both debris-free and debris-covered snout marginal zones.

Figure III-2 shows the cumulative number of collapse events observed on the aerial images, along with the cumulative number of observations from 1938 to present. The 5-year running average and standard deviation of the mean summer air temperature of "collapse" glaciers is also shown. There is an increase in the frequency of observations starting in the early 1980s.

However, the frequency of observed collapse events increases more rapidly after the year 2000, especially from 2016 to present. As climate warming accelerates and as glacier retreat continues, so does the collapse frequency.

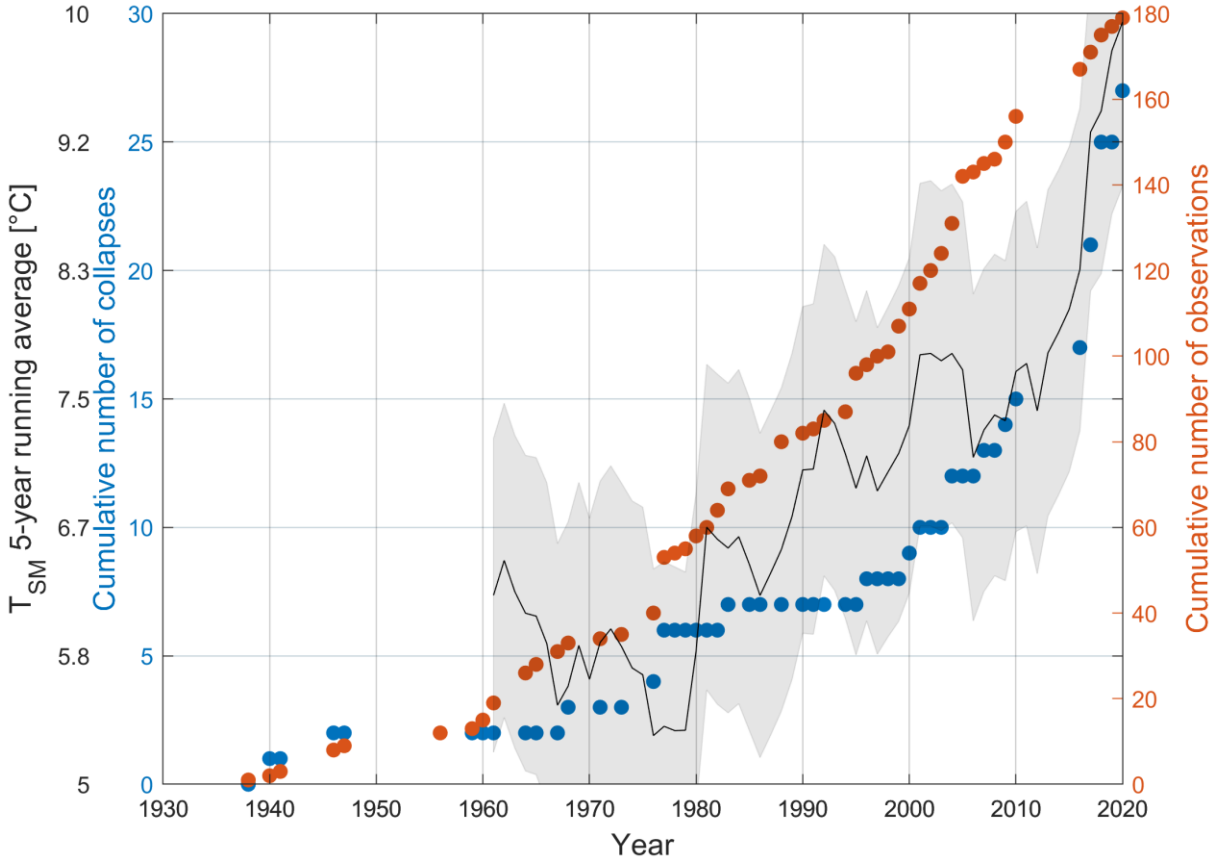

Figure III-2: Cumulative number of collapse events (blue dots) and cumulative number of observations (orange dots) since 1938 for all 22 glaciers considered in our study. Five-year running average of the mean summer temperature (T_{SM}, black line) since 1961 over the 12 glaciers exhibiting one or several collapse events, along with the corresponding standard deviation (grey shaded area).

III.3.3.2 Statistical analysis of collapse conditions

Application of the Mann-Whitney U test with a 95% confidence interval to all 24 properties (Table III-2) shows that collapse and non-collapse groups of glaciers only differ significantly for five variables (Figure III-5) within the vicinity of the collapse areas: (1) ice thickness (Figure III-5a); (2) creep closure rate (Figure III-5b); (3) ice flow velocity (Figure III-5c); and (4) mean surface slope (Figure III-5d, III-5e). Thus, relatively thin ice, a shallow surface slope and low longitudinal flow velocity in the immediate vicinity of a marginal subglacial channel are the

conditions required for collapse. Ice with a thickness of less than 50 m, for example, results in creep closure being small enough that a subglacial channel with a diameter of 5 m does not close over winter (calculations according to Supporting Information section 4.3.1; Table S7, separate file). Combined with a small surface slope (a median of 11.4° for glaciers with collapse features; Table S7, separate file) and a small bed slope (a median of 14.3° for glaciers with collapse features; Table S7, separate file) this shallow ice has low glacier-longitudinal flux, further inhibiting channel closure.

III.3.3.3 Relationship between summer air temperatures and retreat

Mean annual glacier length change, mean summer temperature in the snout zone and the coefficient of variation of retreat did not differ significantly between glaciers exhibiting and not exhibiting collapse features (Student's *t*, p=0.05). However, glaciers with collapse features had systematically more negative correlations between annual glacier length change and mean annual summer temperature (p<0.05) and higher sensitivity of annual glacier length change to mean annual summer temperature (p<0.05) (Figure III-14). For the glaciers with collapse features, 6 out of 12 had significant (p<0.05) negative P_{RT} values compared with 2 out of 10 non-collapse glaciers. Thus, a diagnostic characteristic of glaciers showing collapse features appears to be a stronger sensitivity to mean summer temperature.

III.3.3.4 Measurement of an active collapse at the Glacier d'Otemma

Figure III-3a shows the UAV-based orthoimage of the Glacier d'Otemma for the 7th of August 2018, ablation stake positions and location of a 10-m-wide subglacial channel based on high-resolution GPR data acquired the year before (Egli et al., 2021). The orthoimage shows development of a collapse feature close to the glacier snout near the downstream end of the identified channel.

Figure III-3b shows the surface elevation changes between the 7th and the 23rd of August 2018. General surface height loss is observed all along the glacier tongue. This loss is greatest (up to 1.1 m) in areas of bare ice and reduced where there is greater debris cover (Figure III-3a and III-3b). Figure III-3b also shows increased lowering of the surface above the GPR-identified

subglacial channel. Areas outside of the glacier outline show little vertical change, with the exception of zones of 'dead ice' melt under the debris cover (e.g., top left in Figure III-3b).

Figure III-3c shows surface change after removal of the kriging-interpolated ablation stake measurements. This results in some differences from the original DoD, but the pattern of strong surface lowering in the vicinity of the subglacial channel persists. Small elevation changes outside the area occupied by ablation stakes are within or close to the limit of detection of the DoD. To rule out drivers of surface change other than presence of a subglacial channel, we examined correlations between surface change and glacier surface slope, reflectance, aspect and elevation for small patches (0.5 x 0.5 m) around each ablation stake location. None of these four variables were correlated with elevation change or ablation rate (Table III-4, Figure III-10 and III-11). Thus, the surface change (Figure III-3c) can be attributed to enhanced vertical deformation related to the presence of a subglacial channel that must have been at atmospheric pressure. Evidently this enhanced deformation was not sufficient for the channel to close and to become pressurised.

Surface elevation changes and ablation measurements were compared for three different categories defined according to position: locations known to be above the identified subglacial channel (called on-channel), locations that are likely to be above the channel (called likely-on-channel), and locations that are not above the channel (called off-channel). A Mann-Whitney U test shows no significant difference (p=0.05) in surface ablation between on-channel and off-channel locations. With regard to surface elevation changes, the Mann-Whitney U test shows that on-channel values are significantly different from off-channel ones (p<0.05), whereas

likely-on-channel values are not significantly different from off-channel values (Figure III-15, Table III-5).

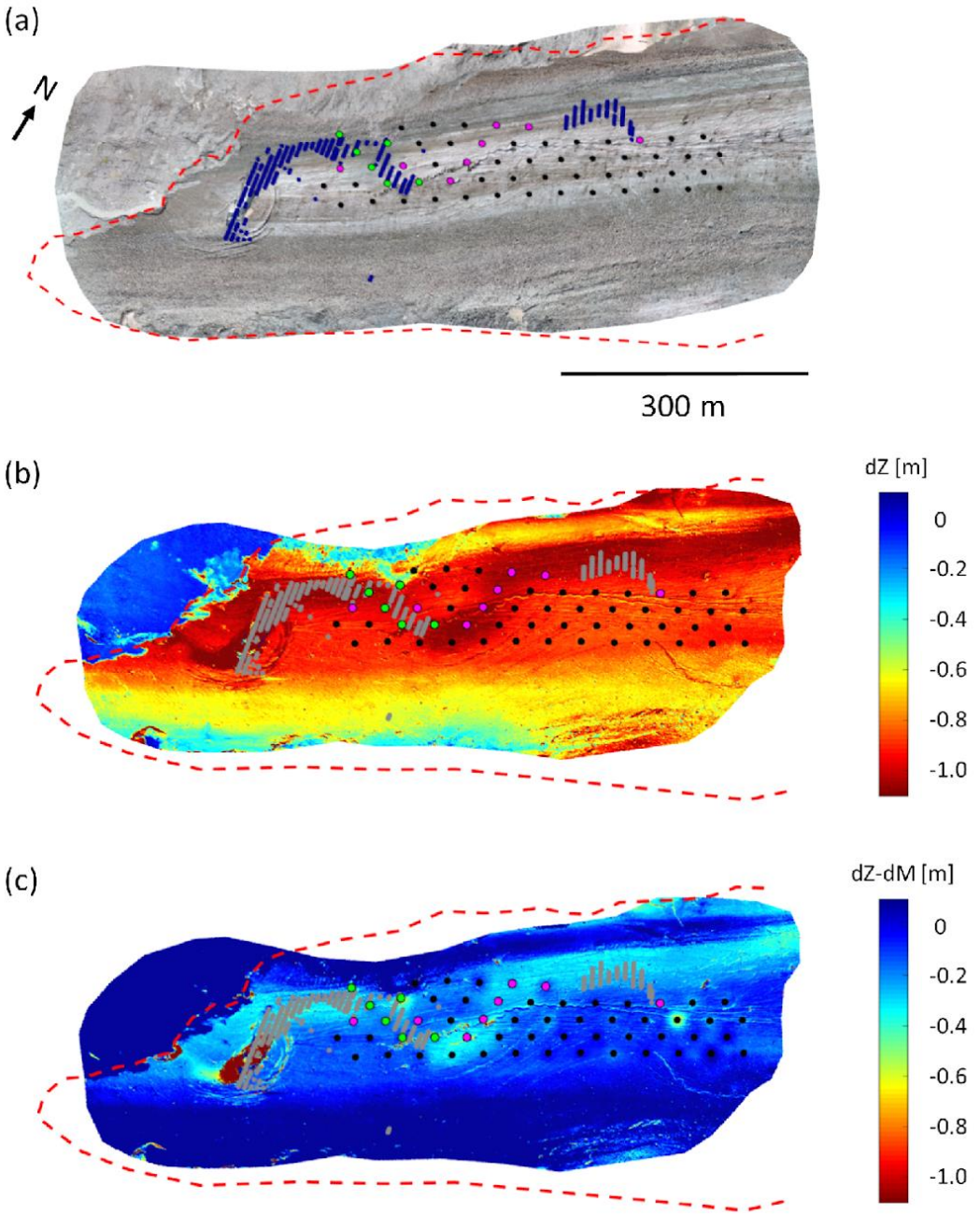

Figure III-3: (a) Orthophoto showing the locations of ablation stakes (black dots) and the positions of a major subglacial channel identified using GPR (Egli et al., 2021) (blue stipples). (b) Change in surface elevation computed between the 7th and the 23rd of August 2018, with channel positions shown as grey stipples. The collapsed area is clearly visible as an elongated dark red spot less than 100 m from the glacier terminus. For readability the DoD value was clipped to 1.1 m. (c) Image in (b) after subtraction of ablation measurements. The ablation stakes are subdivided into off-channel locations (black), almost certainly on-channel locations (cyan), and likely-on-channel locations (magenta).

III.3.4 Discussion

Analysis of historical imagery has revealed a systematic increase in the frequency of surface collapse features due to 'subglacial stoping' or 'block caving' (Loewe, 1957; Paige, 1956) for a set of Swiss glaciers since 2000 (Figure III-2), about 5 to 10 years after the onset of rapid climate warming for this region (Costa et al., 2018). This delay is not surprising as most Alpine glaciers show a lag in the onset of retreat with respect to temperature changes, primarily related to glacier surface slope (Zekollari et al., 2020; Jouvet et al., 2011). The collapse features (Figure III-4) were found to occur predominantly in glaciers having margins comprised of thin ice (generally with a thickness of less than 50 m; Table III-3) and with shallow surface slopes and bed slopes (both less than 23°; Table S7, separate file). Flow velocity calculations suggest these zones had almost no longitudinal ice flux (Figure III-5c) and reduced vertical channel closure rates (Figure III-5b). Given the importance of shallow surface slopes, glaciers currently showing collapse features are only likely to continue to do so if they do not retreat into zones of steeper surface slope. The opposite might apply for glaciers not showing collapse if they retreat into a zone with lower surface slope.

Intensive investigation of one of the 12 glaciers with collapse features showed that collapse was centered directly over a subglacial channel (Figure III-3a). Remarkably, enhanced vertical deformation was observed above this channel for at least 600 m up glacier (Figure III-3b, III-3c). Any void under a glacier should be subject to void-directed ice flow unless water pressure in the void equals the ice overburden pressure (Nye, 1953; Fountain and Walder, 1998). Enhanced vertical deformation above the subglacial channel indicates that the latter was not pressurised for some way up-glacier. The vertical deformation was not enough to close the void. Based on analysis presented in Hooke (1984, Figure 2), with the thickness of ice at the snout of the glacier and a glacier bed slope that is marginally greater than the glacier surface slope, the channel is likely to be open. Our work importantly suggests that locally-increased vertical deformation rates on Alpine glaciers may be used to map the position of such subglacial channels flowing at atmospheric pressure.

The vertical deformation over the subglacial channel at the Glacier d'Otemma was approximately 0.2 to 0.3 m over a 16-day period (Figure III-3c). Theoretical calculations using Hooke (1984) (Supporting Information section 3.1) suggest a closure rate of 0.18 m per year if we assume a 5-m-diameter semi-circular channel. One explanation for a higher closure rate than

predicted by theory is deviation of the channel from a semi-circular shape, as observed in boreholes made at the Glacier d'Otemma during the summer of 2021, and reported for the Rhonegletscher by Church et al. (2021). An analysis using the theory for non semi-circular channels by Hooke et al. (1990) produces closure rate estimates over a 16-day period of ~0.03 to 0.13 m (Supporting Information section 3.5), which is commensurate with our estimations.

Taking into account the DoD detection limit (+/-0.031 m), the 0.2 to 0.3 m of measured surface deformation is greater than theory. The question then becomes why are high vertical deformation rates maintained without returning the subglacial channel to a pressurized state? Field observations revealed large blocks of ice in the braid plain downstream from the glacier during the collapse event. We propose that as the ice overlying the subglacial channel close to the terminus is thin (~5-7 m; Figure III-16) and as it creeps towards the channel, ice blocks fall off the ceiling (block caving; Paige, 1956). Thus, whilst there is an enhanced vertical deformation rate, basal ice is lost via subglacial caving rather than contributing to subglacial channel closure. These findings are supported by the results of a recent study of more than 1400 esker enlargements that suggest ice marginal subglacial channel collapse in the late stages of rapid ice sheet retreat (Dewald et al., 2021). This caving process is rarely considered as a contributor to the mass balance of Alpine glaciers. We can get some idea of its comparable contribution; comparison of Figure III-3a and III-3b suggests vertical deformation that is about 20% of surrounding ablation for clear ice but similar in magnitude for zones of debris-covered ice. The snout marginal zone of the Glacier d'Otemma is about 500 m wide and 40% debris covered. Given that the vertical deformation occurs over a 10-20 m width, and assuming equilibrium between vertical deformation and subglacial channel evacuation of ice, it implies only a 2% increase in mass loss of ice. However, field evidence of large blocks, typically > 1 m diameter, deposited in the proglacial margin during the collapse suggests that the collapse itself may be a much more significant contribution to snout margin retreat in years when it occurs. This merits investigation.

There are two additional mechanisms that may play a role in the development of collapse features that merit further investigation. The first relates to the greater sensitivity in the retreat of glaciers with collapse features to inter-annual summer temperature variation (Figure III-14b). This sensitivity may result from reduced longitudinal flux in the snout margin of such glaciers, but also because of enhanced subglacial exposure to warm air during summers. The measured vertical deformation at the Glacier d'Otemma suggests significant up-glacier extent of water

flow at atmospheric pressure (Figure III-3b and III-3c) and hence subglacial exposure to warm air incursion. Temperature sensitivity may also result from the effects of warm tributary streams that enter the glacier at the snout margin.

The second mechanism to note is suggested in Figure III-3a, which shows that the subglacial channel at the Glacier d'Otemma is meandering and that the collapse feature forms at a bend in the channel. The time-series images of collapse at the Glacier d'Otemma shows that the collapse morphology has meander-parallel crevasses (Figure III-18). The possibility that subglacial channels are sinuous has been recognized, notably in studies of dye breakthrough curves (Kohler, 1995) suggesting the presence of open-channel flow with walls comprised of ice and/or till that can be mechanically eroded. It is well-established that straight rivers that are able to erode their beds and/or banks tend to initiate meandering as a result of the inherent instability related to the effects of turbulent anisotropy on secondary circulation and which tends to grow as a function of time across a wide range of river scales (Dey and Ali, 2017). In theory, deviation from a glacier-longitudinal orientation exposes the channel to greater longitudinal fluxes and hence greater closure so meaning that subglacial channels cannot meander unless they can erode into bedrock. However, the low surface slopes and thin ice in the margins of the glaciers we found showing collapse (Figure III-5a-e), coupled to the possibility that the immediate margins of temperate glaciers may have zones of compression (Reinardy et al. 2019) would slow the rate of closure of laterally-oriented subglacial channels, especially if they are wide and flat. At the Otemma glacier with the estimated longitudinal velocities (1.29 m per year, Table S7) the more than 10-m-wide subglacial channel would only close by around 10 to 15% per year. This would allow maintenance of channels that meander. Thus, as glaciers thin and their longitudinal velocities fall, not only do subglacial channels close less readily, they may be increasingly able to maintain a meandering form, which in turn contributes to surface collapse due to lateral erosion. As technologies for mapping subglacial channels improve, it should become possible to test the hypothesis that meandering open channel flow under glacier snout margins with low longitudinal ice flux is a likely mechanism driving collapse.

III.3.5 Conclusions

The frequency of collapse features in Alpine glaciers has increased markedly since 2000. Such collapse is associated with glaciers that tend to have lower rates of longitudinal ice flux and so reduced compression and longitudinal closure. Low longitudinal flux is a consequence of

glacier thinning related to a tendency for Alpine glaciers to have a negative mass balance due to climate warming. Glacier thinning leads to a long-term reduction of flux of accumulated ice into the ablation zone. Thus, the frequency of collapse at Alpine glacier margins is likely to increase as climate warming continues. The delay between the onset of warming (late 1980s) and the onset of increased collapse (year 2000) is not surprising given it may take some time for a long-term decrease in mass balance to translate into reduction in snout marginal longitudinal ice flux. Not all retreating glaciers are likely to display collapse features at all times; given the dependence of collapse on low longitudinal ice flux, the snout margin should be in a zone of relatively low surface slope.

Intensive study of a collapse event for one glacier confirmed that collapse occurred over a subglacial channel flowing at atmospheric pressure. Two mechanisms are suggested to explain collapse formation; (1) up-glacier incursion of warm air and/or supply of warm water to the glacier snout margins; and (2) development of subglacial channel meanders that can be maintained due to low longitudinal ice flux rates.

III.3.6 Acknowledgments, Samples, and Data

- We acknowledge the extremely helpful reviews of two anonymous reviewers and of Editor Mathieu Morlighem.

- This project was funded by the Canton de Vaud and by Swiss National Science Funding grant 200021_188734 awarded to Lane. We thank the authorities of the Commune de Bagnes for granting access to the field site.

- No real or perceived financial conflicts of interest are present for this article.

- None of the authors has an affiliation that may present a conflict of interest for this article.

- The data supporting the conclusions meets FAIR principles and is supplied with this paper under the following link: https://doi.org/10.5061/dryad.h18931zmh

III.4 Supporting information

III.4.1 Introduction

The data files used for the analysis of 22 swiss glaciers include glacier bed topography data and ice thickness data, ice surface topography as well general glacier characteristics and retreat rates. The data files used for the Glacier d'Otemma case study consist of DEMs, ablation stake data, orthophotos as well as channel outlines resulting from GPR surveys.

Ice thickness distribution and bed topography data were obtained from Grab et al (2021) based upon a combination of large scale GPR measurements and ice thickness modelling. Glacier characteristics are based on GLIMS glacier outline data (digitized from satellite imagery; Paul et al., 2019; Grab et al., 2021), GIS analysis of SwissAlti3D DEMs (SwissTopo, 2020) and bed topography data (Grab et al., 2021). Glacier retreat data was obtained and modified from Glacier Monitoring Switzerland (GLAMOS, 1881-2020).

The datasets for the Glacier d'Otemma were obtained via Structure from Motion MultiView Stereo (SfM-MVS) photogrammetric processing of drone-acquired datasets, each consisting of approximately 1000 photos and supported by Ground Control Points, as well as hand-measured ablation stake data. The channel outlines stem from data published in Egli et al. (2021).

III.4.2 Datasets

III.4.2.1 Swiss glacier data

Glacier length, length change, surface area and (in certain cases) mass balance data were obtained from Glacier Monitoring Switzerland (GLAMOS, 1881-2020). Ice thickness distribution, glacier bed topography and ice surface topography for the year 2016 were obtained from Grab et al. (2021). Historical aerial imagery (both black-and-white, and color) was viewed and analyzed via the Swiss Federal Office of Topography platform (map.geo.admin.ch, 2021), along with Planet satellite imagery acquired by University of Lausanne (Planet Team, 2017).

III.4.2.2 Drone and ablation stake data of Glacier d'Otemma

Drone data were acquired with a Phantom 4 Pro by DJI © for the area of interest in the ablation zone of the Glacier d'Otemma between the 7th and the 23rd of August 2018. For each acquisition day gridded flights at two different altitudes and with different camera angles (90° and 60° from the horizontal) as well as one circular concentric flight centered at the channel collapse area were performed in order to maximize the number of viewing angles and to assure the highest photogrammetric quality (James et al., 2019). In order to maintain similar illumination

conditions all flights were acquired between 9 a.m. and 12 a.m., collecting a total of 1000-1200 images for each day which resulted in an average ground resolution of 2.5 cm.

54 Ground Control Points (GCPs) were distributed in the drone survey area, consisting of crosses spray-painted on boulders or Compact Disks mounted on black cardboards. The positions of the GCPs were measured by dGPS shortly after each drone image acquisition. A base station was established on a bedrock outcrop approximately 1 km from the glacier margin. This continually recorded base station data which had been corrected into the fixed GPS network of SwissTopo using the SwissPos system. The ground control points were measured with a dGPS rover. Average dGPS measurement precision was ±0.013 m in the horizontal (xy) and ±0.025 m in the vertical. Single errors for each GCP and for each study day as well as boxplots of error distributions for each study day are presented in Figure III-8.

III.4.3 Methods

III.4.3.1 Basic calculations of creep closure rate and ice flow velocity for 22 Swiss glaciers

For each glacier creep closure of semi-circular channels and horizontal ice flow velocity in the immediate vicinity of the collapse features as well as for the first 2 km in length of the glacier tongue were estimated based on well-established relationships using ice thickness and surface topography data.

The ice thickness data compiled by Grab et al. (2021) represents data and modelling for the year 2016 for the glaciers considered in this study. Therefore, it is important to note that the ice thickness used for the calculations does not always precisely represent the ice thickness of the glacier tongue or the (imminent) collapse feature at the moment when a collapse event happened. Nevertheless, it allows for relative comparison of glacier tongues with and without collapse features based on their ice thickness and surface slopes with data representing their states at the same moment in time.

Creep closure rate $\dot{r}$ was computed according to Hooke (1984), with the following assumption: isotropic ice, assuming that $\rho_i g H = \tau$ (with τ the shear stress), assuming "there are no frictional forces resisting sliding over the bed in a direction normal to the tunnel axis" (Hooke, 1984, p. 181), assuming a constant ice density in space and time and a constant subglacial channel diameter of 5 m.

III-2

$$\dot{r} = \frac{Ds}{2}\left(\frac{\rho_i g H}{nB}\right)^n$$

(Equation S1)

Where H is the mean ice thickness in the collapse area, computed for a circular area of 100 m radius. B = $1.6 \cdot 10^5$ Pa, $a^{1/3}$ is the viscosity parameter in Glen's flow law (Glen, 1958) defined by $\dot{\varepsilon} = (\tau/B)^n$, with $\dot{\varepsilon}$ the effective strain rate, n = 3 is the Glen's flow law exponent (approximate value), g = 9.81 m/s^2 is the mean gravitational acceleration on the Earth's surface, ρ_i = 916 kg/m^3 is the density of ice and D_s = 5 m is a hypothetical subglacial channel diameter. Creep closure rate is computed in m / a, assuming that creep closure is active both during summer and winter season.

Mean longitudinal ice flow velocity U_m was computed according to Cuffey and Paterson (2010). First, the basal shear stress τ_b, which is a function of temperature and softness of the till, is computed:

III-3

$$\tau_b = f \rho_i g H \sin(\alpha)$$

(Equation S2)

Where f is a scale factor and corresponds to the ratio between driving stress and basal stress along a glacier. It is situated in the range of 0.8 to 1 for temperate glaciers. Here, we use f = 0.8 according to Haeberli and Hoelzle (1995) and Gantayat et al. (2014). α is the mean surface slope in degrees of the collapse area, derived by dividing the elevation difference (derived from the 2016 Swiss Alti 3D elevation model) by the horizontal distance from the upstream end of the circular 100 m radius collapse area to the downstream end of that collapse area and converting to degrees. For most collapse features this satisfies the requirement to use an average slope over a domain that is roughly a magnitude larger than the local ice thickness (i.e. satisfied for collapse features where H = 20 m).

Subsequently, the mean flow velocity is computed by inserting the basal shear stress τ_b:

III-4

$$U_m = H{\tau_b}^n \frac{2A}{n+1}$$

(Equation S3)

Where A = $3.24 \cdot 10^{-24}$ Pa^{-3} s^{-1} is the creep parameter, which depends on temperature, fabric, grain size and impurity content. Therefore, the flow velocity is essentially a function of surface slope and ice thickness, if we assume that the ice properties are similar for different glaciers in the ablation zone.

The ice velocities computed with this method are comparable to ice velocities observed using radar interferometry for Alpine glaciers by Millan et al. (2019).

III.4.3.2 Computation of the Shreve hydraulic potential for the ablation area of Glacier d'Otemma

Glacier bed topography and ice thickness data (Grab et al., 2021) was used to compute the Shreve hydraulic potential for the area of interest of the tongue of Glacier d'Otemma. The Shreve hydraulic potential (φ) assumes that subglacial water flow paths are largely determined by the ice overburden pressure and by glacier bed topography, which leads to equation S4 (Shreve, 1972; Nienow et al., 1998):

III-5

$$\varphi = \rho_w g z + c(\rho_i g H)$$

(Equation S4)

Where ρ_w = 1000 kg/m^3 is the density of water, z is the glacier bed elevation in meters above sea level and c [0 1] is a closure coefficient with a value of 1 for fully pressurized flow and a value of 0 for open channel flow.

To test for different degrees of pressurization of subglacial channels we computed the Shreve potential for c = 0, for c = 0.5 and for c = 1.0 (Figure III-17). Given the shallow ice of H < 60 m in the zone of interest as well as observations made during the subglacial channel collapse event in August 2018, where a large and unpressurized subglacial channel becomes visible, it is likely that the scenario of open channel flow (c = 0) applies (Figure III-17c).

III.4.3.3 UAV data acquisition, DEM extraction from drone imagery and determination of surface change for Glacier d'Otemma

Drone images for the 7th and 23rd of August 2018 were processed using the photogrammetry software Agisoft Metashape ®. We first determined the necessary minimum number of Ground Control Points (GCPs) out of the available 54 GCPs to minimize georeferencing and lens distortion errors for the dataset by using a Monte Carlo approach (James et al., 2017), with a resulting number of 27 GCPs. Using more than 27 GCPs would not have led to a significant reduction in the positioning and orientation errors. Furthermore, Gindraux et al. (2017) suggested an optimal GCP density to be used on Alpine glaciers calculated as a ratio between GCP density and Ground Sampling Distance (GSD) of 6.12×10^{-8} GCP / GSD (vertical) and 2.52×10^{-8} GCP / GSD (horizontal). Applied to this study, considering a GCP density of 172 GCP / km^2 (namely 27 GCPs over 0.157 km^2) and a mean GSD of 3.5×10^{-10} km^2 (namely 1.87 cm), the resulting ratio is 6.02×10^{-8} GCP / GSD, which closely coincides with the suggestion by Gindraux et al. (2017), thereby legitimating the number of GCPs chosen for this study.

Processing with Agisoft Metashape ® involved removal of low-quality images (blurred, unfocused, or bad camera angle), initial image alignment (Bundle Adjustment), optimization of camera parameters, manual and semi-automatic georeferencing using GCPs in at least 5 images per GCP, re-alignment of the georeferenced model (point cloud), generation of a dense point cloud ('medium' quality in Agisoft Metashape, resulting in ~80 Million points, i.e. approximately 267 points/m^2) and mesh, and building of the image texture (Figure III-7).

The precision of the differential GPS measurement errors was in the range ±0.025 m in the horizontal direction (x,y) and ±0.045 m in the vertical direction (z), as shown in Figure III-8. The Root Mean Square (RMS) reprojection errors of the point clouds for both datasets were on the order of ±0.18 m. The mean GCP errors (RMS image residual for each marker) were of ±0.028 – ±0.029 m, where the marker error corresponds to the distance between the GCP position measured by dGPS (i.e. the georeferencing) and the photogrammetric dense cloud fit.

The dense point clouds were interpolated in the Matlab ® environment to create a regular grid with a cell size of 0.05 m. For both datasets the same bounding coordinates were used in Agisoft Metashape ®, such that the data could be interpolated on the exact same grid extent and resolution in Matlab. Change detection was done by simply subtracting the August 23rd dataset from the August 7th dataset in order to obtain a 'DEM of Difference' (DoD), revealing the elevation change. For the two DEMs, we validated the DEM-acquired elevation using dGPS

masurements. These suggested a precision of DEM elevations of +/- 0.011 m, better than the mean GCP errors but commensurate with the dGPS precision.

Differential GPS measurements at the ablation stakes show that horizontal displacement of the ice surface between the 7th and the 23rd of August was less than 0.1 m. Additionally, horizontal surface displacement between the two orthophotos (7th of August and 23rd of August 2018) was estimated by applying the ImGraft template matching algorithm (Messerli and Grinsted, 2015) to be of less than 0.2 m over this 16-day period, indicating that the displacement is negligible for this application and does not significantly influence the results.

III.4.3.4 Using kriging to correct the DEM-derived elevation change for melt at Glacier d'Otemma

We used kriging in the MATLAB ® environment to interpolate melt manually recorded at 49 ablation stakes onto each grid cell of the DEMs (derived from the UAV measurements via the SfM-MSV approach). Since the ablation stakes only cover a small area within the DEM domain, a constant value of mean ablation was assumed for any grid cell further than 5 m away from the ablation stakes.

III.4.3.5 Calculation of creep closure for shallow channels according to Hooke et al. (1990)

Hooke et al. (1990) proposed the following relation for estimating channel shape:

III-6

$$r = Q^{3/8} k^{-3/8} \frac{(\theta + 2sin[\theta/2])^{1/4}}{([\theta - sin\theta]/2)^{5/8}} (\rho_w g)^{3/16} G^{-3/16}$$

(Equation S5)

where r is the radius of the arc that subtends the channel of width W ; Q is the discharge; k is the reciprocal of the Manning roughness parameter n; θ = arcsin(W/2r); ρ_w is the density of water; g is the gravitational acceleration on the Earth's surface; G = (dP/dx + ρ_w g tanβ); dP/dx is the down-channel pressure gradient for a pressurized channel; and β is the glacier bed slope in the down-channel direction. As W and β are known, and given measurements of Q, we can constrain [S5] and so estimate channel height (and hence estimate typical channel height-to-width ratios):

III-7

$$h = r - \left(r^2 - \frac{W^2}{2} \right)^{0.5}$$

(Equation S6)

If the channel is approaching being filled, d*P*/d*x* is zero. With the highest discharges measured for the Glacier d'Otemma (~14 m^3s^{-1}) and varying across a plausible range of *n* values (0.05 to 0.5; Hooke et al. (1990) assumed 0.33) the identified channel height-to-width ratio varies from 0.071 for n = 0.05 to 0.247 for n = 0.5, emphasizing that the channel is likely to be wide and flat. Hooke et al. (1990) showed that wider and flatter channels had higher closure rates and applied a scaling parameter to the ice viscosity to represent the effects of deviations from a semi-cricular shape. The scaling parameter corresponds to ~0.50 for *n*=0.1 and ~0.80 for *n*=0.05. With a 10-m-wide channel and assuming uniform deformation throughout the year this scaling parameter produces closure rate estimates over a 16-days period of ~0.13 m (*n* = 0.05) to ~0.03 m (*n* = 0.5).

III.4.3.6 Definition of the size of the hypothetical collapse zone for glaciers not showing collapse features

The hypothetical collapse zone for glaciers not showing collapse features was used to compute the same variables as those computed for glaciers with collapse features. These involve ice thickness, creep closure, horizontal ice flux and ice surface slope. The hypothetical collapse zone was positioned at the centerline at a horizontal distance of 250 m from the terminus, with a 100 m radius.

A 100-m radius was chosen to represent the mean size, including circular crevasses, of the collapse features observed on different glaciers. The standard deviation of the mean distance between the collapse features and the glacier front is of 281 m, including an outlier, Glacier de Zinal, where the distance of the collapse feature from the glacier front is 1120 m. If this outlier is excluded, then the standard deviation of the mean distance between the collapse features and the glacier front is 69.5 m.

III.4.3.7 Evidence for broad and shallow subglacial channels from field measurements in summer 2021

Boreholes created in July 2021 at the location of the upper portion of the GPR-derived channel position (upper right channel, marked with grain stipples in Figure III-3b, main text) show that there is indeed a very wide (W > 20 m) and shallow non-pressurized subglacial channel present at the glacier bed at a depth of 47 m. The ice at this location is significantly thicker than at the location where the collapse feature appeared, leading to just a few centimeters of air between the water surface and the channel roof. With more shallow ice further downstream it is likely that the cavity above the water surface is larger, allowing for the incursion of warm air and for block caving.

III.4.3.8 Calculation of glacier retreat rates, standard deviation of retreat and the onset of continuous retreat from Glacier Monitoring Switzerland

Based on Glacier Monitoring Switzerland (GLAMOS, 1885-2020) we computed the mean annual retreat rate of each glacier considered, as well as the standard deviation of retreat, for different time intervals: Retreat since the Little Ice Age, retreat since the onset of continuous glacier retreat, retreat since 1987 (the year considered to mark the beginning of rapid glacier retreat in the Alps; Costa et al., 2018), retreat for the last 10 years of the study period, retreat for the last 3 years of the study period, when most of the collapse events happened. It is important to note that years with missing data were excluded from our analysis, as were years after missing data because retreat recorded in such years includes the contribution from years in which the data were missing.

III.4.3.9 Classification of ablation stakes on Glacier d'Otemma as located 'on-channel', 'likely on channel' or 'off channel'

Ablation on Glacier d'Otemma was hand-measured during a 16-days period (from 7th of August to 23rd of August 2018). A total of 49 ablation stakes were installed, of which 41 stakes were useful for the entire duration of the study. In order to investigate the influence of the presence of a subglacial channel on surface elevation change and ablation, the stakes were labeled based on their position relative to the position of the subglacial channel.

A stake could either be labeled on-channel if it was on top of a GPR-derived channel position, or it could be designated "likely-on-channel" if it satisfied at least two of the following criteria: (a) it was within less than 5 meters of a GPR-derived channel position, (b) it was located on or in close vicinity of a main channel pathway computed based on the Shreve potential (Figure

III-17), (c) it was located on a likely flow path between two GPR-derived channel portions. If only one or none of the above criteria were met the ablation stake was labeled off-channel (Figure III-3a, Figure III-17).

III.4.4 Supporting Figures

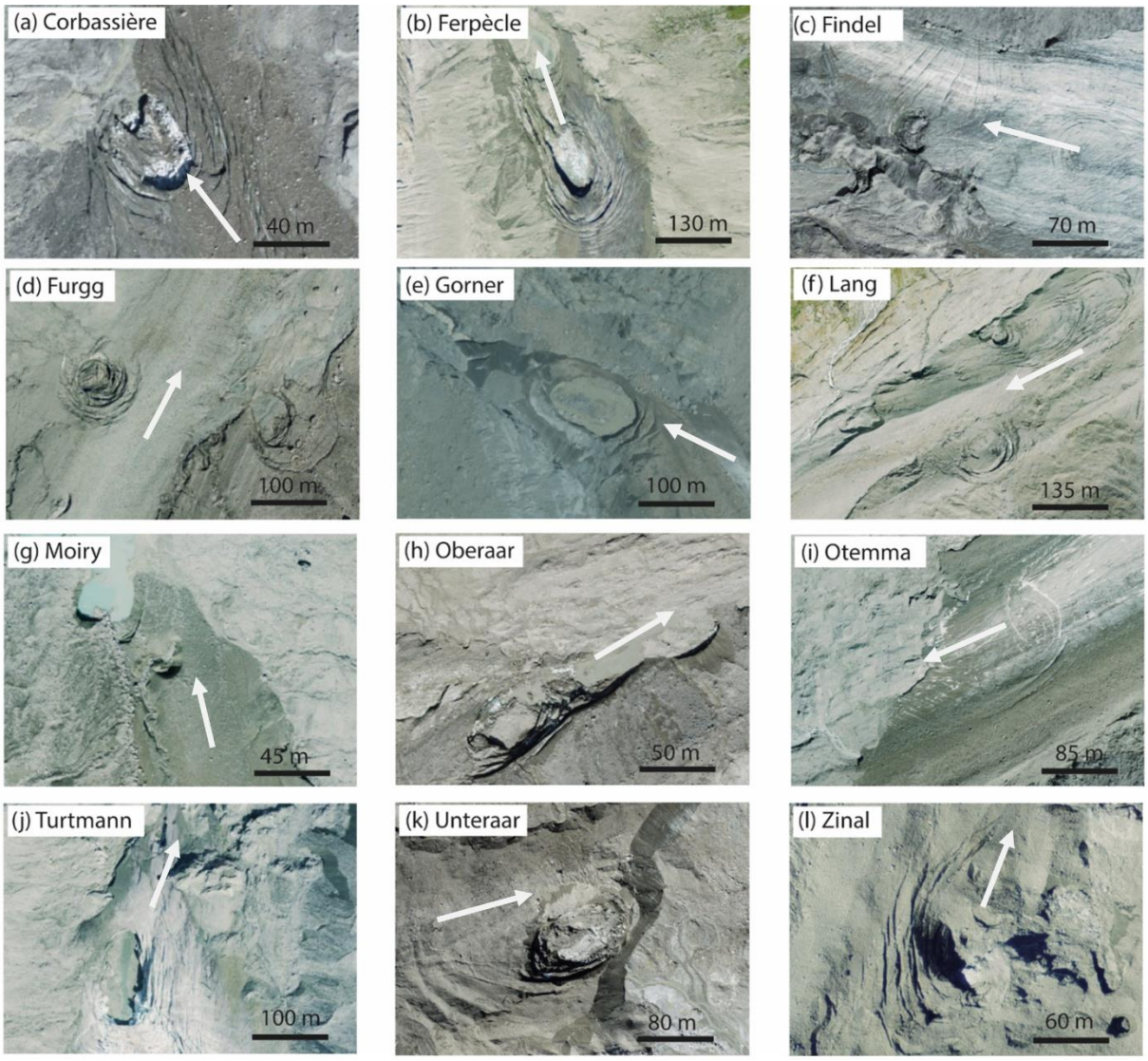

Figure III-4 (Figure S1 in article): Composite image of aerial imagery of collapse features. Geographic North is at the top of the page, and general ice flow direction is indicated with white arrows. (a) Glacier de Corbassière (2020, partly debris covered), (b) Glacier de Ferpècle (2016, partly debris covered), (c) Findelengletscher (2017, debris free), (d), Furggletscher (2019, largely debris covered), (e) Gornergletscher (2006, partly debris covered), (f) Langgletscher (2017, largely debris covered), (g) Glacier de Moiry (2017, partly debris covered), (h) Oberaargletscher (2018, largely debris covered), (i) Glacier d'Otemma (2017, partly debris covered), (j) Turtmanngletscher (2017, debris free), (k) Unteraargletscher (2018, largely debris covered), (l) Glacier de Zinal (2016, largely debris covered)

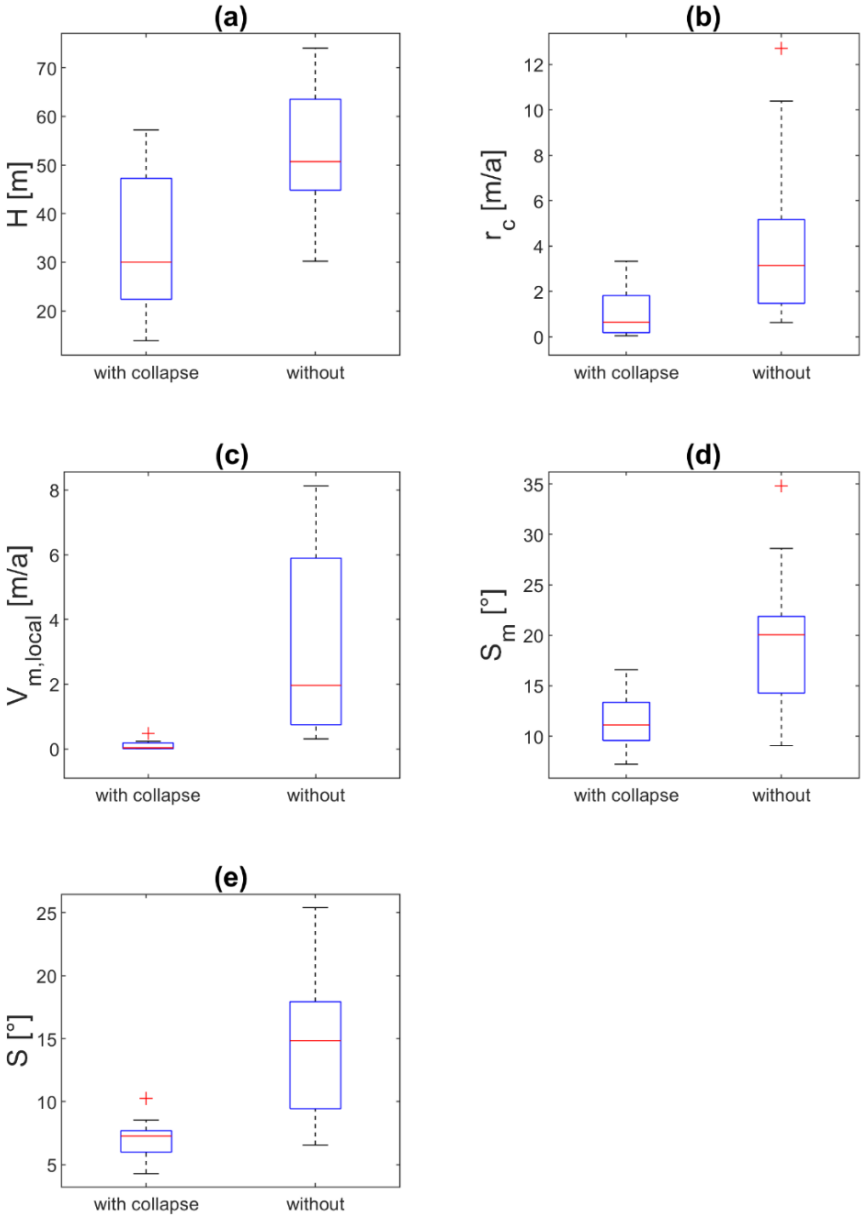

Figure III-5 (Figure S2 in article): Box plots of properties that are significant for glaciers with collapse features and for glaciers without collapse features according to a Mann Whitney U test with a 5% - 95% confidence interval. For each subfigure the plot on the left represents glaciers exhibiting a collapse feature, whereas the plot on the right represents glaciers without collapse features. All variables were calculated for a circular area of 100 m radius. For glaciers with a collapse feature this area was centered at the collapse feature, and for glaciers without collapse features this area was positioned on the centerline of the glacier, 250 m upstream of its terminus in order to simulate a realistic location for a potential collapse feature. The variables shown are (a) ice thickness in meters (H); (b) creep closure in meters/year (ṙ), as computed based on (a); (c) local ice flow velocity in meters/year (Vm,local) computed based on (a) and (e); (d) mean surface slope in degrees (Sm), taken over all cells of the Swiss Alti 3D DEM and (e) mean surface slope in degrees (S) as measured from the upstream end to the downstream end of the circular area

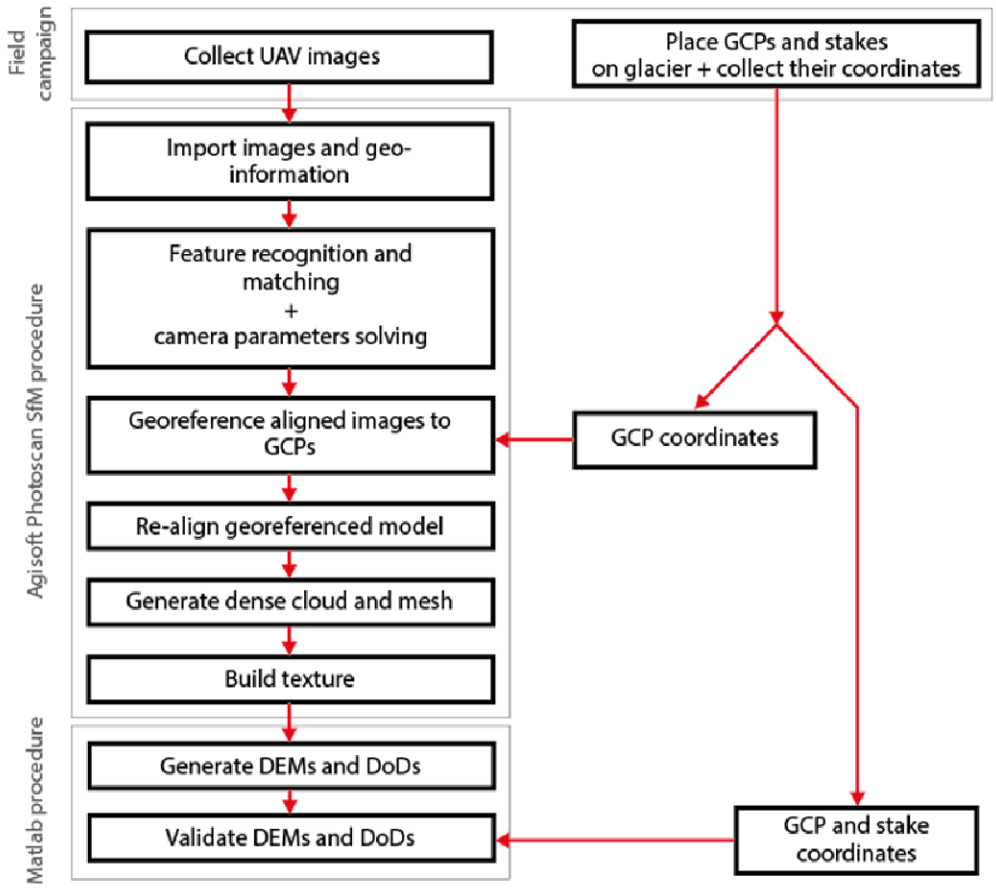

Figure III-6 (Figure S3 in article): Photoscan processing procedure, modified from Rossini et al. (2018), Gindraux et al. (2017) and Westoby et al. (2012).

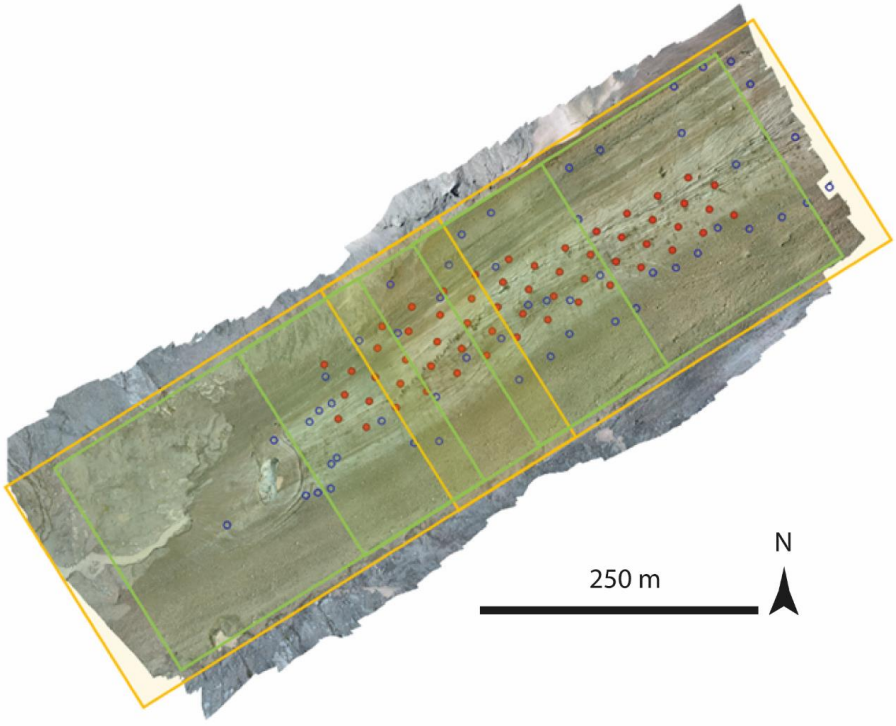

Figure III-7 (Figure S4 in article): Example of flight plans for one daily UAV dataset, locations of ablation stakes (red dots) and of GCPs (blue dots). Superposed to the orthophoto of 09.08.2018.

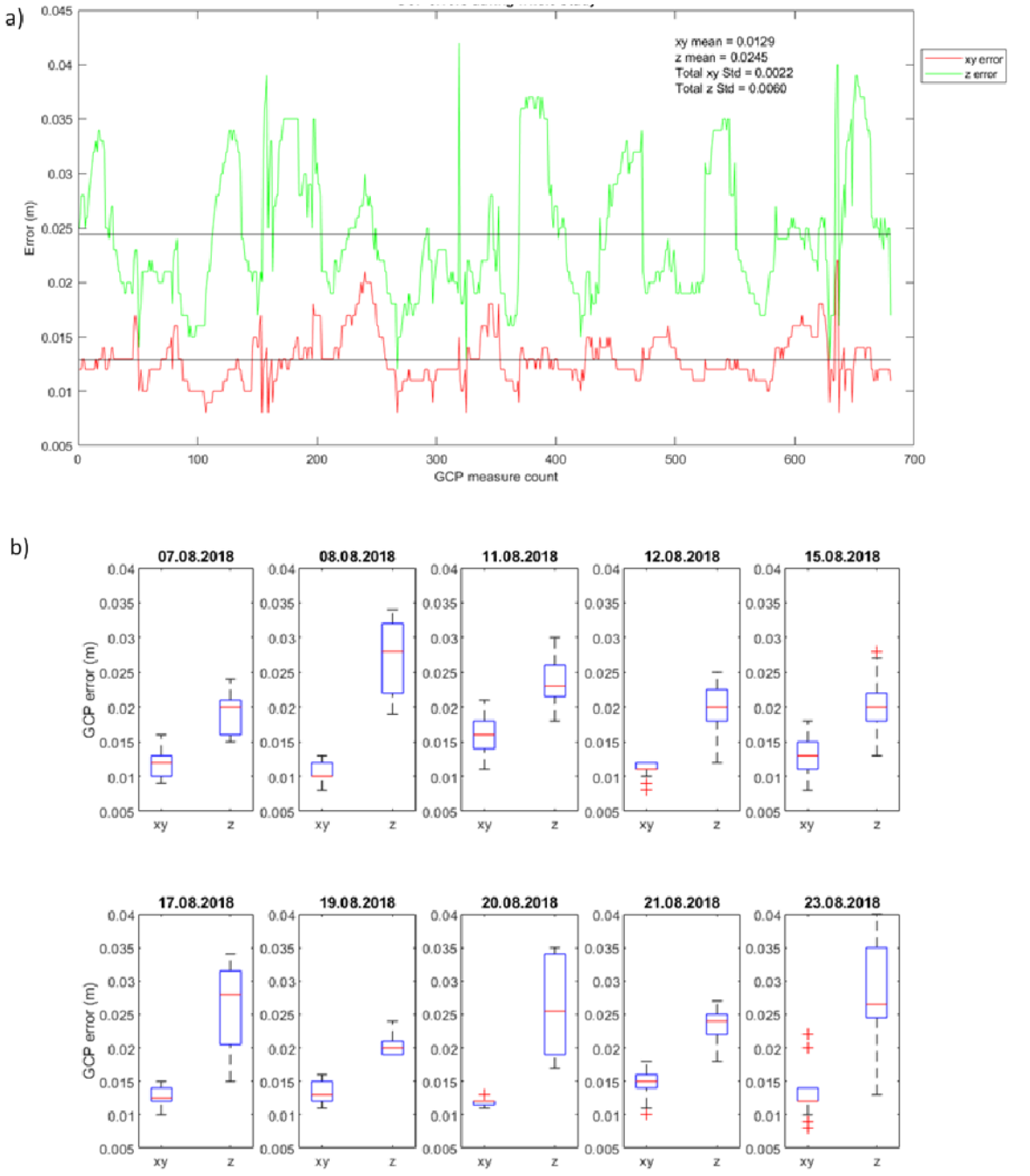

Figure III-8 (Figure S5 in article): (a) Single dGPS errors for all GCP measurements. One day consists of 54 GCP position measurements. (b) Detail boxplots of dGPS errors on GCPs for every study day. Red lines indicate the median, lower and upper box edges indicate the 25th and 75th percentile. Red crosses represent outliers.

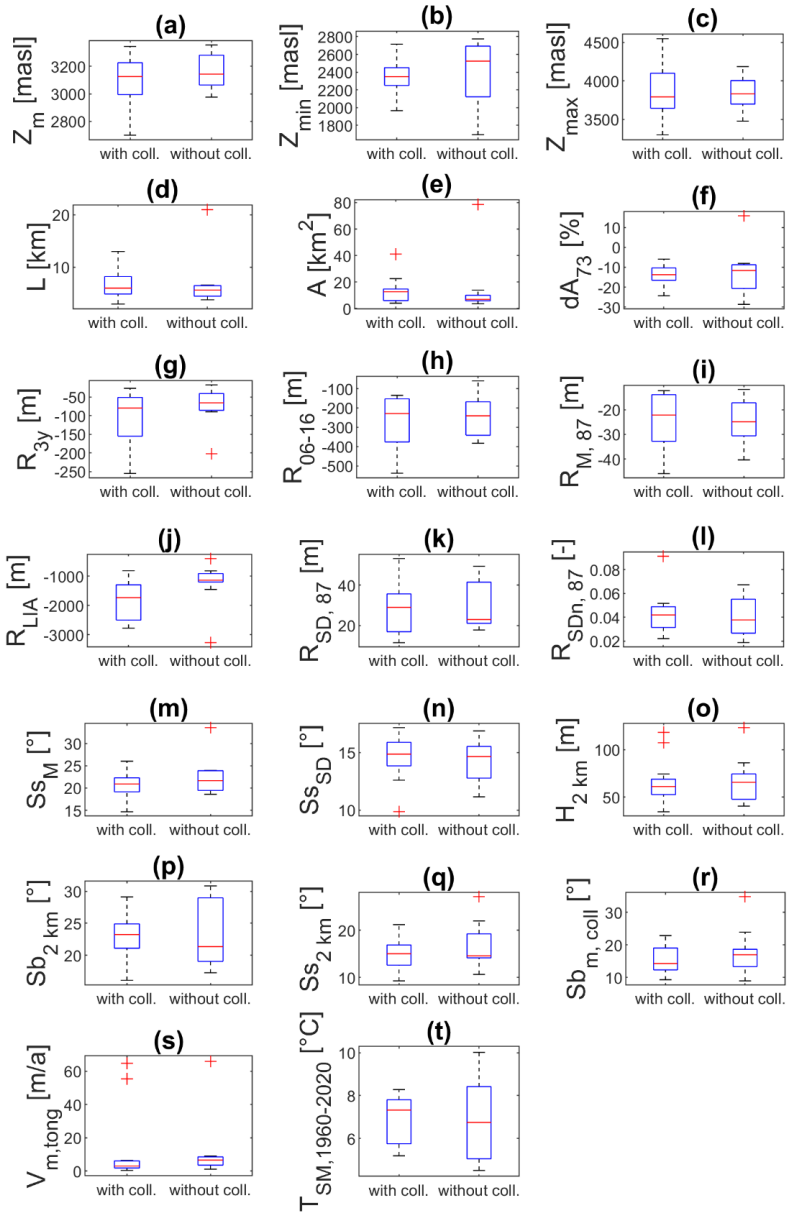

Figure III-9 (Figure S6 in article): Comparative boxplot figures for the group of glaciers with collapse features (left boxplot) and the group of glaciers without collapse features (right boxplot). (a) mean glacier elevation, (b) minimum glacier elevation, (c) maximum glacier elevation, (d) glacier length, (e) glacier area, (f) change in glacier area since 1973, until the latest available Glacier Monitoring Switzerland recording (~2016-2020), (g) retreat over the most recent 3 years of Glacier Monitoring Switzerland measurements, (h) retreat over the most recent common 10-years period of Glacier Monitoring Switzerland measurements, (i) mean annual retreat rate since 1987 (onset of rapid glacier retreat in the Alps), (j) retreat since the end of the Little Ice Age, (k) standard deviation of the annual retreat rate since 1987, (l) standard deviation normalized by the mean of the annual retreat rate since 1987, (m) mean surface slope of the glacier, (n) standard deviation of the surface slope of the glacier, (o) mean ice thickness over the last 2 km of the glacier tongue, (p) mean bed slope over the last 2 km of the glacier tongue, (q) mean surface slope over the last 2 km of the glacier tongue, (r) mean bed slope within a circle of 100 m radius around the most recent collapse feature, (s) mean ice flow velocity for the last 2 km portion of the glacier tongue; for glaciers without collapse feature, the hypothetical location of the feature is chosen to be located at a linear distance of 300 m from the terminus, on the centerline of the glacier (t) Mean summer temperature between 1960 and 2020 for the 2020 terminus location of each glacier.

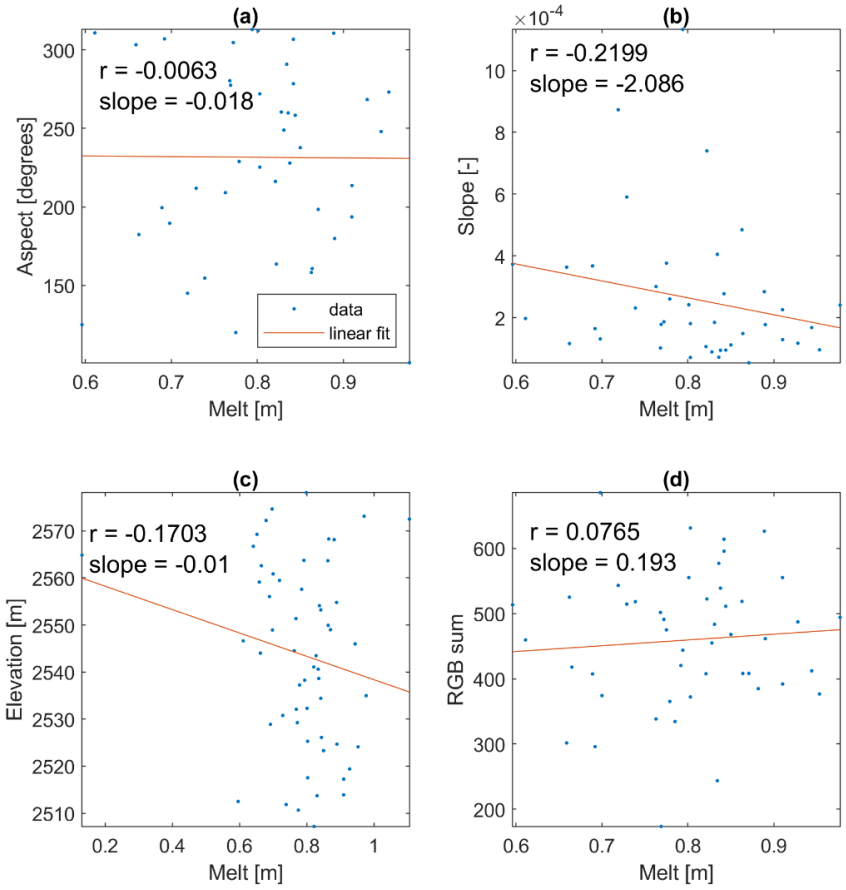

Figure III-10 (Figure S7 in article): Scatterplots with linear regression and Pearson correlation coefficients for the ablation values (hand-measured at ablation stakes) at the locations of 47 ablation stakes on the tongue of Glacier d'Otemma between 7th and 23rd of August 2018 (16 days). Scatterplots are displayed for the variables (a) aspect in degrees, (b) surface slope in m/m, (c) surface elevation in meters, (d) the sum of RGB values of the orthophoto (-). Each variable was computed as the average over a 0.4 x 0.4 m surface area centered at each stake location.

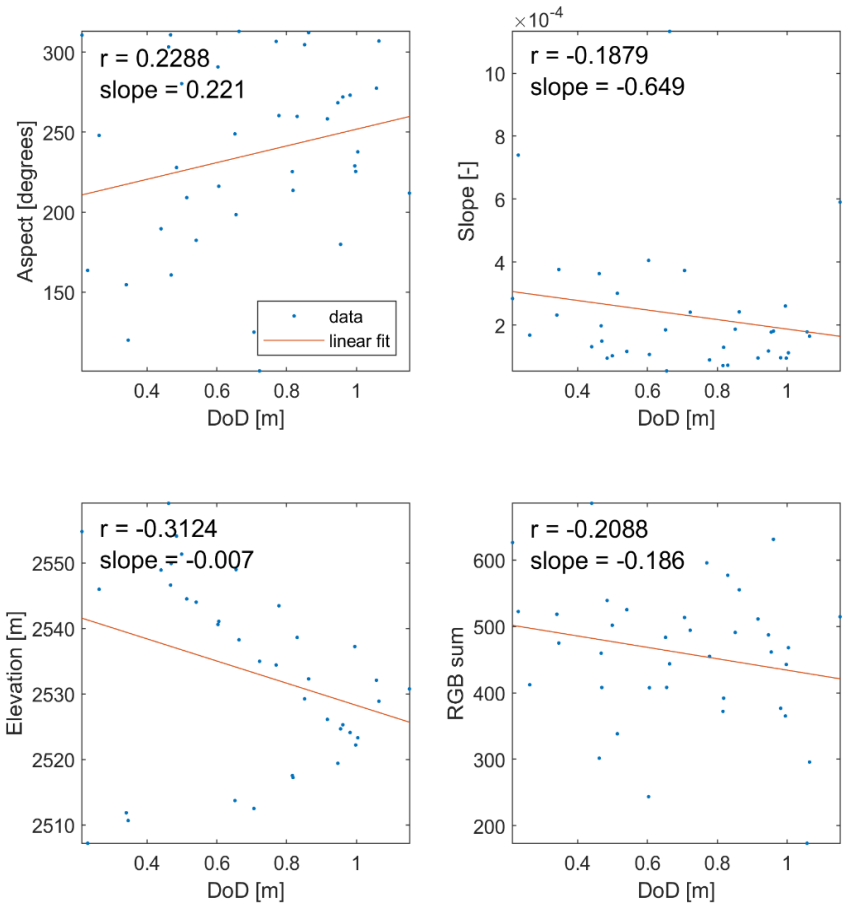

Figure III-11 (Figure S8 in article): Scatterplots with linear regression and Pearson correlation coefficients for the DoD values (elevation change) at the locations of 38 ablation stakes on the tongue of Glacier d'Otemma between 7th and 23rd of August 2018 (16 days). DoD values were taken as the average over a 0.4 x 0.4 m surface area centered at each stake location. Scatterpots are displayed for the variables (a) aspect in degrees, (b) surface slope in m/m, (c) surface elevation in meters, (d) the sum of RGB values of the orthophoto (-).

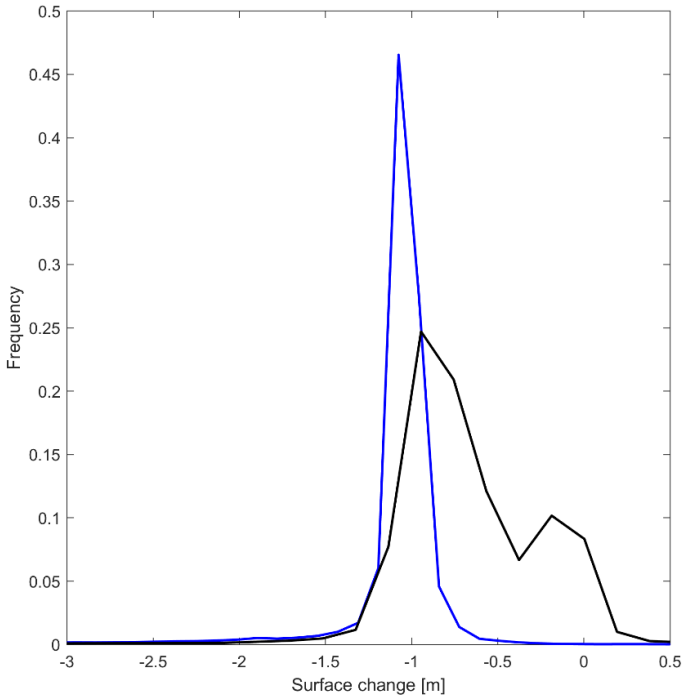

Figure III-12 (Figure S9 in article): Probability density distribution of the values of all DoD cells located on top of the GPR-derived subglacial channel ('on channel', in blue) and of all the remaining values of the DoD ('off channel', in black). 'off channel' cells can potentially still be influenced by undetected channels.

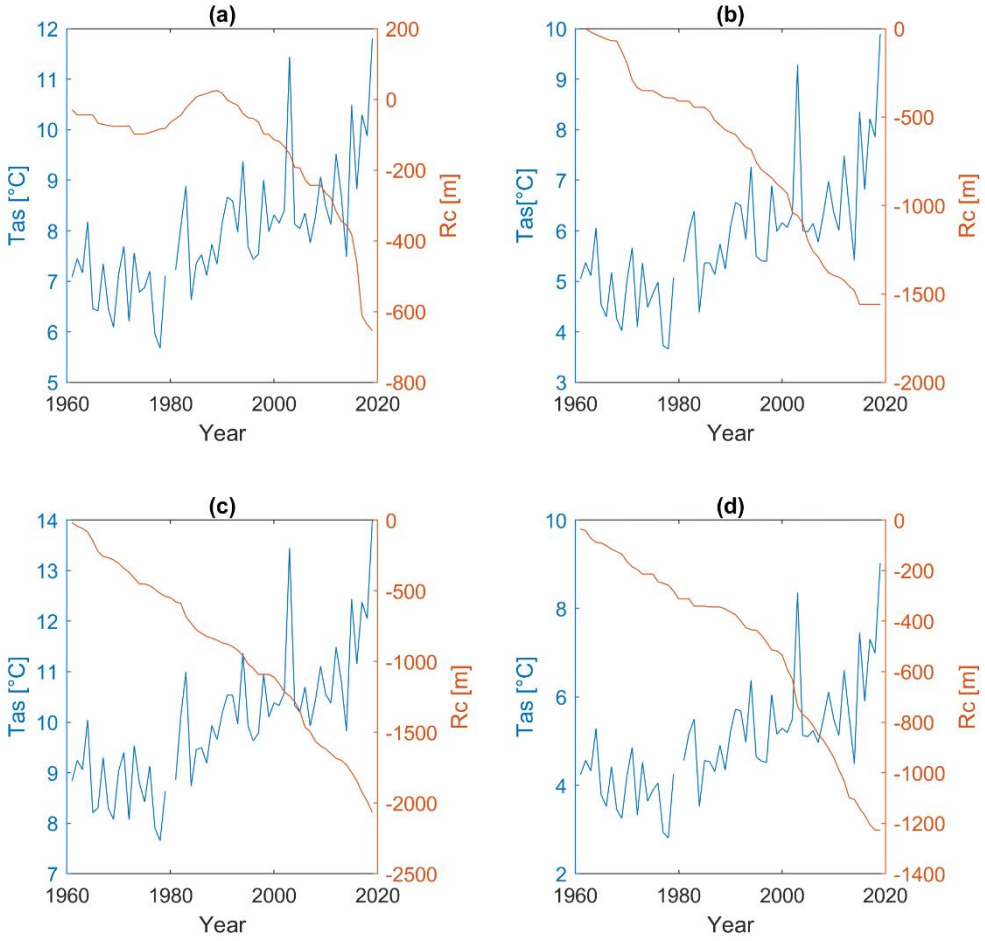

Figure III-13 (Figure S10 in article): The evolution of cumulative retreat (Rc) and mean summer air temperature at the glacier terminus location (Tas) for four Swiss glaciers between 1961 and 2019. (a) is Glacier de Ferpècle (with recent collapse features), (b) is Glacier d'Otemma (with both recent and historical collapse features), (c) is Aletschgletscher (without recent or historical collapse features) and (d) is Glacier de Brenay (without recent or historical collapse features).

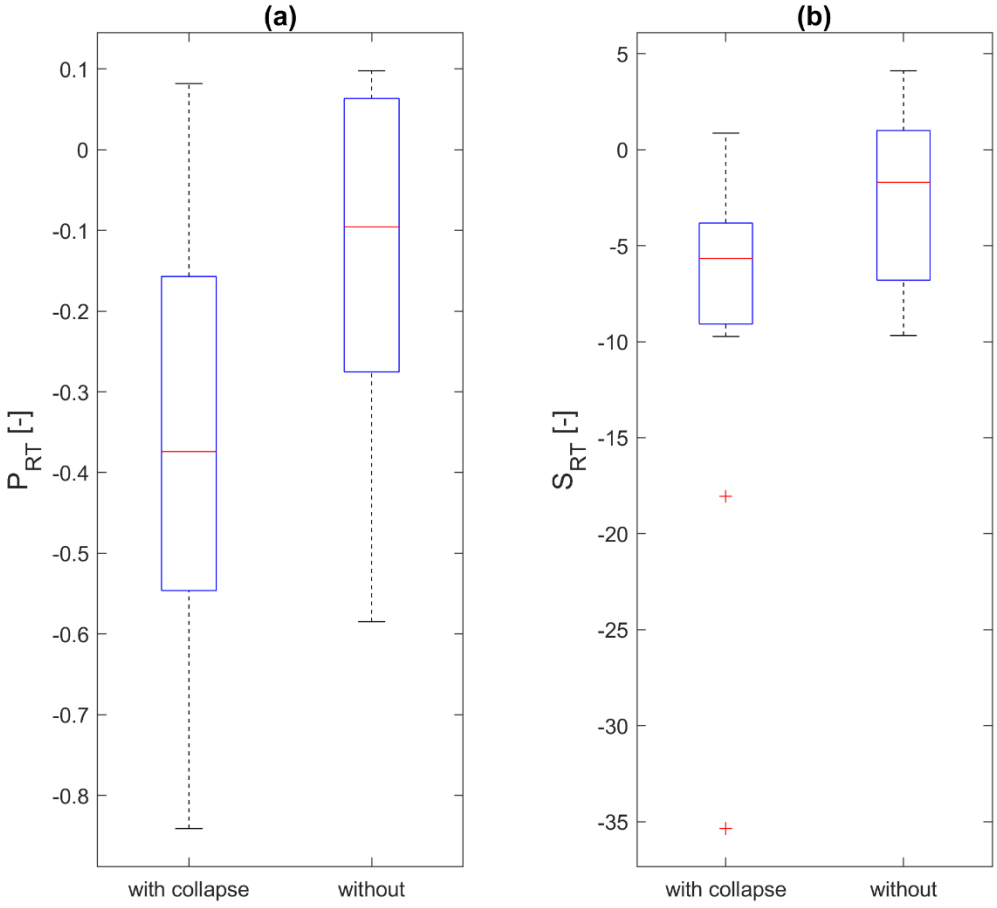

Figure III-14 (Figure S11 in article): For both subfigures the box plot on the left represents glaciers with collapse features and the box plot on the right represents glaciers without collapse features. (a) shows correlation between mean annual summer temperatures and annual variation in glacier length (PRT) and (b) shows sensitivity of annual glacier length change to mean annual summer temperatures (SRT).

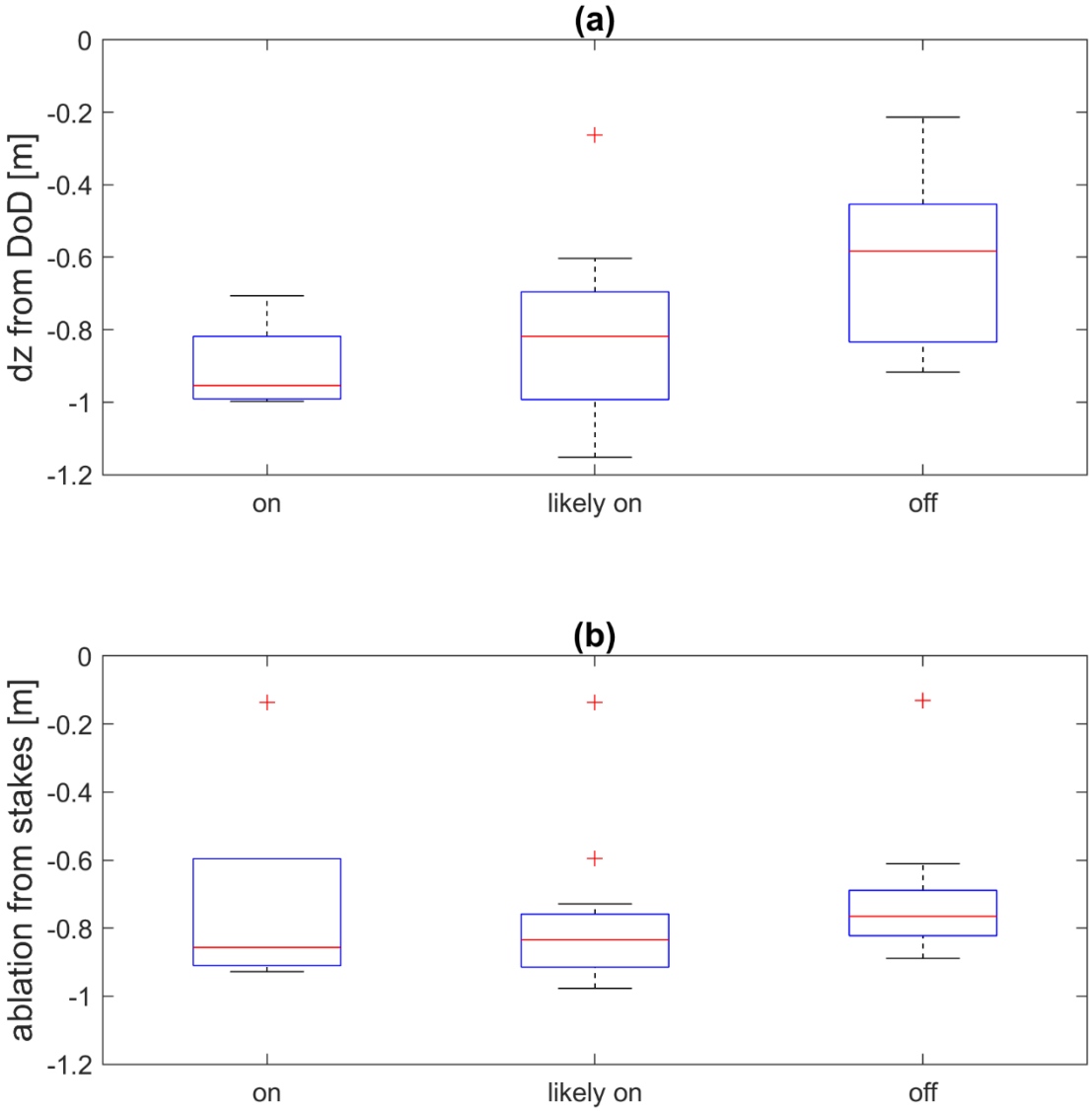

Figure III-15 (Figure S12 in article): Box plots of hand-measured ablation and of surface change based on the DoD for ablation stake locations between the 7th and the 23rd of August 2018. (a-c) show ablation stakes measurements at stakes located (a) on top of the GPR-derived subglacial channel, (b) likely on top of the continuation of this channel (inferred from significant surface lowering in the area, as shown in Figure 2, and from continuity of the channel) and (c) stakes that are unlikely to be located on top of a subglacial channel (based on GPR-derived channel locations and the computed Shreve potential). (d-f) show the change in ice surface elevation (dz) given by the DoD for the same locations as in (a-c).

Figure III-16 (Figure S13 in article): The collapsing subglacial channel at Glacier d'Otemma as seen from the Phantom 4 Pro drone (DJI) on the 23rd of August 2018. The process of 'block caving' (Paige, 1956) is clearly visible. The drone operator (within red circle) is visible on the glacier surface, for scale.

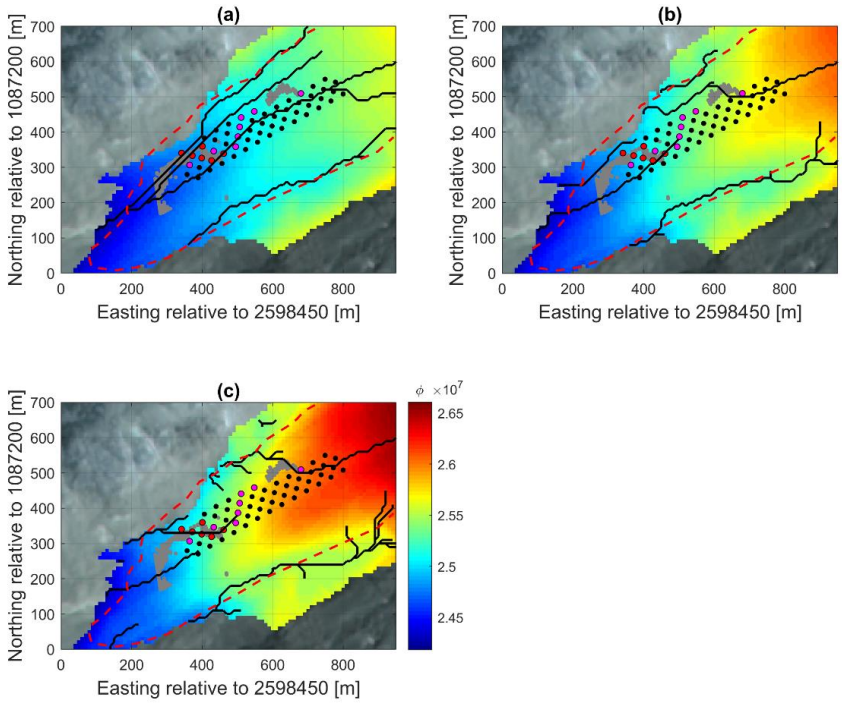

Figure III-17 (Figure S14 in article): Maps showing the computed Shreve hydraulic potential φ and corresponding main subglacial flow pathways in the snout marginal zone of Glacier d'Otemma for different scenarios. The dots represent ablation stakes, with on-channel stakes in cyan, likely on-channel stakes in magenta and off-channel stakes in black. The grey shaded areas are GPR-derived channel outlines and the red dashed line is the 2018 glacier outline. The closure coefficient c is varied in different sub-figures, along with the threshold number of cells for flow accumulation (tacc) to form a channel: (a) c = 0 (open channel flow), tacc = 200, (b) c = 0.5 (partially pressurized flow), tacc = 100, (c) c = 1.0 (fully pressurized flow), tacc = 50. Where c is the closure coefficient in Equation S4.

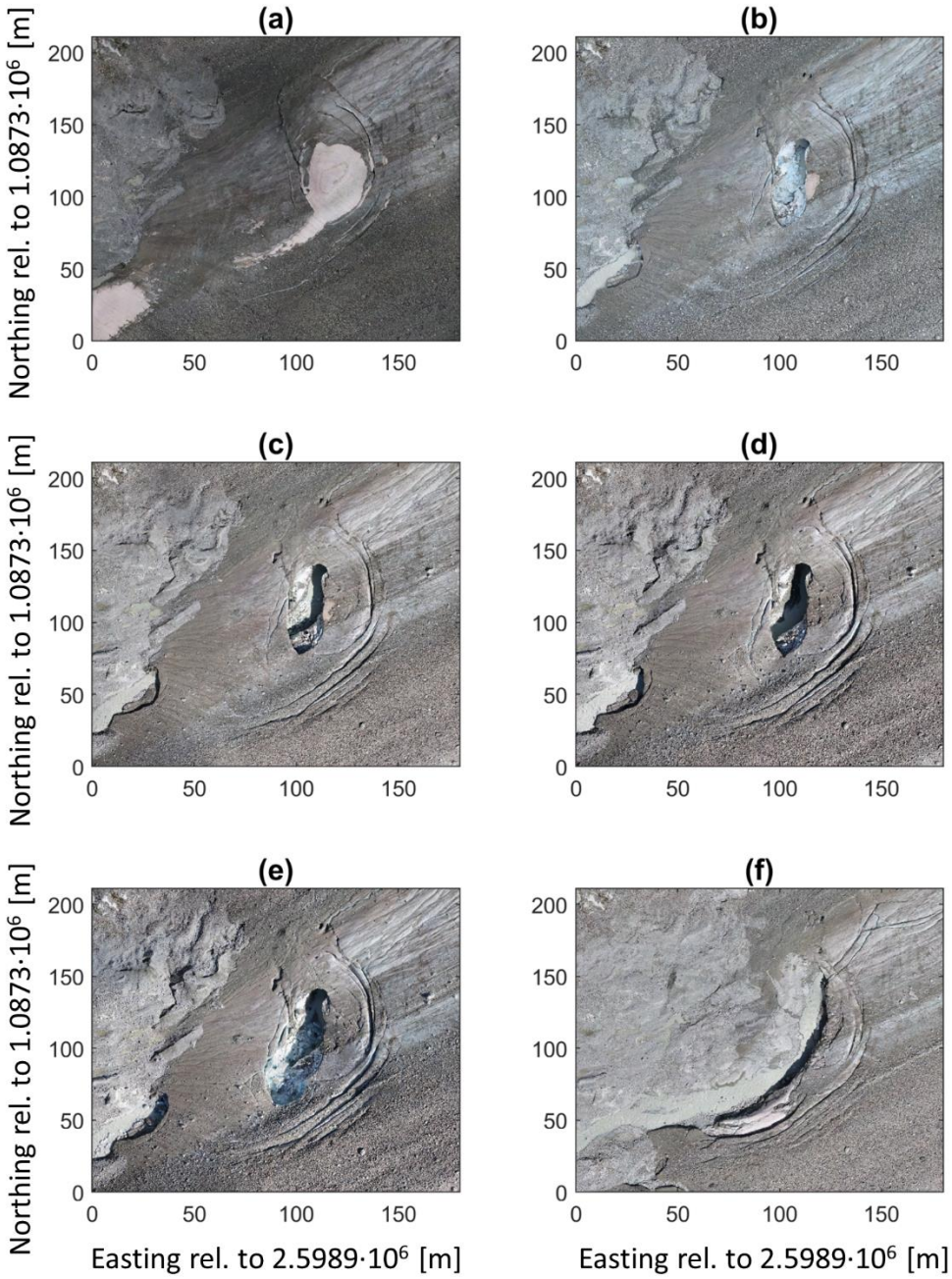

Figure III-18 (Figure S15 in article): Orthophotos of the ice marginal area of Glacier d'Otemma showing the evolution of the subglacial channel collapse feature. The imagery extends from 3rd July 2018 to 31st July 2019. Images were acquired on (a) 3.7.2018, (b) 7.8.2018, (c) 12.8.2018, (d) 20.8.2018, (e) 23.8.2018, (f) 31.7.2019. Relative coordinates in relation to a reference coordinate in the local Swiss Coordinate system CH1903+ are given.

III.4.5 Supporting Tables

Table III-1 (Table S1 in article): Variables used in the text, along with their abbreviations and units.

Variable or parameter name	**Abbreviation**	**Units**
Surface change due to ablation	$dz_{ablation}$	m
Surface change due to ice dynamics	$dz_{dynamics}$	m
Net surface change	dz_{net}	m
Pearson correlation coefficient between annual retreat rate and mean summer air temperature	P_{RT}	-
Vertical creep closure rate	$\dot{r}$	m/a
Coefficient of variation of glacier retreat	R_{CV}	m
Mean glacier retreat since the start of continuous glacier retreat (after the LIA)	R_M	m
Annual glacier retreat	R_A	m
Sensitivity of annual retreat rate to mean summer air temperature	S_{RT}	-
Annual mean summer air temperature	T_{SA}	°C
Mean summer air temperature for the entire retreat period (R_M)	T_{SM}	°C
Lateral ice flow rate	U_m	m/a

Table III-2 (Table S2 in article): Properties analyzed for each glacier, along with their units and data source for calculation. The last column shows if a property was deemed relevant for influencing the presence or absence of a subglacial collapse feature, according to a Mann-Whitney

Property Number	**Property / variable**	**Units**	**Data source used for calculation**	**Relevant for presence/absence of subglacial collapse features according to Mann-Whitney U test**

1	Mean elevation of the glacier	m.a.s.l	GLIMS glacier database	No
2	Minimum elevation of the glacier	m.a.s.l	GLIMS glacier database	No
3	Maximum elevation of the glacier	m.a.s.l	GLIMS glacier database	No
4	Glacier length	km	Measured from map & most recent orthophoto	No
5	Glacier surface area	km2	GLAMOS (1881-2020)	No
6	Area lost since 1973	%	GLAMOS (1881-2020)	No
7	Retreat within the last 3 years of the measurement period	meters	GLAMOS (1881-2020)	No
8	Glacier retreat from 2006 until 2016	meters	GLAMOS (1881-2020)	No
9	Mean annual retreat since 1987	meters/year	GLAMOS (1881-2020)	No
10	Length change since LIA	meters	GLAMOS (1881-2020)	No
11	Standard deviation of retreat from 1987 until the latest measurement	meters	GLAMOS (1881-2020)	No
12	Normalized standard deviation of retreat between 1987 and the latest measurement (normalized with glacier length)	-	GLAMOS (1881-2020)	No
13	Mean slope of glacier surface	degrees	GLIMS glacier database	No

14	Standard deviation of slope of the glacier surface	degrees	GLIMS glacier database	No
15	Mean ice thickness of first 2 km of tongue	meters	Ice thickness dataset, VAW/ETHZ (2021)	No
16	Mean bed slope of first 2 km of tongue	degrees	Ice thickness dataset, VAW/ETHZ (2021)	No
17	Mean surface slope, first 2 km of the glacier tongue	degrees	SwissAlti3D (2016)	No
18	Mean surface slope within circular collapse area (100-m radius)	degrees	SwissAlti3D (2016)	**Yes**
19	Surface slope from upstream end to downstream end of collapse feature, across a circular area with 100-m radius	degrees	SwissAlti3D (2016)	**Yes**
20	Mean bed slope within circular collapse area (100-m radius)	degrees	Ice thickness dataset, VAW/ETHZ (2021)	No
21	Mean ice thickness within circular collapse area (100-m radius)	meters	Ice thickness dataset, VAW/ETHZ (2021)	**Yes**
22	Creep closure r' for a circular collapse area with 100-m radius	meters/year	Computed from (12) and (13)	**Yes**
23	Annual ice flow velocity within the circular collapse area (100-m radius)	meters/year	Computed from (12) and (13)	**Yes**

24	Annual ice flow velocity computed for a 2-km-length section of the glacier tongue	Meters/year	Computed from (4) and (1)	**Yes**

Table III-3 (Table S3 in article): Glaciers considered in our analysis and key properties. Precise retreat rates for Furggletscher are unknown since this glacier has not been monitored by Glacier Monitoring Switzerland. Glaciers with gray shading are glaciers where one or more collapse features have been observed since 1938.

Glacier	**# in Figure S1**	**Mean annual retreat rate R_M since onset of continuous retreat [m/a]**	**Ice thickness [m] in most recent collapse area, or in hypothetical collapse zone located 250 m upstream of the glacier snout (for glaciers without any collapse features)**	**# of collapse events between 1938 and present**
Aletschgletscher	1	-36.3	65.4	0
Allalingletscher	2	-29.0	68.2	0
Glacier du Brenay	3	-24.5	50.7	0
Glacier de Cheilon	4	-18.9	57.88	0
Glacier de Corbassière	5	-35.0	33.05	1
Feegletscher	6	-32.6	30.2	0
Glacier de Ferpècle	7	-24.2	57.18	1
Findelgletscher	8	-44.1	24.66	4
Furggletscher	9	-	22.39	2
Glacier du Giétro	10	-19.6	56.2	0
Gornergletscher*	11	-25.6	-	2
Langgletscher	12	-15.2	38.99	2
Glacier de Moiry	13	-11.4	13.88	1
Glacier du Mont Durand	14	-30.8	35.4	0
Glacier du Mont Miné	15	-26.6	74	0
Oberaargletscher	16	-19.4	48.06	1
Glacier d'Otemma	17	-33.2	22.16	4

Glacier de Saleina	18	-21.6	44.56	0
Glacier de Trient	19	-22.4	46.5	0
Turtmanngletscher	20	-54.8	26.96	2
Unteraargletscher	21	-21.3	47.25	4
Glacier de Zinal	22	-13.8	45.58	3

Table III-4: Pearson correlation coefficient values between melt hand-measured over 15 days at ablation stakes and mean values of surface variables extracted for all DEM cells in a 0.5 x 0.5 m square around each ablation stake.

	Pearson correlation coefficient for hand-measured melt [m/day]	Pearson correlation coefficient for elevation change, DoD value [m/day]
Aspect	-0.006	0.107
Surface slope	-0.220	-0.130
Elevation	-0.170	-0.312
Surface reflectance (Sum of RGB values, Rippin et al., 2015)	0.077	0.017

Table III-5: Results of Mann-Whitney U tests applied to 41 ablation stake positions, of which a minority were determined to be located on top of a subglacial channel (on-channel). Six stakes were located 'strictly' on top of a subglacial channel, whereas 13 stakes

Stake position:	*on-channel VS remaining*	Likely-on-channel & on-channel VS remaining	Likely-on-channel VS remaining
Ablation			
H	0	**1**	**1**
P value	0.327	0.039	0.0458
DoD value (dZ)			
H	**1**	0	0
P value	0.0092	0.157	0.819

Table III-6: Year of occurrence of the most recent collapse feature for each glacier.

Glacier	**Year of latest collapse feature**
Corbassière	2020
Ferpècle	2017
Findelgletscher	2017
Furggletscher	2017
Gornergletscher	2015
Langgletscher	2019
Moiry	2018
Oberaargletscher	2017
Otemma	2018
Turtmanngletscher	2018
Unteraargletscher	2017
Zinal	2018

III.4.6 Datasets

All datasets are available under the following DOI: https://doi.org/10.5061/dryad.h18931zmh

Table S7: Overview of 24 key variables for 22 glaciers. Table available as separate file online.

III.5 Wider implications

Besides explaining the conditions necessary for ice surface collapse features to occur, this study shows that collapse features have become more frequent with time as mean summer air temperatures at glacier terminuses are rising.

For the estimation of future glacier mass balance of temperate Alpine glaciers, it will be important to estimate the contribution of ice marginal collapse events and possible intra-glacial collapse events to total glacier mass loss and to glacier length change. This could be done by precisely quantifying the change of ice volume for years during which collapse features occur and comparing it to years without any collapse features.

There are at least four points of view from which collapse events should be studied in the future:

1) Detailed understanding of the role of subglacial channels in the initiation and development of a collapse feature. As described in this article the occurrence of meanders in subglacial channels (remaining open due to slow horizontal ice flux) seems to contribute to the development of collapse features. It would be valuable to measure in detail the geometry of a meandering subglacial channel close to the terminus, be it with a portable LiDAR system in the inside of the channel or with even more precise GPR surveys on the glacier surface. Further, water flow speeds, turbidity, water temperature and sediment transport inside such a meander should be measured and modelled in order to quantify the potential of the water flow to produce a widening and deepening of such channels in meander bends.
2) Warm air incursion both by air advection through the subglacial channel from the glacier terminus and via crevasses or moulins may be an important contributor to the development of a collapse feature because it drives melt of channel walls and ceiling even without them being exposed to water friction, water pressure or sediment abrasion. The mechanism of ‘block caving’ (Paige et al., 1954) could in part be initiated by melting from the inside and cracks forming in the channel roof. Therefore it would be interesting to place air temperature sensors and high-frequency 3D wind-speed sensors at the inside of a subglacial cavity to quantify heat advection and turbulent transport of sensible as well as latent heat. The sensors would transmit data via radio signal to a receiver on the outside of the cavity and be drilled at least 0.5 m into the ice to keep them in place for a timespan of at least two weeks.

3) Although there are theoretical and semi-empirical formulae describing ice creep and channel closure (Glen, 1958; Hooke, 1984; Hooke et al., 1990), there is a lack of knowledge about the behavior of shallow ice when it is destabilized by rapid melt-out, lateral erosion by a subglacial channel and 'block caving'. Therefore, it would be interesting to conduct modelling studies using an ice flow model such as Elmer/Ice to understand the forces and ice dynamics occurring over time during a collapse event.
4) More large-scale data is needed to better quantify the conditions necessary for the occurrence of collapse features. For this, datasets like the one presented in this article, but at a global scale, could be analyzed in a similar way and 'collapse glaciers' distinguished from glaciers without collapse features to either further establish the findings of this article or to add additional criteria (possibly valid in different climatic or geologic settings) that define if a glacier is prone to exhibit collapse features or not.

5) The impact of collapse features on short- to medium term glacier retreat can be dramatic, as it has been observed at both Glacier de Ferpècle (retreat of several hundred meters in less than 5 years) and Glacier d'Otemma, where collapse activity has been continuing even after the initial observed collapse feature in 2018. This impact on glacier retreat should be studied more quantitatively and the processes involved should be elucidated.

According to these five points of view it seems obvious that little is still known about the formation, development and geographical distribution of collapse features, and that there is an important need for research on this topic, both for the purpose of process understanding and to better estimate the future pace of ice mass loss on the planet's glaciers.

IV QUANTITATIVE ANALYSIS OF HIGH-RESOLUTION ABLATION PATTERNS FOR A TEMPERATE ALPINE GLACIER DERIVED USING REPEATED UAV SFM-MVS PHOTOGRAMMETRY

Pascal E. Egli, Bruno Belotti, Stuart N. Lane

To be submitted to The Cryosphere.

IV.1 Chapter aims and objectives

The main aim of this chapter is to analyze systematically ablation patterns for the ice marginal area of the tongue of Glacier d'Otemma, in its role as a proxy for similar temperate Alpine glaciers at medium elevations, and to investigate which processes are most important for the spatial variability of ablation at a local scale and at a high spatial and temporal resolution. This is achieved with the use of repeated UAV SfM-MVS photogrammetry and more than hundred dGPS validation points that were measured every time a UAV dataset is acquired. With these data, intensive statistical analyses were used to understand decimeter resolution controls on glacier ablation for an Alpine temperate glacier.

There is extensive literature investigating the impact of shortwave radiation, albedo, air temperature as well as surface roughness on surface melt (Carenzo et al., 2009; Brock et al., 2000; Brock et al., 2006; Pellicciotti et al., 2005; Vincent & Six, 2013). But there are only few studies that investigate the importance of different variables on highly resolved ablation patterns whether in time (daily to weekly time-scales) or space (decimeter time-scales). The objective of this article is to fill this gap with a systematic approach by looking at ten different patches on the surface of an Alpine temperate glacier that have a wide variety of surface conditions. The characteristics of single patches include for example: (a) a relatively smooth ice surface with low variability in albedo and only few supraglacial streams, (b) a rougher ice surface with deeply incised and meandering supraglacial streams involving variations in albedo due to dust accumulation, (c) heavily debris covered ice involving some barely visible supraglacial channels and (d) areas involving all of the above. With this experimental design it was possible to quantify the relative importance of the effect of solar radiation on microtopography, of surface roughness, albedo, and the presence of supraglacial streams on the spatial distribution of ablation for each patch by applying stepwise linear regressions; and so

determine the variables that are the most important for determining surface melt in each situation (i.e., for each patch). Potentially, this knowledge could be included in melt models.

IV.2 Personal contribution to the article

I co-organized the entire logistics and concept of the fieldwork campaign in August 2018 at Glacier d'Otemma, with the help of Boris Ouvry and Stuart Lane. Subsequently, I trained Bruno Belotti and two other students in the use of the UAV and in the measurement of ground targets and ablation stakes with dGPS. The majority of the UAV flight acquisitions were carried out by Bruno Belotti, with my assistance. Daily measurement of dGPS points was carried out by Bruno Belotti, Boris Ouvry, Valentin Pipoz, Stuart Lane and I with the help of other students. The raw data processing for photogrammetry was carried out by Bruno Belotti under my guidance. Further data processing to interpolate DEMs, validate DEMs, extract and clean ablation stake data was carried out by myself with help from Bruno Belotti and advice from Stuart Lane. I developed the concept for this article with feedback from Stuart Lane and undertook the specific data processing and statistical analysis again with feedback from Stuart Lane. Writing of the manuscript and generation of all figures except one (adopted from Bruno Belotti) was done by myself. Data and code curation and submission of the article and dataset was done by myself. Stuart Lane supported the writing and edited the paper.

IV.3 Article 3

IV.3.1 Introduction

It is well established that glaciers worldwide have been retreating since the end of the Little Ice Age, but especially since the middle of the 20th century (Marzeion et al., 2018; Zemp et al., 2019). Since the 1980s most alpine glaciers worldwide have been receding more rapidly than ever observed in human history. Even in the unlikely event that anthropogenic warming can be stopped soon, most glaciers will continue to retreat for several decades because they are still adapting to the current climate (IPCC, 2019).

In recent years the European Alps have experienced several exceptionally warm summers, with seven of the ten warmest summers since the beginning of measurements taking place since 2000 (IPCC, 2021). Mean summer temperatures in the Alps have risen by 0.10-0.17°C per decade since 1864, with a cumulated annual mean temperature increase of approximately 2°C since 1864 (IPCC, 2021). Temperatures in the Alpine environment, i.e., especially at elevations above 1500 m, have been increasing more strongly than the global mean since the Little Ice

Age, and they are projected to continue to do so over the course of the 21st century (Gobiet et al., 2014).

Warmer summer air temperatures imply an increase in ablation. They may also reduce solid precipitation, reducing the duration of snow cover during summer melt, and so lead to more rapid exposure of lower albedo ice as well as a reduction in accumulation. If total ablation exceeds total accumulation over the time span of several years this leads to glacier retreat. This is also reflected in systematic reports of rises in the Equilibrium Line Altitude (ELA; Braithwaite, 2008; Zekollari et al., 2020; Braithwaite, 2022). Several studies have attempted to model and to predict future Alpine glacier retreat as a response to global warming (Huss et al., 2010; Jouvet et al., 2011; Jouvet and Huss, 2019; Zekollari et al., 2019), and the implications for water resources management and sediment management (Schaefli et al., 2007; Finger et al., 2012; Lane et al., 2017; Lane & Nienow, 2019). In the Alps, surface melt in the ablation zone is a primary driver of glacier retreat, but it can vary spatially over very small distances as a result of heterogeneity in surface reflectance related to the presence of debris cover, surface roughness, aspect, slope, and the dimensions and density of supraglacial streams (Parker, 1975; Strasser et al., 2004; Gabbud et al., 2015; Rossini et al., 2018). Several studies have analyzed melting patterns for both Alpine and Arctic glaciers and their dependence on glacier surface properties (Cathles et al., 2011; Rippin et al., 2015; Rossini et al., 2018; Wojcik and Sobota, 2020). This has included a focus on the effect of albedo and supraglacial dust on ablation (Brock et al., 2000; Adhikary et al., 2002; Brock, 2004; Azzoni et al., 2016; Naegeli et al., 2019). However, there are very few studies of Alpine glacier ablation at a high temporal resolution (a few days) simultaneously with a high spatial resolution. Yet, such studies are important if we are to improve the parameterisation of surface melt models. The equilibrium surface energy balance for a temperate glacier can be written as (Cuffey & Paterson, 2010):

IV-1

$$E_n = E_s + E_l + E_h + E_e + E_p$$

there, E_n is the net energy flux into the surface, E_s is net shortwave radiation, E_l is net longwave radiation, E_h is sensible heat flux, E_e is latent heat flux and E_p is heat added by liquid precipitation. The variables considered in our analysis each directly influence several energy fluxes. Solar radiation affects net shortwave and longwave radiation. The formation of supraglacial flow paths (‘flow accumulation’) affects nearly all energy fluxes because it

changes the surface topography via erosion by water flow and therefore the radiation pathways as well as sensible and latent heat exchanges. Surface roughness mainly influences turbulent exchange of sensible and latent heat, but it also influences the absorption and reflection of shortwave radiation. Reflectance determines net shortwave radiation.

The aim of this paper is to quantify and to explain the spatial heterogeneity of glacier ablation over small spatial scales with a view to elucidating the key drivers of melt. We use an Uncrewed Aerial Vehicle (UAV) to acquire repeat high resolution (cm-scale) imagery of a temperate Alpine glacier during the peak part of the ablation season. We applied Structure-from-Motion Multi-View Stereo (MVS) photogrammetry to generate Digital Elevation Models (DEMs) for investigating the variability of ablation at the scale of decimetres to meters. We used the associated imagery and DEMs to derive key drivers of ablation based on topography and RGB values, notably incoming solar radiation computed based on latitude and time of the year, corrected for local micro-topographical variability, flow accumulation as an indicator of ablation due to surface water flow, surface roughness as a driver of turbulent heat exchange, and reflectance to represent debris cover effects on albedo. We identified 10 zones from the ablation zone of the glacier, each 50 m x 50 m in extent for three overlapping time periods during the ablation season and used stepwise regression to model ablation patterns and so tease out the key drivers of ablation.

IV.3.2 Methods

IV.3.2.1 Study site

The Glacier d'Otemma is a temperate Alpine valley glacier located in the Val de Bagnes in the south-western Swiss Alps. In 2018, it was 6.5 km long, with a surface area of 10 km^2, and extended from 2500 m a.s.l. to 3790 m a.s.l. Its terminus was located at 45°56′20.029″N / 7°25′23.502″E. The only active remaining tributary glaciers are the Glacier de Blanchen and the Glacier du Petit Mont Collon (Figure IV-1). The final 900 m of the ablation zone have been studied to quantify subglacial channel form using GPR (Egli et al., 2021a) and to investigate an ice surface collapse feature that occurred close to the terminus during summer 2018 (Egli et al., 2021b). Earlier studies include glacio-hydrological modelling of the wider Mauvoisin catchment (Schaefli et al., 2007; Gabbi et al., 2012), GPR measurements at the surface of Glacier d'Otemma (Gabbi et al., 2012; Langhammer et al., 2017) as well as studies of sediment connectivity in the proglacial margin (Mancini & Lane, 2020).

The region of interest for this study is located in the ablation zone and it covers an area of 800 x 350 m extending from 2470 m a.s.l to 2590 m a.s.l. (Figure IV-1; Figure IV-10). The glacier surface contains a high diversity of different features and surface types, which is representative of the ablation area of many temperate glaciers in the Alps (Rossini et al., 2018). The orographical left-hand side of the glacier tongue is occupied by a wide strip of debris cover ('lateral moraine' issuing from the confluence of Glacier du Petit Mont Collon and Glacier d'Otemma), the central band consists mostly of bare ice which is sparsely covered with rocks and dust, there are several areas with deeply incised supraglacial channels or moulins and other areas with more superficial supraglacial channels, and the right-hand side of the glacier is also covered in debris of varying thickness. Located roughly 50 m upstream of the terminus there was a major subglacial channel collapse feature, which developed shortly before the survey period in August 2018 and kept growing until the end of the ablation season 2018 (Egli et al., 2021b).

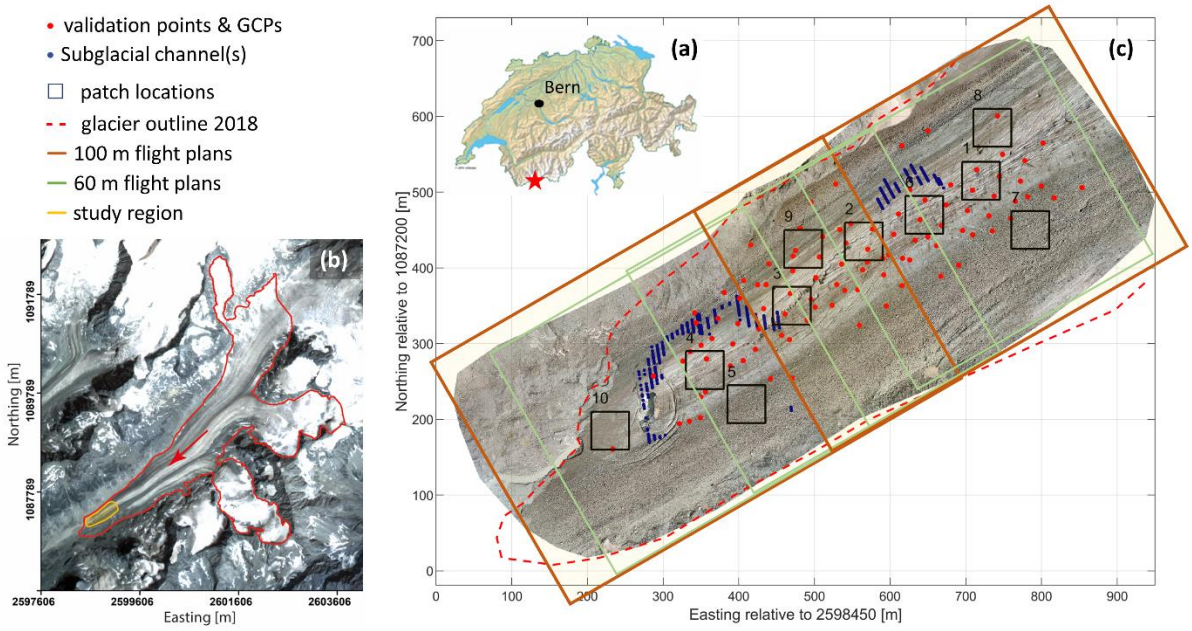

Figure IV-1: (a) Location of Glacier d'Otemma in the South-Western Swiss Alps. The insert map was obtained from the Swiss Federal Office of Topography (http://map.geo.admin.ch). (b) Overview of Glacier d'Otemma; glacier outline in red, study region in orange. The background satellite image was obtained from 2019 imagery (Planet Team, https://api.planet.com). (c) Study area: In red, the position of Ground Control Points for each DEM, superposed onto the orthophoto of the 9th of August 2018. In blue stipples the position of the subglacial channels as derived from GPR (Egli et al., 2021b). The black squares are the patches selected for the statistical analysis in this article. Please note that all coordinates in the figures of this paper are given in meters in the local Swiss coordinate system 'CH1903+'.

IV.3.2.2 Datasets

This study employs UAV imagery to obtain a set of high-resolution Digital Elevation Models (DEMs) and so to examine ablation patters on the lower part of the tongue of Glacier d'Otemma. The region of interest covers a surface area of approximately 0.24 km^2 (Figure IV-1). Data comprise four high-resolution DEMs, selected as the best quality datasets out of 10 DEMs generated for different days spanning a time period of 16 days in August 2018. Image processing was supported by Ground Control Points (GCPs) and validation points (composed of check points and ablation stake locations). The position and extent of a major subglacial channel was previously documented in the same area, derived from GPR measurements carried out in August 2017 (Egli et al., 2021a).

IV.3.2.3 UAV data and GCP acquisition

Each UAV data acquisition consisted of approximately 1250 photographs taken by a DJI® Phantom 4 Pro drone with a sensor size of 5472 x 3648 pixels and a focal length of 9 mm (Table IV-1). The photographs were acquired during five grid-shaped flights, of which three flights were at 60 m above ground level (AGL) with a 90° camera angle and 70-80% overlap and two flights were at 100 m AGL with a 75° camera angle and a 70-80% overlap (Figure IV-1; Figure IV-2). The flight paths for the 60 m AGL flights were a set of parallel lines with a 32 m offset oriented in upstream-downstream direction, and for the 100 m AGL flights they were perpendicular to the upstream-downstream orientation, with a 35 m offset, resulting in an overlap of 70-80% between same-flight images. In order to obtain similarly illuminated images for every campaign, flights started at around 9:00 a.m. and lasted until 12:00 a.m. A total of 54 GCPs were used comprised of 1 m x 1 m black boards with a white cross and a reflecting CD-ROM at the centre of each cross. As locations on the glacier surface may be moving, the GCPs were re-measured on the same day as the imagery was acquired using a Trimble® RC-10 differential GPS System (dGPS, Figure IV-18 in Appendix). A GPS base station was instrumented on a bedrock outcrop immediately downstream from the snout of the glacier. It monitored continuously during data acquisition and the full base station dataset was corrected into the Swiss national co-ordinate system using the RINEX dataset from the Swiss automatic GNSS network (AGNES) provided by swipos (Swipos, 2022). All GCPs were measured using real-time kinematic processing involving a rover. Occupancy of each point was required until horizonal precision was better than ±0.02 m and vertical precision better than ±0.05 m. More than 100 validation data points were also measured on the same day as the imagery and these

comprised either additional targets (i.e. check points) or measurements at 47 ablation stakes installed on the glacier surface.

IV.3.2.4 Photogrammetric processing

The photogrammetric processing procedure made use of the software Agisoft Metashape® and closely followed the procedure described in Rossini et al. (2018), Gindraux et al. (2017) and Westoby et al. (2012) (Figure IV-2). In a first step, images with low visual quality were discarded. An initial image alignment (Bundle Adjustment) by feature recognition was computed. Subsequently, the GCPs were manually marked on several (at least 5) images to achieve georeferencing. Now, the georeferenced model was re-aligned and a dense point cloud and mesh generated, and texture built. The dense point clouds were imported into Matlab® to interpolate them onto a pre-defined regular grid with a cell size of 0.2 x 0.2 m to obtain DEMs. Finally, the DEMs were validated using the check points and ablation stakes.

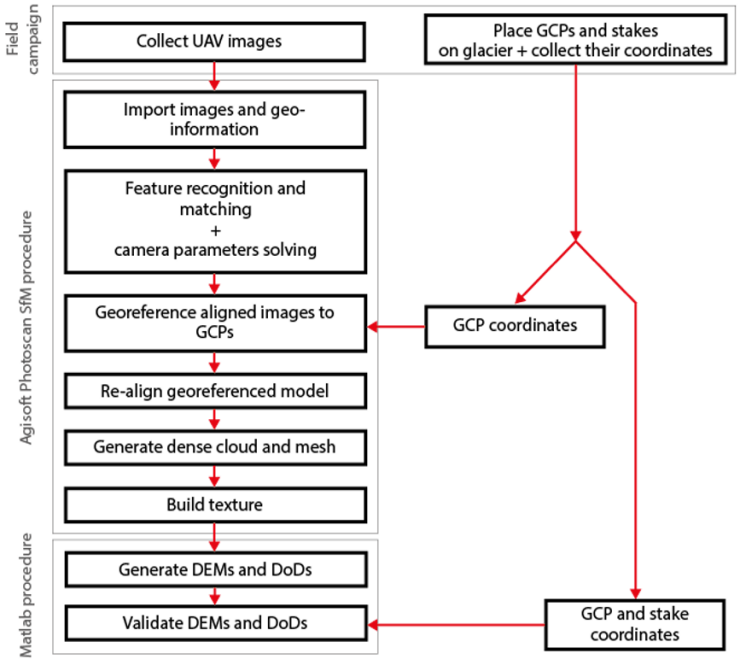

Figure IV-2: Photogrammetric processing procedure: field data acquisition, photogrammetric processing with Agisoft® Metashape and processing with Matlab® (Modified from Rossini et al., 2018 ; Gindraux et al., 2017 ; Westoby et al., 2012).

IV.3.2.5 Initial quality control and correction for systematic error

It is well established that uncertainties in the estimation of camera geometry can lead to systematic DEM errors, even with the use of GCPs, and normally manifest as tilt or doming

(James et al., 2017, 2020). Table IV-1 gives the mean error for the validation data points for the four DEMs used in this study. Mean errors (vertical accuracy) were relatively small (between -0.021 and -0.042 m) (Table IV-1). Standard deviations of error were between ±0.088 and ±0.097 m (Table IV-1). Inspection of DEMs of difference suggested a weak tendency towards doming and for this reason it was decided to correct the DEMs for systematic error (James et al., 2019).

Systematic error can commonly be identified as zones of change where there should be no change (e.g. bedrock exposures, buildings). With a glacier surface, identification of such error is a challenge as it is highly unlikely that there are extensive areas of no change even over time-scales of a few days. Instead, here, we used the validation dataset, consisting of points measured with dGPS at the glacier surface, to model the error by fitting the following relationship to obtain a 3-D model of the glacier surface;

IV-2

$$E = f(x, y, x^2, y^2, xy) = a_1 + a_2x + a_3y + a_4x^2 + a_5y^2 + a_6xy$$

where E is the error for the set of validation data points, x and y are the horizonal coordinates of each point and a(i), i = 1…6, are the six calibration parameters. The calibrated form of (Equation IV-2) was applied to the DEM co-ordinates. The modelled error surface was then subtracted from each original DEM to obtain a corrected DEM. For all the DEMs the residual mean error after correction is smaller than 10^{-4} m and the standard deviation of the error is slightly reduced after correction, resulting in standard deviations of error between ±0.087 m and ±0.096 m (Table IV-1).

Table IV-1 : DEM numbers, dates of UAV acquisition, vertical accuracy and errors before and after correction based on validation points.

DEM #	**DATE**	**#Images** (5472 x 3648 pixels)	**# valid. points**	**Vertical accuracy [m]**	**Stddev error [m]**	**Mean error (corrected) [m]**	**Stddev error (corrected) [m]**
1	07.08.2018	1252	102	-0.0417	0.0967	0.0000	0.0957
2	12.08.2018	1359	109	-0.0248	0.0883	0.0000	0.0872
3	20.08.2018	1253	109	-0.0212	0.0964	0.0000	0.0936

4	23.08.2018	1258	109	-0.0234	0.0902	0.0000	0.0866

IV.3.2.6 Generation of DEMs of Difference

DEMs of Difference (DoDs) were generated by subtracting a DEM with an earlier date from a DEM with a later date to yield a surface showing elevation change. This surface change will be a function of both ablation and ice dynamics. Assessment of dGPS coordinates measured daily at ablation stakes distributed over the region of interest indicated that the glacier dynamics resulted in a horizontal surface movement of less than 0.1 m over the course of 11 days reported in this study (12th – 23rd August 2018, Figure IV-18). Since the horizontal resolution of each DEM is 0.2 m and the observed horizontal displacement was less than half the resolution it was not necessary to correct DEMs for ice dynamics before the computation of DoDs. In this study we focus on ablation, but in certain areas there is an important signal of vertical ice motion on the order of 0.2 m / 16 days contributing to surface change (Egli et al., 2021b).

The uncertainty in the elevation difference dZ for each cell in a DoD is equal to the root of the sum in quadrature (Taylor, 1997) of the uncertainties in each individual DEM (Lane et al., 2003):

IV-3

$$\sigma_{DoD} = \sqrt{\sigma_{DEM1}^2 + \sigma_{DEM2}^2}$$

Where σ_{DEM1} and σ_{DEM2} are the uncertainties in surface elevation of two different DEMs and σ_{DoD} is the uncertainty in elevation difference of the resulting DoD after subtracting DEM1 and DEM2. The 'level of detection' (LoD) for a 95% confidence level with t = 1.96 under the t distribution is therefore (James et al., 2017)

IV-4

$$LoD = t\,\sigma_{DoD}$$

Cells with dZ smaller than the LoD are regarded as having zero change. For any DoD computed from the DEMs in Table IV-1 the maximum uncertainty in elevation difference is $\sigma_{DoD} = 0.130$ m (Equation IV-3), yielding an $LoD_{95\%}$ of 0.254 m (Equation IV-4). This compares to a minimum elevation change on the glacier surface of 0.3 m observed over the shortest observation period, 8 days between DEM2 and DEM3, whereby dZ was higher than 0.7 m for

the majority of cells, showing that even the lowest values of ablation are still above the limit of detection for the shortest time interval considered.

IV.3.2.7 Definition of four key variables on the glacier surface

To quantify controls on spatial patterns of surface melt develop we determined four variables that account for the most important processes and properties reigning at the glacier surface: incoming solar radiation, supraglacial flow accumulation, surface roughness and reflectance. Below we describe how these are computed and what they represent. The spatial extent of the dataset (800 x 350 m) is small enough to be able to exclude any significant influence of difference in cloud cover, altitude-related temperature gradient or other spatially varying external factors within the scale of the region of interest.

Potential incoming shortwave radiation was computed using the method of Kumar et al., (1997), adapted into Matlab® code by Felix Hebeler at the University of Zurich, Switzerland, in 2008. The input for this method consists of a DEM, the local latitude, and the time interval of the year over which the incoming solar radiation should be integrated to yield total solar radiation for a given cell of the DEM. Therewith, solar radiation accounts for aspect and slope as well as for local shading on the glacier surface. DEM 4 (12th August 2018) was used, since this DEM has the lowest mean error and the highest precision, and it is in the middle of the period of interest for the three different DoDs considered.

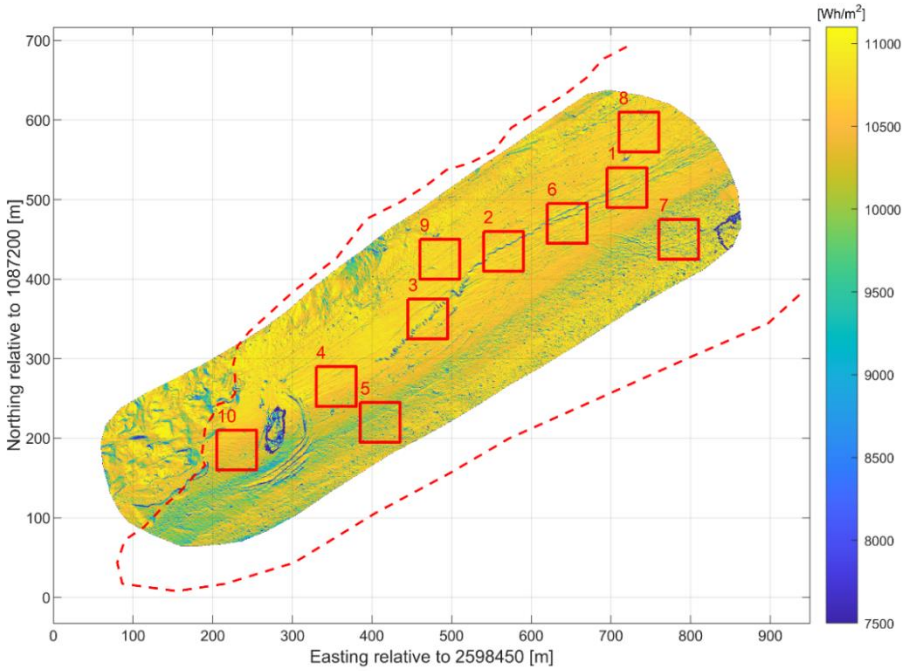

Figure IV-3: Solar radiation, in Wh/m2, computed for the DEM of 12.08.2018, shown with the patch locations and glacier mask manually drawn for 2018.

Melt processes on glacier surfaces can be increased by the frictional melt induced by water flow (e.g. Hambrey, 1977; Isenko and Mavlyudov, 2002; Isenko et al., 2005; Karlstrom et al., 2013; Kamintzis et al., 2019). The formation and evolution of supraglacial channels over the course of an ablation season has been studied increasingly in recent years (Mantelli et al (2015); St Germain & Moorman (2019); Bash et al., 2020; Hill & Dow, 2021; Hill et al., 2021). To represent the contribution of such channels to ablation, flow accumulation was computed using the TopoToolbox package in the Matlab® environment (Schwanghart and Scherler, 2014). As for solar radiation, the 12th August 2018 DEM was used. Sinks were filled and the flow accumulation algorithm was run with the D infinity method by Tarboton (1997) that distributes the flow to the steepest triangular facet in vicinity of the current grid cell. Given the gently sloping terrain of the glacier tongue this method was deemed as the most reliable and realistic method for the given situation. Flow accumulation is supposed to approximate the positioning and action of actual supraglacial channels due to meltwater flow gathering upstream and concentrating in depressions carved into the ice surface by supraglacial channels. Figure IV-4 visualizes stream lines computed for a flow accumulation threshold of 300 upstream contributing cells needed to form a channel. Although this threshold has been chosen for visualization, the entire flow accumulation starting at 1 upstream contributing cell has been taken into account for subsequent statistical analysis, so as not to miss the contribution of the smallest channels.

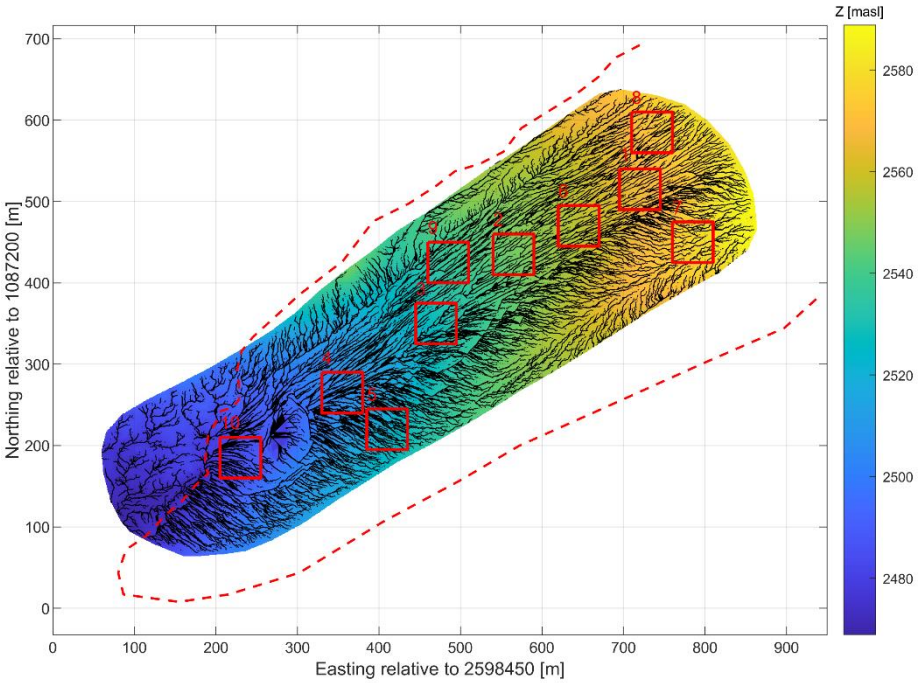

Figure IV-4: Stream lines (in black) computed from flow accumulation, with a threshold of 300 upstream contributing cells. The background colouring corresponds to the DEM for the 12th of August 2018, shown with the patch locations (in red) and glacier mask manually drawn for 2018 (dashed red line).

The micro-roughness of glacier surfaces has been shown to be an important influence on glacier surface melt (e.g. Brock et al., 2006; Smith et al., 2016; Steiner et al., 2018) and one that can be readily parameterised from high resolution DEMs (e.g. Chambers et al., 2020). As for solar radiation and flow accumulation, surface roughness was computed based on the 12th August DEM. Several studies in Earth Sciences proposed a relation for estimating the roughness height of surfaces based upon the standard deviation of local surface elevation (e.g., Kuipers, 1957; Munro, 1989; Smith, 2014). Here it was defined as the standard deviation of surface elevation within squares of 0.8 x 0.8 m (4 times the DEM cell resolution) and was calculated for the entire area located within the region of interest (Figure IV-5). As we were not concerned with precise roughness estimates but simply a measure of local surface variability and as the slopes of the glacier were low (< 10^{o}) we did not need to locally detrend each square (cf. Chambers et al., 2020); Figure IV-5 shows that standard deviations were generally higher than the maximum possible increase of standard deviation due to a 10^{o} slope on a 0.8 m x 0.8 m patch (±0.023 m). Larger window sizes for computing the standard deviation were assessed (Figure IV-20), but the smallest option was deemed to best reflect the actual surface roughness of the glacier surface and to offer the highest feasible resolution.

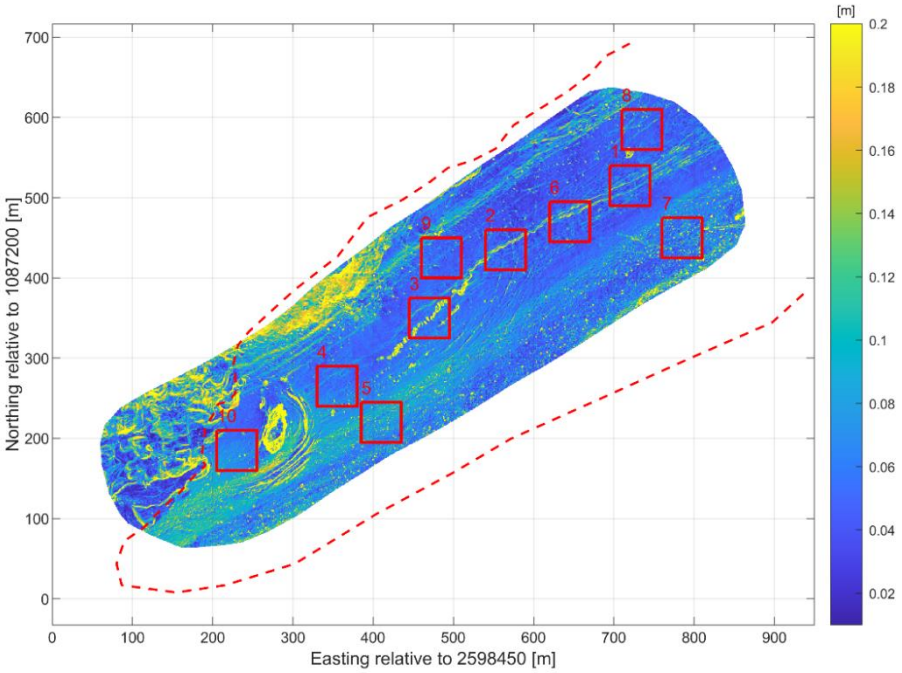

Figure IV-5: Surface roughness for an 0.8 m x 0.8 m window, shown with the patch locations and glacier mask manually drawn for 2018.

Reflectance was computed as a proxy for albedo because no precise large-scale albedo measurements were available for calibration at the time when the UAV data was collected. Following Rippin et al. (2015), reflectance is computed as the sum of the Red, Green and Blue components for each pixel of the orthophoto. Here, this was done by sampling the orthophoto at the same resolution as the DEM, in order to obtain the reflectance for the precise same locations as the remaining variables (Figure IV-6).

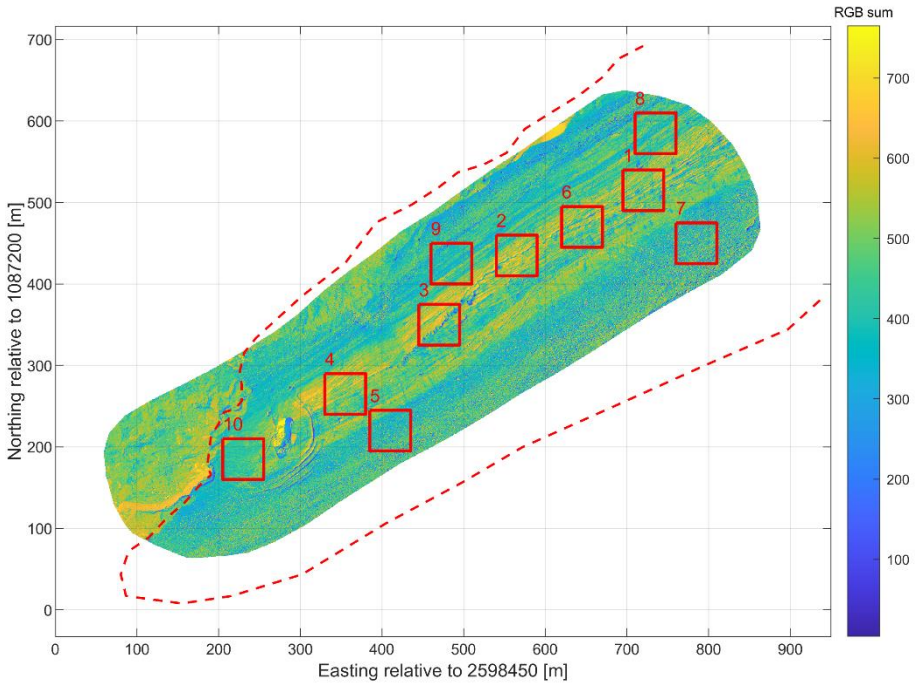

Figure IV-6: Reflectance at Glacier d'Otemma, computed for the orthophoto of the 9th of August 2018, shown with the patch locations and glacier mask manually drawn for 2018.

IV.3.2.8 Patch choice and characteristics for the statistical analysis

Ablation was assessed for 10 different patches, sized 50 x 50 m and each representing a specific environment on the glacier surface (Figure IV-10 &Figure IV-11), a certain surface topography feature (e.g., a deeply incised meandering channel, or a crevasse) or an area of interest from the point of view of surface texture and surface roughness (e.g., supraglacial debris cover or an area occupied by a particularly dense network of supraglacial channels). The patch size was chosen large enough to be able to perform a statistically significant spatial analysis, but small enough to exclude any wider spatial trends such as temperature gradients or ice dynamics. Table IV-3 describes each patch in detail in a qualitative way, and Figure IV-7 and Figure IV-8 show each variable for each patch along with the orthophoto. Figure IV-9: DoD_1 and potential incoming solar radiation for each patch, with individual color scale in order to accentuate local variations. Subfigure titles correspond to patch numbers. compares the elevation change (DoD) and the potential incoming shortwave radiation as an example for the importance of a single variable on elevation change.

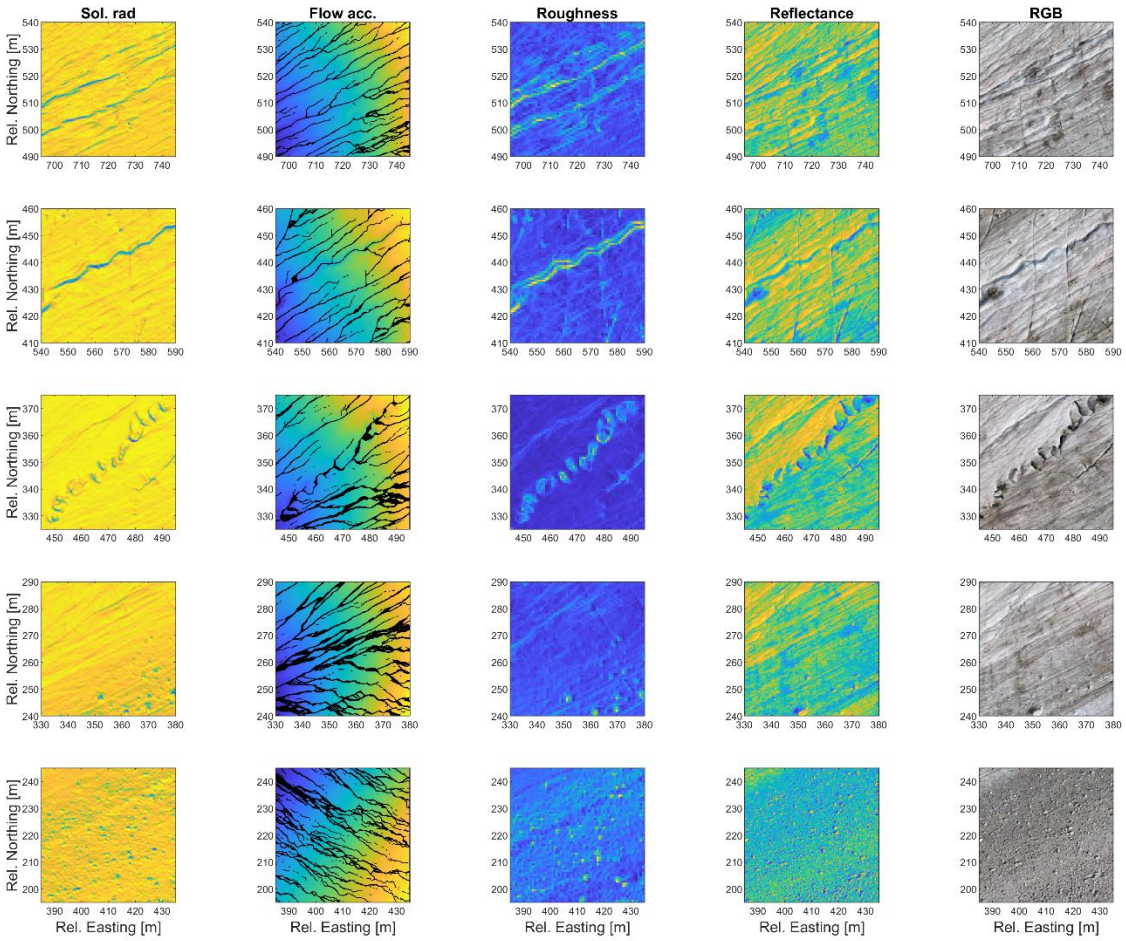

Figure IV-7 : Patches 1-5, each of size 50 x 50 m. From left to right, the plots show solar radiation, flow accumulation (superposed here on DEM altitude), surface roughness, reflectance and the orthoimage for reference. Each row represents one patch (1-5).

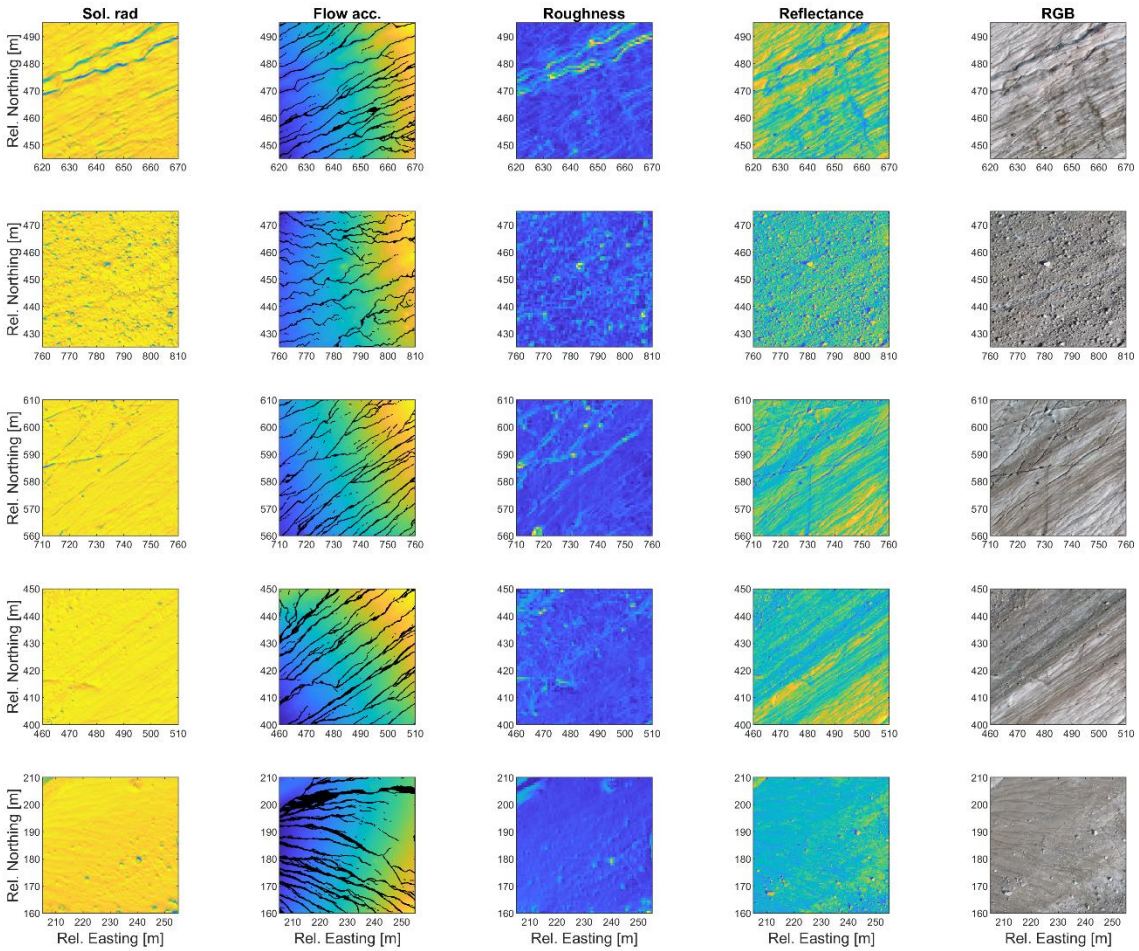

Figure IV-8 : Patches 6-10, each of size 50 x 50 m, with cell size 0.2 m. From left to right, the plots show solar radiation, flow accumulation (superposed here on DEM altitude), surface roughness, reflectance and the orthoimage for reference. Each row represents one patch (6-10).

Table IV-2: Description of patches of interest on the glacier surface, chosen to quantify the influence of four different variables (incoming shortwave radiation, flow accumulation, surface roughness and reflectance) on ablation. Orthophotos for each patch are displayed in the 5th column of Figures IV-9 and IV-10, where each row represents one patch number (1-5, resp. 6-10, going top to bottom).

Patch number	**Description of morphology and explanation for using this patch**
1,4 and 6	**Patches 1, 4 and 6** were chosen to represent a low-gradient surface on nearly bare glacier ice (high reflectance) near the centerline, with a dense network of near-parallel supraglacial channels. Patches 1 and 6 are located upstream, in the far north-east corner where the glacier surface is rather flat, but channel incision is fairly significant. Patch 4 is located close to the terminus and just upstream of a major subglacial channel collapse. Due to the local topography and supraglacial stream routing this patch contains less deeply incised supraglacial channels.

2	**Patch 2** displays a particularly marked supraglacial channel on bare ice and close to the centerline, flanked in the south and in the north by low-gradient, less incised topography.
3	**Patch 3** contains a supraglacial channel feature that deeply incised into the glacier surface while cutting strong meanders. On polythermal or cold-based glaciers such features are called 'cut-and-closure channels' (Rippin et al., 2015). Since this channel was incised mainly in the previous summer, with most of the meltwater flow being diverted into a moulin thereafter, this feature was not very active anymore in August 2018 at the time of this study. Nevertheless there was strong surface lowering at this location due to the response to solar radiation of the marked topography and due to an underlying subglacial channel that led to enhanced ice creep at this location.
5	**Patch 5** mainly consists of large boulder-sized supgraglacial debris cover constituting the left moraine of Glacier d'Otemma. The topography here is sloping north-west towards the center of the glacier. This patch also contains a small part of bar ice in its north-western corner.
7	**Patch 7** is rather uniform and, like patch 5, contains gravel- to boulder-sized debris cover of the left moraine. From the DoD one can also distinguish a supraglacial channel that is eroding into the ice despite the debris cover.
8	**Patch 8** marks a bare-ice area on the right margin partly covered with a very thin dust- or debris layer, featuring a low-gradient topography with few supraglacial drainage pathways.
9	**Patch 9** is located the furthest in the North-West, on the right margin of the glacier, and contains a mix of bare ice, dust-covered ice, thinly debris-covered ice and the beginning of the right lateral moraine. This patch contains some shallow supraglacial channels.
10	**Patch 10** occupies a relatively steep slope located immediately at the glacier margin. The ice surface is covered with a very thin layer of dust and gravel as well as with several boulders. It is located downstream of a major subglacial channel collapse feature and a channel is flowing underneath the ice. Towards the end of the study period the collapse feature extends into the eastern portion of this patch. The aspect of the patch is essentially west-north-west.

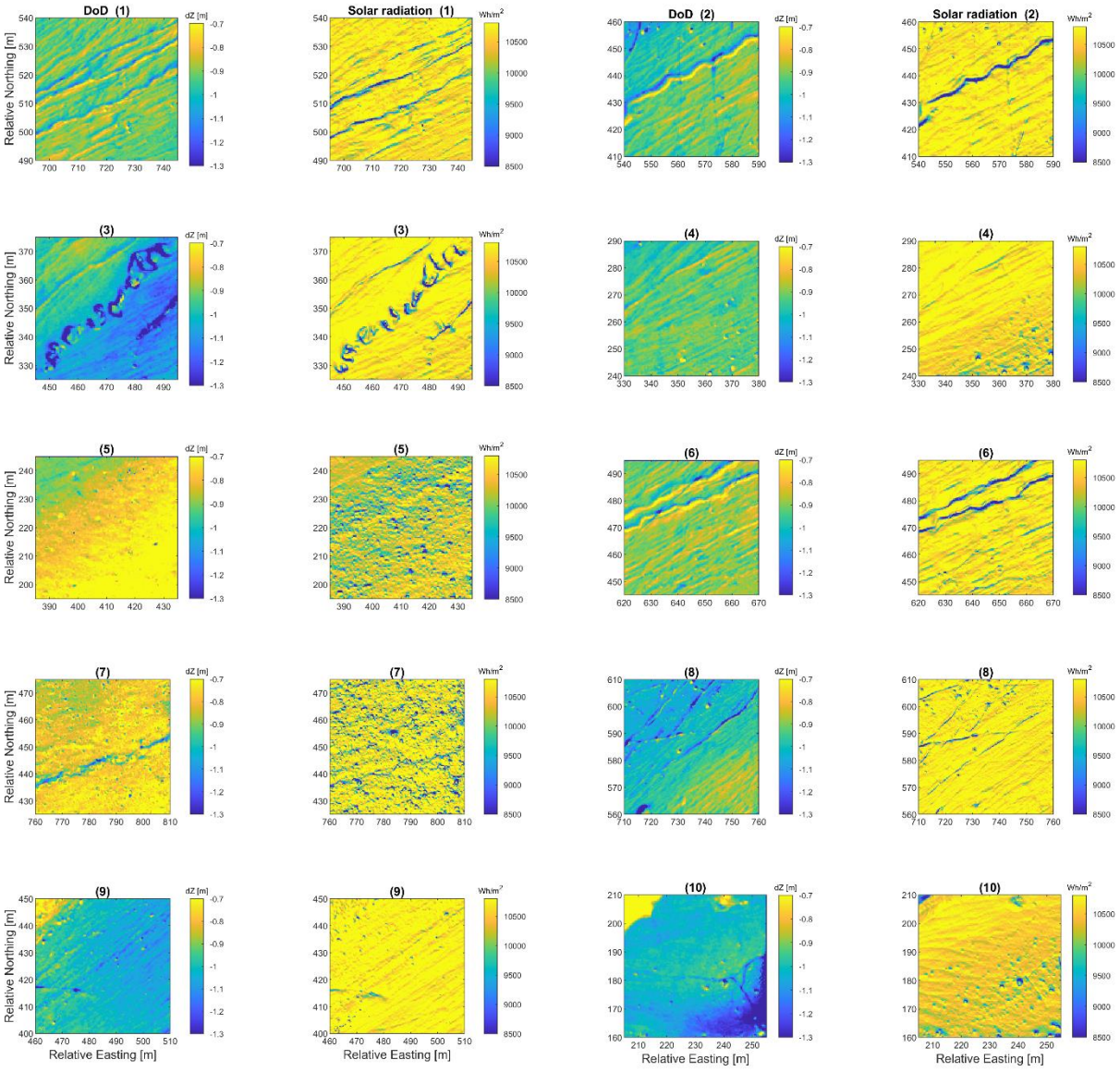

Figure IV-9: DoD_1 and potential incoming solar radiation for each patch, with individual color scale in order to accentuate local variations. Subfigure titles correspond to patch numbers.

IV.3.2.9 Statistical analysis

The objective of the statistical analysis was to determine the contribution of each of the four variables to surface lowering for a set of ten spatially restricted zones of interest (thereafter called 'patches', for delimitation see Figure IV-1c). The patches are described below.

The statistical analysis used a stepwise linear regression, computed for the target variable 'ablation' for each patch for three different (and overlapping) time intervals, resulting in 30 stepwise linear regression models. Each stepwise linear regression model was computed for one DoD and using the more significant uncorrelated variables (i.e., those that better explain

the ablation signal) of the four variables explained above ('solar radiation', 'surface roughness', 'reflectance' and 'flow accumulation'). E.g., if reflectance and solar radiation were correlated, only solar radiation was retained because it explains the ablation signal better than reflectance. The time intervals between DEMs were chosen to be as long as possible in order to maximize the ablation signal over the limit of detection. DoD_1 was designed to cover the full study period - 7th-23rd August. We then also considered DoD_2 (12th-23rd August) and DoD_3 (12th-20th August). We did not consider the 7th-12th August and the 20th to the 23rd August as these were deemed to be too short given the amplitude of the ablation signal and the standard deviation of error in the DEMs (Table IV-1), resulting in a small margin between signal and limit of detection. Comparing different time intervals and thereby making use of different DEMs adds statistically more significance to the result in view of the uncertainty involved in each DEM. That is because, despite using GCPs to correct DEMs and removing error using validation points, each DEM still contains some systematic error locally which may influence the outcome of the analysis. Also, the four variables may act differently on ablation over different time periods – especially with increasing surface incision by supraglacial channels over the duration of the ablation season.

Table IV-3 : Details for the DoDs used to compute stepwise linear regressions using four variables on ten patches. Percent difference in elevation change is referring to DoD_1.

DEM of difference	DEM date 1	DEM date 2	# days	Mean total elevation change dZ for # days (ten patches) [m]	mean daily elevation change dZ (ten patches) [m/day]	percent difference in mean daily elevation change (DoD_1 / DoD_i)
DoD_1	07.08.	23.08.	16	-0.938	-0.0586	0.00
DoD_2	12.08.	23.08.	11	-0.630	-0.0573	2.22
DoD_3	12.08.	20.08.	8	-0.473	-0.0591	-0.85

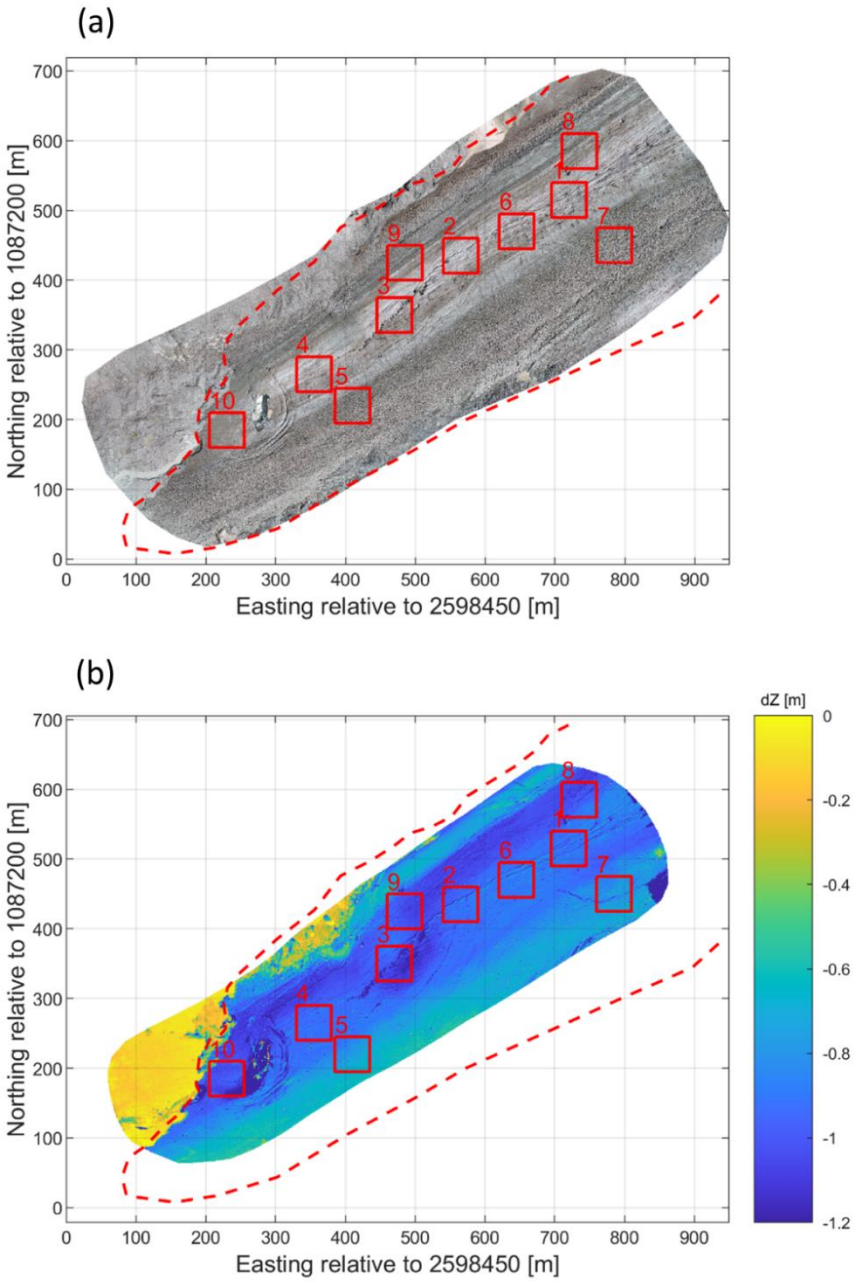

Figure IV-10: The position of ten patches measuring 50 x 50 m. In (a) shown on the backdrop of a high-resolution orthophoto from the 9th of August 2018 and in (b) with the DoD between the 7th and the 23rd of August 2018. The 2018 glacier outline is drawn as a dashed red line.

The stepwise linear regression was computed in Matlab®. Data for each patch was normalized by the maximum value of each variable within the given patch to account for different ranges of absolute values of each variable. The stepwise regression added variables in order of decreasing importance checking that, as each new variable was added, the increase in R^2 was

significant (p<0.05). If this new variable was correlated significantly with a variable already included in the regression, it was removed, and the search for significant variables continued. The analysis was conducted for each patch for each of the three DoDs. The stepwise regression outputs were then used to define a final multiple linear regression model that was computed for each patch and for each DoD using the 'regress' function in Matlab®. These multiple linear regression models were of the form

IV-5

$$Elevation\ change\ dZ = f(significant\ variables)$$

Which written in vector form becomes:

IV-6

$$dZ = X \cdot B$$

,where dZ is a vector containing elevation change for each cell of a patch, B is a vector containing regression coefficients (one for each variable) and X is a matrix containing columns with the values of predictor variables for this patch.

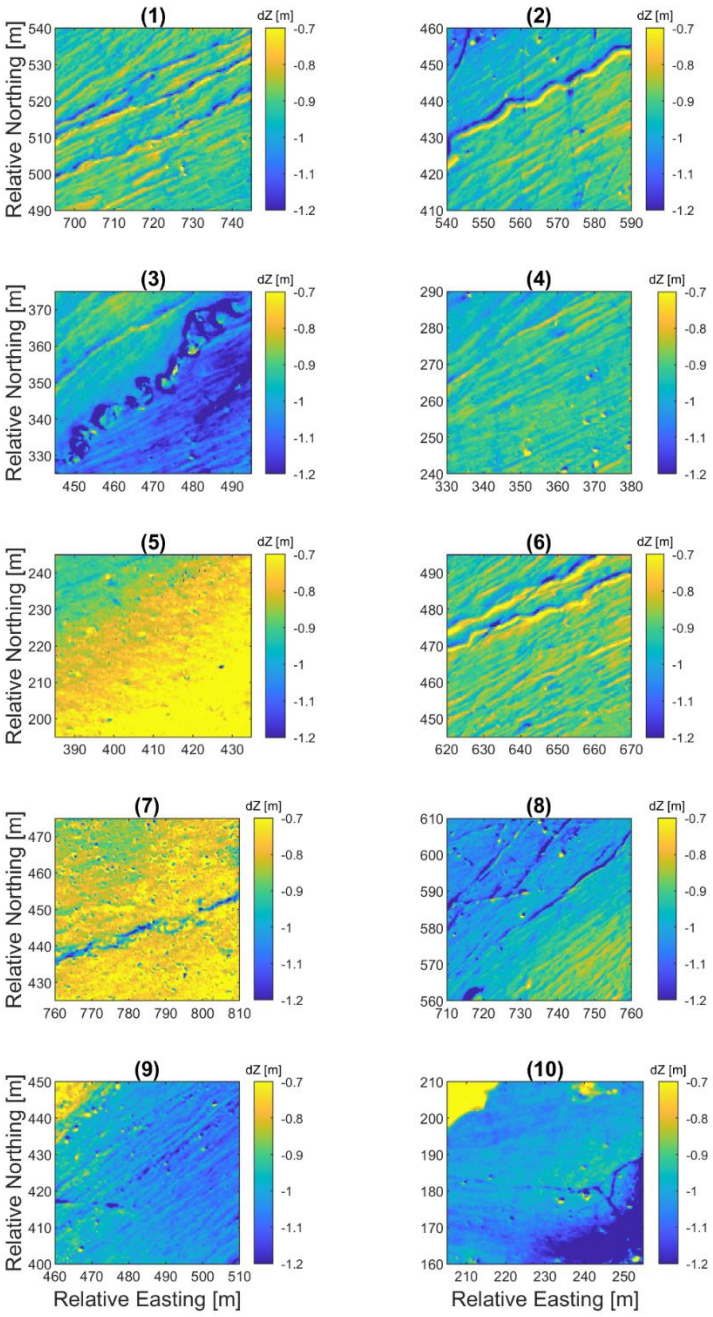

Figure IV-11 : DEM of difference number 1 (DoD_1) displayed for each patch, with individual color scale. Each subplot title corresponds to the number of the patch shown.

IV.3.2.10 Importance of microtopography

As a secondary analysis, to test for the link between solar radiation and surface microtopography, a DEM smoothing test was undertaken. The DEM of 12.08.2018 was progressively smoothed using a 2D median filter with window sizes of 3×3, 5×5, 7×7, 9×9, 11×11, 13×13 and 15×15 cells. For each degree of smoothing solar radiation for the 12th of August 2018 was computed. The correlation between solar radiation and ablation was

established for each DoD and for each patch to assess how important microtopographical features are for local effects of ablation.

IV.3.3 Results

IV.3.3.1 Correlations between predictor variables

Correlations between the four variables were assessed to rule out collinearity within the stepwise linear regression model. Solar radiation and surface roughness show significant correlation for nearly all patches (Figure IV-12Figure I-1). Reflectance and solar radiation have slightly elevated correlation ($|r| > 0.1$) for four patches, while reflectance and surface roughness are slightly correlated in two patches. Therefore, for each correlated couple the 'less significant' variable (i.e., the variable less prone to explain surface change) was removed before fitting the stepwise linear regression model.

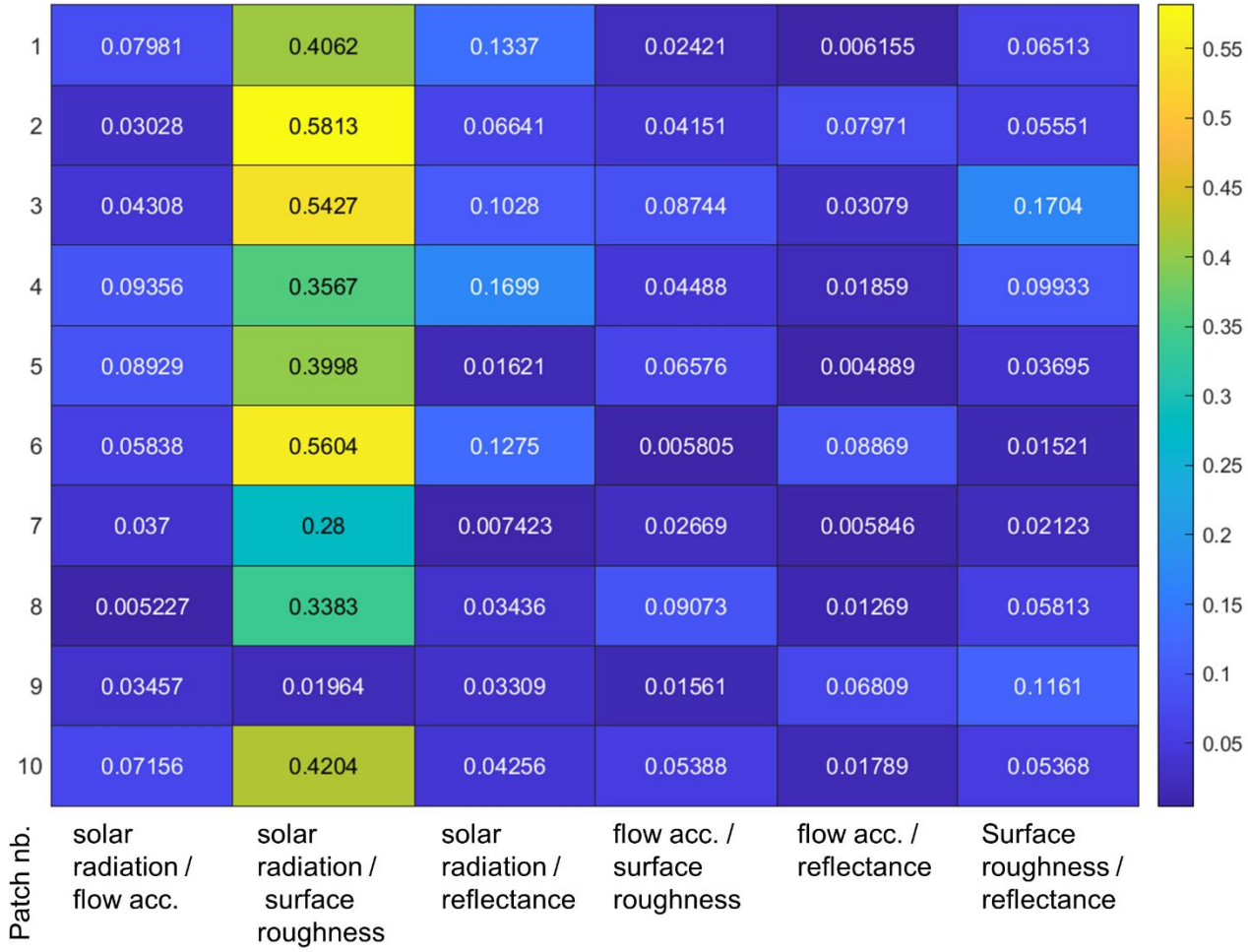

Figure IV-12: Absolute values of correlation coefficients (|r|) for the various pairs of variables used in the linear regression model, shown for different patches.

IV.3.3.2 Stepwise linear regression models

Figure IV-13 toFigure IV-15 show the t-statistic of the stepwise linear regression results. The t-statistic is an indicator for the importance of a certain variable in the stepwise linear regression. If its absolute value is high, the variable is important, if it is low, the variable is less important. If there is no value this means that the variable was not significant enough to be included in the regression model.

Solar radiation is the most important variable for most patches (1,2,4,5,6,7) on all dates. It is included in the regression model described in equation IV-6 on all dates for patches 3 and 9, but as the second or third variable added. For patch 10 it is included on two dates and only for patch 8 not at all. Flow accumulation is included for almost all patches on almost all dates, as either the second or the third variable added. Surface roughness is added first for patches 8 and 9, but then only rarely as a second or third variable. This is predominantly because it is correlated with the incoming solar radiation and since the former is dominant surface roughness is forced out of the analysis. Reflectance is of variable importance: It is the first variable added for patch 3 on all dates and patch 10 on two dates, and ranks as the second variable added for patches 2 and 8 on all dates.

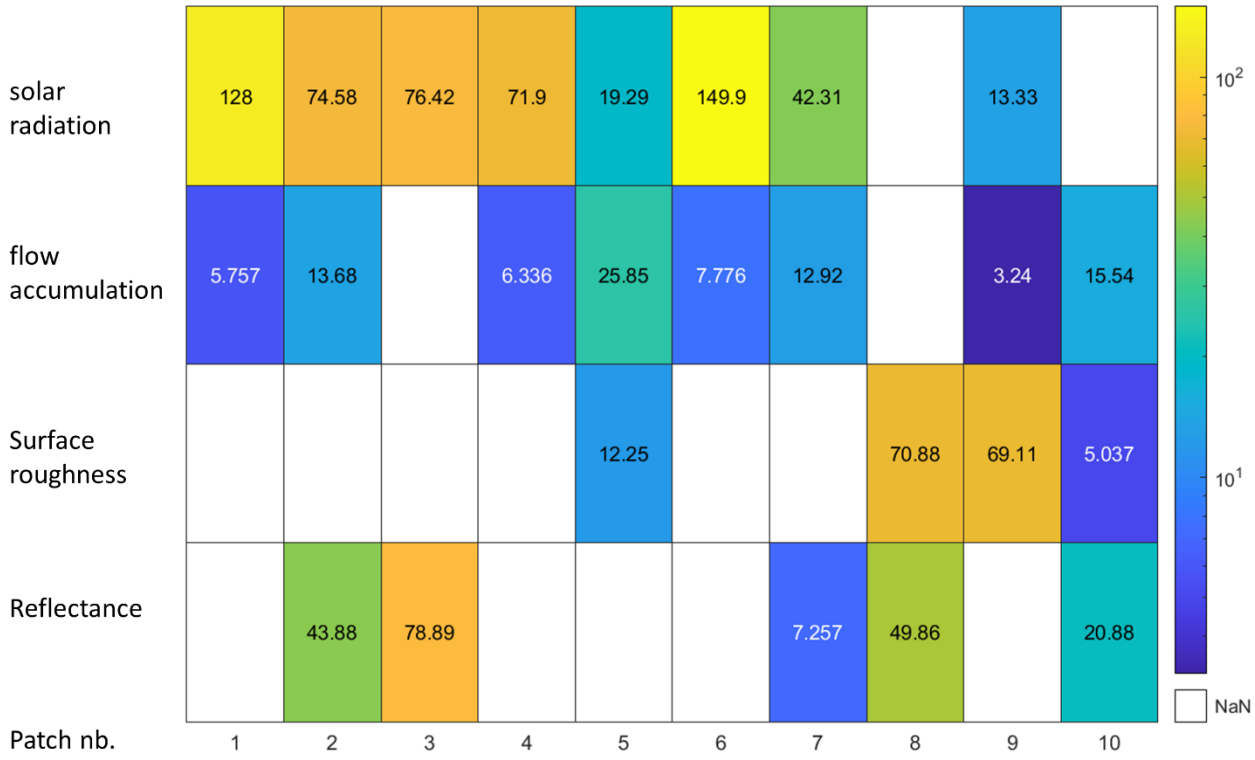

Figure IV-13: Absolute values of t-statistic for the results of a stepwise linear regression model for DoD1. The color map is logarithmic. Fields with no value indicate variables that were not significant enough in a given patch to be included in the stepwise linear regression model.

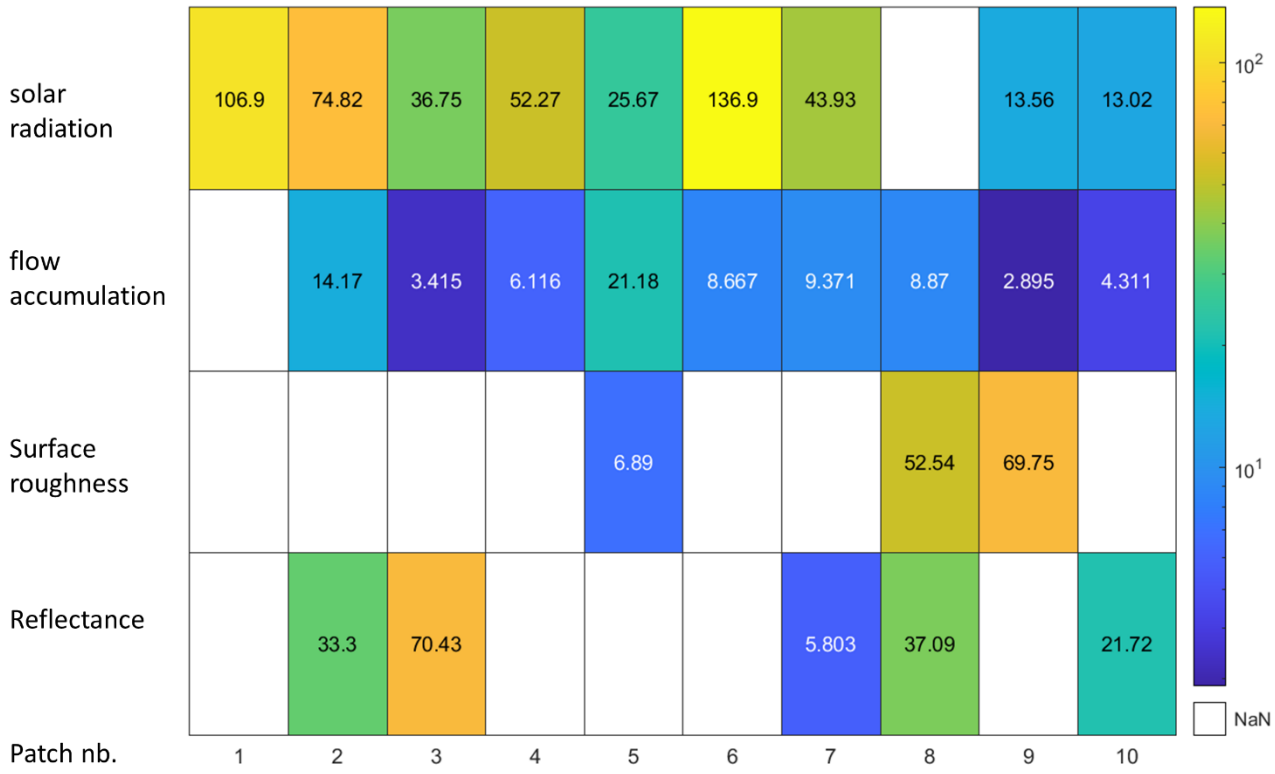

Figure IV-14: Absolute values of t-statistic for the results of a stepwise linear regression model for DoD2. The color map is logarithmic. Fields with no value indicate variables that were not significant enough in a given patch to be included in the stepwise linear regression model.

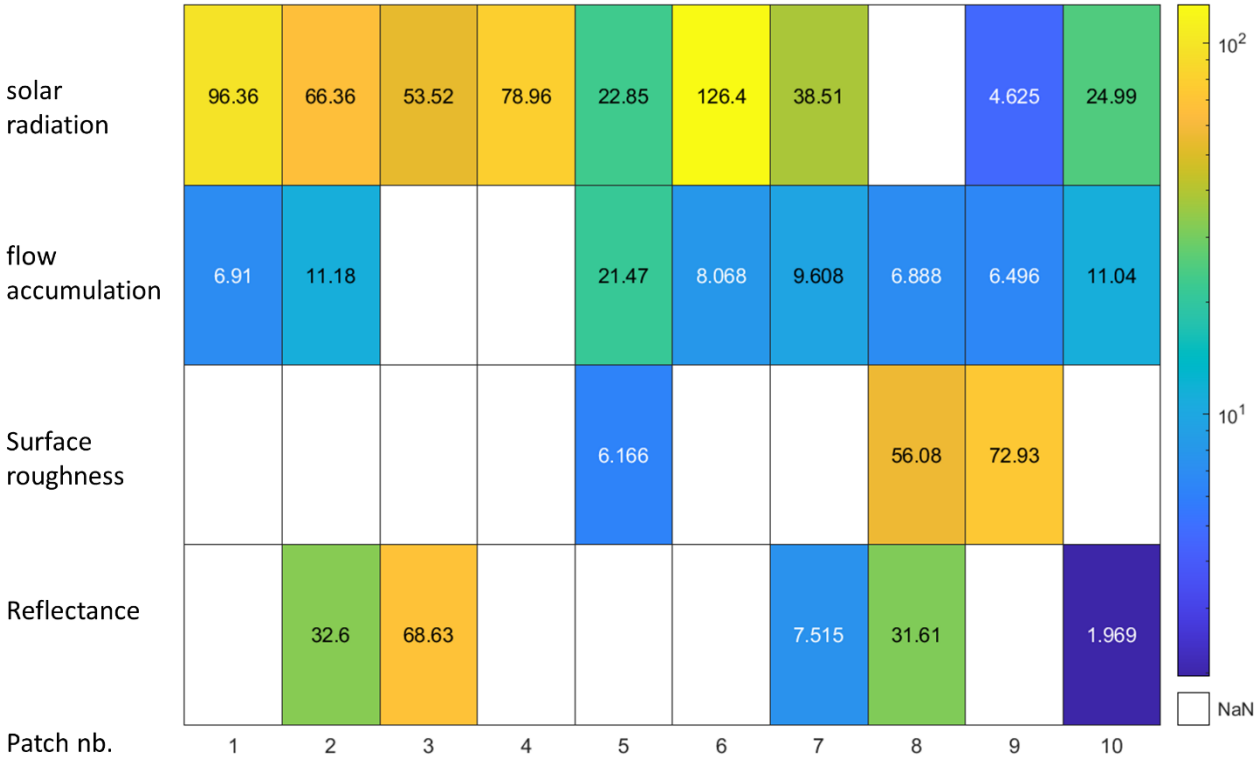

Figure IV-15: Figure IV 13: Absolute values of t-statistic for the results of a stepwise linear regression model for DoD2. The color map is logarithmic. Fields with no value indicate variables that were not significant enough in a given patch to be included in the stepwise linear regression model.

Tables IV-8 to IV-10 show the coefficients obtained by applying a multiple linear regression to the significant variables determined from the stepwise linear regression model. Table IV-11 shows the model performance for each patch and for each DoD, by looking at three different performance measures. It shows that the model performs best for patches 1 (r^2 = 0.129 – 0.208) and 6 (r^2 = 0.204 – 0.264), but also yields good results for patches 2, 3 and 8. The patches with the worst fit are patches 5,7 and 10. Both patches 5 (r^2 = 0.018 – 0.022) and 7 (r^2 = 0.025 – 0.031) are heavily debris covered, and patch 10 (r^2 = 0.011 – 0.013) contains part of the collapse feature on its eastern edge. The collapsing ice surface introduces a surface change signal that is not related to ablation and therefore the common variables predicting ablation fail there.

Table IV-4: Coefficients of the final multiple regression model for DoD1, i.e., values of vector B in equation 16-4.

coefficients	patch number									
	1	**2**	**3**	**4**	**5**	**6**	**7**	**8**	**9**	**10**
intercept	-0.132	-0.508	-2.110	-0.461	-0.898	-0.105	-1.002	-1.024	-0.886	-0.793

solar radiation	-0.824	-0.520	0.883	-0.481	0.162	-0.831	0.220		-0.190	
flow accumulation	0.016	0.062		-0.012	-0.156	0.024	-0.068		-0.017	0.611
surface roughness					-0.045			-0.308	0.280	0.309
reflectance		0.096	0.303				0.015	0.155		-0.673

Table IV-5: Coefficients of the final multiple regression model for DoD2, i.e., values of vector B in equation 16-4.

coefficients	patch number									
	1	**2**	**3**	**4**	**5**	**6**	**7**	**8**	**9**	**10**
intercept	-0.167	-0.337	-1.161	-0.341	-0.622	-0.120	-0.693	-0.715	-0.585	-1.250
solar radiation	-0.492	-0.343	0.326	-0.260	0.159	-0.510	0.165		-0.138	0.983
flow accumulation		0.042	0.207	-0.019	-0.094	0.018	-0.036	0.040	-0.011	0.260
surface roughness					-0.019			-0.166	0.202	
reflectance		0.048	0.029				0.009	0.084		-0.687

Table IV-6: Coefficients of the final multiple regression model for DoD3, i.e., values of vector B in equation 16-4.

coefficients	patch number									
	1	**2**	**3**	**4**	**5**	**6**	**7**	**8**	**9**	**10**
intercept	-0.188	-0.295	-0.948	-0.102	-0.437	-0.152	-0.485	-0.515	-0.489	-0.817
solar radiation	-0.319	-0.223	0.348	-0.386	0.117	-0.344	0.123		-0.040	0.255
flow accumulation	0.010	0.024			-0.079	0.012	-0.031	0.023	-0.021	0.090
surface roughness					-0.014			-0.129	0.177	
reflectance		0.034	0.148				0.010	0.052		-0.008

Table IV-7: Error statistics for the final multiple regression models, for each DoD and for each patch. r2 is the coefficient of determination, r2= 1- (residual sum of squares / total sum of squares).

Error statistic	patch number									
DoD_1	1	2	3	4	5	6	7	8	9	10
r^2	0,208	0,114	0,177	0,077	0,022	0,264	0,031	0,113	0,073	0,012
variance of error [m^2]	0,004	0,006	0,021	0,002	0,007	0,004	0,007	0,009	0,005	0,355
mean residual $\times 10^{-16}$	-4,4	-2,3	-3,2	9,0	6,9	2,4	-2,3	2,7	6,6	2,5
DoD_2	1	2	3	4	5	6	7	8	9	10
r^2	0,155	0,103	0,100	0,045	0,021	0,231	0,031	0,066	0,075	0,011
variance of error [m^2]	0,002	0,002	0,012	0,001	0,004	0,002	0,004	0,005	0,003	0,343
mean residual $\times 10^{-16}$	2,4	0,09	-3.0	2,5	4,6	17,6	0,90	3,0	4,3	24,6
DoD_3	1	2	3	4	5	6	7	8	9	10
r^2	0,129	0,085	0,119	0,091	0,018	0,204	0,025	0,065	0,079	0,013
variance of error [m^2]	0,001	0,001	0,007	0,001	0,003	0,001	0,003	0,003	0,002	0,006
mean residual $\times 10^{-16}$	-4,4	-3,6	3,0	12,9	5,7	5,2	-0,53	-0,10	1,4	3,7

IV.3.3.3 Importance of microtopography

The correlation between the smoothed DEM and each DoD is shown in Figure IV-17. For the patches 1,2,6, and 7 the correlation between solar radiation and elevation change decreases with increasing smoothing, and this is in accordance with model fitting results (Tables IV-5 to IV-7), where the effect of solar radiation on microtopography is the most important variable (highest absolute t-statistic) for these same patches. For the debris covered patch 5 as well as for patch 10 there is an increase in correlation and for the remaining patches there is no significant change. This means that microtopography is important for the effect of solar radiation on ablation, but only in certain situations, when other factors such as reflectance, debris cover or surface roughness are less so. Figure IV-16 visualizes the effect of progressive smoothing on topography in patch 1 and Figure IV-21 visualizes the same effect on the variable solar radiation. The effect of a decreasing correlation between solar radiation and ablation could probably be shown more clearly if an even stronger smoothing filter was applied to the DEM.

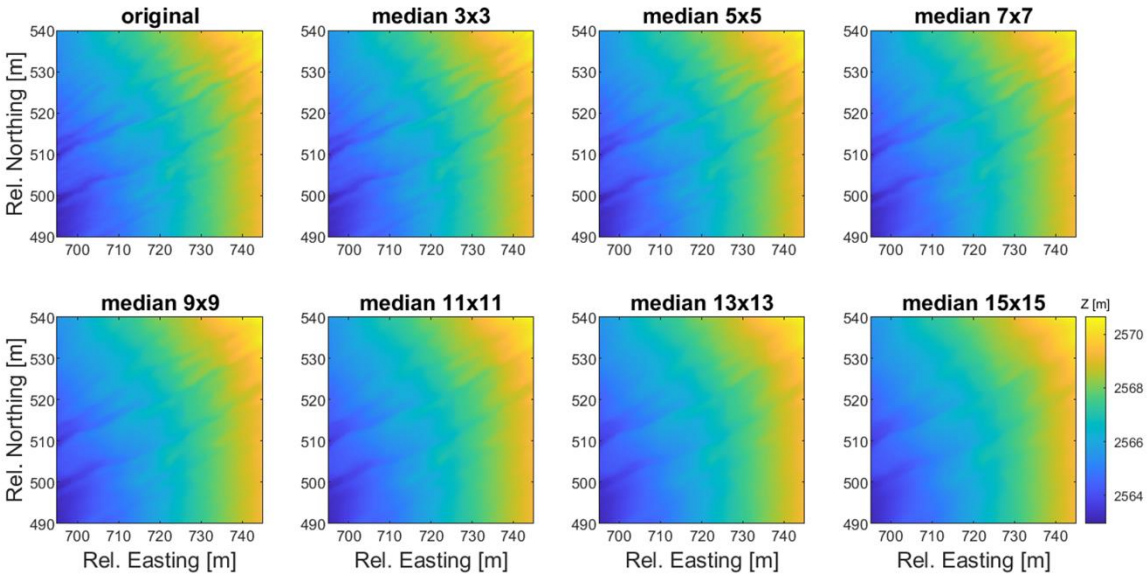

Figure IV-16: Smoothing experiment, visualized for patch 1. A median filter with a window size of 6x6 cells, 10x10 cells and 16x16 cells was applied to the DEM of 12.08.2018.

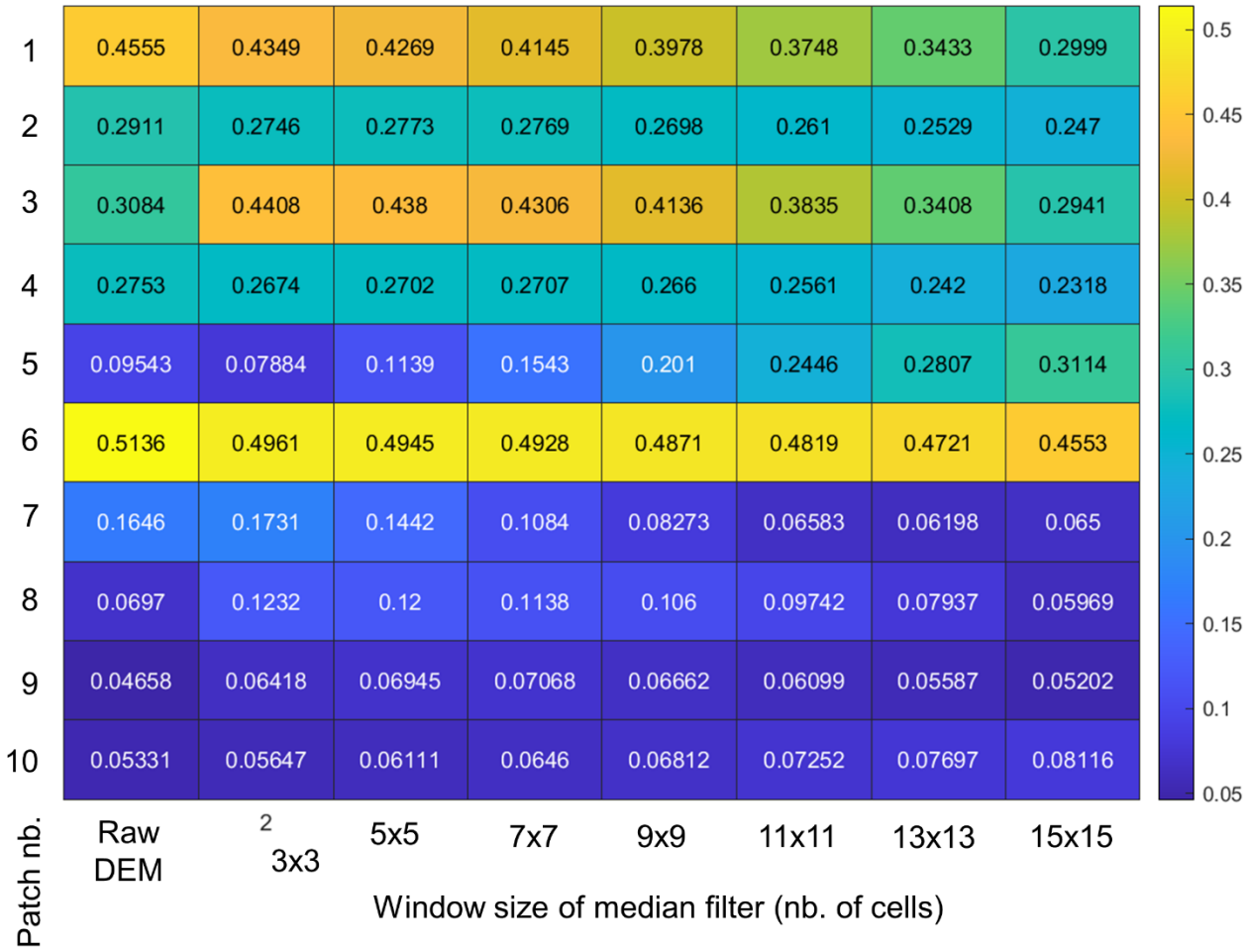

Figure IV-17: Correlation between solar radiation and ablation (DoD) for different degrees of surface smoothing (2D median filter with a window size of 3x3, 5x5, … ,15x15 cells), computed for DoD1. Lines 1,2,6 and 7 have decreasing absolute values of correlation with increasing smoothing, while lines 5 and 7 have increasing correlation with increasing smoothing. The remaining lines show no significant change in correlation. The results for DoD2 and DoD3 are shown in Tables A2 and A3.

IV.3.4 Discussion

IV.3.4.1 Importance of different variables for melt

The stepwise linear regression analysis showed the dominance of micro-topographical controls on melt in explaining small-scale variations in glacier surface ablation. This was reflected in two variables that were highly correlated: solar radiation and surface roughness. These variables cannot be considered separately, since they are correlated for nearly all patches (Figure IV-12Figure IV-4) and they partly describe the same properties of the glacier surface: microtopography, including local variations in aspect and slope. Nevertheless, incoming shortwave radiation also includes the local patterns of shadowing due to topographic features such as boulders, supraglacial channels, moulins, crevasses or steep ice walls in general. Such

features can produce shading for nearby areas, whilst sun-facing surfaces may absorb much more direct solar radiation than an equivalent flat surface. This is visible in places such as patch 2 (Figure IV-7), where the channel in the north of the patch has a flank that is exposed to the sun due to a southerly aspect and thus melts more quickly than the flank with a more northerly aspect. This impact of microtopography on potential incoming shortwave radiation has previously been found to increase total ablation when small scale topography was taken into account by using DEMs with increasing resolution (Hopkinson et al., 2010).

In contrast to reflectance, surface roughness does not consider the positioning, precise geometry or directionality of topographic features, but it is simply a measure of variability in surface elevation. Surface roughness can be important for creating additional melt due to reflected sunlight (Cathles et al., 2011) and for shading, but a higher surface roughness especially increases the turbulent exchange of sensible and latent heat at the surface (Braithwaite, 1995; Wagnon et al., 1999; Oerlemans & Klok, 2002; Mölg & Hardy, 2004; Conway & Cullen, 2013; Azam et al., 2014; Fitzpatrick et al., 2017; Steiner et al., 2018).

The stepwise linear regression shows that surface reflectance is indeed an important variable for ablation, especially for patches that contain both bare ice and debris covered ice – be it ice covered with a thin layer, leading to enhanced ablation (patches 2,3,8 and 10 in Tables IV-6 to IV-8 / Figure IV-7 and Figure IV-8), or a significant thick debris cover leading to insulation and reduced ablation. The importance of surface reflectance may be underestimated in this analysis since some patches (e.g., patches 5 and 7) include important debris cover for which the thickness and insulating effect is unknown here, adding additional uncertainty and lower predictability to the model.

Finally, even though the analysis shows that flow accumulation is a less important variable for the stepwise linear regression models in most patches, it plays a role in nearly all patches (especially in patches 5,6 and 7). Therefore, flow accumulation is a significant variable that can also determine the spatial distribution of ablation, as it has been shown previously (e.g., Isenko & Mavlyudov, 2002; Bash et al., 2020). In the results presented here the indirect contribution of flow accumulation may in fact be underestimated: Once a supraglacial channel erodes into the ice due to turbulence friction and sensible heat advected by the water (e.g., patches 2,3 and 6), the microtopography thereby created subsequently evolves due to incoming shortwave radiation being magnified (change in aspect, and reflected radiation), or reduced / shaded. Supraglacial channels can be regarded as the initiating process (e.g., Mantelli et al., 2015) in

creating microtopography, which is then taken over and magnified by incoming shortwave radiation. Thus, the parameters considered in this analysis may feedback onto one another.

IV.3.4.2 Influence of other factors

Apart from the four variables considered here, there may be different variables influencing the observed ablation patterns. Properties of the local topography such as slope and aspect are supposed to be indirectly included in the variable 'solar radiation', as well as partly in the variable 'surface roughness'. An important variable not considered in this study is supraglacial debris thickness. Surface reflectance accounts for the presence of debris cover, but it does not account for the debris thickness, which is essential for quantifying ablation. It is well established that a thin debris cover of less than 0.01 m enhances melt, while melt decreases for debris thicknesses of > 0.01 m (or slightly less or more, depending on the lithology), until reaching a plateau at around 1 m, where melt remains almost constant (Ostrem, 1959; Nakawo et al., 1999; Nicholson & Benn, 2006; Bosson & Lambiel, 2016; Herreid & Pellicciotti, 2021). For debris-covered glaciers located in permafrost environments melting continues until the debris cover thickness corresponds to the active layer thickness (Bosson & Lambiel, 2016).

For this specific field site at Glacier d'Otemma an important process influencing ablation is surface lowering due to creep closure of the ice towards a major non-pressurized subglacial channel close to the glacier snout. While the surface lowering itself may lead to a strong signal in the DoD that is wrongly interpreted as 'ablation', when it is due to ice dynamics as observed in patch 10 (Egli et al., 2021b), there is also a secondary and more subtle effect: Due to local surface lowering the topography changes, potentially exposing previously flat ice surfaces to a more or less intense solar radiation by changing their aspect and slope. Such a localized lowering may also contribute to the accumulation of dust and debris in a surface depression, leading to a change in albedo. These effects are expected to be observed mainly for patches 3, 10 and potentially 9, which are located above or in close vicinity to a subglacial channel (Figure IV-1). In this study, the influence on variability in ablation/surface change of an underlying subglacial channel within a patch is likely to be small, since the patches are of a relatively small dimension (50 x 50 m) when compared to the width of the subglacial channel, which extends to up to 20-25 m (Egli et al., 2021b). An underlying subglacial channel will therefore either influence a large proportion of a patch (if located underneath), or not influence the patch at all (if it is located more than 20 m away). In most cases, except for patches 3 and 10, the channel was located more than 20 m away from the edges of a patch and any influence could therefore be discarded.

IV.3.4.3 Further analyses

As a next step it would be valuable to use the variables solar radiation, flow accumulation, surface roughness and reflectance to predict melt with a physically based model that computes the entire energy balance at the glacier surface for a complex geometry including reflection and backscattering of shortwave and longwave radiation and turbulent heat exchanges (e.g., Buri et al., 2016a; Steiner et al., 2019; Bash & Moorman, 2020). This would allow to test and further refine the findings made in this article.

More information about the contribution of each variable could be gained by looking at even more highly resolved datasets at even shorter temporal time scales down to single days. This is possible with improved UAV systems, with optimized survey geometries (e.g. concentric flights added) and by employing a lower flying height.

IV.3.5 Conclusions

Incoming solar radiation and its associated microtopography is the main variable explaining small-scale variability in ablation. Surface roughness and reflectance are very important variables also, noting that surface roughness is intimately linked to local surface topography. If surface roughness is high, the variability in incoming solar radiation will also be high. Reflectance will especially be the most important variable in situations where a surface is very smooth or flat, and the only variability observed is in its colour or texture. The results of fitting a stepwise linear regression model have shown that flow accumulation is also a significant variable to take into account when aiming to explain ablation patterns – probably more important than previously assumed and with possible feedback effects on the former variables.

This study shows that reflectance and flow accumulation play an important role at a local scale. They are both important in shaping the ice surface with an initial signal that is later enhanced by the action of solar radiation, leading to both positive and negative feedbacks when shortwave radiation is shaded or backscattered by microtopography. Surface roughness is an important variable because it controls the exchange of turbulent heat at the glacier surface.

IV.3.6 Appendices

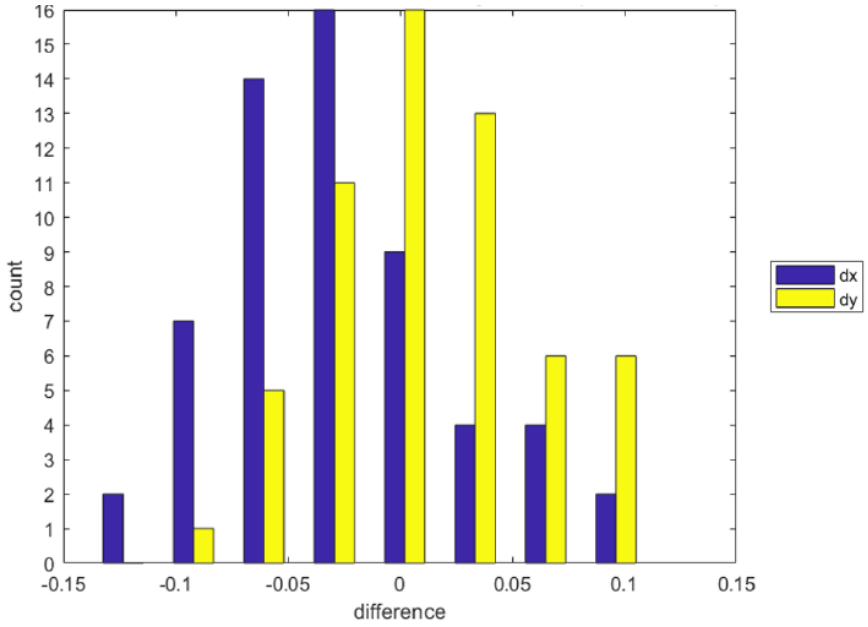

Figure IV-18 (Figure A1 in article): Total horizontal positioning differences measured with dGPS at the location of ablation stakes and computed for the time frame 12th – 23rd August 2018 (all values in meters).

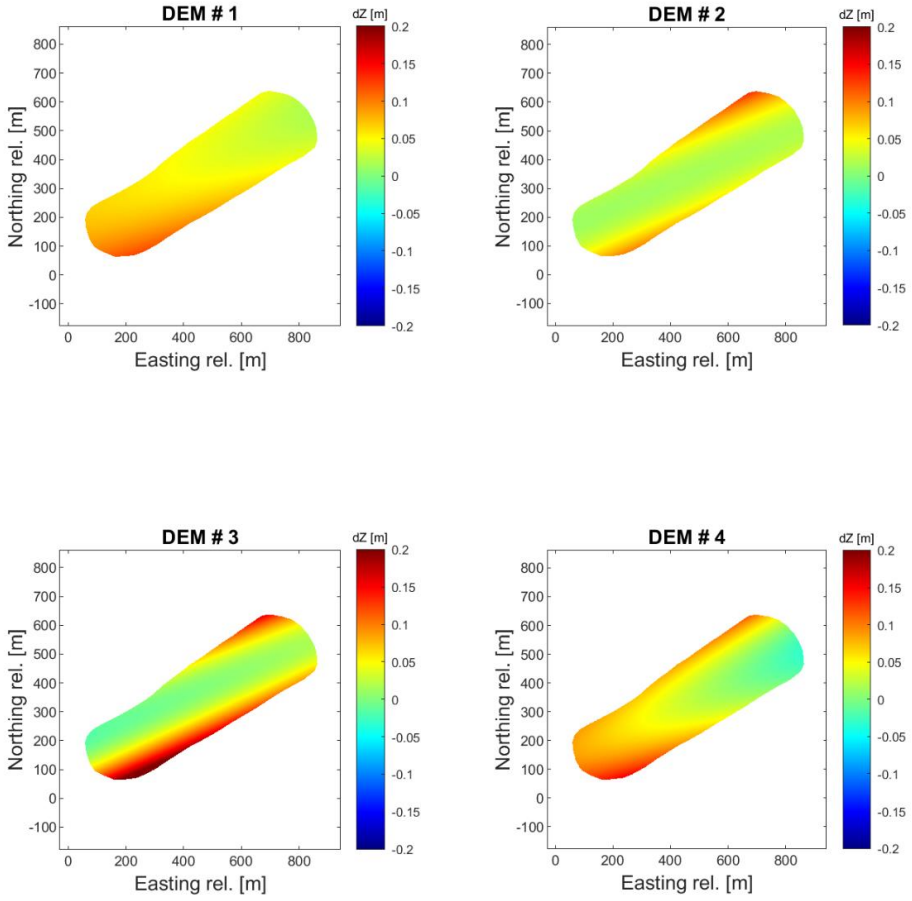

Figure IV-19 (Figure A2 in article): Error model for each DEM. The systematic error is given in meters. The surface shown is dZ = DEMcorrected-DEMoriginal in meters.

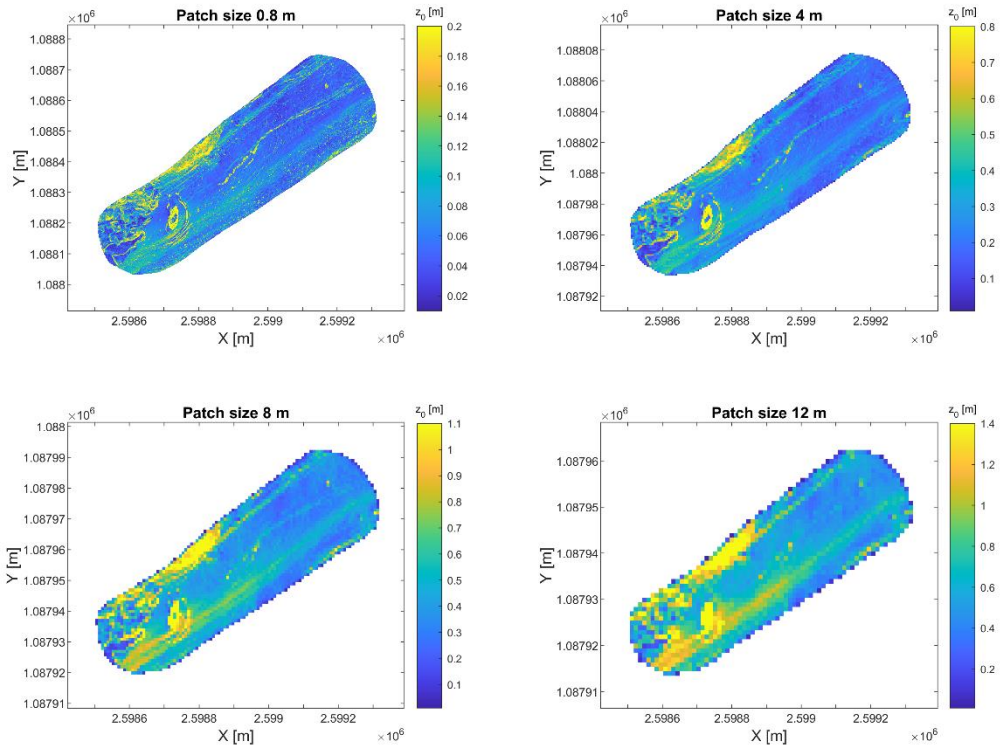

Figure IV-20 (Figure A3 in article): Surface roughness computed at different spatial scales. The scale of 0.8 m was used for the statistical analysis.

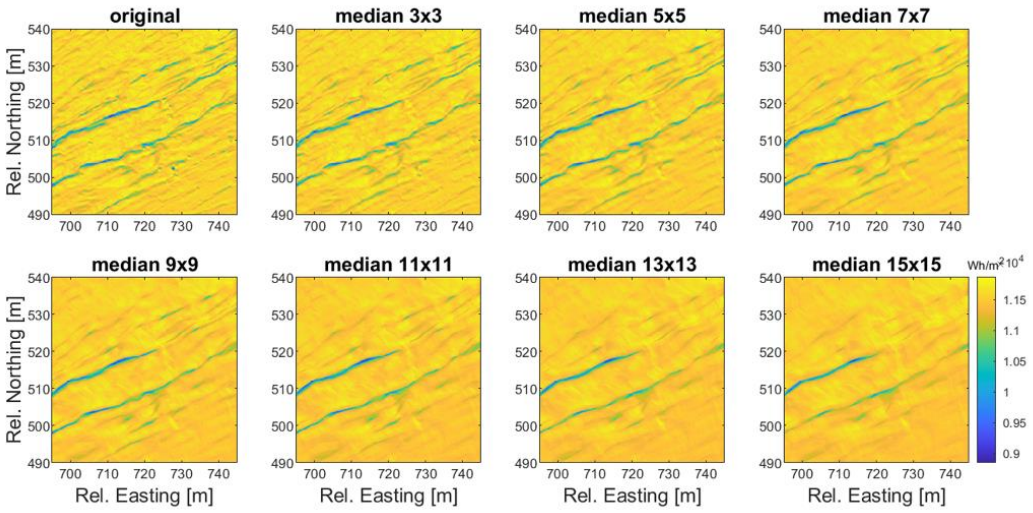

Figure IV-21 (Figure A4 in article): Solar radiation over one day (12.08.2018) shown for patch 1 for different degrees of smoothing of the DEM: Median filters of 3x3 to 15x15 cells were applied to the original DEM.

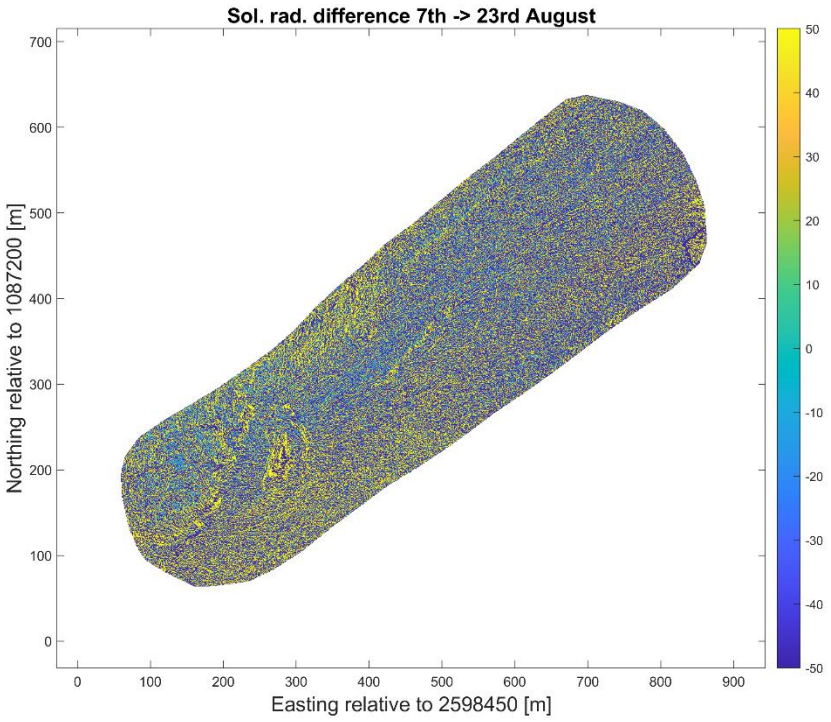

Figure IV-22 (Figure A5 in article): Difference between solar radiation computed for the 7th and the 23rd of August 2018

Table IV-8 (Table A1 in article): Statistics of fitting a stepwise linear model to DoD1.

p-value	1	2	3	4	5	6	7	8	9	10
solar radiation	0,0E+00	0,0E+00	0,0E+00	0,0E+00	1,2E-82	0,0E+00	0,0E+00		1,7E-40	
flow accumulation	8,6E-09	1,6E-42	1,6E-01	2,4E-10	1,5E-146	7,6E-15	3,9E-38	1,5E-01	1,2E-03	2,5E-54
surface roughness					1,8E-34			0,0E+00	0,0E+00	4,7E-07
reflectance		0,0E+00	0,0E+00				4,0E-13	0,0E+00		1,7E-96
std. dev. (error)	**1**	**2**	**3**	**4**	**5**	**6**	**7**	**8**	**9**	**10**
solar radiation	0,0064	0,0070	0,0116	0,0069	0,0084	0,0055	0,0052		0,0143	
flow accumulation	0,0029	0,0045	0,0113	0,0035	0,0060	0,0031	0,0053	0,0062	0,0054	0,0393

surface roughness					0,0037			0,0043	0,0041	0,0613
reflectance		0,0022	0,0038				0,0021	0,0031		0,0322
coefficients	**1**	**2**	**3**	**4**	**5**	**6**	**7**	**8**	**9**	**10**
solar radiation	-0,824	-0,520	0,883	-0,494	0,162	-0,831	0,220		-0,190	
flow accumulation	0,016	0,062	0,016	0,022	-0,156	0,024	-0,068	-0,009	-0,017	0,611
surface roughness					-0,045			-0,308	0,280	0,309
reflectance		0,096	0,303				0,015	0,155		-0,673
variable used / rejected	**1**	**2**	**3**	**4**	**5**	**6**	**7**	**8**	**9**	**10**
solar radiation	1	1	1	1	1	1	1		1	
flow accumulation	1	1	0	1	1	1	1	0	1	1
surface roughness					1			1	1	1
reflectance		1	1				1	1		1

Table IV-9 (table A2 in article): Correlation between solar radiation and ablation (DoD) for different degrees of surface smoothing (2D median filter with a window size of 3x3, 5x5, … ,15x15 cells), computed for DoD2. Lines with red font have decreasing absolute values of correlation with increasing smoothing, while blue font highlights increasing correlation with increasing smoothing. Lines with black font show no significant change in correlation.

	For DoD_2	window size of median filter (# cells)						
patch #	**raw DEM**	**3x3**	**5x5**	**7x7**	**9x9**	**11x11**	**13x13**	**15x15**
1	-0,393	-0,377	-0,375	-0,370	-0,363	-0,349	-0,327	-0,291

2	-0,291	-0,265	-0,270	-0,272	-0,268	-0,261	-0,254	-0,248
3	0,167	0,323	0,315	0,303	0,282	0,251	0,221	0,199
4	-0,203	-0,195	-0,200	-0,213	-0,228	-0,235	-0,228	-0,223
5	0,116	0,108	0,130	0,152	0,184	0,217	0,247	0,274
6	-0,479	-0,463	-0,462	-0,462	-0,459	-0,458	-0,454	-0,443
7	0,172	0,219	0,194	0,154	0,119	0,093	0,083	0,082
8	0,052	0,118	0,111	0,102	0,096	0,091	0,080	0,070
9	-0,047	-0,049	-0,067	-0,079	-0,081	-0,079	-0,074	-0,071
10	0,057	0,064	0,070	0,075	0,081	0,087	0,092	0,097

Table IV-10 (Table A3 in article): Correlation between solar radiation and ablation (DoD) for different degrees of surface smoothing (2D median filter with a window size of 3x3, 5x5, … ,15x15 cells), computed for DoD2. Lines with red font have decreasing absolute values of correlation with increasing smoothing, while blue font highlights increasing correlation with increasing smoothing. Lines with black font show no significant change in correlation.

	For DoD_3	window size of median filter (# cells)						
patch #	**raw DEM**	**3x3**	**5x5**	**7x7**	**9x9**	**11x11**	**13x13**	**15x15**
1	-0,359	-0,352	-0,348	-0,341	-0,330	-0,315	-0,292	-0,258
2	-0,262	-0,228	-0,234	-0,237	-0,233	-0,227	-0,221	-0,216
3	0,229	0,383	0,371	0,355	0,334	0,299	0,259	0,218
4	-0,301	-0,296	-0,308	-0,330	-0,356	-0,373	-0,378	-0,383
5	0,102	0,094	0,118	0,145	0,182	0,219	0,251	0,278
6	-0,450	-0,430	-0,429	-0,430	-0,428	-0,427	-0,423	-0,413
7	0,151	0,195	0,178	0,150	0,129	0,112	0,106	0,106
8	0,039	0,124	0,120	0,113	0,110	0,106	0,090	0,073
9	-0,013	-0,006	-0,019	-0,031	-0,036	-0,037	-0,035	-0,034
10	0,103	0,079	0,084	0,084	0,078	0,084	0,090	0,097

IV.3.7 Data and code availability

The research data underlying this article can be accessed via the following permanent link: https://doi.org/10.5061/dryad.bg79cnpcq

IV.3.8 Author contribution

BB and PE collected the field data (investigation), SL acquired the funding. Conceptualization was done by all authors together initially, but PE had the lead in the final phase. Formal analysis was done by BB and PE with help by SL. Software for the statistical analyis and visualization was developed by PE. Validation was done by BB and PE with help from SL. Writing of the original draft was done by PE, with edits by SL. Project administration was handled by SL. Data curation was taken care of by PE.

IV.3.9 Competing interests

The authors declare that they have no conflict of interest.

IV.3.10 Acknowledgements

This project was funded by the Canton de Vaud of Switzerland and by Swiss National Science Funding grant 200021_188734 awarded to Lane. The authors thank the authorities of the municipality of Bagnes for granting access to the field site. No real or perceived financial conflicts of interest are present for this article. None of the authors has an affiliation that may present a conflict of interest for this article. Open access funding is provided by Université de Lausanne. The authors acknowledge Boris Ouvry (University of Zurich) for help with fieldwork and logistics.

IV.4 Wider implications

Despite extensive past research focusing on ablation processes and energy balance at the surface of temperate Alpine glaciers, the contribution of factors such as microtopography to local melt patterns was still poorly understood, and this chapter has started to fill that knowledge gap. The results of this article may have important implications on how we understand the evolution of supraglacial topography such as supraglacial channels over time.

As temperatures warm due to anthropogenic climate change, the elevation of equilibrium lines increases, and the ablation zones of glaciers worldwide will grow until a point where the ablation zone encompasses entire glaciers. As the proportion of the ablation zone increases, ablation processes become the single most important drivers of glacier recession. It is key to better understand how ablation is controlled in order to be able to predict glacier retreat more accurately. As glaciers retreat, glacier surfaces tend to become more rugged and heterogeneous, suggesting that the effects of microtopography, surface roughness and reflectance on melt are going to become more important as time progresses and the climate warms. Since some studies predict an increase in the proportion of dust and debris cover on Alpine glaciers as they retreat, insulation by debris cover and the effect of albedo may become more important, too, in the future.

A logical next step would be to perform a similar study with an even higher spatial (i.e., to 0.01-0.02 m horizontal resolution) and temporal (i.e., to daily time scale) resolution, while also measuring all the important meteorological variables needed to compute the energy balance. Such findings could be integrated into a spatially and temporally highly resolved surface energy balance model.

V CONCLUSIONS AND PERSPECTIVES

V.1 Synthesis of major research findings

This thesis aimed to improve our knowledge of ice melt at the margins of temperate Alpine glaciers by looking at them from both below and above. This required consideration of the geometry of subglacial channels that form at temperate Alpine glacier beds; their relationship with rapid glacier retreat due to channel melt-out and collapse; and surface patterns of melt on what is often a morphologically heterogenous surface.

Chapter II arrived at three major conclusions. First, as a means to answering wider scientific questions, the chapter showed that the planform geometry of subglacial channels close to glacier terminuses can be determined with the use of 3-D analysis of GPR data for ice thicknesses of at least 50 m, according to the GPR system used. Second, and following from this, results suggested (i) that subglacial channels in the vicinity of glacier margins are rather wide, shallow (> 12 m width for Glacier d'Otemma and > 10 m width for Haut Glacier d'Arolla) and often meandering, and (ii) that the glacier bed topography has an important control on the location and shape of subglacial channels in the ablation zone of temperate glaciers.

The latter finding has been evoked or hypothesized by earlier studies, involving both field studies and theoretical considerations (Röthlisberger, 1972; Shreve, 1972; Sharp et al., 1993). But so far very few studies have been able to show the influence of bed topography on the position and geometry of subglacial channels underneath temperate Alpine glaciers. Recent studies of the Greenland ice sheet and of the Antarctic ice shelf (paleo streams) obtained results similar to those described in Chapter II of this thesis, even at these larger spatial scales, indicating that bed topography may remain significant even under thicker ice cover (Livingstone et al., 2017; Simkins et al., 2021).

The width of the observed subglacial channels at Haut Glacier d'Arolla and Glacier d'Otemma usually exceeds 10 m and reaches up to 25 m for the uppermost GPR recordings at Glacier d'Otemma – something that has been confirmed by hot water drilling and inspection with a camera during fieldwork carried out by Matthew Jenkin of UNIL in summer 2021. The field inspections also showed that the channel was rather shallow (< 0.5 m height) and unpressurized during most of the day.

There is a contrast between channel geometry underneath the ice and the dimensions of the same channels when they flow in the proglacial margin after leaving the glacier. Our GPR results show that the subglacial channels are significantly wider than the single thread channels

observed in the proglacial margins of both Glacier d'Otemma (< 10 m) and Haut Glacier d'Arolla (< 6 m) (Perolo et al., 2019; Warburton, 1992). This suggests that subglacial snout marginal channels are likely to have different fluvial hydraulics than proglacial channels. They are very shallow and wide – up to 25 m as observed from GPR data (Chapter II and Chapter III) – and therefore very inefficient at transporting coarse sediment (White et al., 1975; Smart, 1984; Rickenmann, 1997). This may explain why small variations in discharge can lead to deposition under the ice close to the margin, as described by Perolo et al. (2019) for Haut Glacier d'Arolla.

Chapter III reaches three core findings. First, the collapse features at temperate Alpine glaciers in the Swiss Alps have become more frequent since 2000, but especially since 2015, associated with a strong increase in mean summer air temperature and an increase in glacier retreat rates for these glaciers. There was a delay of a little more than a decade between the onset of increased temperatures in the mid to late 1980s (when many Alpine glaciers in Switzerland were still advancing) and the increase in collapse frequency. This is likely because the 1960s and 1970s increase in ice accumulation compensated for temperature driven increases in ablation by maintaining an enhanced ice flux during this period (Zemp et al., 2008). Second, analysis suggested that the occurrence of collapse features is statistically related to reduced ice flux (nearly stagnating ice flow), shallow ice in the vicinity of the collapse features, reduced creep closure of the ice, a low-angle ice surface slope and the presence of a meandering subglacial channel immediately underneath the collapse features. Third, and drawing upon data collected in relation to Chapter II, the mechanisms leading to a collapse feature were found to be likely related to lateral erosion of a major and meandering subglacial channel due to water friction and sediment erosion, low creep closure of that channel due to shallow and stagnating ice, melt-out of the channel by turbulent heat exchange due to the incursion of warm air (connection between terminus and glacier surface via cracks in the glacier surface), 'block caving' inside the subglacial channel, evacuation of ice blocks towards the glacier terminus, and eventual break-up of the ice surface leading to even faster melt-out due to solar radiation and more block caving. Although these conclusions cannot yet be definitive, Chapter III provided the first study that was able to prove (not only hypothesize) that the position of a subglacial drainage channel in an Alpine glacier was directly related to where collapse features were forming. Recently, a study of ~1400 Esker enlargements at the locations of the Fennoscandian (Scandinavian Arctic) and Keewatin (northern Canada) paleo ice sheets hypothesized that these enlargements of former major subglacial channels correspond to the

location of collapse features that formed during the rapid retreat of the outlet glaciers of the ice sheet (Dewald et al., 2021). The inferred processes leading to collapse in that study are very similar, although at a larger scale, to the processes described in Chapter III, and thereby yield further support for the theory about mechanisms and conditions of rapid retreat leading to an increase in collapse events.

Two recent studies, mentioned in Chapter III (Kellerer-Pirklbauer & Kulmer, 2019; Stocker-Waldhuber et al., 2017) addressed collapse features in the Austrian Alps and suggest very similar mechanisms as those described in Chapter III. At Pasterze Glacier in the Glockner area of the Austrian Alps, Kellerer-Pirklbauer & Kulmer (2019) note that collapse features usually initiate in areas of stagnating and thinning ice dominated by thrust faults and normal faults, which lead to a disintegration of the glacier surface and enable the infiltration of water and air into the subglacial domain. They also mention the presence of subglacial cavities where block caving occurs, and they hypothesize that these cavities may be ultimately responsible for ice surface collapse (Kellerer-Pirklbauer & Kulmer, 2019). Although not explicitly mentioned in the study, it can be observed that the locations of depressions or collapse features seem to coincide with the position of a subglacial channel (Figure 2g and Figure 10 in Kellerer-Pirklbauer & Kulmer, 2019). Stocker-Waldhuber et al. (2017) observed how the position of a supraglacial collapse feature at Gepatschferner coincided with the presence of a meander bend in a subglacial channel, as is shown in Figure I-5 (Figure A3 in Stocker-Waldhuber et al., 2017). The flushing-out of large amounts of sediment during a storm event contributed to the collapse of the glacier surface. This study also reports collapse features at three more glaciers in the Austrian Alps, with similar characteristics to the one observed at Gepatschferner. Common observations to both Austrian studies are that collapse features coincide with the presence of a major subglacial cavity or channel, they always happen when the ice flux is nearly stagnating and when the glaciers are in a phase of rapid retreat. The findings from Chapter III corroborated these observations and showed more quantitatively how significant ice surface lowering takes place in the exact location of subglacial channels, and is not just due to ablation, but due to ice creep. Chapter III also provided for the first time a statistical comparison between glaciers with collapse features and glaciers without collapse features in recent years.

Whereas Chapters II and III looked at Alpine glaciers from below, Chapter IV considered an Alpine glacier from above, focusing on surface melt. Although consideration of ablation processes at the surface of Alpine glaciers is well-developed, new technologies provide new opportunities for quantifying this melt using remote sensing, specifically using UAV-SfM

photogrammetry, and especially if its application is correct. Chapter IV used rigorous UAV-SfM methods to make three scientific conclusions regarding what controls surface ablation for a temperate Alpine glacier. First, the impact of solar radiation on microtopography is a key driver of local ablation patterns where a glacier is now increasingly debris-covered. Second, surface roughness and albedo are secondary factors controlling ablation in most areas of the glacier surface. Third, supraglacial streams incised into the glacier surface can have a non-negligible influence on ablation patterns, and they notably generate an initial microtopography that will subsequently be further shaped and influenced by solar radiation and the two remaining variables. This work suggests that the spatial patterns of surface melt at Alpine glacier margins are likely more complex than hitherto described. Although there has been extensive research on the effect of incoming shortwave radiation on ablation (e.g., Pellicciotti et al., 2005), on the importance of albedo (e.g., Oerlemans & Knap, 1998), on surface roughness (e.g., Brock et al., 2006), on the effect of supraglacial streams (e.g., Pitcher et al., 2019) as well as about the effect of debris cover (e.g., Nicholson et al., 2018), there is not much literature available that compares the relative importance of these variables and quantifies it especially at a high spatial resolution.

A recent article about debris covered and debris free areas at Baltoro Glacier in the Karakoram also found that the influence of solar radiation on topography and shading may have been underestimated so far (Huo et al., 2021). Although debris covered glaciers function differently from the Alpine glacier investigated in this thesis, the effect of solar radiation on topography remains largely the same. Like the findings by Hopkinson et al. (2010) for a debris free glacier, Huo et al. (2021) acknowledge that a complex topography may enhance ablation for debris-covered areas. Since satellite data was used for this study, the calculations were done at a much coarser scale than in Chapter IV (DEM resolution was 0.2 x 0.2 m), with 30 x 30 m grid cells used in Huo et al. (2021) at Baltoro Glacier. Despite this coarser resolution the effect of topography for ablation was significant in the Baltoro study and it therefore corroborates the findings from Chapter IV.

There are numerous studies supporting the importance of surface roughness for ablation through the enhancement of turbulent fluxes within the atmospheric boundary layer (e.g., Steiner et al., 2019). One recent study at Hintereisferner in the Austrian Ötztal Alps shows how surface roughness on a bare ice surface increases as the ablation season progresses, with increasing influence on ablation processes as the microtopography becomes more important (Smith et al., 2020). This supports two findings in Chapter IV, namely the effect of solar radiation on the local microtopography and the importance of surface roughness for ablation. If

there are many studies confirming the importance of albedo for variability in melt (e.g., Nakawo & Young, 1999), there are much fewer studies examining the effect of supraglacial channels on the evolution of macro- and microtopography and on melt (Isenko et al., 2005; Irvine-Fynn et al., 2011; Karlstrom et al., 2013), and the study presented in Chapter IV contributes to filling this gap.

The analysis in Chapter IV successfully compared and evaluated the importance of four variables on the glacier surface for melt. When looking at existing studies it becomes obvious that the relative importance of each of these variables for ablation had rarely been assessed before, especially at a high spatial and temporal resolution.

V.2 Future research needs

Newly raised scientific questions following from the findings of this thesis, as well as proposed future research are identified in this section. In a first part, the detailed study of subglacial channel geometry in space and time with GPR and additional methods is discussed. In the second part, open questions and proposed research on surface collapse features and their relationship with sub- and supraglacial processes is presented. And finally, research needs and proposed future research related to ablation processes at the glacier surface and their relationship with rapid glacier retreat and collapse features are outlined.

V.2.1 Geometry and hydraulics of subglacial channels

V.2.1.1 Large-scale mapping of subglacial channels with GPR

This thesis has investigated the planform geometry of subglacial channels for Alpine glaciers. Because measurements were carried out manually on foot, the area of interest on each glacier remained relatively small compared to the size of the entire ablation area. Now the research needs involve obtaining a larger-scale picture of subglacial channels in the ablation zone of temperate Alpine glaciers. This would improve the understanding of subglacial hydrology (Church et al., 2021), especially the efficiency of water and sediment evacuation, and it may significantly contribute to improving glacio-hydrological models (Werder et al., 2013; Beaud et al., 2018). To obtain such knowledge, the objective should be to perform similar GPR measurements to those presented in Chapter II, but spanning over large parts of the ablation zone and which can be repeated on a weekly or monthly time scale to gain a bigger picture of

channel geometry and of the evolution of subglacial channels through time. UAV-based GPR surveys are the perfect solution for this, as we will see below.

New research in the field of GPR-based detection of subglacial channels underneath temperate Alpine glaciers is already happening and further campaigns are planned. The logical continuation of the fieldwork being done at Glacier d'Otemma in the summers of 2017 and 2018 is to mount a similar radar antenna onto an UAV and thereby cover a larger proportion of the ablation zone at higher precision with the same type of measurements. The first trials for this type of survey have already been carried out in summer 2021 by University of Lausanne PhD students Bastien Ruols and Johanna Klahold, who are working with Dr. James Irving. It would be extremely valuable to record high-resolution GPR data over the entire ablation zone, at least to an ice depth of 100 m. This is roughly the depth limit for the real-time-sampling Radarteam® GPR system used in our studies (Chapter II) because of a fixed listening time of 1600 ns. Although this listening time could be increased easily in other systems, limits to data quality and resolution will occur as the depth increases, making the detection of channel features of a width of 10-25 m challenging. Nevertheless, even in shallow ice zones a lot can be learned about subglacial channels, both about their 3-D geometry and about their evolution in time (4-D GPR). Ultimately such research will lead to more realistic 3D-models of the sub- and englacial drainage systems, and possibly their evolution over the time scale of weeks to years. This will benefit the design and testing of glacio-hydrological models and potentially allow for a much more realistic representation of subglacial drainage processes.

V.2.1.2 Detailed 3D geometry of subglacial channels, and validation of GPR data

A next step would be to map subglacial channels in 3D and with greater detail in order to be able to quantify hydraulic parameters such as the perimeter, hydraulic radius, cross-section and the surface roughness inside the channel. This would enable us to better quantify flow velocities inside such channels, improve sediment transport estimations and integrate this knowledge into the design and parameterization of glacio-hydrological models.

A technically difficult, but methodologically straightforward and interesting field campaign for a major subglacial channel underneath a temperate glacier would involve portable LiDAR scans and hydraulic modelling similar to what has been done for a polythermal arctic glacier in Svalbard, Norway (Chen et al., 2018). This would involve using a portable Light Detection and Ranging (LiDAR) to manually scan a portion of a major subglacial channel underneath a temperate Alpine glacier, positioning reflective metal targets on the inside and 3-D UAV targets

on the outside of the channel, and connecting the scan to a UAV survey of the glacier surface via these targets. As a new and novel part compared to the study by Chen et al. (2018), a gridded high-resolution GPR survey (using an UAV carrying a radar antenna) could be executed nearly simultaneously to cover the same channel. The targets in the inside of the channel can be detected in the GPR survey. Such a setup would make it possible to validate GPR surveys of subglacial channels in temperate ice reliably, and at the same time it would provide a large amount of precious information about the surface roughness inside a subglacial channel, about detailed geometry and about the effect of air and water on the radar signal in terms of reflection strength, amplitude changes, phase change and radar wave velocity. Such a survey would have to be undertaken at the end of autumn or at the beginning of winter, to ensure that there is very little meltwater flowing in the subglacial channel, that ice dynamics are negligible and potential hazards due to falling ice blocks or breaking water pockets are very small due to sub-zero air temperatures (at least at night), and low levels of incoming solar radiation. Ideally there would be no snow cover (or only a thin centimeter to decimeter layer) present on the glacier during this survey, so as not to impact radar measurements or to obstruct the entry way into the channel, which can be via a moulin or via the glacier terminus.

Once LiDAR data of the inside of the channel has been successfully collected, a 3-D hydrodynamics simulation (preferably LES – Large Eddy Simulation, see Bradbrook et al., 2000; Bates et al., 2005; Giometto et al., 2017) of water flow inside the subglacial channel could be performed to quantify the velocity, shear stress and water level for typical discharges observed at this glacier. This would allow determination of whether the subglacial channel is unpressurized most of the time (Egli et al., 2021b; Hooke et al., 1990) - by testing various discharges in the LES - or if there are periods of pressurization even close to the glacier snout, which would enable the spontaneous evacuation of sediment and which would explain why sediment transport is intermittent in this environment (Perolo et al., 2019). Depending on water level in the channel, the relative surface roughness will vary significantly, leading to very low flow velocities for low water levels (Gulley et al., 2012b; Mankoff et al., 2017).

V.2.2 Surface collapse features

V.2.2.1 Wider study of glacier surface collapse features

The next step in research about collapse features will be to collect and to analyze data over a wide range of temperate glaciers, potentially encompassing the entire Alps and part of the

Himalayas, or similar mountain ranges. The same analysis as presented in Chapter III (Egli et al., 2021b) could be reconducted for all glaciers where distributed ice thickness estimations and medium- to high-resolution surface DEMs are available. With such a sample size the results could become much more significant and conclusive, and it would be possible to learn more about the different conditions under which collapse features form. In such a study, at least half the glaciers would have to be glaciers without any collapse features since the beginning of satellite or aerial imaging in order to be able to compare two groups. But it would also be possible to compare data only for the past 10-20 years, since atmospheric warming has started to accelerate, and the geometry of the glaciers may not have changed significantly (e.g., from a low-gradient tongue to a steep tongue) over this short timescale. Thanks to such an assessment, the findings and hypotheses made in Chapter III could be further consolidated, partly rejected, or become more nuanced. Such a large-scale study would then make it possible to identify zones on a global scale where more such collapse features are likely to happen in the near future, further accelerating glacier retreat.

V.2.2.2 Detailed process-based study of collapse features

The detailed study of processes at Glacier d'Otemma in Chapter III involved inferences of processes thanks to calculations of creep closure and longitudinal ice flow velocity as well as measurements of surface lowering and melt, there were no measurements available to estimate sensible or latent heat exchange inside the cavity of the collapse feature. A future study could undertake such measurements, including wind speed, turbulence, air temperature, surface temperature and water temperature to estimate heat fluxes, similarly to previous studies undertaken at ice cliffs in the Nepal Himalayas (Brun et al., 2015; Buri et al., 2021; Buri et al., 2016a, 2016b; Steiner et al., 2015; Steiner et al., 2019; Watson et al., 2017). Such measurements would have to be undertaken in an already open collapse feature where the ceiling has collapsed, and the inside of the feature would have to be reached by rappelling down one of the more stable ice walls.

Subsequently, a detailed ice dynamics model at a local scale of a few tens to hundreds of meters could be set up (e.g., using the software Elmer/Ice; Gagliardini et al., 2011) to better understand the creep closure process above a large cavity and the critical thickness of the ice roof above a subglacial channel before a collapse occurs. Such a model would have to include 'block caving' and melt processes, as well as subglacial processes, possibly via calving parameterizations at a high spatial resolution. Results from the model could tell us for what sizes of subglacial cavities (channels) and for what ice thicknesses a collapse event is likely. This, in turn, would make it

possible to identify glaciers and zones on glacier tongues where such collapse features will form in the future. At the same time, such measurements and modelling will bring us closer to corroboration of the hypothesis that collapse features accelerate glacier retreat.

V.2.3 Surface ablation and its relationship with rapid glacier retreat

As mentioned above, the topics of the three articles are strongly interrelated. If the lateral erosion into ice inside a subglacial channel becomes extensive enough, and the channel ceiling starts to lower due to ice creep, there is a third process that significantly contributes to channel roof collapse, and that is ice surface ablation. In the discussion of the third article (Chapter IV) it was mentioned that in such situations (subsidence of the surface, deformation, …) ice topography changes, leading to a change in melt patterns and possibly a localized acceleration of melt due to the accumulation of dust in a depression (leading to a lower albedo) and due to a change in microtopography (e.g. aspect; an ice surface may suddenly be more, or less, exposed to solar radiation than before). In short, there are feedbacks between ice dynamics and surface ablation, and these may have been underestimated so far.

There are two ways to improve estimates of surface ablation: (a) gather better data that is more highly resolved both in space and time or (b) improve physical modelling of the energy balance at the glacier surface by representing individual processes more closely, and both are important. Therefore, it would be useful to conduct a combined study involving field data and physics-based modelling, with elevation data at a daily / centimeter scale collected either with a laser scanner directed with a right angle onto the glacier surface, or from high resolution UAV surveys (as done in Chapter IV, but with lower flying height and over a smaller surface area). Thereby, daily changes in surface topography could be mapped at even higher accuracy and precision than in Chapter IV, and the processes causing these changes would be modelled for the given surface, by computing the complete energy balance from day to day (including the backscattering of incoming shortwave radiation, and processes such as shading). To compute the energy balance very precisely a temporary automatic weather station (AWS) on the glacier very close to the study area is needed. The AWS should measure all the relevant variables, such as: Incoming and outgoing shortwave and longwave radiation, surface temperature, air temperature 2 m above the ground, wind speed 5 cm above the ground and 2 m above the ground, relative humidity, etc. These measurements should be done during a multi-day period with both clear sky and varying cloud cover, but without precipitation. The ultimate goal of

such a study would be to integrate the results into a highly resolved surface energy balance model that allows to estimate ablation at a high spatial and temporal resolution, but able to downscale the processes to lower resolutions if only a coarse DEM is available. Such a highly resolved surface energy balance model could help better understand local small-scale processes such as ice cliff backwasting or the formation and melt-out of surface collapse features.

An advanced application of the knowledge gained from both Chapters III and Chapter IV would be to design an integrated model of glacier snout retreat including both processes at the surface and underneath, at a high spatial and temporal resolution (e.g., decimeter scale and hourly scale). This could be achieved by following the example of models that quantify ice cliff melt-out on debris-covered Himalayan glaciers (Buri et al., 2016a,b), but additionally including sub- and englacial processes as well as local ice dynamics, such as it has been performed at a small scale for Tête Rousse Glacier (France) in 2010 (Gagliardini et al., 2011). This would help to improve our understanding of collapse features, but it may also lead to a more holistic understanding of processes driving ablation.

With this PhD thesis I hope to have contributed with new knowledge and methods in the fields of subglacial hydrology, internal melt and collapse features as well as surface ablation. I hope that this thesis has raised new research questions and encouraged more research being done to better understand the features, processes and methods discussed in this work and to address present and future challenges related to the rapid retreat of Alpine glaciers in the light of global warming.

VI REFERENCES

Adhikary, S., Yamaguchi, Y., & Ogawa, K. (2002). Estimation of snow ablation under a dust layer covering a wide range of albedo. Hydrological processes, 16(14), 2853-2865.

Ahlmann, H. W. S., and Thorarinsson, S. (1938). Chapter V. The Ablation. *Geografiska Annaler*, *20*(3-4), 171-233.

Alley, R. B. (1992). How can low-pressure channels and deforming tills coexist subglacially? Journal of Glaciology, 38(128), 200-207.

Alley, R. B., Cuffey, K. M., Evenson, E. B., Strasser, J. C., Lawson, D. E., and Larsonh, G. J. (1997). How glaciers entrain and transport basal sediment: Physical constraints. Quaternary Science Reviews, 16(9), 1017–1038.

Allroggen, N., Tronicke, J., Delock, M., and Böniger, U. (2015). Topographic migration of 2D and 3D ground-penetrating radar data considering variable velocities. Near Surface Geophysics, 13(3), 253-259.

Arcone, S. A. (2002). Airborne-radar stratigraphy and electrical structure of temperate firn: Bagley Ice Field, Alaska, USA. *Journal of Glaciology*, *48*(161), 317-334.

Arnold, N. (2005). Investigating the sensitivity of glacier mass-balance/elevation profiles to changing meteorological conditions: Model experiments for Haut Glacier d'Arolla, Valais, Switzerland. Arctic, Antarctic, and Alpine Research, 37, 139-145.

Arnold, N. S., Willis, I. C., Sharp, M. J., Richards, K. S., and Lawson, W. J. (1996). A distributed surface energy-balance model for a small valley glacier. I. Development and testing for Haut Glacier d'Arolla, Valais, Switzerland. *Journal of Glaciology*, *42*(140), 77-89.

Arnold, N., Richards, K., Willis, I., and Sharp, M. (1998). Initial results from a distributed, physically based model of glacier hydrology. *Hydrological Processes*, *12*(2), 191-219.

Azam, M. F., Wagnon, P., Vincent, C., Ramanathan, A. L., Favier, V., Mandal, A., and Pottakkal, J. G. (2014). Processes governing the mass balance of Chhota Shigri Glacier (western Himalaya, India) assessed by point-scale surface energy balance measurements. The Cryosphere, 8(6), 2195-2217.

Azzoni, R. S., Senese, A., Zerboni, A., Maugeri, M., Smiraglia, C., and Diolaiuti, G. A. (2016). Estimating ice albedo from fine debris cover quantified by a semi-automatic method: the case study of Forni Glacier, Italian Alps. The Cryosphere, 10(2), 665-679.

Bælum, K., and Benn, D. I. (2011). Thermal structure and drainage system of a small valley glacier (Tellbreen, Svalbard), investigated by ground penetrating radar. The Cryosphere, 5(1), 139-149.

Bamber, J. L., Layberry, R. L., and Gogineni, S. P. (2001). A new ice thickness and bed data set for the Greenland ice sheet: 1. Measurement, data reduction, and errors. *Journal of Geophysical Research: Atmospheres*, *106*(D24), 33773-33780.

Bartholomaus, T. C., Anderson, R. S., and Anderson, S. P. (2011). Growth and collapse of the distributed subglacial hydrologic system of Kennicott Glacier, Alaska, USA, and its effects on basal motion. Journal of Glaciology, 57, 985-1002.

Bash, E. A., Moorman, B. J., and Gunther, A. (2018). Detecting short-term surface melt on an Arctic glacier using UAV surveys. *Remote Sensing*, *10*(10), 1547.

Bash, E. A., and Moorman, B. J. (2020). Surface melt and the importance of water flow–an analysis based on high-resolution unmanned aerial vehicle (UAV) data for an Arctic glacier. *The Cryosphere*, *14*(2), 549-563.

Bates, P. D., Lane, S. N., and Ferguson, R. I. (2005). Computational fluid dynamics modelling for environmental hydraulics. *Computational Fluid Dynamics: Applications in Environmental Hydraulics*, 1.

Bauder, A., Funk, M., and Gudmundsson, G. H. (2003). The ice-thickness distribution of Unteraargletscher, Switzerland. *Annals of Glaciology*, *37*, 331-336.

Beaud, F., Flowers, G. E., and Venditti, J. G. (2018). Modeling sediment transport in ice-walled subglacial channels and its implications for esker formation and proglacial sediment yields. Journal of Geophysical Research: Earth Surface, 123(12), 3206-3227.

Beniston, M., Farinotti, D., Stoffel, M., Andreassen, L. M., Coppola, E., Eckert, N., ... and Vincent, C. (2018). The European mountain cryosphere: a review of its current state, trends, and future challenges. *The Cryosphere*, *12*(2), 759-794.

Benn, D., Gulley, J., Luckman, A., Adamek, A., and Glowacki, P. S. (2009a). Englacial drainage systems formed by hydrologically driven crevasse propagation. Journal of Glaciology, 55(191), 513-523.

Benn, D. I., Kristensen, L., and Gulley, J. D. (2009b). Surge propagation constrained by a persistent subglacial conduit, Bakaninbreen–Paulabreen, Svalbard. Annals of Glaciology, 50(52), pp.81-86.

Bentley, C., Glough, J., Jezek, K., and Shabtaie, S. (1979). Ice-thickness patterns and the dynamics of the Ross Ice Shelf, Antarctica. Journal of Glaciology, 24(90), 287-294. doi:10.3189/S0022143000014805

Bingham, R. G., and Siegert, M. J. (2007). Radio-echo sounding over polar ice masses. Journal of Environmental and Engineering Geophysics, 12(1), 47-62.

Booth, A. D., Linford, N. T., Clark, R. A., and Murray, T. (2008). Three-dimensional, multi-offset ground-penetrating radar imaging of archaeological targets. Archaeological Prospection, 15(2), 93-112.

Bosson, J. B., & Lambiel, C. (2016). Internal structure and current evolution of very small debris-covered glacier systems located in alpine permafrost environments. *Frontiers in Earth Science*, *4*, 39.

Bradbrook, K. F., Lane, S. N., Richards, K. S., Biron, P. M., and Roy, A. G. (2000). Large eddy simulation of periodic flow characteristics at river channel confluences. *Journal of Hydraulic Research*, *38*(3), 207-215.

Bradford, J. H., McNamara, J. P., Bowden, W., and Gooseff, M. N. (2005). Measuring thaw depth beneath peat-lined arctic streams using ground-penetrating radar. *Hydrological Processes: An International Journal*, *19*(14), 2689-2699.

Bradford, J. H., Nichols, J., Mikesell, T. D., and Harper, J. T. (2009). Continuous profiles of electromagnetic wave velocity and water content in glaciers: an example from Bench Glacier, Alaska, USA. *Annals of Glaciology*, *50*(51), 1-9.

Braithwaite, R. J. (2008). Temperature and precipitation climate at the equilibrium-line altitude of glaciers expressed by the degree-day factor for melting snow. Journal of Glaciology, 54(186), 437-444.

Braithwaite, R. J., and Hughes, P. D. (2022). Positive degree-day sums in the Alps: a direct link between glacier melt and international climate policy. Journal of Glaciology, 1-11.

Brock, B. W., Willis, I. C., and Sharp, M. J. (2000). Measurement and parameterization of albedo variations at Haut Glacier d'Arolla, Switzerland. Journal of Glaciology, 46(155), 675-688.

Brock, B. W., Willis, I. C., and Sharp, M. J. (2006). Measurement and parameterization of aerodynamic roughness length variations at Haut Glacier d'Arolla, Switzerland. Journal of Glaciology, 52(177), 281-297.

Brun, F., Wagnon, P., Berthier, E., Shea, J. M., Immerzeel, W. W., Kraaijenbrink, P. D., ... and Arnaud, Y. (2018). Ice cliff contribution to the tongue-wide ablation of Changri Nup Glacier, Nepal, central Himalaya. The Cryosphere, 12(11), 3439-3457.

Buri, P., Miles, E. S., Steiner, J. F., Immerzeel, W. W., Wagnon, P., and Pellicciotti, F. (2016a). A physically based 3-D model of ice cliff evolution over debris-covered glaciers. Journal of Geophysical Research: Earth Surface, 121(12), 2471-2493.

Buri, P., Miles, E. S., Steiner, J. F., Ragettli, S., and Pellicciotti, F. (2021). Supraglacial ice cliffs can substantially increase the mass loss of debris-covered glaciers. Geophysical Research Letters, 48(6), e2020GL092150.

Buri, P., Pellicciotti, F., Steiner, J. F., Miles, E. S., and Immerzeel, W. W. (2016b). A grid-based model of backwasting of supraglacial ice cliffs on debris-covered glaciers. Annals of Glaciology, 57(71), 199-211.

Carenzo, M., Pellicciotti, F., Rimkus, S., and Burlando, P. (2009). Assessing the transferability and robustness of an enhanced temperature-index glacier-melt model. Journal of Glaciology, 55(190), 258-274.

Cathles, L. M., Abbot, D. S., Bassis, J. N., and MacAyeal, D. R. (2011). Modeling surface-roughness/solar-ablation feedback: application to small-scale surface channels and crevasses of the Greenland ice sheet. Annals of Glaciology, 52(59), 99-108.

Chambers, J. R., Smith, M. W., Quincey, D.J., Carrivick, J. L., Ross, A. N., and James, M. R. (2020). Glacial aerodynamic roughness estimates: uncertainty, sensitivity, and precision in field measurements. Journal of Geophysical Research: Earth Surface, 125, e2019JF005167

Chen, Y., Liu, X., Gulley, J. D., and Mankoff, K. D. (2018). Subglacial conduit roughness: Insights from computational fluid dynamics models. Geophysical Research Letters, 45(20), 11-206.

Chiarle, M., Iannotti, S., Mortara, G., and Deline, P. (2007). Recent debris flow occurrences associated with glaciers in the Alps. *Global and Planetary Change*, *56*(1-2), 123-136.

Church, G., Bauder, A., Grab, M., Rabenstein, L., Singh, S., and Maurer, H. (2019). Detecting and characterising an englacial conduit network within a temperate Swiss glacier using active seismic, ground penetrating radar and borehole analysis. Annals of Glaciology, 1-13.

Church, G., Grab, M., Schmelzbach, C., Bauder, A., and Maurer, H. (2020). Monitoring the seasonal changes of an englacial conduit network using repeated ground-penetrating radar measurements. The Cryosphere, 14(10), 3269-3286.

Church, G., Bauder, A., Grab, M., and Maurer, H. (2021). Ground-penetrating radar imaging reveals glacier's drainage network in 3D. The Cryosphere, 15, 3975–3988,

Clayton, L. (1964). Karst topography on stagnant glaciers. Journal of Glaciology, 5(37), 107-112.

Conway, J. P., and Cullen, N. J. (2013). Constraining turbulent heat flux parameterization over a temperate maritime glacier in New Zealand. Annals of Glaciology, 54(63), 41-51.

Cook, J.C. (1960). Proposed monocycle-pulse very-high-frequency radar for air-borne ice and snow measurement. Transactions of the American Institute of Electrical Engineers, Part I: Communication and Electronics, 79(5), 588-594.

Corripio, J. G. (2004). Snow surface albedo estimation using terrestrial photography. International journal of remote sensing, 25(24), 5705-5729.

Costa, A., Molnar, P., Stutenbecker, L., Bakker, M., Silva, T. A., Schlunegger, F., ... and Girardclos, S. (2018). Temperature signal in suspended sediment export from an Alpine catchment. Hydrology and earth system sciences, 22, 509-528.

Cuffey, K. M., and Paterson, W. S. B. (2010). The physics of glaciers. Academic Press.

Cutler, P. M. (1998). Modelling the evolution of subglacial tunnels due to varying water input. Journal of Glaciology, 44, 485-497.

Davis, J. L., and Annan, A. P. (1989). Ground-penetrating radar for high-resolution mapping of soil and rock stratigraphy 1. Geophysical prospecting, 37(5), 531-551.

de Fleurian, B., Werder, M. A., Beyer, S., Brinkerhoff, D. J., Delaney, I. A. N., Dow, C. F., ... and Sommers, A. N. (2018). SHMIP The subglacial hydrology model intercomparison Project. Journal of Glaciology, 64(248), 897-916.

Dewald, N., Lewington, E. L., Livingstone, S. J., Clark, C. D., and Storrar, R. D. (2021). Distribution, characteristics and formation of esker enlargements. *Geomorphology*, *392*, 107919.

Dey, S., and Ali, S. Z. (2017). Origin of the onset of meandering of a straight river. Proceedings of the Royal Society A: Mathematical, Physical and Engineering Sciences, 473, Article number 20170376.

Diolaiuti, G., Kirkbride, M. P., Smiraglia, C., Benn, D. I., D'agata, C., and Nicholson, L. (2005). Calving processes and lake evolution at Miage glacier, Mont Blanc, Italian Alps. Annals of qGlaciology, 40, 207-214.

Diolaiuti, G. A., Maragno, D., D'Agata, C., Smiraglia, C., and Bocchiola, D. (2011). Glacier retreat and climate change: Documenting the last 50 years of Alpine glacier history from area and geometry changes of Dosde Piazzi glaciers (Lombardy Alps, Italy). Progress in Physical Geography, 35, 161-182.

Egli, P. E., Irving, J., and Lane, S. N. (2021a). Characterization of subglacial marginal channels using 3-D analysis of high-density ground-penetrating radar data. Journal of Glaciology, 67(264), 759-772.

Egli, P. E., Belotti, B., Ouvry, B., Irving, J., and Lane, S. N. (2021b). Subglacial channels, climate warming, and increasing frequency of Alpine glacier snout collapse. Geophysical Research Letters, 48(21), e2021GL096031.

Evans, S. (1967). Progress report on radio echo sounding. Polar Record, 13(85), 413-420.

Farinotti, D., Huss, M., Bauder, A., and Funk, M. (2009a). An estimate of the glacier ice volume in the Swiss Alps. Global and Planetary Change, 68(3), 225-231.

Farinotti, D., Huss, M., Bauder, A., Funk, M., and Truffer, M. (2009b). A method to estimate the ice volume and ice-thickness distribution of alpine glaciers. Journal of Glaciology, 55(191), 422-430.

Farinotti, D., Round, V., Huss, M., Compagno, L., and Zekollari, H. (2019). Large hydropower and water-storage potential in future glacier-free basins. *Nature*, *575*(7782), 341-344.

Finger, D., Heinrich, G., Gobiet, A., and Bauder, A. (2012). Projections of future water resources and their uncertainty in a glacierized catchment in the Swiss Alps and the subsequent effects on hydropower production during the 21st century. Water Resources Research, 48(2).

Fischer, A. (2009). Calculation of glacier volume from sparse ice-thickness data, applied to Schaufelferner, Austria. *Journal of Glaciology*, *55*(191), 453-460.

Fischer, U., and Hubbard, B. (1999). Subglacial sediment textures: Character and evolution at Haut Glacier d'Arolla, Switzerland. Annals of Glaciology, 28, 241-246.

Fischer, M., Huss, M., and Hoelzle, M. (2015). Surface elevation and mass changes of all Swiss glaciers 1980–2010. The Cryosphere, 9, 525-540.

Fitzpatrick, N., Radić, V., and Menounos, B. (2017). Surface energy balance closure and turbulent flux parameterization on a mid-latitude mountain glacier, Purcell Mountains, Canada. Frontiers in Earth Science, 5, 67.

Fountain, A. G., and Jacobel, R. W. (1997). Advances in ice radar studies of a temperate alpine glacier, South Cascade Glacier, Washington, USA. *Annals of Glaciology*, *24*, 303-308.

Fountain, A. G., and Walder, J. S. (1998). Water flow through temperate glaciers. Reviews of Geophysics, 36(3), 299-328.

Fountain, A. G., Jacobel, R. W., Schlichting, R., & Jansson, P. (2005). Fractures as the main pathways of water flow in temperate glaciers. *Nature*, *433*(7026), 618-621.

Gabbi, J., Farinotti, D., Bauder, A., and Maurer, H. (2012). Ice volume distribution and implications on runoff projections in a glacierized catchment. Hydrology and Earth System Sciences, 16(12), 4543-4556.

Gabbud, C., Micheletti, N., and Lane, S. N. (2015). Lidar measurement of surface melt for a temperate Alpine glacier at the seasonal and hourly scales. Journal of Glaciology, 61(229), 963-974.

Gades, A. M., Raymond, C. F., Conway, H., and Jagobel, R. W. (2000). Bed properties of Siple Dome and adjacent ice streams, West Antarctica, inferred from radio-echo sounding measurements. *Journal of Glaciology*, *46*(152), 88-94.

Gagliardini, O., Gillet-Chaulet, F., Durand, G., Vincent, C., and Duval, P. (2011). Estimating the risk of glacier cavity collapse during artificial drainage: The case of Tête Rousse Glacier. *Geophysical research letters*, *38*(10).

Gantayat, P., Kulkarni, A. V., and Srinivasan, J. (2014). Estimation of ice thickness using surface velocities and slope: case study at Gangotri Glacier, India. Journal of Glaciology, 60, 277-282.

Garambois, S., Legchenko, A., Vincent, C., and Thibert, E. (2016). Ground-penetrating radar and surface nuclear magnetic resonance monitoring of an englacial water-filled cavity in the polythermal glacier of Tête Rousse. *Geophysics*, *81*(1), WA131-WA146.

Geological Atlas of Switzerland (2020). http://www.map.geo.admin.ch

Gimbert, F., Nanni, U., Roux, P., Helmstetter, A., Garambois, S., Lecointre, A., ... and Walter, F. (2021). A multi-physics experiment with a temporary dense seismic array on the Argentière glacier, French Alps: The RESOLVE project. *Seismological Society of America*, *92*(2A), 1185-1201.

Gindraux, S., Boesch, R., and Farinotti, D. (2017). Accuracy assessment of digital surface models from unmanned aerial vehicles' imagery on glaciers. Remote Sensing, 9, Article number 186.

Giometto, M. G., Christen, A., Egli, P. E., Schmid, M. F., Tooke, R. T., Coops, N. C., and Parlange, M. B. (2017). Effects of trees on mean wind, turbulence and momentum exchange within and above a real urban environment. *Advances in Water Resources*, *106*, 154-168.

GLAMOS (1881-2020). The Swiss Glaciers 1880-2018/19, Glaciological Reports No 1-140, Yearbooks of the Cryospheric Commission of the Swiss Academy of Sciences (SCNAT), published since 1964 by VAW / ETH Zurich, doi:10.18752/glrep_series.

Glen, J. W. (1958). The flow law of ice: A discussion of the assumptions made in glacier theory, their experimental foundations and consequences. IASH Publ, 47(171), e183.

Glen, J. W., and Paren, J. G. (1975). The electrical properties of snow and ice. *Journal of Glaciology*, *15*(73), 15-38.

Glover, J. M., and Rees, H. V. (1992). Radar investigations of firn structures and crevasses. *Geol. Surv. Can. Pap*, 90-4.

Gobiet, A., Kotlarski, S., Beniston, M., Heinrich, G., Rajczak, J., and Stoffel, M. (2014). 21st century climate change in the European Alps—A review. Science of the Total Environment, 493, 1138-1151.

Goodman, R. H. (1975). Radio echo sounding on temperate glaciers. *Journal of glaciology*, *14*(70), 57-69.

Goodsell, B., Hambrey, M. J., and Glasser, N. F. (2002). Formation of band ogives and associated structures at Bas Glacier d'Arolla, Valais, Switzerland. *Journal of Glaciology*, *48*(161), 287-300.

Gogineni, S., Chuah, T., Allen, C., Jezek, K., and Moore, R. K. (1998). An improved coherent radar depth sounder. *Journal of Glaciology*, *44*(148), 659-669.

Gogineni, S., Tammana, D., Braaten, D., Leuschen, C., Akins, T., Legarsky, J., ... and Jezek, K. (2001). Coherent radar ice thickness measurements over the Greenland ice sheet. Journal of Geophysical Research: Atmospheres, 106(D24), 33761-33772.

Grab, M., Mattea, E., Bauder, A., Huss, M., Rabenstein, L., Hodel, E., ... and Maurer, H. (2021). Ice thickness distribution of all Swiss glaciers based on extended ground-penetrating radar data and glaciological modeling. Journal of Glaciology, First View: 1-19.

Grasmueck, M., Weger, R., and Horstmeyer, H. (2005). Full-resolution 3D GPR imaging. Geophysics, 70(1), K12-K19.

Gulley, J. (2009). Structural control of englacial conduits in the temperate Matanuska Glacier, Alaska, USA. *Journal of Glaciology*, *55*(192), 681-690.

Gulley, J. D., Spellman, P. D., Covington, M. D., Martin, J. B., Benn, D. I., and Catania, G. (2014). Large values of hydraulic roughness in subglacial conduits during conduit enlargement: implications for modeling conduit evolution. Earth Surf. Process. Landforms, 39: 296–310. doi:10.1002/esp.3447

Gulley, J. D., Grabiec, M., Martin, J. B., Jania, J., Catania, G., and Glowacki, P. (2012a). The effect of discrete recharge by moulins and heterogeneity in flow-path efficiency at glacier beds on subglacial hydrology. Journal of Glaciology, 58(211), 926–940.

Gulley, J. D., Walthard, P., Martin, J., Banwell, A. F., Benn, D. I., and Catania, G. (2012b). Conduit roughness and dye-trace breakthrough curves: why slow velocity and high dispersivity may not reflect flow in distributed systems. Journal of Glaciology, 58(211), 915–925.

Haeberli, W., and Hölzle, M. (1995). Application of inventory data for estimating characteristics of and regional climate-change effects on mountain glaciers: a pilot study with the European Alps. Annals of Glaciology, 21, 206-212.

Haeberli, W., Hoelzle, M., Paul, F., and Zemp, M. (2007). Integrated monitoring of mountain glaciers as key indicators of global climate change: the European Alps. Annals of Glaciology, 46, 150-160.

Haeberli, W., and Weingartner, R. (2020). In full transition: Key impacts of vanishing mountain ice on water-security at local to global scales. *Water Security*, *11*, 100074.

Hambrey, M. J. (1977). Supraglacial drainage and its relationship to structure, with particular reference to Charles Rabots Bre, Okstindan, Norway. Norwegian Journal of Geography, Vol. 31, Issue 2, 69-77.

Harper, J. T., Bradford, J. H., Humphrey, N. F., and Meierbachtol, T. W. (2010). Vertical extension of the subglacial drainage system into basal crevasses. *Nature*, *467*(7315), 579-582.

Hart, J. K., Rose, K. C., Clayton, A., and Martinez, K. (2015). Englacial and subglacial water flow at Skálafellsjökull, Iceland derived from ground penetrating radar, in situ Glacsweb probe and borehole water level measurements. *Earth Surface Processes and Landforms*, *40*(15), 2071-2083.

Herreid, S. (2021). What can thermal imagery tell us about glacier melt below rock debris?. Frontiers in Earth Science, 9, 738.

Herreid, S., and Pellicciotti, F. (2020). The state of rock debris covering Earth's glaciers. Nature Geoscience, 13(9), 621-627.

Hill, T., and Dow, C. F. (2021). Modeling the dynamics of supraglacial rivers and distributed meltwater flow with the Subaerial Drainage System (SaDS) model. *Journal of Geophysical Research: Earth Surface*, *126*(12), e2021JF006309.

Hill, T., Dow, C. F., Bash, E. A., and Copland, L. (2021). Application of an improved surface energy balance model to two large valley glaciers in the St. Elias Mountains, Yukon. *Journal of Glaciology*, *67*(262), 297-312.

Hock, R. (1999). A distributed temperature-index ice- and snowmelt model including potential direct solar radiation, J. Glaciol., 45(149), 101– 111.

Hock, R. (2005), Glacier melt: A review of processes and their modelling, Prog. Phys. Geogr., 29(3), 362– 391.

Hooke, R. (1984). On the role of mechanical energy in maintaining subglacial water conduits at atmospheric pressure. Journal of Glaciology, 30(105), 180–187.

Hooke, R. L. (1989). Englacial and subglacial hydrology: a qualitative review. *Arctic and Alpine Research*, *21*(3), 221-233.

Hooke, R. L., Laumann, T., and Kohler, J. (1990). Subglacial water pressures and the shape of subglacial conduits. Journal of Glaciology, 36, 67-71.

Hopkinson, C., Chasmer, L., Munro, S., and Demuth, M. N. (2010). The influence of DEM resolution on simulated solar radiation-induced glacier melt. Hydrological Processes: An International Journal, 24(6), 775-788.

Hubbard, B., and Nienow, P. (1997). Alpine subglacial hydrology. *Quaternary Science Reviews*, *16*(9), 939-955.

Hubbard, B., Sharp, M., Willis, I. C., Nielsen, M. K. and Smart, C. (1995). Borehole water-level variations and the structure of the subglacial hydrological system of Haut Glacier d'Arolla, Valais, Switzerland. Journal of Glaciology, 41(139), 572–583.

Huo, D., Bishop, M. P., Young, B., and Chi, Z. (2021). Modeling the feedbacks between surface ablation and morphological variations on debris-covered Baltoro Glacier in the central Karakoram. *Geomorphology*, *389*, 107840.

Huss, M. (2010). Mass balance of Pizolgletscher. *Geographica Helvetica*, *65*(2), 80-91.

Huss, M., Jouvet, G., Farinotti, D., and Bauder, A. (2010). Future high-mountain hydrology: a new parameterization of glacier retreat. Hydrology and Earth System Sciences, 14(5), 815-829.

IPCC, 2019: IPCC Special Report on the Ocean and Cryosphere in a Changing Climate [H.-O. Pörtner, D.C. Roberts, V. Masson-Delmotte, P. Zhai, M. Tignor, E. Poloczanska, K. Mintenbeck, A. Alegría, M. Nicolai, A. Okem, J. Petzold, B. Rama, N.M. Weyer (eds.)]. In press.

IPCC, 2021: Climate Change 2021: The Physical Science Basis. Contribution of Working Group I to the Sixth Assessment Report of the Intergovernmental Panel on Climate Change [MassonDelmotte, V., P. Zhai, A. Pirani, S. L. Connors, C. Péan, S. Berger, N. Caud, Y. Chen, L. Goldfarb, M. I. Gomis, M. Huang, K. Leitzell, E. Lonnoy, J. B. R. Matthews, T. K. Maycock, T. Waterfield, O. Yelekçi, R. Yu and B. Zhou (eds.)]. Cambridge University Press. In Press

Irvine-Fynn, T. D., Hodson, A. J., Moorman, B. J., Vatne, G., and Hubbard, A. L. (2011). Polythermal glacier hydrology: a review. *Reviews of Geophysics*, *49*(4).

Irvine-Fynn, T. D. L., Moorman, B. J., Williams, J. L. M., and Walter, F. S. A. (2006). Seasonal changes in ground-penetrating radar signature observed at a polythermal glacier, Bylot Island, Canada. *Earth Surface Processes and Landforms: The Journal of the British Geomorphological Research Group*, *31*(7), 892-909.

Isenko, E., and Mavlyudov, B. (2002). On the intensity of ice melting in supraglacial and englacial channels, Bull. Glaciol. Res., 19, 93– 99

Isenko, E., Narus, R., and Mavlyudov, B. (2005). Water temperature in englacial and supraglacial channels: Change along the flow and contribution to ice melting on the channel wall. Cold Regtions Science and Technology, 42, 53–62.

Jacobel, R. W., and Anderson, S. K. (1987). Interpretation of radio-echo returns from internal water bodies in Variegated Glacier, Alaska, USA. *Journal of Glaciology*, *33*(115), 319-323.

Jacobel, R., and Raymond, C. (1984). Radio echo-sounding studies of englacial water movement in Variegated Glacier, Alaska. *Journal of Glaciology*, *30*(104), 22-29.

James, M. R., Antoniazza, G., Robson, S., and Lane, S. N. (2020). Mitigating systematic error in topographic models for geomorphic change detection: accuracy, precision and considerations beyond off-nadir imagery. Earth Surface Processes and Landforms, 45(10), 2251-2271.

James, M. R., Chandler, J. H., Eltner, A., Fraser, C., Miller, P. E., Mills, J. P., ... and Lane, S. N. (2019). Guidelines on the use of structure-from-motion photogrammetry in geomorphic research. Earth Surface Processes and Landforms, 44(10), 2081-2084.

James, M. R., Robson, S., and Smith, M. W. (2017). 3-D uncertainty-based topographic change detection with structure-from-motion photogrammetry: Precision maps for ground control and directly georeferenced surveys. Earth Surface Processes and Landforms, 42(12), 1769-1788.

Jarque, C. M., and Bera, A. K. (1980). Efficient tests for normality, homoscedasticity and serial independence of regression residuals. Economics Letters, 6, 255–259

Jouvet, G., and Huss, M. (2019). Future retreat of great Aletsch glacier. Journal of Glaciology, 65(253), 869-872.

Jouvet, G., Huss, M., Funk, M., and Blatter, H. (2011). Modelling the retreat of Grosser Aletschgletscher, Switzerland, in a changing climate. Journal of Glaciology, 57(206), 1033-1045.

Kääb, A., Leinss, S., Gilbert, A., Bühler, Y., Gascoin, S., Evans, S. G., ... and Yao, T. (2018). Massive collapse of two glaciers in western Tibet in 2016 after surge-like instability. *Nature Geoscience*, *11*(2), 114-120.

Kamintzis, J. E., Irvine-Fynn, T. D. L., Holt, T. O., Jones, J. P. P., Tooth, S., Griffiths, H. M., and Hubbard, B. (2019). Knickpoint evolution in a supraglacial stream. Geografiska Annaler: Series A, Physical Geography, 101(2), 118-135.

Karlstrom, L., Gajjar, P., and Manga, M. (2013). Meander formation in supraglacial streams. Journal of Geophysical Research: Earth Surface, 118(3), 1897-1907.

Kellerer-Pirklbauer, A., and Kulmer, B. (2019). The evolution of brittle and ductile structures at the surface of a partly debris-covered, rapidly thinning and slowly moving glacier in 1998–2012 (Pasterze Glacier, Austria), Earth Surface Processes and Landforms, 44, 1034-1049.

Kohler, J. (1995). Determining the extent of pressurized flow beneath Storglaciären, Sweden, using results of tracer experiments and measurements of input and output discharge. Journal of Glaciology, 41, 217-231.

Konrad, S. K. (1998). Possible outburst floods from debris-covered glaciers in the Sierra Nevada, California. Geografiska Annaler: Series A, Physical Geography, 80(3-4), 183-192.

Kovacs, A., Gow, A. J., and Morey, R. M. (1995). The in-situ dielectric constant of polar firn revisited. *Cold Regions Science and Technology*, *23*(3), 245-256.

Kuipers, H. (1957). A reliefmeter for soil cultivation studies. *netherlands Journal of Agricultural science*, *5*(4), 255-262.

Kulessa, B., Booth, A. D., Hobbs, A., and Hubbard, A. L. (2008). Automated monitoring of subglacial hydrological processes with ground-penetrating radar (GPR) at high temporal resolution: scope and potential pitfalls. Geophysical Research Letters, 35(24).

Kumar, L., Skidmore, A.K., and Knowles, E. (1997). Modelling topographic variation in solar radiation in a GIS environment. Int.J.Geogr.Info.Sys. 11(5), 475-497

Lane, S. N., and Nienow, P. W. (2019). Decadal-scale climate forcing of alpine glacial hydrological systems. Water Resources Research, 55(3), 2478-2492.

Lane, S. N., Bakker, M., Gabbud, C., Micheletti, N., and Saugy, J. N. (2017). Sediment export, transient landscape response and catchment-scale connectivity following rapid climate warming and Alpine glacier recession. Geomorphology, 277, 210-227.

Lane, S. N., Westaway, R. M., and Murray Hicks, D. (2003). Estimation of erosion and deposition volumes in a large, gravel-bed, braided river using synoptic remote sensing. Earth Surface Processes and Landforms: The Journal of the British Geomorphological Research Group, 28, 249-271.

Langhammer, L., Rabenstein, L., Bauder, A., and Maurer, H. (2017). Ground-penetrating radar antenna orientation effects on temperate mountain glaciers. Geophysics, 82(3), H15-H24.

Lapazaran, J. J., Otero, J., Martín-Español, A., and Navarro, F. J. (2016). On the errors involved in ice-thickness estimates I: ground-penetrating radar measurement errors. Journal of Glaciology, 62(236), 1008-1020.

Layberry, R. L., and Bamber, J. L. (2001). A new ice thickness and bed data set for the Greenland ice sheet: 2. Relationship between dynamics and basal topography. *Journal of Geophysical Research: Atmospheres*, *106*(D24), 33781-33788.

Lindström, E. (1993), Esker enlargements in Northern Sweden, Geografiska Annaler: Series A, Physical Geography, 75, 95-110

Loewe, F. (1957). Subglacial stoping or block caving. Journal of Glaciology, 3, 152-152.

Mair, D., Willis, I., Fischer, U. H., Hubbard, B., Nienow, P., and Hubbard, A. (2003). Hydrological controls on patterns of surface, internal and basal motion during three"spring events": Haut Glacier d'Arolla, Switzerland. Journal of Glaciology, 49(167), 555–567.

Mair, D. W., Nienow, P., Sharp, M. J., Wohlleben, T. and Willis, I. C. (2002a). Influence of subglacial drainage system evolution on glacier surface motion: Haut Glacier d'Arolla, Switzerland. Journal of Geophysical Research, 107(B8).

Mair, D. W., Sharp, M. J., and Willis, I. C. (2002b). Evidence for basal cavity opening from analysis of surface uplift during a high-velocity event: Haut Glacier d'Arolla, Switzerland. Journal of Glaciology, 48(161), 208-216.

Mankoff, K. D., Gulley, J. D., Tulaczyk, S. M., Covington, M. D., Liu, X., Chen, Y., Benn, D. I., and GŁowacki, P. S. (2017). Roughness of a subglacial conduit under Hansbreen, Svalbard. Journal of Glaciology, 63(239), 423-435.

Mann, H. B., Whitney, D. R. (1947). On a test of whether one of two Random variables is stochastically larger than the other. Annals of Mathematical Statistics, 18, 50–60.

Mantelli, E., Camporeale, C., and Ridolfi, L. (2015). Supraglacial channel inception: Modeling and processes. *Water Resources Research*, *51*(9), 7044-7063.

Marchi, L., Arattano, M., and Deganutti, A. M. (2002). Ten years of debris-flow monitoring in the Moscardo Torrent (Italian Alps). *Geomorphology*, *46*(1-2), 1-17.

Margreth, S., Funk, M., Tobler, D., Dalban, P., Meier, L., and Lauper, J. (2017). Analysis of the hazard caused by ice avalanches from the hanging glacier on the Eiger west face. *Cold Regions Science and Technology*, *144*, 63-72.

Marzeion, B., Kasser, G., Maussion, F., and Champollion, N. (2018). Limited influence of climate change mitigation on short-term glacier mass loss. Nature Climate Change 8, 305–308.

Mavlyudov, B. R. (2005). Glacial karst as possible reason of quick degradation of Scandinavian glacier sheet. *Glacier caves and glacial karst in high mountains and polar regions. Ed. BR Mavlyudov*, 68-73.

Messerli, A., and Grinsted, A. (2015). Image georectification and feature tracking toolbox: ImGRAFT. Geoscientific Instrumentation, Methods and Data Systems, 4, 23-34.

Millan, R., Mouginot, J., Rabatel, A., Jeong, S., Cusicanqui, D., Derkacheva, A., and Chekki, M. (2019). Mapping surface flow velocity of glaciers at regional scale using a multiple sensors approach. Remote Sensing, 11, 2498.

Mölg, T., and Hardy, D. R. (2004). Ablation and associated energy balance of a horizontal glacier surface on Kilimanjaro. Journal of Geophysical Research: Atmospheres, 109(D16).

Moorman, B. J., and Michel, F. A. (2000). Glacial hydrological system characterization using ground-penetrating radar. *Hydrological Processes*, *14*(15), 2645-2667.

Moran, M. L., Greenfield, R. J., and Arcone, S. A. (2003). Modeling GPR radiation and reflection characteristics for a complex temperate glacier bed. Geophysics, 68(2), 559-565.

Morlighem, M., Williams, C. N., Rignot, E., An, L., Arndt, J. E., Bamber, J. L., ... and Zinglersen, K. B. (2017). BedMachine v3: Complete bed topography and ocean bathymetry mapping of Greenland from multibeam echo sounding combined with mass conservation. *Geophysical research letters*, *44*(21), 11-051.

Munro, D. S. (1989). Surface roughness and bulk heat transfer on a glacier: Comparison with eddy correlation. Journal of Glaciology, 35(121), 343– 348

Murray, T., Booth, A., and Rippin, D. M. (2007). Water-content of glacier-ice: Limitations on estimates from velocity analysis of surface ground-penetrating radar surveys. Journal of Environmental & Engineering Geophysics, 12(1), 87-99.

Murray, T., Stuart, G. W., Fry, M., Gamble, N. H., and Crabtree, M. D. (2000a). Englacial water distribution in a temperate glacier from surface and borehole radar velocity analysis. Journal of Glaciology, 46(154), 389-398.

Murray, T., Stuart, G. W., Miller, P. J., Woodward, J., Smith, A. M., Porter, P. R., and Jiskoot, H. (2000b). Glacier surge propagation by thermal evolution at the bed. *Journal of Geophysical Research: Solid Earth*, *105*(B6), 13491-13507.

Nakawo, M., and Rana, B. (1999). Estimate of ablation rate of glacier ice under a supraglacial debris layer. *Geografiska Annaler: Series A, Physical Geography*, *81*(4), 695-701.

Nakawo, M., Yabuki, H., and Sakai, A. (1999). Characteristics of Khumbu Glacier, Nepal Himalaya: recent change in the debris-covered area. *Annals of Glaciology*, *28*, 118-122.

Narod, B. B., and Clarke, G. K. C. (1980). Airborne UHF radio echo-sounding of three Yukon glaciers. *Journal of Glaciology*, *25*(91), 23-32.

Narod, B. B., and Clarke, G. K. (1994). Miniature high-power impulse transmitter for radio-echo sounding. *Journal of Glaciology*, *40*(134), 190-194.

Navarro, F. J., Macheret, Y. Y., and Benjumea, B. (2005). Application of radar and seismic methods for the investigation of temperate glaciers. *Journal of Applied Geophysics, 57*(3), 193-211.

Nicholson, L., and Benn, D. I. (2006). Calculating ice melt beneath a debris layer using meteorological data. Journal of Glaciology, 52(178), 463-470.

Nicholson, L. I., McCarthy, M., Pritchard, H. D., and Willis, I. (2018). Supraglacial debris thickness variability: impact on ablation and relation to terrain properties. *The Cryosphere, 12*(12), 3719-3734.

Nienow, P., Sharp, M., and Willis, I. (1996). Temporal switching between englacial and subglacial drainage pathways: Dye tracer evidence from the Haut Glacier d'Arolla, Switzerland. Geografiska Annaler. Series A, Physical Geography, 78(1), 51.

Nienow, P., Sharp, M., and Willis, I. (1998). Seasonal changes in the morphology of the subglacial drainage system, Haut Glacier d'Arolla, Switzerland. Earth Surface Processes and Landforms, 23, 825-843.

Nigrelli, G., and Chiarle, M. (2021). Evolution of temperature indices in the periglacial environment of the European Alps in the period 1990–2019. Journal of Mountain Science, 18(11), 2842-2853.

Nye, J. F. (1959). The motion of ice sheets and glaciers. Journal of Glaciology, 3(26), 493-507.

Nye, J. F. (1953). The flow law of ice from measurements in glacier tunnels, laboratory experiments and the Jungfraufirn borehole experiment. Proceedings of the Royal Society of London. Series A. Mathematical and Physical Sciences, 219, 477-489.

Oerlemans, J., and Klok, E. J. (2002). Energy balance of a glacier surface: analysis of automatic weather station data from the Morteratschgletscher, Switzerland. Arctic, Antarctic, and Alpine Research, 34(4), 477-485.

Oerlemans, J., and Knap, W. H. (1998). A 1 year record of global radiation and albedo in the ablation zone of Morteratschgletscher, Switzerland. Journal of Glaciology, 44, 231-238.

Östrem, G. (1959). Ice melting under a thin layer of moraine, and the existence of ice cores in moraine ridges. Geografiska Annaler, 41(4), 228-230.

Paige, R. (1956). Subglacial stoping or block caving: a type of glacier ablation. Journal of Glaciology, 2, 727-729.

Parker, G. (1975). Meandering of supraglacial melt streams. Water Resources Research, 11(4), 551-552.

Paul, F., Azzoni, R.S., Fugazza, D., Le Bris, R., Nemec, J., Paul, F., Rabatel, A., Ramusovic, M., Rastner, Ph., Schaub, Y., Schwaizer (née Bippus), G. (2019) GLIMS Glacier Database. Boulder, CO. National Snow and Ice Data Center. http://dx.doi.org/10.7265/N5V98602

Paul, F., Kääb, A., Maisch, M., Kellenberger, T., and Haeberli, W. (2004). Rapid disintegration of Alpine glaciers observed with satellite data. Geophysical Research Letters, 31, Article number 2004GL020816

Pellicciotti, F., Brock, B., Strasser, U., Burlando, P., Funk, M., and Corripio, J. (2005). An enhanced temperature-index glacier melt model including the shortwave radiation balance: development and testing for Haut Glacier d'Arolla, Switzerland. Journal of Glaciology, 51(175), 573-587.

Perolo, P., Bakker, M., Gabbud, C., Moradi, G., Rennie, C., and Lane, S.N. (2019). Subglacial sediment production and snout marginal ice uplift during the late ablation season of a temperate valley glacier. Earth Surface Processes and Landforms, 44(5), 1117-1136.

Pitcher, L. H., and Smith, L. C. (2019). Supraglacial streams and rivers. *Annual Review of Earth and Planetary Sciences*, *47*, 421-452.

Plewes, L.A., and Hubbard, B. (2001). A review of the use of radio-echo sounding in glaciology. Progress in Physical Geography, 25(2), 203-236.

Reinardy, B. T. I., Booth, A. D., Hughes, A. L. C., Boston, C. M., Åkesson, H., Bakke, J., Nesje, A., Giesen, R. H., and Pearce, D. M. (2019). Pervasive cold ice within a temperate glacier – implications for glacier thermal regimes, sediment transport and foreland geomorphology. The Cryosphere, 13, 827–843

Rickenmann, D. (1997). Sediment transport in Swiss torrents. Earth Surface Processes and Landforms: The Journal of the British Geomorphological Group, 22(10), 937-951.

Rippin, D. M., Pomfret, A., and King, N. (2015). High resolution mapping of supra-glacial drainage pathways reveals link between micro-channel drainage density, surface roughness and surface reflectance. Earth Surface Processes and Landforms, 40(10), 1279-1290.

Robin, G. D. Q. (1975). Velocity of radio waves in ice by means of a bore-hole interferometric technique. *Journal of Glaciology*, *15*(73), 151-159.

Rossini, M., Di Mauro, B., Garzonio, R., Baccolo, G., Cavallini, G., Mattavelli, M., ... and Colombo, R. (2018). Rapid melting dynamics of an alpine glacier with repeated UAV photogrammetry. Geomorphology, 304, 159-172.

Röthlisberger, H. (1972). Water pressure in intra- and subglacial channels. Journal of Glaciology, 11(62), 177–203.

Rutishauser, A., Maurer, H., and Bauder, A. (2016). Helicopter-borne ground-penetrating radar investigations on temperate alpine glaciers: A comparison of different systems and their abilities for bedrock mapping. Geophysics, 81(1), WA119-WA129.

Salzmann, N., Machguth, H., and Linsbauer, A. (2012). The Swiss Alpine glaciers' response to the global '2 C air temperature target'. Environmental Research Letters, 7(4), 044001.

Schaefli, B., Hingray, B., and Musy, A. (2007). Climate change and hydropower production in the Swiss Alps: quantification of potential impacts and related modelling uncertainties. Hydrology and Earth System Sciences, 11(3), 1191-1205.

Schaefli, B., Manso, P., Fischer, M., Huss, M., and Farinotti, D. (2019). The role of glacier retreat for Swiss hydropower production. *Renewable energy*, *132*, 615-627.

Schneider, W.A. (1978). Integral formulation for migration in two and three dimensions. Geophysics, 43(1), 49-76.

Schroeder, D. M., Bingham, R. G., Blankenship, D. D., Christianson, K., Eisen, O., Flowers, G. E., Karlsson, N. B., Koutnik, M. R., Paden, J. D., and Siegert, M. J. (2020). Five decades of radioglaciology. Annals of Glaciology, 1-13.

Schwanghart, W., Groom, G., Kuhn, N. J., and Heckrath, G. (2013). Flow network derivation from a high resolution DEM in a low relief, agrarian landscape. Earth Surface Processes and Landforms, 38(13), 1576-1586.

Schwanghart, W., and Scherler, D. (2014). TopoToolbox 2–MATLAB-based software for topographic analysis and modeling in Earth surface sciences. Earth Surface Dynamics, 2(1), 1-7.

Shabtaie, S., and Bentley, C. R. (1987). West Antarctic ice streams draining into the Ross Ice Shelf: configuration and mass balance. *Journal of Geophysical Research: Solid Earth*, *92*(B2), 1311-1336.

Shabtaie, S., and Bentley, C. R. (1988). Ice-thickness map of the West Antarctic ice streams by radar sounding. *Annals of glaciology*, *11*, 126-136.

Sharp, M., Richards, K., Willis, I., Arnold, N., Nienow, P., Lawson, W., and Tison, J. L. (1993). Geometry, bed topography and drainage system structure of the Haut Glacier d'Arolla, Switzerland. Earth Surface Processes and Landforms, 18(6), 557–571.

Shreve, R. L., (1972). Movement of water in glaciers. Journal of Glaciology, 11(62), 205–214.

Simkins, L. M., Greenwood, S. L., Munevar Garcia, S., Eareckson, E. A., Anderson, J. B., and Prothro, L. O. (2021). Topographic controls on channelized meltwater in the subglacial environment. *Geophysical Research Letters*, *48*(20), e2021GL094678.

Smart, G. M. (1984). Sediment transport formula for steep channels. *Journal of Hydraulic Engineering*, *110*(3), 267-276.

Smith, M. W. (2014). Roughness in the earth sciences. *Earth-Science Reviews*, *136*, 202-225.

Smith, M. W., Quincey, D. J., Dixon, T., Bingham, R.G., Carrivick, J. L., Irvine-Fynn, T. D. L., and Rippin, D. M. (2016). Aerodynamic roughness of glacial ice surfaces derived from high-resolution topographic data, J. Geophys. Res. Earth Surf., 121, 748– 766

Smith, T., Smith, M. W., Chambers, J. R., Sailer, R., Nicholson, L., Mertes, J., Quincey, D. J., Carrivick, J. L., and Stiperski, I. (2020). A scale-dependent model to represent changing aerodynamic roughness of ablating glacier ice based on repeat topographic surveys. *Journal of Glaciology*, *66*(260), 950-964.

Sommer, C., Malz, P., Seehaus, T. C., Lippl, S., Zemp, M., and Braun, M. H. (2020). Rapid glacier retreat and downwasting throughout the European Alps in the early 21 st century. Nature Communications, 11, 1-10.

Steenson, B.O. (1951). Radar methods for the exploration of glaciers (Doctoral dissertation, California Institute of Technology).

Steiner, J. F., Buri, P., Miles, E. S., Ragettli, S., and Pellicciotti, F. (2019). Supraglacial ice cliffs and ponds on debris-covered glaciers: spatio-temporal distribution and characteristics. Journal of Glaciology, 65(252), 617-632.

Steiner, J. F., Litt, M., Stigter, E. E., Shea, J., Bierkens, M. F., and Immerzeel, W. W. (2018). The importance of turbulent fluxes in the surface energy balance of a debris-covered glacier in the Himalayas. Frontiers in Earth Science, 144.

Steiner, J. F., Pellicciotti, F., Buri, P., Miles, E. S., Immerzeel, W. W., and Reid, T. D. (2015). Modelling ice-cliff backwasting on a debris-covered glacier in the Nepalese Himalaya. Journal of Glaciology, 61(229), 889-907.

St Germain, S. L., and Moorman, B. J. (2019). Long-term observations of supraglacial streams on an Arctic glacier. *Journal of Glaciology*, *65*(254), 900-911.

Stocker-Waldhuber, M., Fischer, A., Keller, L., Morche, D., and Kuhn, M. (2017). Funnel-shaped surface depressions—indicator or accelerant of rapid glacier disintegration? A case study in the Tyrolean Alps. Geomorphology, 287, 58-72.

Stolt, R. H., and Benson, A. (1986). Seismic Migration: Theory and Practice, 382 pp., Geophys. Press, London.

Strasser, U., Corripio, J., Pellicciotti, F., Burlando, P., Brock, B., and Funk, M. (2004). Spatial and temporal variability of meteorological variables at Haut Glacier d'Arolla (Switzerland) during the ablation season 2001: Measurements and simulations. Journal of Geophysical Research: Atmospheres, 109(D3).

Stuart, G., Murray, T., Gamble, N., Hayes, K., and Hodson, A. (2003). Characterization of englacial channels by ground-penetrating radar: An example from austre Brøggerbreen, Svalbard. *Journal of Geophysical Research: Solid Earth*, *108*(B11).

Swift, D. A., Nienow, P. W., and Hoey, T. B. (2005). Basal sediment evacuation by subglacial meltwater: suspended sediment transport from Haut Glacier d'Arolla, Switzerland. Earth Surface Processes and Landforms, 30(7), 867–883. http://doi.org/10.1002/esp.1197

Swipos (2022). https://www.swisstopo.admin.ch/en/geodata/geoservices/swipos.html

Swisstopo (2020). SwissAlti3D Digital Elevation Model datasets, https://www.swisstopo.admin.ch/en/home.html

SwissTopo (2021). https://map.geo.admin.ch

Taner, M. T., Koehler, F., and Sheriff, R. E. (1979). Complex seismic trace analysis. Geophysics, 44(6), 1041-1063.

Tarboton, D. G. (1997). A new method for the determination of flow directions and upslope areas in grid digital elevation models. Water resources research, 33(2), 309-319.

Taylor, J. (1997). Introduction to error analysis, the study of uncertainties in physical measurements.

Temminghoff, M., Benn, D. I., Gulley, J. D., and Sevestre, H. (2019). Characterization of the englacial and subglacial drainage system in a high Arctic cold glacier by speleological mapping and ground-penetrating radar. Geografiska Annaler: Series A, Physical Geography, 101(2), 98-117.

Tranter, M., Sharp, M. J., Lamb, H. R., Brown, G. H., Hubbard, B. P., and Willis, I. C. (2002). Geochemical weathering at the bed of Haut Glacier d'Arolla, Switzerland—a new model. Hydrological Processes 16, 959–993.

Trevisani, S., & Cavalli, M. (2016). Topography-based flow-directional roughness: potential and challenges. *Earth Surface Dynamics*, *4*(2), 343-358.

Vincent, C., Descloitres, M., Garambois, S., Legchenko, A., Guyard, H., and Gilbert, A. (2012). Detection of a subglacial lake in Glacier de Tête Rousse (Mont Blanc area, France). *Journal of Glaciology*, *58*(211), 866-878.

Vincent, C., and Six, D. (2013). Relative contribution of solar radiation and temperature in enhanced temperature-index melt models from a case study at Glacier de Saint-Sorlin, France. Annals of glaciology, 54(63), 11-17.

Vincent, C., Thibert, E., Harter, M., Soruco, A., and Gilbert, A. (2015). Volume and frequency of ice avalanches from Taconnaz hanging glacier, French Alps. *Annals of Glaciology*, *56*(70), 17-25.

Vincent, C., Kappenberger, G., Valla, F., Bauder, A., Funk, M., and Le Meur, E. (2004). Ice ablation as evidence of climate change in the Alps over the 20th century. Journal of Geophysical Research: Atmospheres, 109, Article Number 2003JD003857

Vivero, S., and Lambiel, C. (2019). Monitoring the crisis of a rock glacier with repeated UAV surveys. *Geographica Helvetica*, *74*(1), 59-69.

Wagnon, P., Ribstein, P., Francou, B., and Pouyaud, B. (1999). Annual cycle of energy balance of Zongo glacier, Cordillera Real, Bolivia. Journal of Geophysical Research: Atmospheres, 104(D4), 3907-3923.

Walder, J. S., and Fowler, A. (1994). Channelized subglacial drainage over a deformable bed. Journal of Glaciology, 40, 3-15

Warburton, J. (1992). Observations of bed load transport and channel bed changes in a proglacial mountain stream. *Arctic and Alpine Research*, *24*(3), 195-203.

Watson, C. S., Quincey, D. J., Carrivick, J. L., and Smith, M. W. (2017). Ice cliff dynamics in the Everest region of the Central Himalaya. *Geomorphology*, 278, 238-251.

Werder, M. A., Hewitt, I. J., Schoof, C. G., and Flowers, G. E. (2013). Modeling channelized and distributed subglacial drainage in two dimensions. *Journal of Geophysical Research: Earth Surface*, *118*(4), 2140-2158.

Westoby, M. J., Brasington, J., Glasser, N. F., Hambrey, M. J., and Reynolds, J. M. (2012). `structure-from-motion' photogrammetry: A low-cost, effective tool for geoscience applications. *Geomorphology*, 179, 300-314.

White, W. R., Meyer Peter, E., Rottner, J., Engelund, Ackers, P., Milli, H., ... and Toffaleti, F. (1975). Sediment transport theories. *Proceedings of the Institution of Civil Engineers*, *59*(2), 265-292.

Wilson, N. J., Flowers, G. E., and Mingo, L. (2014). Mapping and interpretation of bed-reflection power from a surge-type polythermal glacier, Yukon, Canada. *Annals of Glaciology*, 55(67), 1-8.

Wójcik, K. A., and Sobota, I. (2020). Spatial and temporal changes in ablation, distribution and evolution of glacial zones on Irenebreen, a small glacier of the High Arctic, Svalbard. Polar Science, 23, 100503.

Zekollari, H., Huss, M., and Farinotti, D. (2019). Modelling the future evolution of glaciers in the European Alps under the EURO-CORDEX RCM ensemble. The Cryosphere, 13, 1125-1146.

Zekollari, H., Huss, M., and Farinotti, D. (2020). On the imbalance and response time of glaciers in the European Alps. Geophysical Research Letters, 47, Article number 2019GL085578.

Zirizzotti, A., Cafarella, L., Baskaradas, J. A., Tabacco, I. E., Urbini, S., Mangialetti, M. and Bianchi, C. (2010). Dry–wet bedrock interface detection by radio echo sounding measurements. IEEE Transactions on Geoscience and Remote Sensing, 48(5), 2343

Zemp, M., Haeberli, W., Hoelzle, M., and Paul, F. (2006). Alpine glaciers to disappear within decades?. *Geophysical Research Letters*, *33*(13).

Zemp, M., Paul, F., Hoelzle, M., and Haeberli, W. (2008). Glacier fluctuations in the European Alps, 1850–2000. *Darkening Peaks Glacier Retreat Sci. Soc*.

VII INDEX OF FIGURES

VIII INDEX OF TABLES